UNIVERSITY OF SOUTHAMPTON

# NEOGENE BIOGENIC SILICA FLUXES IN THE EASTERN EQUATORIAL PACIFIC

by

Stephanie Jane Rance

This thesis was submitted in partial fulfilment of the requirements for the degree of Doctor of Philosophy.

Department of Oceanography

December 1997

UNIVERSITY OF SOUTHAMPTON

ABSTRACT

FACULTY OF SCIENCE
OCEANOGRAPHY

Doctor of Philosophy

# NEOGENE BIOGENIC SILICA FLUXES IN THE EASTERN EQUATORIAL PACIFIC

by Stephanie Jane Rance

Recently discovered Neogene diatom mat deposits in the eastern equatorial Pacific afford an unprecedented opportunity to quantify ancient fluxes associated with individual depositional periods and provide important new information for use in models of biogeochemical cycling in the ancient oceans on a scale directly comparable with data from the modern observations. In the equatorial Pacific, laminated diatom mat (LDM) deposits dominated by diatoms from the *Thalassiothrix longissima* Group form important horizons that can be correlated for distance of over 2000km, at key intervals associated with major change in the ocean/climate system. Bundles of mats form laminae which correspond to single, seasonal-scale deposition events. Because of their great tensile strength, individual mats and laminae can be peeled off sediment cores and analyzed directly.

This study concentrates on the youngest (Zanclean) LDM deposited cored during ODP Leg 138 with some reference to older deposits. Fine scale sediment structure was studied in resin impregnated samples using the scanning electron microscope (SEM) and back-scatter electron imagery (BSEI). Millimetre-scale subsamples were analyzed for opaline silica, organic carbon and carbonate. Modification of the Mortlock and Fröelich opal determination method allowed the estimation of lamina *T. longissima* Group content using differential dissolution. A new method of quantifying diatom frustule dissolution within deep sea sediments was developed, allowing the detection and quantification of a trend of increasing diatom frustule preservation levels with increasing sedimentary opal content.

High levels of fabric preservation associated with the dense meshwork of the diatom mats results in the preservation of lamina couplets. These couplets are interpreted as episodic mat flux events, similar to that observed in the eastern equatorial Pacific by the JGOFS Fall '92 survey, separated by more normal deep sea sedimentation patterns. Spectral analysis of lamina couplet thickness records identified two significant periodicities of 6-7 and 21 years.

Sedimentation rates for LDM intervals are calculated as 410m/Ma using two independent methods (sediment fabric and $^{3}He$ accumulation). Minimum sedimentation rates for LDM deposits (204m/Ma) are calculated by comparing the Gamma Ray Attenuation Porosity Evaluator (GRAPE) records from LDM-bearing and LDM-free sites with the insolation cycle.

The millimetre-scale sampling possible through LDM intervals enabled the construction of decadal (or shorter) scale records of silica fluxes to the deep ocean. Correlation of the records from the 60cm thick basal unit of the Zanclean LDM depositional event at Sites 847 and 850 show a remarkable similarity. Spectral analysis of these records at the two sites demonstrates the existence of cyclicities with century-scale periods.

Regional export of biogenic silica associated with the Zanclean LDM event falls in the range 0.76-2.78TmolSi/yr. This flux rate was sustained over about 1.46k.y. during the accumulation of the '4.4Ma' basal unit, and then occurred episodically (over 20-200year periods) for the next 57k.y. These fluxes represent 6-50% of annual biogenic silica deposition in the modern ocean (7.1±1.8TmolSi/yr). Organic carbon flux related to LDM deposition is estimated using (1) diatom Si/C ratios and modelled remineralization rates, and (2) comparison with the diatom rich layers of the Mediterranean sapropel S-5. These methods suggest that LDM deposition resulted in organic carbon fluxes of 5.1-18.5TmolC/yr, of which around 2.1-7.6TmolC/yr reached the deep ocean. For comparision, modern estimates of primary production range from 3700-4200TmolC/yr, of which about 1% is thought to reaches the deep ocean. LDM deposition on this scale would represents 5-21% on modern organic carbon accumulation.

LDM deposition appears to be initiated by ocean-wide processes (e.g. major climate change) that result in either (1) addition of nutrients to the ocean, or (2) the redistribution of nutrients within the ocean system. More detailed information on oxygen isotope stratigraphy and weathering regimes is needed to determine the exact temporal relationship between LDM deposition and these glaciation events.

# CONTENTS PAGE

LIST OF FIGURES

LIST OF TABLES

ACKNOWLEDGEMENTS

Firstly, I would like to thank my supervisors Alan Kemp and Peter Statham, for all the guidance and support I have receive throughout this project. I also acknowledge receipt of Natural Environmental Research Council Research Studentship GT4/93/256/G.

ODP provided the eastern equatorial Pacific samples used in this study while Nick McCave and Barbara Manigetti provided samples from the North Atlantic. Richard Brothers provided material from the Peru margin. Dan Conley and Penny King provided material during biogenic silica and carbon inter-laboratory calibration experiments. Richard Pearce provided many of the polished thin sections and initial back-scatter electron imagery photomosaics for the eastern Equatorial Pacific sediments. Franco Marcantoni carried out the helium accumulation rate measurements.

I would like to thank all the participants of the 1996 OPALEO meeting in Brest for the many useful discussions I had during the meeting. I especially thank Bob Anderson who put me in touch with Franco Marcantoni, and Mark Brzezinski whose work on diatom carbon/silica concentrations was so useful. Dave DeMaster provided a number useful details and discussions.

Instruction and technical support within Southampton Oceanography Centre were provided by Barbara Cressy, Shir Akbari, Paul Goody, Bob Foster and Kate Davis. My special thanks go to the Cartography Centre for providing colour copies at short notice. This project has benefitted from discussions with Richard Pearce, Jenny Pike, Dave Bull, Jean Dean, Penny King and numerous others. I am especially grateful to Mark Bean for sharing his expertise in computing and number crunching.

The last four years have been made all the more fun and interesting by the lunch-time crew including Dave, Richard, Jean, Matt, Emma, Sarah, Andy, David, Duncan, Helene, Lisa, Ian and of course Greg. Dave requires a special mention for putting up with me on long, but necessarily boring, trans-Alantic flights.

Last, but by no means least, my thanks to Mark who kept me (relatively) sane through long experiments and an even longer write-up. Without his support I would have finished this project a lot poorer than I am!

# CHAPTER 1: INTRODUCTION

## 1.1 BACKGROUND

The eastern equatorial Pacific is the location for up to half of global new production (Chavez and Barber, 1987; Chavez *et al.*, 1990) and is a focus for modern oceanic and climatic processes studies, such as the 1992 U.S. JGOFS program. Sedimentation in this area frequently records major palaeoceanographic events and reorganizations in the ocean-climate system (van Andel *et al.*, 1975; Mayer *et al.*, 1985; Mayer *et al.*, 1992). Material examined in this study was cored during ODP Leg 138 from equatorial sites between 90° and 110°W and shows evidence for repeated biosiliceous flux events (Kemp and Baldauf, 1993; Kemp, 1995). These flux events are recorded by laminated diatom mat (LDM) deposits, each mat consisting of a dense meshwork of the pennate diatom *Thalassiothrix longissima* in near-monospecific assemblages. Laminations are preserved by the dense meshwork of elongate frustules and the rapid deposition overwhelming the benthos and reducing bioturbation to insignificant levels (Kemp and Baldauf, 1993; King *et al.*, 1995).

## 1.2 PREVIOUS RESEARCH ON LAMINATED DIATOM MAT DEPOSITS

Laminated diatom mat deposits were first recognized in ODP Leg 138 sediments (Kemp and Baldauf, 1993) and have since been identified in a number of other sites in the eastern equatorial Pacific, North Pacific, equatorial Atlantic and Southern Oceans (D. DeMaster, pers. comm.; Kemp *et al.*, 1993; Bodén and Backman, 1995; Dickens and Barron, 1997). These studies found that LDM deposits tend to occur beneath frontal regions, similar to other near-monospecific diatom deposits (e.g. Gardener and Burkle, 1975; Mikkelsen, 1977; Jordan *et al.*, 1991). The frontal depositional mechanism for LDM accumulation is based on analogy with observations of concentrations of the buoyant diatom *Rhizosolenia* spp. during the JGOFS Fall '92 survey (Barber, 1992; Yoder *et al.*, 1994; Kemp *et al.*, 1995; Smith *et al.*, 1996). A detailed discussion of previous research related to LDM deposits and depositional mechanisms is given in Chapter 2.

Previous studies have focused on sedimentological descriptions and the depositional mechanism of LDM sediments (Kemp and Baldauf, 1993; Bodén and Backman, 1995; Kemp, 1995; Kemp *et al.*, 1995; Pearce *et al.*, 1995). This study aims to integrate detailed sedimentological studies with high-resolution biogeochemical analysis of biogenic silica and

carbon in order to investigate the factors controlling LDM deposition on both local and global scales.

## 1.3 LAMINATED DIATOM MAT UNIT NAMES USED THROUGHOUT THIS STUDY

Initial studies of LDM deposits in the eastern equatorial Pacific region found LDM deposits occurred intermittently between 15 and 4.4Ma, concentrated in restricted intervals. For convenience LDM packets were referred to using the period over which they were deposited, e.g the Zanclean or '4.4Ma' LDM deposits, on which this study concentrates (Kemp and Baldauf, 1993; Kemp, 1995; Kemp *et al.*, 1995; Pearce *et al.*, 1995). These depositional periods were calculated using biostratigraphic datums derived from the timescale of Berggren *et al.* (1985a,b). Since the publication of these papers this timescale has been superseded by those based on the revised geomagnetic polarity timescale (GPTS) of Cande and Kent (1992). In the interests of consistency with previous work on the LDM deposits (Kemp *et al.*, 1993; Kemp, 1995; Kemp *et al.*, 1995; Pearce *et al.*, 1995) and to avoid confusion with timescales published after this study (e.g. a recalculation of Shackleton *et al.* (1996) timescale which takes the rapid sedimentation rates of the LDM units into account), this thesis continues to use the original (Berggren, 1985) LDM depositional periods to refer to LDM packets. For example, the Zanclean or '4.4Ma' LDM depositional event occurred between 4.78 and 4.58Ma on the Cande and Kent (1992) timescale.

## 1.4 TIMESCALES USED IN THIS STUDY

Ages are assigned to the sediment used in this study using the occurrence of biostratigraphic and geomagnetic datums. These sediments were cored during 1991, prior to the publication of the most recent revision of the GPTS by Cande and Kent (1992). Consequently the published ages for these sediments are based on the older biostratigraphic timescale of Berggren *et al.* (1985a, b) which is based on the GPTS of LaBreque *et al.* (1977). In this study datum ages are reassigned using the most recent biostratigraphic timescales (Berggren *et al.*, 1995; Shackleton *et al.*, 1995; Backman and Raffi, in press) which are based on the Cande and Kent (1992) GPTS.

## 1.5 STRUCTURE OF THESIS

Regional oceanography of the eastern equatorial Pacific region is summarized in Chapter 2, including discussion of modern circulation patterns, interannual variability and

palaeoceanography. A review of the literature on the effect of physical processes on biological production and the influence of positively buoyant diatoms on sedimentation patterns is also given. Chapter 3 (Experimental Methods) gives a description of observational and analytical techniques used during this study. Modifications to published methods are detailed and a new method to quantify dissolution levels in diatom frustules is presented.

The results of sedimentological studies of the '4.4Ma' LDM are given in Chapter 4 (Sedimentology). These are analyzed using spectral analysis to investigate the laminated sections. Quantification of dissolution levels within the LDM sections provides evidence for rapid sinking and sedimentation rates related to LDM deposition. Methods of calculating timescales and sedimentation rates associated with accumulation of the '4.4Ma' LDM basal unit are reviewed in Chapter 5 (Timescales, Correlation and Sedimentation Rates). The sedimentation rates used in the estimation of regional fluxes are also presented. Chapter 6 (High Resolution Results) gives the results of millimetre-scale opal measurements through the '4.4Ma' LDM from two sites over 2000km apart. The records show a remarkable level of statistical correlation and demonstrate a number of 70-900 year periodicities.

Chapter 7 (Implications for Global Biogeochemical Cycling) uses the results of Chapter 4, 5 and 6 to investigate the implications of LDM deposition for global biogeochemical fluxes. Additional measurements of opal content are presented to support the argument for increased silica availability during the deposition of LDM sediments. These results are evaluated using a simple box model of the global silica cycle. The findings of this study are collated and summarized in Chapter 8 which also contains suggested directions for further research.

# CHAPTER 2: OCEANOGRAPHY OF EASTERN EQUATORIAL PACIFIC REGION

## 2.1 INTRODUCTION

This chapter describes the physical oceanography of the eastern Equatorial Pacific region and examines the ecology of mat forming diatoms found in LDM deposits. The frontal deposition model suggested by Kemp *et al.* (1993), Barber (1993) and Yoder (1995) to explain the emplacement of these sediments is introduced. Locations of ODP and DSDP sites and a summary of LDM occurrence are given in Figure 2.1. Plate tectonic back-tracking of the ODP site positions shows the LDM sediments were deposited in two separate areas; (1) within 2° of the Equator; and, (2) over the Costa Rica Dome (Fig. 2.2).

## 2.2 MODERN CIRCULATION PATTERN OF THE EASTERN EQUATORIAL PACIFIC REGION

### 2.2.1 MODERN CIRCULATION PATTERNS

The circulation and nutrient distribution of the eastern Equatorial Pacific region, are summarized by Wyrtki and Kilsonsky (1984). Between 4°N and 9°N the surface flow is generally to the west, in the North Equatorial Countercurrent (NECC); to the south and north the surface waters flow to the east in the South and North Equatorial Currents (SEC and NEC) respectively (Fig. 2.3). The Equatorial Undercurrent (EUC) forms a localized east-west flow approximately 300km wide and symmetrical about the Equator between depths of 20-50m to 220-250m (Wyrtki, 1966).

Superimposed on this zonal circulation is a mean meridional circulation pattern related to the equatorial divergence. Compared with the zonal circulation, this meridional circulation is comparatively weak (less than 1Sv compared to 10-20Sv) but has important biogeochemical consequences. Equatorial divergence is caused by trade winds carrying surface waters towards the poles. These surface waters are replaced by cool, nutrient-rich waters from depths of around 100m that form a 'cold tongue' along the equator. To the north, this tongue reaches 1-3°N, where it is terminated by downwelling of SEC waters along the Equatorial Front. To the south the flow is unimpeded and productivity is enhanced as far south as 11°S (Bender and McPhaden, 1990).

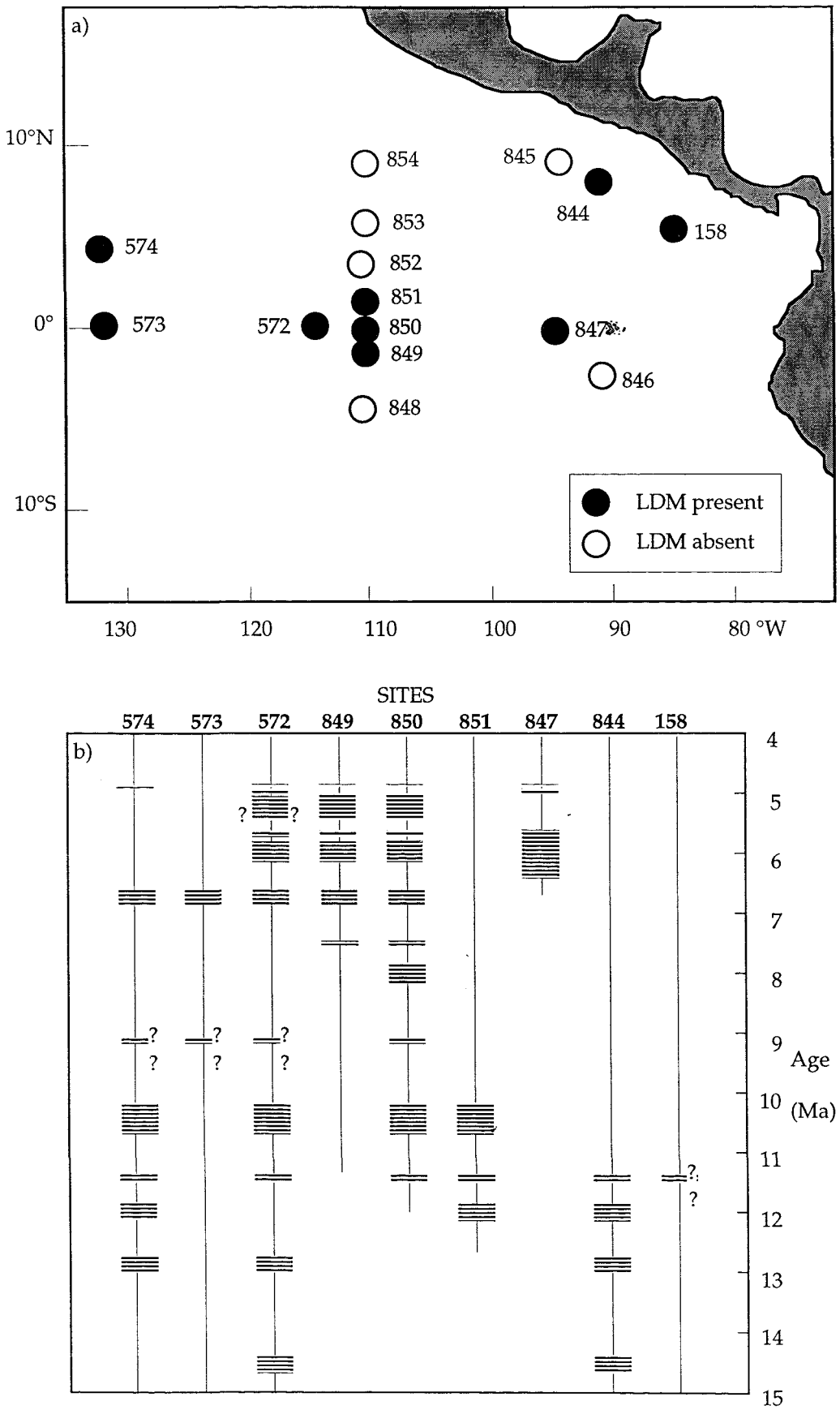


Figure 2.1. a) Location of ODP and DSDP drill sites in the eastern Equatorial Pacific region showing sites containing LDM deposits. b) Periods of LDM occurrence at these sites plotted against time demonstrating discrete periods of widespread LDM deposition (? denotes weakly developed sections). See text for futher discussion.

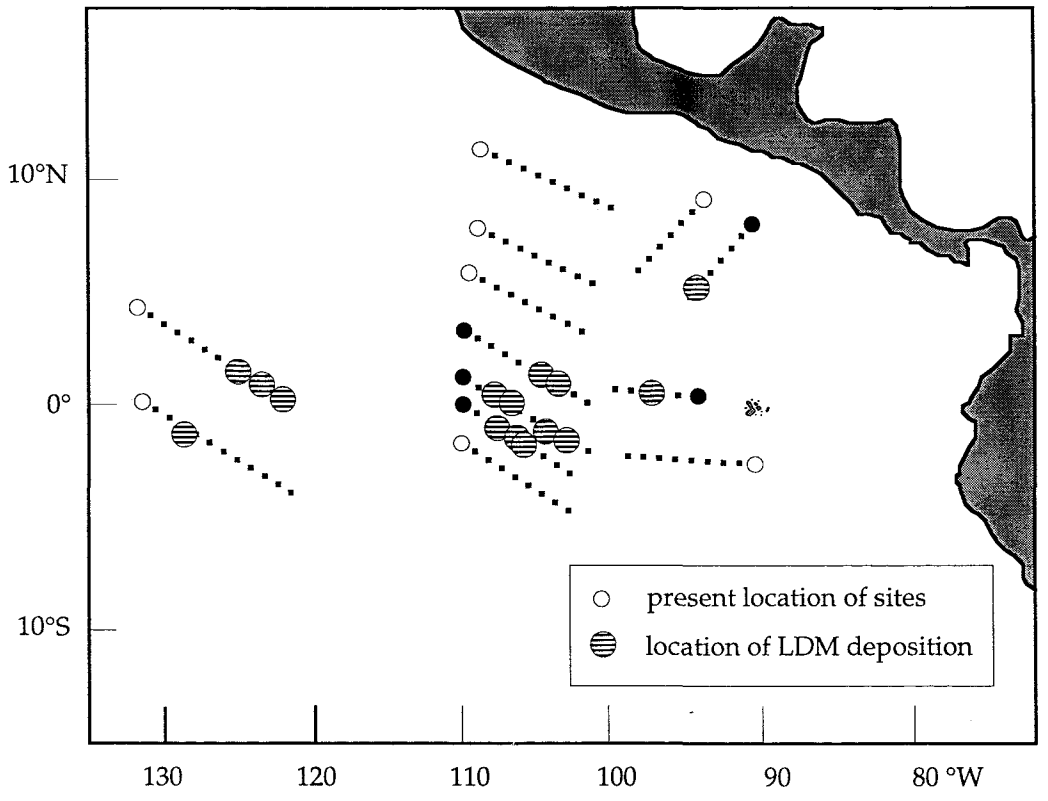


Figure 2.2. Backtracked location of LDM deposition at ODP Leg 138 and DSDP Leg 85 sites. Data from van Andel *et al.* (1975) and Duncan and Clague (1985). Note the cluster of deposition located within 2° of the Equator. Deposits found at Site 844 correspond with the location of the Costa Rica Dome upwelling zone. Data not available for sites 158 and 572.

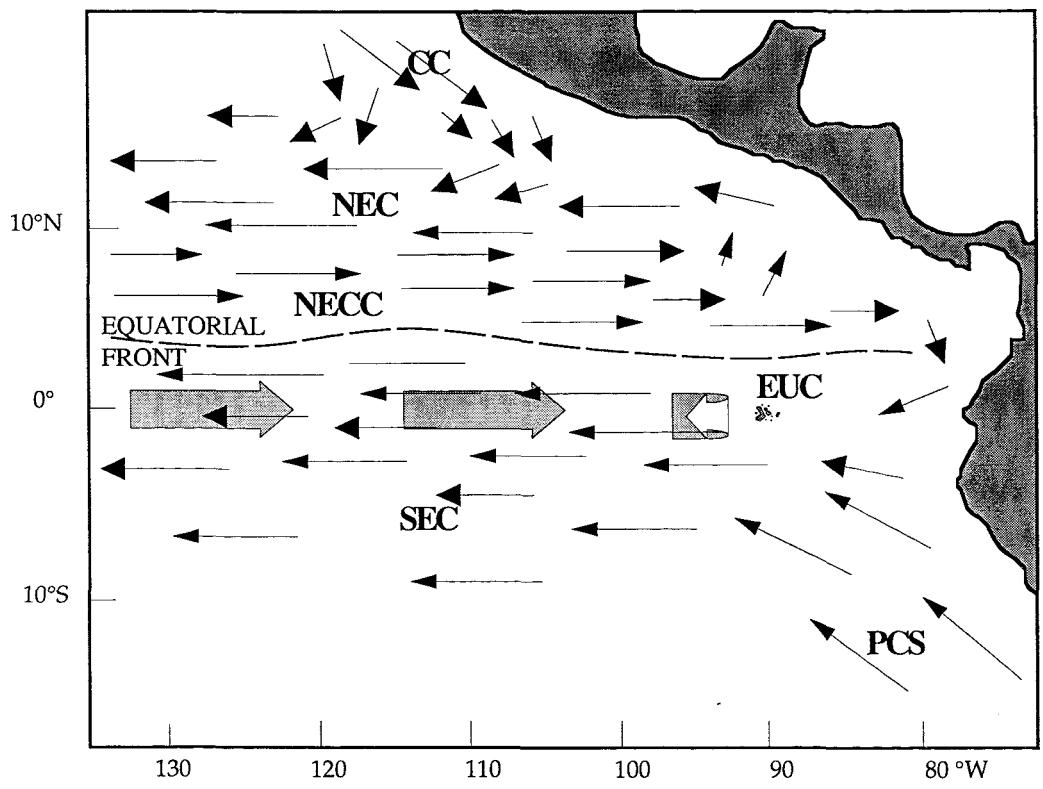


Figure 2.3. Major zonal surface and subsurface currents in the Eastern Equatorial Pacific, modified from Wyrtki (1966). NEC - North Equatorial Current, NECC- North Equatorial Countercurrent, SEC - South Equatorial Current, EUC - Equatorial Undercurrent, CC- California Current, and PCS - Peru Current System.

Surface Current

Subsurface Current

This ocean circulation pattern reflects atmospheric circulation patterns and the change in sign of the Coriolis Force across the equator. The asymmetry of surface currents to the north and south of the Equator reflects the general position of the inter-tropical convergence zone (ITCZ), marking the convergence between the north-east and south-east trade winds. Seasonal variations in the movement of the ITCZ and associated changes in the wind strength are reflected in equatorial current system (Wyrtki, 1966). The zonal circulation pattern is most strongly developed when the ITCZ is in its most northerly position (around 10°N) between August and September. Between February and April, the ITCZ is in its most southerly position, suppressing the development of the NECC and SEC.

### 2.2.2 The Equatorial Front

In the Equatorial Pacific, the Equatorial Front runs approximately east-west, between 1° and 3°N, separating the tropical water of the NECC, from the cooler, more saline water of the SEC (see Figure 2.3). At the Equatorial Front, the colder more saline water of the dense SEC sinks beneath the warmer, less saline water of the NECC. At the surface these vertical circulation patterns are mirrored in breaking waves (white caps) caused by water turbulence and mixing (Yoder *et al.*, 1994). As with fronts found in coastal waters, the Equatorial Front is associated with enhanced biological activity.

### 2.2.3 Interannual variability

#### 2.2.3.1 Tropical instability waves (TIWs)

Propagation of seasonal TIW along the Equatorial Front causes significant variability in the circulation patterns (Fig. 2.4). These features were first recorded in the Atlantic Ocean (Düing *et al.*, 1975), and TIW have since been observed on infrared satellite images of the Pacific Ocean as undulations of the Equatorial Front (Legeckis, 1979; Legeckis *et al.*, 1983). Current measurements and drifting buoy experiments have now provided more information on circulation patterns and rates (Hansen *et al.*, 1980; Pullen *et al.*, 1987; Halpern *et al.*, 1988). The waves are best developed in the eastern Pacific (90°W to 140°W, occasionally reaching as far as 170°W (Legeckis *et al.*, 1983; Perigaud, 1990)) having periods of 15-35 days, wavelengths of 400-1600km and westward phase velocities of 40-90cms$^{-1}$ (Legeckis *et al.*, 1983; Pullen *et al.*, 1987; Eldin *et al.*, 1992).

TIWs are generated by shearing between the NECC and SEC, the SEC and the northern flank of the Equatorial Undercurrent, and within the SEC itself (Philander, 1978; Wilson and Leetmaa, 1988; Luther and Johnson, 1990). This TIW occurrence is highly correlated with direction of zonal surface flow on seasonal timescales. Consequently, TIW are subject to significant seasonal and interannual variability (e.g. Philander *et al.*, 1985). During periods of strong westward flow of the SEC, TIW activity is strong. Conversely, during the boreal spring reversal of the SEC, or periods of weak SEC flow related to El Niño-Southern

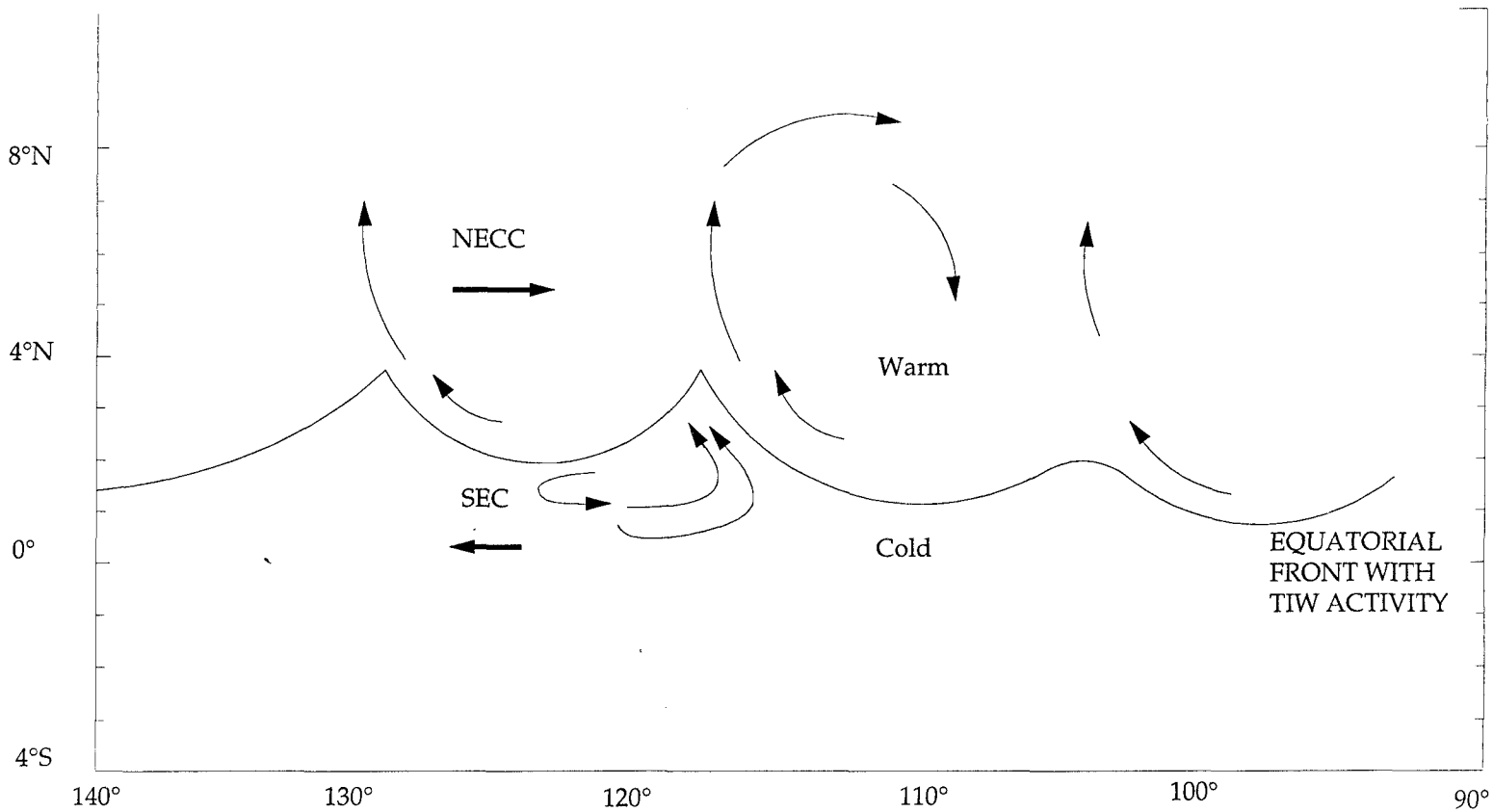


Figure 2.4. Tropical instability waves in the Equatorial Pacific showing the direction of drift of buoys around marcoscopic eddies (modified from Legeckis, 1983 and Hanson and Paul, 1984).

Oscillation (ENSO) events, TIW are weakly developed. Annually the onset of TIW formation is variable, ranging from May to July, after this they are strong for four to six months (Legeckis *et al.*, 1983). Towards the end of the seasonal cycle waves tend to be confined to the easternmost area (90 to 100°W) with shorter wavelengths and periods (Legeckis *et al.*, 1983).

#### 2.2.3.2 El Niño events

Under 'normal' (non-El Niño) conditions the easterly trade winds combined with the Earth's rotation cause a steady movement of water away from the equator in both hemispheres (Ekmann Transport). An El Niño occurs when the trade winds are suddenly weakened allowing the warm water accumulated in the western Pacific to return eastward as equatorially trapped Kelvin waves (Cane, 1983). Apart from increases in the sea surface temperature (SST) of the eastern Equatorial Pacific region, this movement of water raises the thermocline in the western Pacific and, with the arrival of the Kelvin waves, lowers the thermocline in the east. Lowering the thermocline and slackening of the trade winds means that equatorial upwelling is weaker and entrains water from the mixed layer rather than from below the thermocline. As the cold region warms, atmospheric convection, usually absent over the cold water, spreads eastward towards the central Pacific and the trade winds west of the new convective centre are weakened or reversed. These changes feed back into the ocean system, building on the initial effects to form a full-blown El Niño event. It is not clear whether El Niño events are caused by the slackening trade winds causing the SST to rise, or by a rise in SST causing the trade winds to slacken (Philander, 1990). An El Niño is usually followed by an anti-El Niño (La Niña). This is recovery to non-El Niño conditions, immediately followed by an intensification of the trade winds above their non-El Niño levels resulting in a period of unusually strong equatorial upwelling (Fielder *et al.*, 1992) and increased TIW activity.

## 2.3 PALAEOCEANOGRAPHY OF THE EASTERN EQUATORIAL PACIFIC REGION

### 2.3.1 Position of Equatorial Front over the last 10 m.y.

Diachronous radiolarian events in Leg 138 sites over the last 3 m.y. show a close correspondence between temporal-spatial patterns of first and last appearance of species and the modern patterns of temperature, productivity and near-surface circulation (Moore *et al.*, 1993). Based on this observation, similar patterns of extinction and first occurrence can be used to reconstruct circulation patterns over the last 10 m.y. (Moore *et al.*, 1993). Prior to approximately 7.9Ma (based on Berggren *et al.* 1995 time scale) strong zonal gradients at 2°-3°N and 3°-4°S suggest the SEC was slightly north of its modern position. Conversely, between 6.6Ma and 3.9Ma the southern boundary of the NECC appears to have been located at 0°-1°N, south of its modern position. The northern boundary of the NECC was also located

further south than at present. Changes between 3.9Ma and 3.6Ma marked the onset of the modern circulation pattern, possibly related to the closure of the Panama Isthmus cutting the supply of water to the NEC, causing both the NEC and the NECC to shift northwards (Moore *et al.*, 1993). The shifts in the Equatorial Front are consistent with the locations of LDM deposits reported in the eastern Equatorial Pacific (Kemp and Baldauf, 1993), see Figure 2.5.

### 2.3.2 Ancient El Niño Events

To prove that an El Niño-type event occurred in the geological record, evidence is needed for both; (1) a demonstrably short-lived event; and, (2) advection of warm coastal water into the SE Pacific (DeVries, 1987). The glaciological records of Andean highland ice-cores are the only source of data meeting both these criteria. These records reach back 1500 years, before this there is no single line of evidence that can be used to provide proof of El Niño events. Geological data can give evidence of warm periods, but cannot distinguish between water masses present for months or centuries ( DeVries, 1987). Varved sediments form an exception to this generalization, but it is notoriously difficult to prove timescales of deposition for laminated sediments (Weinheimer *et al.*, 1986). Possible senarios involving the presence or absence of warm coastal water are illustrated in Figure 2.6.

El Niño events have been identified on the basis of the radiolarian flux and assemblage (Weinheimer *et al.*, 1986). The diminishing strength of the California Current during El Niño conditions results in high standing crops of both warm and cold radiolarian species over the southern California continental shelf. This results from (1) warm species diffusing in from the west (central gyre water) and south (gyre and eastern tropical waters); and, (2) a strongly developed Californian Countercurrent aiding the build-up of a geostrophic dome off the Californian Coast allowing cold faunas to invade from the north. Similar high levels of mixed warm and cold radiolarian species are found in Holocene laminated sediments of the Santa Barbara Basin. Using lamina counts, these assemblages can be correlated to known El Niño events in 1957-1958 and 1964. Using the same method, El Niño events have been identified in the laminated sedimentary rocks from the Monterey Formation at Lompoc dated at about 6.6Ma (using radiolarian dating related to Berggren 1995 timescale, Weinheimer *et al.*, 1986). Of the 21 paired layers sampled, only one year met the criteria of exhibiting a greater percentage of both warm and cold species than the bounding years. In laminated sediments at Newport Bay, about 8.8Ma old (again dated using radiolarian occurrences on the Berggren 1995 timescale, Weinheimer *et al.*, 1986), similar analysis suggests that El Niño-type events occurred one year in every four. Diatom and foram data indicate that the 6.6Ma time-slice fell in a cold interval whereas the 8.8Ma time-slice was during a warm period (Barron and Keller, 1983). Weinheimer *et al.* (1986) suggested that the palaeotemperatures reported for these periods are related to the frequency of El Niño events rather than longer term periods of warming and cooling.

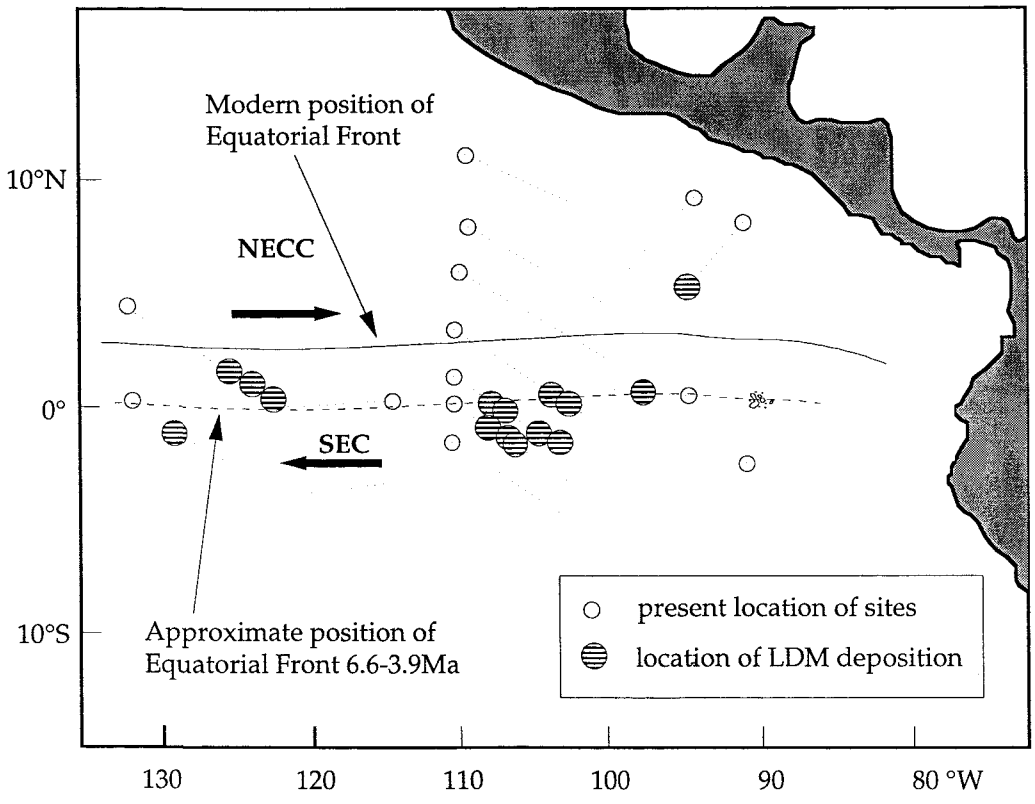


Figure 2.5. Approximate position of the Equatorial Front between 3.9 and 6.6Ma based on diachronous radiolarian events identified by Moore *et al.* (1993). This estimated position agrees closely with the location of LDM deposition calculated using backtrack data.

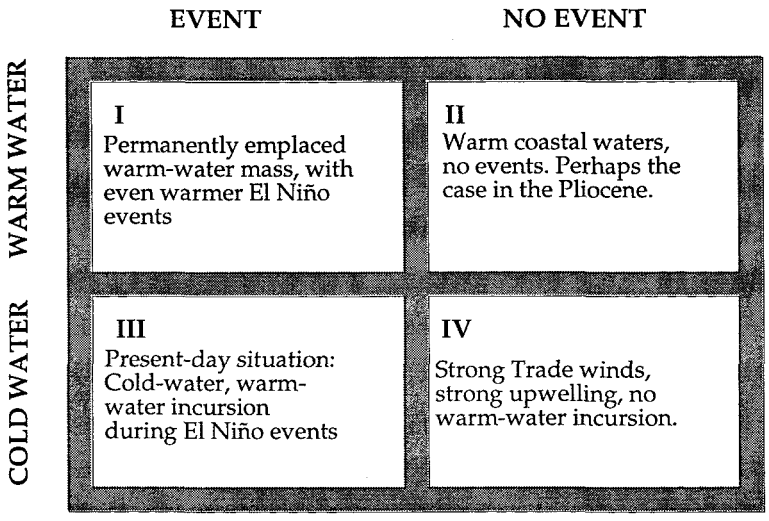


Fig. 2.6. Table of senarios for warm-water El Niño events and El Niño-like conditions (warm water) and absence of these conditions. Geological evidence of cold water off the coast of Peru and short lived, warm-water events is needed to demonstrate the evidence of past El Niño events (senario III). The results of most studies do not permit a distinction between senarios II and III (modified from Devries, 1987). The two extremes of El Niño events against a background regional of global warming, and an absence of such events despite intensified South Pacific circulation are given by senarios I and IV respectively. The modern situation is that of senario III, normally cold waters are replaced episodically by warm water for a period of months. Senario II represents El Niño like-conditions lasting for centuries with warm coastal waters present off-shore for long periods, possibly with oceanic productivity patterns and onshore precipitation patterns that resemble that of recent El Niños.

On the basis of physical oceanographic extent and depth of the oxygen minimum zone inferred from radiolarian distribution, Casey *et al.* (1989) divided modern El Niño events into 'strong' and 'weak' events. Reconstructions of radiolarian abundance at about 6.1Ma indicate that circulation was analogous to the modern regime with 'weak' and 'strong' El Niño events. Similar reconstructions at 7.2Ma and 8.8Ma show increases in radiolarian abundances, taken to indicate the existence of El Niño-type events, but these time-slices do not show the variation between 'strong' and 'weak' events. Casey *et al.* (1989) use this evidence to suggest that El Niño events directly analogous to modern observations did not occur before 6.1Ma.

### 2.3.3 The importance of the Panama Gateway

Changes in benthic foraminiferal and sediment distribution patterns on the Pacific and Caribbean sides of NW South America indicate a change in deep water circulation patterns at 15.2Ma that have been related to the early tectonic uplift of the Panamanian Sill (Keller, 1985; McDougall, 1985). This was followed by abrupt palaeobathymetric changes across the Panamanian Sill during the middle Miocene, 13.0-12.1Ma (Duque-Caro, 1990). The radiolarian and foraminifera records indicate a continued shallowing of the sill from late Miocene to Pleistocene times (Bandy, 1970; Duque-Caro, 1972; Bandy and Casey, 1973; Duque-Caro, 1975).

Immediately following the uplift of the Panamanian Sill to 1000m (at around 12.1Ma) a distinctive Pacific benthic foraminiferal fauna developed, extending from Ecuador to California (Duque-Caro, 1990). This pattern of occurrence has been interpreted as evidence of a circulation barrier between the Pacific and Caribbean, formed by an intensification of the California Current between 12.1 and 6.5Ma (Duque-Caro, 1990). Radiolarian data from DSDP and land-based sites along the California coast is not consistent with this hypothesis. Samples taken from datums at 5.6Ma, 8.8Ma and 10.6Ma show the California Current was strongest at 5.6Ma during the Neogene cold period, but weakened and narrowed during warm periods (8.8 and 10.6Ma), diverting into the coast at around 35°N (Weinheimer *et al.*, 1986).

Palaeobathymetric studies show three major interoceanic passageways through the Panamanian island arc; (1) the Panama Strait, now the Panama Canal Basin; (2) the San Carlos Basin in northern Costa Rica and southern Nicaragua; and, (3) the Atrato Basin in NW Columbia (Collins *et al.*, 1996 and references therein). By around 8.8Ma only the strait through the Atrato Basin was open with a water depth 200-750m (Duque-Caro, 1990; Collins *et al.*, 1996). Tectonic activity thorough the Pliocene-Pleistocene (van Andel *et al.*, 1971; Emiliani *et al.*, 1972) resulted in further reorganization of the central American archipelago. The Atrato Basin records a shallowing to around 150m by 5.3Ma (Duque-Caro, 1990), while the strait through the Panama Canal Basin re-opened to depths greater than 200m deep between 7.1 and 6.5Ma (Collins *et al.*, 1996). The sediment deposited in the Panama Canal

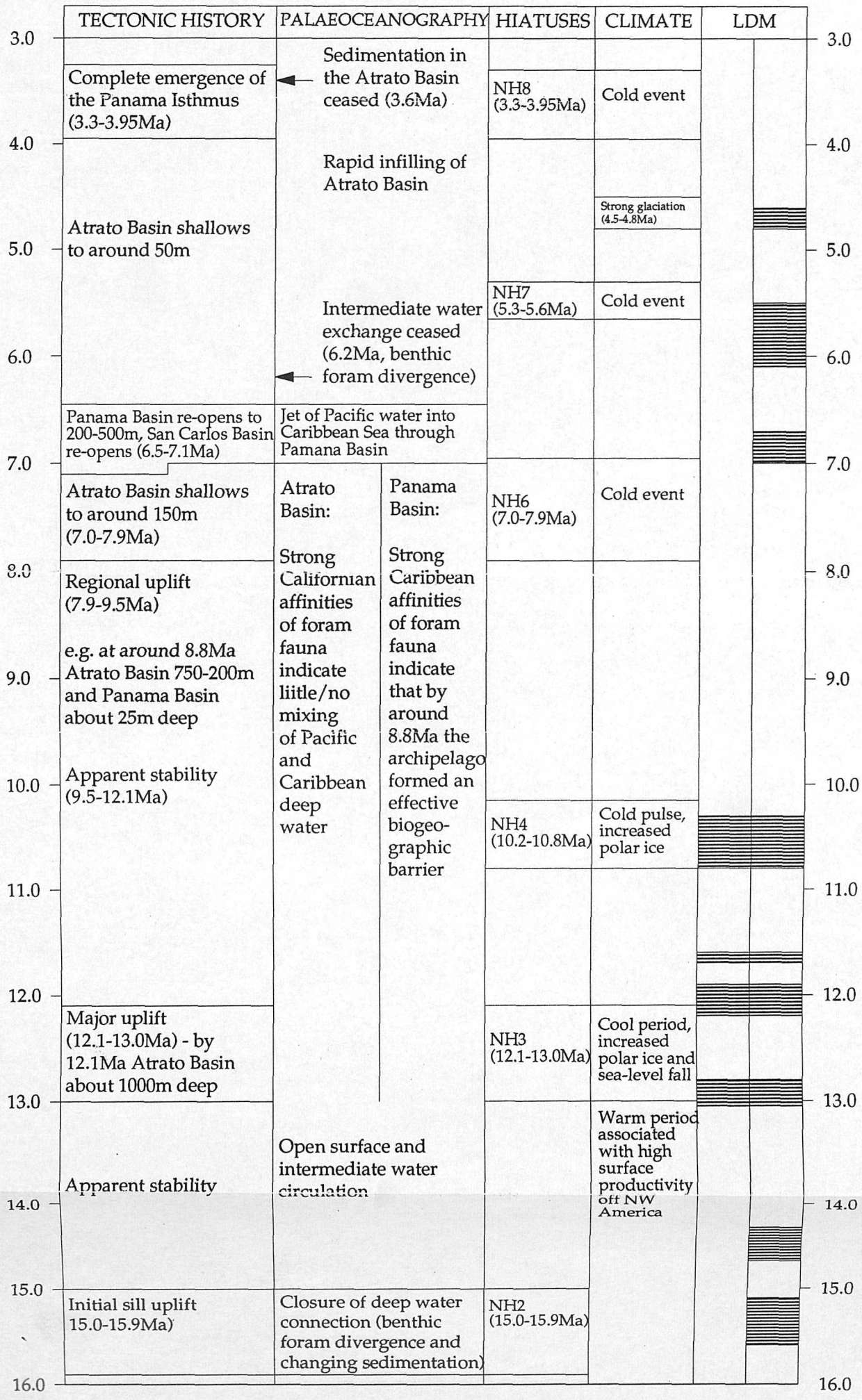


Figure 2.7. Schematic summary of tectonic history and influence of the Panama Isthmus on the palaeoceanography of the eastern Equatorial Pacific region over the period 3.0Ma to 16.0Ma. Variation in the climate, LDM deposition and regional hiatus development are shown for comparison. LDM deposition only occurred during the closure of the Panamanian Seaway to surface and intermediate waters. There is no evidence for LDM accumulation either during the gradual restriction of deep water circulation or after complete closure, modified from Duque-Caro (1990) with additional data from Emiliani (1971), Kemp*et al.* (1993), McDougall (1996) and Collins*et al.* (1996). See text for further discussion and references.

Basin over this period consist of coarse grained sandstone with thick prograding cross-sets with the grain size decreasing away from the axis of the strait, interpreted as deposited beneath a jet of the NECC-EUC as it passed through the narrow Panamanian Strait (Collins *et al.*, 1996). The unusual co-occurrence of foraminifera typical of both cool and warm waters on the Caribbean side of the archipelago is interpreted as mixing of the jet waters from the cool Pacific with the warm water of the Caribbean Sea (Collins *et al.*, 1996). The onset of the jet approximately coincides with major erosion of the Blake Plateau, associated with the onset of strong Gulf Stream circulation at around 7.9Ma (Emiliani *et al.*, 1972). At this time, surface water mixing between the Pacific and Caribbean was also re-established in the Atrato Basin (Duque-Caro, 1990). At 6.2Ma the strait through the Panama Canal Basin was finally closed, coinciding with the divergence of deep and intermediate benthic foraminiferal assemblages in the Caribbean Sea and Pacific Ocean. The foraminifera also reflect a change in the temperature of the bottom water masses at this time (McDougall, 1996).

Following the emergence of the Panama Canal Basin, the Atrato Basin continued to shallow gradually despite an overall increase in sea level (Duque-Caro, 1990). Sedimentation ceased at approximately 3.6Ma, coinciding with the Early Pliocene Hiatus NH8 (3.9-3.3Ma, Barron and Keller, 1983; 1986). This hiatus marks the base of terrestrial formations exhibiting major intermingling of terrestrial faunas between North and South America, and is associated with final emergence of the Panama Isthmus (3.7-3.3Ma) (Saito and Ozima, 1976; Keigwin, 1978; Keigwin, 1982; Duque-Caro, 1990). The above discussion of the Panamanian uplift is summarized in Figure 2.7.

**2.3.3.1 Modelled ocean circulation related to the Panama Gateway**

Modelled ocean circulation shows that upwelling and surface circulation in the eastern Equatorial Pacific is not strongly affected by replacing the Panama Isthmus with a sill with depths of either 2711 or 4100m although the Gulf stream is weakened consistent with observed erosion patterns over the Blake Plateau (Mikolajewicz *et al.*, 1993). But these results should be treated with caution, since it is known that upwelling in this region is due to coupled ocean-atmosphere interactions; in the model atmospheric forcing is fixed which may artificially constrain upwelling (Mikolajewicz *et al.*, 1993).

Under modern conditions, the long fetch of the trade winds coupled with the low salinity of the Pacific Ocean, results in the western Pacific having a higher surface topography than the western equatorial Atlantic (mean sealevels are 80cm higher in the western Pacific relative to eastern levels). With the isthmus removed, this topography is reduced to 60cm in the western Pacific and rises by 20cm in the western Atlantic. This hydrostatic head causes a west-east flow of around 10Sv from the Pacific to the Atlantic, through the Panama Gateway

(Mikolajewicz *et al.*, 1993). The trade winds produce an east-west surface current, analogous to the SEC, of around 1Sv, but the dominant flow is west-east, analogous to the modern NECC-EUC flow. The model does not constrain the effect of changing the horizontal extent of the gateway, or the effect of an island archipelago between the two land masses making any direct interpretation of the results tenative.

## 2.4 BIOLOGICAL OCEANOGRAPHY OF THE EASTERN EQUATORIAL PACIFIC REGION

### 2.4.1 MODERN BIOLOGICAL PRODUCTIVITY IN EEP REGION

New production in the Equatorial Pacific is estimated to contribute 18-56% of the total global new production (Chavez and Barber, 1987). Difficulties encountered in constraining estimates of new production in this region include (1) the level of interannual variability in production related to El Niño events; and, (2) uncertainties in the value chosen for new production as a fraction of total production.

Despite the availability of nutrients, new production as a proportion of total production in the eastern equatorial Pacific region varies from low (Murray *et al.*, 1989; Dugdale *et al.*, 1992) at 150°W, to only moderately high (Chavez and Barber, 1987). Since export production is low compared to the nutrient availability, this region is defined as HNLC (High Nitrate, Low Chlorophyll, e.g. Walsh, 1976; Thomas, 1979; Cullen, 1991). Modelling ecosystems suggests that silica ($Si(OH)_4$) limitation will occur in upwelling areas, except where there is a poleward undercurrent or $Si(OH)_4$ concentrations are enriched through silica regeneration (Dugdale *et al.*, 1995). Silica limitation has been used to interpret the relatively low productivity in the Peruvian upwelling at 15°S (Dugdale *et al.*, 1992) and also to explain the HNLC conditions in the eastern Equatorial Pacific upwelling region (Bender and McPhaden, 1990).

### 2.4.2 THE FRONTAL DEPOSITION MODEL

The current model for deposition of laminated sediments in the eastern Equatorial Pacific (Kemp, 1995; Kemp *et al.*, 1995) is based on analogy with observations of the Equatorial Front during the JGOFS Fall '92 survey (Barber, 1992; Yoder *et al.*, 1994). Diatoms growing in the nutrient rich waters of the equatorial upwelling region are advected north and south within the flow of the SEC. To the north these waters sink below the warmer waters of the NECC, see Figure 2.8. Most plankton carried with the subducted waters is removed from the euphotic zone and are presumably recycled within the water column, but the diatoms with an internal buoyancy control are able to return to the surface waters. This results in near-monospecific concentrations of buoyant *Rhizosolenia* spp. diatoms in the warm surface waters immediately north of the front. Rapid depletion of the available nutrients and the warmer conditions in

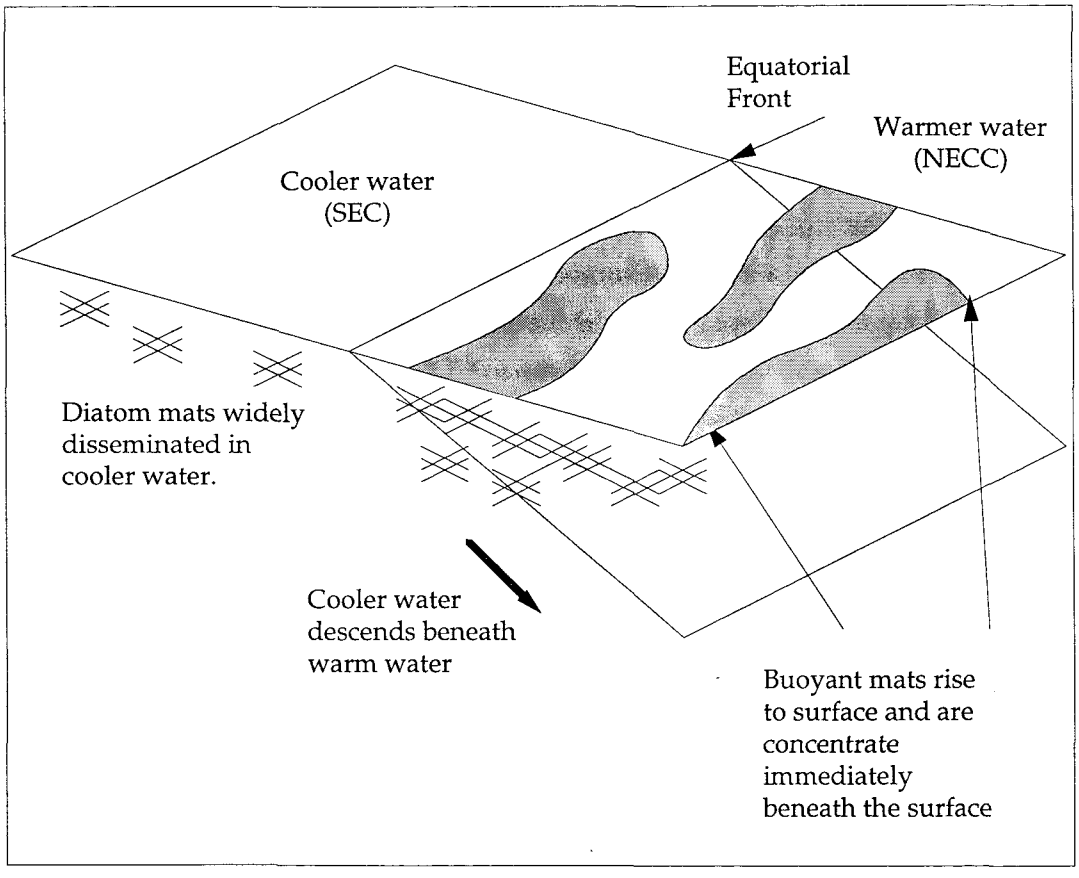


Figure 2.8.Frontal zone model for the concentration of diatom mats, after Kemp *et al.* (1995). Diatom mats are widely disseminated and growing actively in the cooler water upwelled along the equator. These mats are carried to the north in the divergent waters. As the cooler water meets the warm waters of the NECC along the Equatorial Front they descend below the less dense (warmer and fresher) water. The positive buoyancy of the diatom mats in the descending water mass allows them to rise up to the surface where they form patches and streamers a few metres below the surface on the northern side of the front.

these waters results in the death and subsequent mass sinking of the surface diatom concentrations (Smith *et al.*, 1996).

Similar deposits of giant diatoms have been cored beneath the Equatorial Front (Gardener and Burkle, 1975; Stabell, 1986) and the Sub-Arctic Front in the Atlantic Ocean (McCave and Party, 1994; Bodén and Backman, 1995), the polar front in the North Pacific Ocean (Dickens and Barron, 1997) and the Antarctic Polar Front. These occurrences suggest that this frontal mechanism is responsible for the periodic, rapid removal of large quantities of biogenic silica and associated organic carbon from the ocean reservoir.

### 2.4.3 The effect of tropical instability waves on biological processes

During the passage of TIWs along the Equatorial Front observed during the JGOFS Fall '92 study, concentrations of the mat forming diatom *Rhizosolenia* spp. with associated high chlorophyll (Yoder *et al.*, 1994) formed an undulating dark line running approximately east-west across the eastern Equatorial Pacific observed by satellites, aircraft, ships and the Space Shuttle Atlantis (Yoder *et al.*, 1994). Similar features have been recorded by NASA astronauts, between 2° and 7°N latitude and 105° and 170°W longitude, on six separate occasions since 1984 (Yoder *et al.*, 1994). All of the observations of a visible line marking the Equatorial Front by NASA astronauts were made between August and the following January, the period for TIW formation and propagation. The model proposed to account for *Rhizosolenia* concentrations requires strong convergence along the Equatorial Front. The common factor of strong current and convergence rates may explain why visible fronts (caused by both *Rhizosolenia* patches and breaking waves) are observed only during the TIW season and within the longitudinal boundaries where the waves are common (Yoder *et al.*, 1994). Maximum convergence rates and diatom concentrations are found along the leading edge of TIW peaks (Figure 2.9). What is still unclear is why a diatom species typical of low nutrient, oligotrophic regions, such as *Rhizosolenia*, was growing so prolifically in an upwelling region.

TIW activity has also been suggested to explain the occurrence of *Rhizosolenia* spp. mats, thought to be derived from the frontal zone concentrations, in sediment traps as far as 5° north during the JGOFS Fall '92 surveys (Smith *et al.*, 1996). Drifting buoy experiments to the north of the Equatorial Front show large-scale anticyclonic eddies translating westwards with the same velocities as the TIW activity along the front (Fig. 2.9, Hansen *et al.*, 1980). Transport of the diatom material within these eddies would result in the occurrence of diatom mats in the more northerly sediment traps.

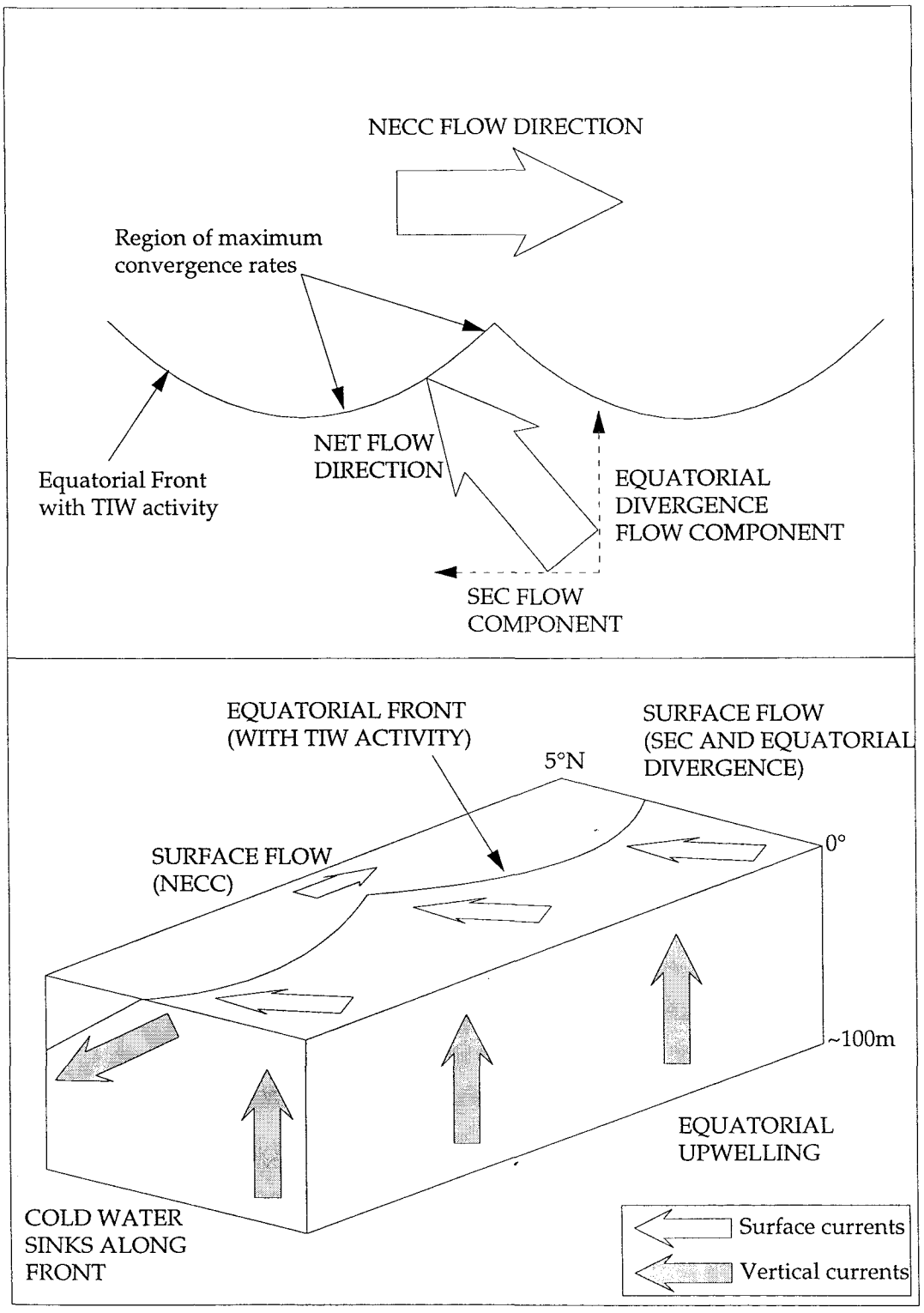


Figure 2.9. Schematic figures showing the effect of TIW activity and Equatorial Upwelling (and divergence) on net convergence along the Equatorial Front. The lower figure illustrates the vertical circulation patterns associated with Equatorial Upwelling and the Equatorial Front in relation to surface circulation patterns.

### 2.4.4 Effects of El Niño on biological processes

Upwelling is driven by trade wind activity and is thus strongly affected by El Niño events with the drop in wind strength resulting in reduced upwelling. Upwelled waters are generally derived from depths of 40-80m, but never greater than 100m (Smith, 1982; Halpern and Freitag, 1987). During El Niño events the thermocline (usually 100m at 140°W and 40m at90°W) is deepened to greater than 100m across the entire region. This deepening of the thermocline coincides with a shallowing in the upwelling source depths, resulting in upwelled waters being derived from the mixed layer. Consequently surface nutrient concentrations are reduced, and temperature and salinity are increased so that they are similar to surrounding surface waters. As the thermocline progressively deepens, the cold tongue contracts to the east and the thermohaline gradients across the Equatorial Front are reduced.

After an El Niño event, the thermocline returns to its normal position and upwelling strength increases, reducing the SST and increasing the nutrient availability in the upwelled waters (Bender and McPhaden, 1990). During this return to cold tongue conditions, surveys of the 1986-1989 event showed the thermocline had shoaled to 20m above its normal level, resulting in SSTs decreasing to 2.5°C below normal which enhanced the gradients across the Equatorial Front (Fielder *et al.*, 1992). Conditions of reduced upwelling persisted for 7-9 months and during this time the thermocline waters continued to accumulate remineralized nutrients. When the thermocline finally shoaled, its waters had much higher nutrient concentrations than under normal conditions (Fielder *et al.*, 1992). This 'overshoot' (anti-El Niño event) during the return to normal conditions enhances both biological activity and the thermohaline gradients across the Equatorial Front, consistent with the frontal model of mat accumulation (Yoder *et al.*, 1994). Anomalies in the silicon to nitrogen ratios suggest rapid biogenic removal of the usually abundant silica occurs during the return to cold tongue conditions, possibly in the form of diatom blooms (Bender and McPhaden, 1990) or related to increased concentrations of diatoms along the Equatorial Front.

## 2.5 BIOLOGY OF GIANT DIATOMS

Deep-sea laminated diatomaceous deposits are exclusively near-monospecific accumulations of giant and/or mat-forming diatoms. Understanding of giant diatom ecology is based on laboratory studies and diver observations of *Rhizosolenia* spp. and *Ethmodiscus rex* (Alldredge and Silver, 1982; Villareal, 1988; Villareal and Carpenter, 1989; Villareal, 1992). Similar occurrence patterns within the sedimentary record are used to support the use of these species as analogies for other giant diatom species such as *Thalassiothrix* and *Bruniopsis* (Kemp and Baldauf, 1993; Yoder *et al.*, 1994). From studies of *Rhizosolenia* spp. in

the North Pacific, Villareal *et al.* (1993) propose that giant diatoms have adapted to low nutrient environments by controlling their buoyancy to use both the deeper nutricline and the shallow euphotic zone. It may be this positive buoyancy that bring the diatoms back to the surface from sinking water masses in frontal regions.

### 2.5.1 POSITIVE BUOYANCY

Positive buoyancy in large diatoms, *Rhizosolenia* spp. and *Ethmodiscus* spp. has been demonstrated in laboratory experiments (Villareal, 1988; Villareal and Carpenter, 1989; Villareal, 1992). The large size of these diatoms reduces the surface:volume ratio, decreases the mass of opal required in the frustule thus lowering cellular density (Villareal and Carpenter, 1989). This result contradicts the traditional assumption that small size minimizes loss of phytoplankton cells from the photic zone (Smayda, 1970), but is consistent with the characteristic occurrence of large diatoms *Rhizosolenia* spp. and *Ethmodiscus* spp. in oligotrophic regions (Villareal and Carpenter, 1994). Guillard and Kilham (1977) advance the argument of large size resulting in increased sinking rates to explain the low abundance of diatoms greater than 15-20μm in the open ocean.

Smayda (1970) suggested mechanisms for reducing sinking rates can be divided into:
(1) physiological (fat secretion, light and nutrient availability, and cell sap composition);
(2) morphological (shape, protrubences, size and colony formation); and,
(3) physical (water viscosity and circulation, such as upwelling and turbulence).
The positive buoyancy observed in recent experiments is explained in terms of variations in the ionic composition of the cell sap (Villareal, 1988; Villareal and Carpenter, 1989; Villareal, 1992; Villareal and Carpenter, 1994), building on the physiological mechanisms given in (1) above.

#### 2.5.1.1 Cell sap buoyancy regulation

In large diatoms the bulk of the cell volume is taken up by the vacuole. Changes in the ionic composition and water content of the vacuole have been considered as possible mechanisms for buoyancy regulation since the turn of the century (Verworn, 1893 referenced in Smayda, 1970). Work on the dinoflagellate *Pyrocystis noctiluca* indicates that positive buoyancy can be related to cell sap composition using three possible mechanisms: (1) the exclusion of heavy divalent ions, such as $SO^2{}_4{}^-$; (2) high concentrations of $Na^+$ relative to $K^+$, the latter being 40% heavier; and, (3) high concentrations of light $NH_{4+}$ ions (Smayda, 1970). Similar trends have been measured in the diatoms *E. rex* and rhizosolenid species (Beklemishev et al, 1961 refd. in Smayda, 1970; Villareal, 1988; Villareal and Carpenter, 1989; Villareal, 1992; Villareal and Carpenter, 1994).

Sediment trap studies show $^{15}N/^{14}N$ ratios ($\delta^{15}N$) of exported organic matter higher than those of suspended matter (Altabet, 1988; Altabet, 1989). These data suggest that the deep nitrate pool below the euphotic zone is the source of 'new' nitrogen to the upper ocean (Villareal *et al.*, 1993). Diffusion and mixing are not strong enough to explain the steep vertical gradient in $\delta^{15}N$, raising the question of how the nitrate reached the surface. Analysis of cellular nitrogen show that ascending *Rhizosolenia* spp. mats contain significantly larger internal nitrate pools (9.7±2.9mg/ml) than sinking mats (2.0±2.3mg/ml), and that mat $\delta^{15}N$ is similar to sub-nutricline ratios, consistently heavier than surface values (Villareal *et al.*, 1993).

Villareal *et al.* (1994) conclude that buoyancy regulation allows these diatoms to exploit the higher nutrient levels of the nutricline (80m to 150m) as well as the high light levels at the surface. Large internal pools of $NO_{3-}$ accumulate within diatoms at the nutricline, decrease cell density by up to 0.2mg/ml. The cells rise to the surface under the resulting positive buoyancy. As the $NO_{3-}$ is used in the photosynthetic process, cell density increases and the cell sinks back to the nutricline. Using laboratory determined sinking rates and the time taken to accumulate and utilize an internal $NO_{3-}$ pool, the period of a complete cycle to and from the nutricline is estimated as 7.3 to 12.5 days (Villareal and Carpenter, 1994).

### 2.5.2 *THALASSIOTHRIX* ECOLOGY

*Thalassiothrix* is giant, oceanic mat-forming diatom with up to 13 recognized species (Round *et al.*, 1990 and references therein). The frustules are pennate; elongate and slightly tapered - the head pole being narrower with two prominent spines. They form one of the longest known genus of diatoms, reaching up to 4mm in length but are only a maximum of 5µm wide (Round *et al.*, 1990). All species have a wide sternum, narrowing towards each end, with a row of areolae (holes) along either side (Fig. 2.10). The internal holes of the areolae are circular or slightly elongate. Externally, the areolae are separated by narrow ribs from the centre of the sternum and covered by a porate cribrum (Round *et al.*, 1990), in heavily silicified species the cribrum can appear to completely occlude the areolae (Hallegraeff, 1986). Spines arise between the areolae pointing towards the head pole. In most frustules preserved in the sedimentary record, dissolution has destroyed the delicate cribrum and spines, leaving only the spine bases (Fig 4.17e,f). Colony formation is restricted to *T. antarctica* which forms stellate colonies of strongly sigmoidal cells linked at the foot-pole (Hasle and Semina, 1987). Other *Thalassiothrix* species, such as *T. longissima* form tangled mats (Quilty *et al.*, 1984) similar to the rhizosolenid mats described by Villareal (1993). Documented occurrences of *Thalassiothrix* in the sedimentary record and the modern ocean are summarized in Table 2.1. Since very little is known about the ecology of *Thalassiothrix*, the diatom *Rhizosolenia* is used as an analogue to the LDM sediments (Section 2.4.2). Both*Thalassiothrix longissima*,

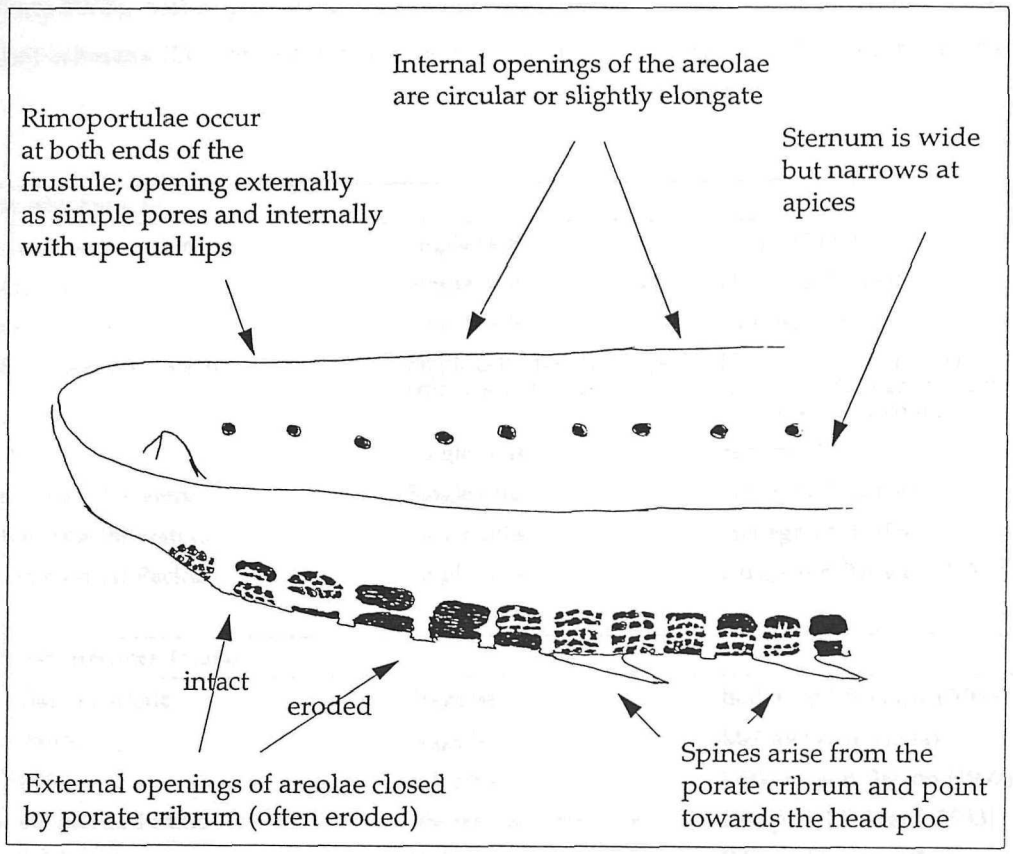


Figure 2.10. Line drawing of typical *T. longissima* Group frustule showing major skeletal features.

which dominates LDM samples, and *Rhizosolenia castracanei*, observed in massive surface concentations during the JGOFS Fall '92 survey, are common in the modern North Pacific gyre (Beers *et al.*, 1975). Although, *Thalassiothrix* species tend to occur in the lower euphotic zone (100-120m) whereas *Rhizosolenia* are common in the upper ephotic zone (0-80m, Beers *et al.*, 1975).

| **Modern occurrences** | | |
|---|---|---|
| Eastern equatorial Atlantic | Single cells | Lange (1994) |
| South Atlantic | Single cells and colonies | Hallegraeff (1986) |
| North Pacific Gyre | Single cells | Sancetta (1992) |
| Antarctic/ Southern Ocean | Single cells, bundle shaped colonies and mats | Hasle (1990), Quilty *et al.*(1984), Hallegraeff (1986), DeMaster (pers comm.) |
| Bering Sea | Single cells | Semina (1981) |
| Japanese Coastal Waters | Single cells | Hallegraeff (1986) |
| Australian coastal waters | Single cells | Hallegraeff (1986) |
| Eastern equatorial Pacific | Single cells | Lange and Berner (1993) |
| **Ancient occurrences (mats)** | | |
| North Atlantic/Arctic | Stage 5e | Boden and Backman(1996) |
| North Atlantic | Stage 5e | McCave *et al.* (1994) |
| North Pacific | 5.2-5.9Ma | Dickens and Barron (1997) |
| Eastern equatorial Pacific | Miocene and Pliocene | Kemp and Baldauf (1993) |
| Gulf of California | Holocene | Pike and Kemp (1996) |
| Southern Ocean, Frontal Zones | Holocene | ODP Leg 177, Initial Results |

Table 2.1. Modern and ancient records of *Thalassiothrix* occurrences.

Mats of intertwined *Rhizosolenia* chains 1-30cm long are buoyant, occurring over broad expanses of the North Atlantic, North Pacific, Indian Ocean and Southern Ocean (Beers *et al.*, 1975; Carpenter *et al.*, 1977; Alldredge and Silver, 1982; Quilty *et al.*, 1984; Villareal and Carpenter, 1989). Mats are reported only in warm, oligotrophic waters; there are no records of mat-forming life-styles in cold, turbulent, neritic environments (Alldredge and Silver, 1982). Mats are sporadic and occur at concentrations of $10^{-3}$mats $m^{-3}$ or less in the North Atlantic (Carpenter *et al.*, 1977); there are no estimates for the Indian or Southern Oceans. In the North Pacific mats are present all year round, at concentrations of up to 4.9 mats $m^{-3}$. They are strongly buoyant and physiologically healthy despite low surface nutrient concentrations (Carpenter *et al.*, 1977; Alldredge and Silver, 1982). Rhizosolenia mats represent 98% of annual biogenic silica accumulated at a station to the north of Hawaii (Villareal and Carpenter, 1989).

### 2.5.3 SINKING AND BURIAL RATES

Rapid sinking rates of diatom frustules result in frustules spending less time in the strongly undersaturated water column, thus reducing the predepositional dissolution period. The rate at which diatoms sink through the water column is related to their weight, size, shape and colony size (Smayda, 1970). Since this study only quantifies dissolution levels in *Thalassiothrix* frustules, only the effect of colony or aggregate formation is examined here. In positively buoyant giant diatoms (see Section 2.5), the ionic composition of the cell sap (responsible for positive buoyancy in life) equilibrates with the surrounding sea water in dead or dying cells resulting in the loss of positive buoyancy. Sinking rates measured directly for giant and mat-forming diatom species are compared in Table 2.2, sinking rates measured for smaller diatoms is given for comparison.

| Cell/aggregate type | Dimensions (mm) | Sinking rate (m/day) | Reference |
|---|---|---|---|
| 'Small diatoms' | <0.01 (max dimension) | 0.06-9.2 | from Smayda, 1970 |
| *Rhizosolenia* single cells (living) | 0.2-0.4 (length) | 0.11-6.3 | Smayda and Boleyn, 1966 |
| *Rhizosolenia* chains (dead) | n.d. | 69-84 | Villereal, 1988 |
| *Ethmodiscus rex* single cells (dead) | <1.9 (diameter | 86.4 | Villereal, 1992 |
| *Ethmodiscus rex* single cells (living) | <1.9 (diameter) | 1.6 | Villereal, 1992 |
| Rhizosolenia aggregates (living) | 19.5-75 | 50-200 | Alldrege and Gotschalk, 1989 |
| Faecal pellets | n.d. | 36-376 | Osterburg *et al.*, 1963; Smayda, 1963 |

Table 2.2. Sinking rates of diatoms giving rates for single cells, faecal pellets and colonial aggregates.

From Table 2.2 it is clear that aggregates sink significantly faster than single cells and sinking rate is related to aggregate size (Smayda, 1970; Alldredge and Gotschalk, 1989). Using *Rhizosolenia* aggregates, Alldredge and Gotschalk (1989) suggest this relationship is approximately linear and give an estimate of the relationship as:

$$S = 8.4\ (D)^{0.95} \qquad \text{Equation 2.1}$$

where S is the sinking rate (m/day) and D the aggregate diametre (mm). In the case of LDM deposits, *Thalassiothrix* mats up to 6cm across have been observed (A. Kemp, pers. comm.). Using this relationship for mats of 2cm across (dimensions typically observed in BSEI photomosaics of LDM deposits) gives a sinking rate of 147m/day, significantly larger than the sinking rates measured for small diatoms and solitary giant diatoms. Mats of *Rhizosolenia* spp. with diametres up to 30cm have been observed in the Sargasso Sea (Alldredge and Silver, 1982).

### 2.5.4 EXPORT FLUXES ASSOCIATED WITH GIANT DIATOMS

Following the observations of *Rhizosolenia* concentrations along the Equatorial Front in the eastern Equatorial Pacific during the JGOFS Fall '92 survey accumulations of dark green 'fluff' made up of fresh phytoplankton detritus were observed in sea floor photographs, core top samples (Smith *et al.*, 1996) and sediments traps (Honjo *et al.*, 1995). This layer covers over 95% of the sea-floor between 2° N and 2° S and has an approximately uniform thickness of 0.5mm (Smith *et al.*, 1996). Microscopic examination of this material showed it contained relatively intact diatoms frustules including *Rhizosolenia* spp. Excess activities of $^{234}Th$ suggest that this material had been either on the sea-floor or in the water column for less than 100 days before sampling. This time period coincides with the observed surface concentrations of *Rhizosolenia* along the Equatorial Front 8-40 days prior to sampling. This interpretation is supported by the absence of zooplankton fecal pellets and estimated sinking rates (Smith *et al.*, 1996). Measurements of organic carbon from the fluff layer are given in Table 2.3.

| Location | $\%C_{org}$ in fluff layer | $\%C_{org}$ in sediment trap | % seafloor covered |
|---|---|---|---|
| 5°N | 1.05±0.07 | 5.72 | - |
| 2°N | - | - | 95.3±0.8 |
| 0 | 2.04±0.80 | 3.76 | 95.8±0.7 |

Table 2.3. Organic carbon ($\%C_{org}$) measurements and %seafloor cover by phytodetritus fluff. Sediment traps located 700m above the sea-floor. Data from Smith *et al.* (1996).

Unlike the LDM deposits, the fluff layer observed by Smith *et al.* (1995) did not contain a high proportion of diatom aggregates. While aggregates were observed in the JGOFS study, they covered less than 1% of the sea floor. As the individual *Rhizosolenia* chains fragment after death, the aggregates become increasingly delicate and prone to breaking up. Mats of *Thalassiothrix* frustules are much more robust. The meshwork is made up of interlocking individual elongate frustules which do not fragment after death. Rapid break up of *Rhizosolenia* mats results in a difference in aggregate size meaning that after internal buoyancy has been lost (after death) the larger *Thalassiothrix* mats should sink much faster than the smaller *Rhizosolenia* aggregates, increasing the proportion of associated organic carbon reaching the deep-ocean.

# CHAPTER 3: EXPERIMENTAL METHODS

## 3.1 INTRODUCTION: OVERVIEW OF METHODS USED

The methods used in this study fall into two categories; optical examination methods and wet-chemical analytical techniques. Optical examination of the sediments is carried out using traditional light and binocular microscope techniques. These results are enhanced by high-resolution back-scatter electron imagery (BSEI) images. Light microscope examination of the sediments uses both resin and water mounted smear slides for point counting and checking levels of frustule dissolution. Sediments were cleaned with hydrochloric acid and hydrogen peroxide to remove carbonate and organic carbon respectively, and disaggregated using an ultrasonic bath prior to examination. Wet-chemical analysis of the sediments included measurement of proportions of biogenic opal, carbonate and organic carbon. Data available from previous studies included oxygen isotope measurements, information on physical properties (grain and dry bulk density, porosity etc.) and GRAPE (Gamma Ray Porosity Evaluator) data.

## 3.2 ANALYTICAL STRATEGY

The samples used in this study where either contiguous blocks of LDM sediments or spaced samples through non-laminated sections of the LDM dominated units. Core photos and examination of archive sections were used to isolate laminated intervals and produce detailed sedimentary logs. A 5mm slice was removed from one side of the block samples to be used in polished thin section production. The remaining sample was split into lamina defined subsamples used in chemical analysis. The results of these analyses combined with information from BSEI photomosaics of the polished thin section were used to define areas of interest for further investigations into sedimentary fabrics (depositional dissolution, mat fabrics etc) and biogenic composition. Subsamples of the spaced samples were analyzed for biogenic opal, carbonate and organic carbon alongside the laminated samples. This sample strategy is summarized in Figure 3.1.

The unique laminated, matted fabric of the LDM sediments used in this study was exploited to produce high resolution records (minimum sample interval of 0.5mm) of biogenic opal and carbonate. The dense fibrous meshwork inhibited bioturbation of these sediments (Kemp *et al.*, 1995) combined with the lack of depositional and sedimentary dissolution, evidenced in

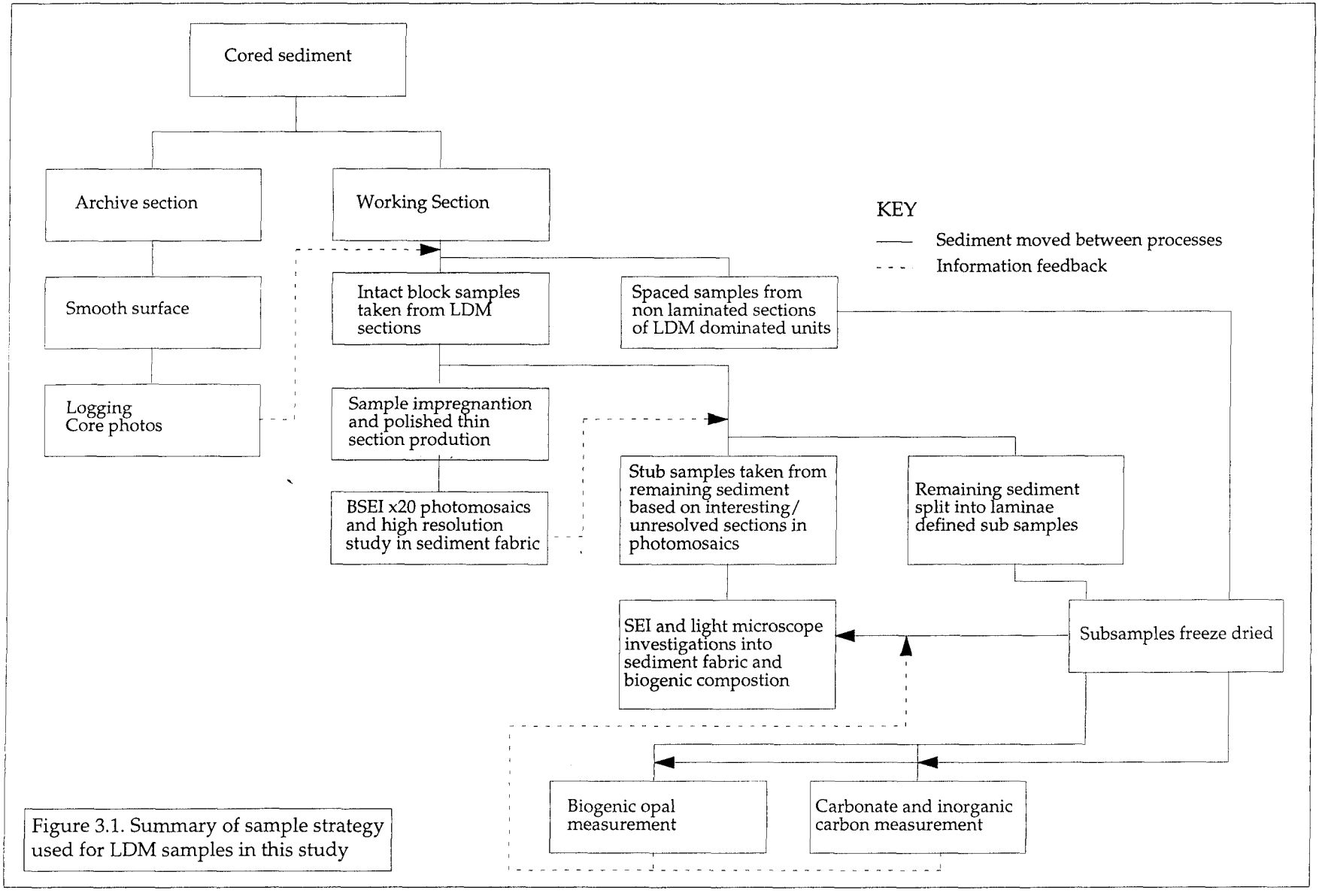


Figure 3.1. Summary of sample strategy used for LDM samples in this study

the delicate structure visible in SEM images, results in an almost pristine record of sedimentation during these periods of the Pliocene and Miocene.

The same meshwork allows accurate sampling for chemical analysis based on lamination and colour changes. Using a binocular microscope to identify laminae boundaries, the sediment could be split along actual laminae boundaries with a micro-surgical scalpel. This method of sampling was capable of producing a sample interval as small as 0.5mm. This fine scale sampling forced the adaption of the published opal analysis technique to use 500% smaller samples. In addition, the high biogenic purity of these sediments (<1% clay) allowed a second adaptation of the published method to produce an estimate of the radiolarian/diatom ratio of the biogenic silica component.

## 3.3 SCANNING ELECTRON MICROSCOPE (SEM) METHODS

The high magnification and compositional differentiation capabilities of the SEM, make it an invaluable observational tool in the investigation of sedimentary fabrics. This section is not intended to be detailed description of the principles and method surrounding SEM techniques, rather a general description of methods employed in this study. Goldstein (1981) gives a more detailed discussion of SEM methods.

### 3.3.1 SAMPLE IMPREGNATION

For examination in the SEM, polished thin sections were made from sediment samples. Unconsolidated samples were impregnated using a chemically inert, low viscosity epoxy resin. Using a vacuum impregnation unit (Logitech IU-20) the samples were vacuum dried before the resin was introduced to fill the pore spaces. Once the resin-impregnated block had been oven cured, the sample was mounted on a glass slide and cut to thickness of 100μm, using a low speed saw. The mounted sample was then polished, using progressively finer diamond powders, to a thickness of 30μm. The samples were then coated with a conductive carbon coating for SEM examination. The remaining section of the impregnated block was used for comparison between the SEM image produced and the untreated sediment.

### 3.3.2 BSEI TECHNIQUES

METHOD

Backscattered electrons are produced by elastic collisions of the electron beam with the surface of the sample (Goldstein *et al.*, 1981). The number of backscatter electrons generated, and hence the brightness of the image, is controlled primarily by the backscatter coefficient of the target (related to the atomic number). Targets with high atomic numbers such as pyrite, carbonate and clays give a bright image where as those with low atomic numbers

produce dark areas on the image. The low atomic number of the resin used to impregnate unconsolidated samples allows images of these thin sections to be regarded as porosity maps, with dark areas indicating high porosity and light areas indicating low porosity. In laminated sediments the changes in biogenic composition often result in porosity as well as compositional changes. In LDM deposits, the open diatom framework results in high porosity sediment. Mixed assemblage and foram-nannofossil ooze sediments have much lower porosity, related to an increase in abundance of coccoliths and clay particles decreasing the mean grain size. The higher atomic number of calcium in the carbonate frustules also increases the brightness of these image areas.

APPLICATIONS

Thin section analyses started with the production of a x20 photomosaic which acted as a base map for higher magnification work. The photomosaic was used to identify individual depositional events for further examination; laminae thickness was measured and the sediment was logged for compositional and sedimentary fabric analysis. A series of logged sections was used for spectral analysis of compositional variations. These photomosaics and logs formed the basis of sampling strategies for both chemical analysis and SEM stub samples and strew mount investigations.

### 3.3.3 SEI IMAGES

High magnification SEI images of stub samples can be used to investigate the sedimentary fabrics and composition of individual laminae. Species composition of biogenic material is also possible using this method. Mounted filter samples of acid clean sediment residues aid the investigation into both experimental and depositional dissolution levels in biogenic opal particles.

METHOD

Sediment subsamples or strews are mounted on SEM stubs with carbon mounting discs and gold coated for SEI examination. Backscattered electrons from surfaces directly facing the detector contribute to the secondary electron signal, these surfaces will appear brightest in the SEI image. This edge effect depends on the accelerating voltage, lowering the voltage reduces the penetration depth of incident electrons reducing the bright edge portions and allowing microstructures to be seen more easily.

### 3.3.4 LOW VACUUM SEM

METHOD

Low vacuum SEM uses backscatter electrons energetic enough to move through the low vacuum (~6%) in the sample chamber to the detector. This allows the direct examination of wet sediment or strew mounts without the need for sample coating.

APPLICATIONS

This method has similar uses to the conventional SEI methods without the destruction of samples through the coating process. Following examination samples can be used in other analytical methods.

### 3.3.5 ENERGY DISPERSIVE X-RAY MICROANALYSIS

METHOD

X-radiation is produced during the loss of electrons from the target atoms, the wavelength of this radiation being characteristic of the element involved. The energy dispersive spectrometery (EDS) system connected to the SEM uses the X-ray spectra produced during these interactions to provide a compositional analysis of the target atoms. Linescans, point analysis and high resolution X-ray intensity maps provide quantitative and qualitative compositional information on the minerals in a thin section.

APPLICATIONS

EDS measurements can be made over much smaller scales than wet-chemical analysis techniques. This method was useful in determining the composition of individual frustules

## 3.4 OPAL DETERMINATION

Biogenic opal is the main component of LDM deposits. A number of methods have been used in the past to determine both particulate and biogenic silica within marine sediments. The method used in this study is based on the wet-alkaline extraction technique published by Mortlock and Fröelich (1989) modified to use smaller sample volumes and to ensure complete extraction of biogenic opal. These modifications also allow estimation of the proportion of *Thalassiothrix* spp., the main component of the siliceous microfossils, relative to the total siliceous assemblage with each sample, reducing the need for microscope examination.

Several methods have been used for the separation and determination of biogenic silica. The first determinations of silica in sediments used fusion of samples with alkali-borates and HF digestion analysis (Goulterman, 1969). This method measures the total particulate silica and is not selective for biogenic material. Since then several techniques have been developed and modified, these fall into six groups and are summarised in Table 3.1. Recently the use of X-ray diffraction (XRD) methods has fallen with the widespread acceptance of the simpler wet-chemical digestion techniques (Conley, in press). The validity of XRD methods has also been questioned, especially those involving heat treatment of samples to produce low cristobalite (Hurd, 1983).

In a recent extensive inter-laboratory calibration experiment, Conley (in press) demonstrated that the XRD methods measuring amorphous silica directly without conversion to cristobalite (Eisma and Van Der Gaast, 1971) consistently overestimate the biogenic silica concentration as determined by the wet chemical extraction methods. The XRD techniques are most applicable to sediments containing small amounts of clay, as the presence of clays interferes with the XRD measurement (Hurd, 1983). The samples used in the calibration experiment all contained a significant amount of clay (Conley, in press).

| | Method | References |
|---|---|---|
| 1 | X-ray diffraction using heat conversion of opal to cristobalite | Ellis and Moore (1973) |
| 2 | direct X-ray diffraction of amorphous opal | Eisma and van der Gaast (1971) |
| 3 | infra-red spectroscopy of amorphous opal | Chester and Elderfield (1968) |
| 4 | elemental normative partitioning of sample bulk chemistry | Leinen (1977 and ODP Leg 138, Initial Results) |
| 5 | wet-alkaline extraction, measuring dissolved silica in resulting solution | Hurd (1972), Eggimann, *et al.* (1980), DeMaster (1981), Mortlock and Fröelich (1989), Muller and Schnieder (1993), Landen (1996) |
| 6 | microfossil point counts converted to estimates of opal content | Pokras *et al.* (1986), Pudsey (1992) |

Table 3.1. Summary of published methods for measurement of biogenic opal in sediment samples.

### 3.4.1 WET-ALKALINE EXTRACTION METHODS

Wet-alkaline extraction methods can be divided into two groups; a) differential extraction, and b) single extraction. Differential extraction methods (e.g. Eggiman *et al.*, 1980 and DeMaster, 1981) measures the silica dissolved after 1, 2, 3 and 5 hours of alkaline extraction, the dissolved silica is then plotted against the dissolution period. A similar method is used by Conley who showed that consistent results could be produced using only three dissolution periods (Conley, 1996). Since biogenic silica dissolves more readily than clay and aluminosilicates particles, the biogenic fraction should be taken into solution leaving a residue of lithogenic particles. The lithogenic particles are assumed to dissolve constantly and thus the curve of a graph of dissolved silica against time should flatten out as the biogenic silica goes into solution. The biogenic silica is calculated by extrapolating the upper, straight section of the curve back to the dissolved silica axis, see Figure 3.2.

Mortlock and Fröelich (1989) found that the linear section of the differential extraction curve is reached between 5 to 8 hours. In their experiments, dissolution of pure diatom samples took 4 to 5 hours. Comparing results obtained using differential extraction and linear extrapolation with values measured after 5 hours of a single wet-alkaline extraction, a good agreement was found, even for opal poor samples. This argument forms the basis for Mortlock and Fröelich's (1989) single extraction method using a dissolution period of 5 hours. The single

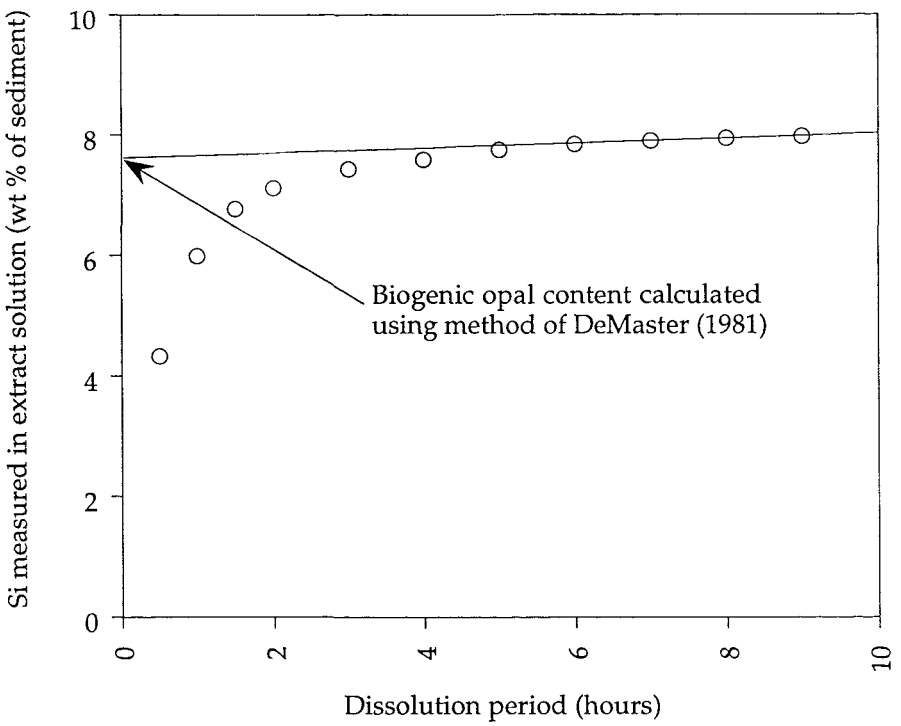


Figure 3.2. Calculation of biogenic opal content in internal standard (diatomaeous mud from the Peruvian Upwelling zone) using sequential dissolution method of DeMaster (1981).
Sub-samples are removed from the dissolution process at given intervals and biogenic silica content is calculated assuming constant, slow release of silica from clays.

extraction method appears to be as accurate and is much less cumbersome than differential extraction methods (Mortlock and Fröelich, 1989).

### 3.4.2 METHODS USED IN THIS STUDY

Based on its accuracy and relative simplicity, this study used a method based on the single extraction method of Mortlock and Fröelich (1989), hereafter referred to as MF. MF dissolved a sample mass of 25-200mg (with a maximum of 25mg biogenic opal in each sample) in 40ml of 2M sodium carbonate held at 85°C for 5 hours. The dissolved silica is determined using molybdate blue spectrophotometry based on the method described by Strickland and Parsons (1972) for the measurement of silica in sea water, see Appendix A1 for full details. In order to optimize the dissolution period used for each sample type, a representative set of samples was chosen (usually 4-6 samples) representing the extremes in compositional variation. The biogenic silica content of these samples was then measured using the differential dissolution method over 2-8 hours. The plots used to calculate the BSi content are then used to choose the optimal dissolution period for the entire sample batch.

#### 3.4.2.1 Modifications to published method

MODIFICATION 1 (All samples): Reduction of required sample weight

In order to both reduce the mass of sediment required for analysis and to increase the number of samples analyzed at one time, the volumes used in MF were scaled down by a factor of 5 to use sample masses of 5-20mg (maximum opal content of 5mg) dissolved in 8ml of alkaline solution.

MODIFICATION 2 (LDM samples only): Increased dissolution period

Preliminary trials of the modified MF method on LDM sediments showed a residue of partially dissolved opaline frustules. Simple mass balance calculations indicated that at least 16% of the total opal remained undissolved. Light microscope and SEM examination showed around 70% of the residues consisted of partially dissolved *Thalassiothrix* spp. frustules. The remaining 30% consisted of a variety of radiolarian and centric diatom frustules with low levels of dissolution.

Mortlock and Fröelich (1989) acknowledged that partial dissolution may be a problem with their method. They found up to 20-50% of a sample's radiolarian content can escape complete dissolution in 2M sodium carbonate, but argue that radiolarians represent less than 2% of most marine sediments and hence this problem can be ignored. However, the preliminary trials during this study demonstrated that the problem of partial dissolution significantly affected the diatom fraction as well as the radiolarian fraction in these sediments. The resistance of these samples to experimental dissolution is related to the heavy silicification and lack of depositional dissolution of the siliceous microfossils in the eastern Equatorial Pacific LDM.

The 5 hour extraction period of the MF method is based on the time it takes for a significant proportion of lithogenic silica to be mobilized by 2M sodium carbonate, as well as time required for total dissolution of the biogenic opal. SEM (optical examination and EDS) and light microscope studies indicate that the eastern Equatorial Pacific LDM sediments contain negligible quantities of lithogenic material, making the time required for complete dissolution of biogenic opal the sole consideration in defining the dissolution period.

In order to achieve complete dissolution of the sample opal, the undissolved residue was rinsed, dried and the extraction process repeated. After a total of 10 hours of dissolution, the residues still showed a noticeable *Thalassiothrix* spp. content, although the dissolution was much further advanced and the frustules were around half the size of those observed after 5 hours dissolution. The *Thalassiothrix* spp. fragments accounted for approximately 20% of the residue, see Table 3.2. This proportion could represent a major underestimate since smaller particles can be held at the surface of the extraction solution during centrifugation and are subsequently lost during removal of the supernatant. After 10 hours, mass balance calculations suggested that at least 4% of the total sample volume was accounted for in this undissolved residue.

MODIFICATION 3 (LDM samples only): Estimation of biosiliceous frustule assemblage
The difference between the dissolution rates of diatom and radiolarian opal was utilized to give a proxy for the ratio of opal associated with *Thalassiothrix* spp. to radiolarian and centric diatoms within samples without the need for detailed microscope work.

| Dissolution period (hours) | Percentage of original weight | %Rad (of residue) | %Rad (of original weight) | %Diatom (of residue) | %Diatom (of original weight) |
|---|---|---|---|---|---|
| 0 | 100% | - | 10% | - | 90% |
| 5 | 16% | 30% | 4% | 70% | 12% |
| 10 | 4% | 80% | 3.2% | 20% | 0.8% |

Table 3.2. Weight of siliceous frustules remaining after 5 and 10 hours of dissolution in 2M $Na_2CO_3$ compared to the approximate proportions of radiolarian and diatom frustules remaining in the residue.

By increasing the dissolution periods for the two extraction stages complete dissolution was obtained and the differential dissolution pattern was preserved. The first stage was extended to 8 hours, and the second stage was modified to use 2N NaOH rather than 2N $Na_2CO_3$ (Mortlock and Froelich, 1989) to ensure complete dissolution of the radiolarian content, and was run over 8 hours, after which the water bath was turned off and the samples allowed to stand over night before the residue was removed. Filtered samples of the residue showed a negligible quantity of undissolved debris after the extended extraction procedures (Fig. 3.3 and Appendix A1).

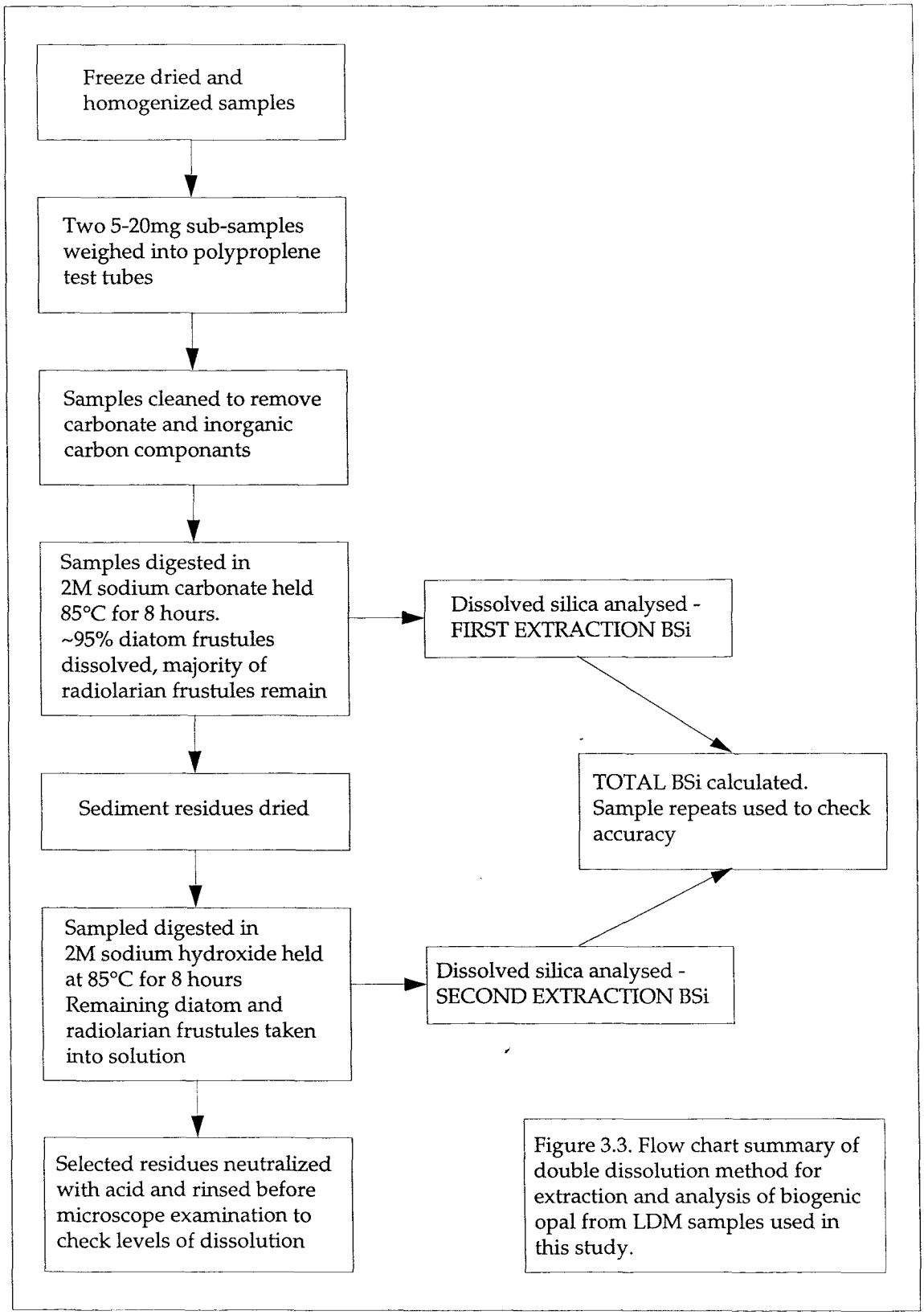


Figure 3.3. Flow chart summary of double dissolution method for extraction and analysis of biogenic opal from LDM samples used in this study.

### 3.4.2.2 Calculation of %OPAL-water content of biogenic opal

Analysis of dissolved silica was carried out using molybdate blue spectrophotometry (Mortlock and Fröelich, 1989) to measure the concentration of silicon present in the form of biogenic opal, %BSi. Since biogenic opal contains water, having the composition $SiO_4.nH_2O$, the water content, $n$, must be known in order to calculate the percentage of biogenic opal contained in the sample, %OPAL. Mortlock and Fröelich (1989) recommend using average values, calculated from the literature, of 10% water ($n$ = 0.4) for diatom opal and 15% ($n$ = 0.6) for radiolarian opal. Since the majority of silica dissolved in the first extraction cycle is derived from diatoms, the water content was taken as 10%. Conversely, in the second extraction cycle radiolarians contribute the majority of silica, hence a water content of 15% was used for calculation of biogenic opal in the 2nd dissolution leachate.

### 3.4.2.3 Verification of the modified method

In order to test the accuracy of this method four of the samples used in the inter-laboratory calibration experiment organised by Conley *et al.* (in press) were analyzed. The results fell well within the spread of results for low, medium and high biogenic opal samples confirming the accuracy of this method across the whole range of sample compositions, see Table 3.3. Results for the high %BSi samples (2 and 4) fall in the upper section of laboratory spread while samples with lower BSi contents (1 and 3) fall slightly below the overall mean. In the case of the high %BSi samples, laboratories using much weaker bases than used in this study consistently gave lower values for these samples (Conley, in press). The use of a strong base ensures complete dissolution of the biogenic material without exhaustion of the carbonate ion during the digestion process (Gehlen and van Raaphorst, 1993). The inclusion of XRD based results in the overall mean resulted in a artificial increase in the mean value, with the values obtained for intermediate and low %BSi samples falling below the overall mean.

An independent test of %BSi measurements is possible for LDM samples which contain only biogenic material (confirmed using SEM examination). Since the samples consist of opal, carbonate and organic carbon, measurements of these components should sum to 100%. In 34 samples tested in this way the mean sum was 99.94% (standard deviation of 2.12). This is well within the combined errors of the three measurements.

| Sample number and type | This study (%$SiO_2$) | Overall mean (%$SiO_2$) |
|---|---|---|
| 1 Low %BSi | 2.15±0.01 | 2.80±1.33 |
| 3 Intermediate %BSi | 6.26±0.01 | 6.61±2.17 |
| 2 High %BSi | 46.15±0.36 | 44.90±9.78 |
| 4 High %BSi | 41.48±0.62 | 38.8±10.0 |

Table 3.3 Results for inter-laboratory calibration experiment showing results obtained by this study compared with the overall mean of results obtained by participating laboratories (total 27) (Conley *et al.*, in press)

Long term statistical reproducibility is tested using two internal sediment standards of a diatomaceous mud from the Peruvian upwelling zone and a composite sample of LDM material. These standards are run with each set of samples. Results for these measurements are summarised in Table 3.4.

| Standard | Mean wt% ±1SD | |
|---|---|---|
| | First digestion period (2M $Na_2CO_3$ for 8 hours) | Second digestion period (2M NaOH for 8 hours) |
| LDM composite | 63.48±1.60 | 7.16±0.93 |
| Peruvian mud | 20.90±1.41 | 6.43±0.84 |

Table 3.4. Long term statistical reproducibility of internal standards over 21 sample sets showing results for both first and second digestion period.

### 3.4.3 ESTIMATION OF *T. LONGISSIMA* GROUP CONTENT FROM DOUBLE EXTRACTION METHOD

The differing resistances of diatoms and radiolarians to experimental alkaline dissolution were noted by Mortlock and Fröelich (1989), but have also been observed in water column and post-depositional dissolution patterns appear to be mainly due to the surface:volume ratio of the frustules (Berger, 1976; Calvert, 1974; and references therein). Differences have also been observed between individual species, dependant on frustule size, thickness and surface to volume ratio (Lisitzin, 1972). Radiolarians tend to have compact, near spherical shapes with thick walls, whereas diatoms tend to have a more delicate, open structure with a higher surface to volume ratio. Large surface areas and relatively lightly silicified walls make *T. longissima* Group frustules more prone to dissolution, than the co-occurring centric diatoms and radiolarians.

Based on the proportions of *T. longissima* Group frustules remaining after 5 and 10 hours of dissolution (Table 3.2), a second set of experiments was carried out using the double dissolution method (8 hours in 2M $Na_2CO_3$ followed by 8 hours in 2M NaOH), see Figure 3.3. The opal taken into solution during the second extraction (as a percentage of the total opal taken into solution during in the two extraction cycles) was compared with the proportion of *T. longissima* Group frustules in the siliceous microfossil assemblage for each sample estimated using point counts of carbonate-free smear slides (prepared and counted using procedures and criteria in Battarbee, 1973). Plotting the two variables against each other shows a linear relationship between the proportion of *T. longissima* Group frustules and second extraction opal in the eastern Equatorial Pacific LDM sediments, see Figure 3.4. The correlation is significant at the 99% confidence interval, with most points plotting onto the linear relationship within the bands of experimental error. Hence, the *T. longissima* Group frustules as a proportion of the total biosiliceous assemblage can be estimated using the equation;

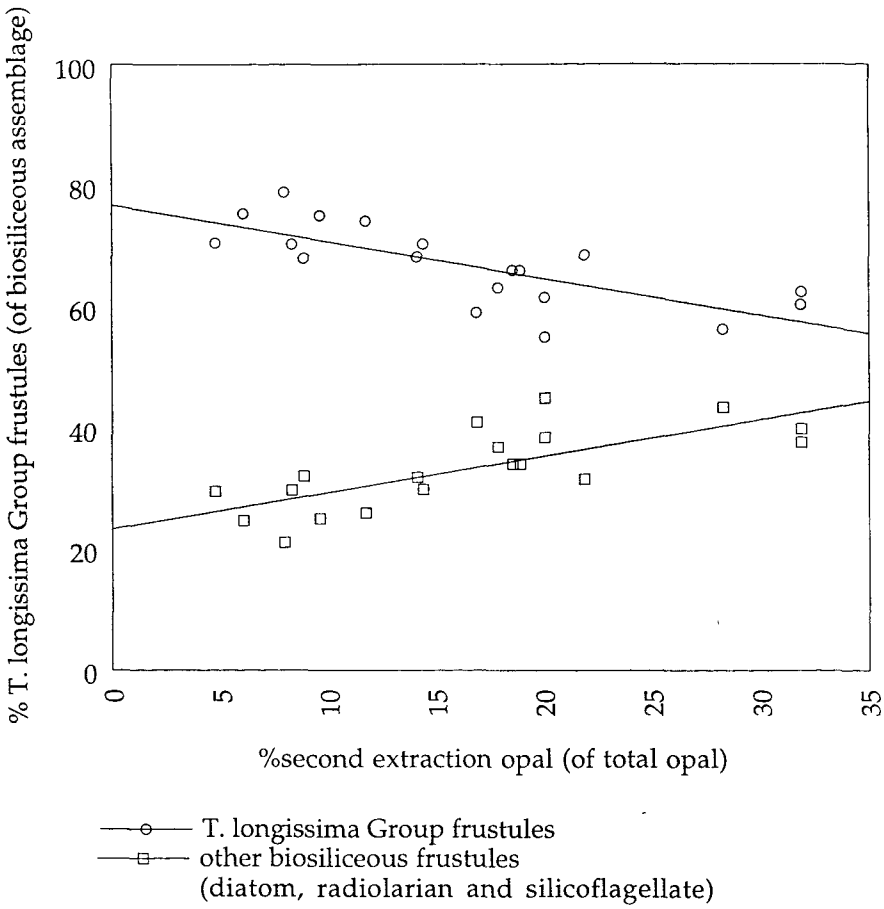


Therefore;

%T. longissima Group (biosiliceous assemblage)
= 76.71 - 0.61 x %second extraction opal (of total opal)
$r^2$= 0.555

Figure 3.4. Plot showing relationship between opal released in the second extraction process and the relative T. longissima Group component in the biosiliceous assemblage.

$$\%\ T.\ longissima\ \text{Group} = 76.71 - (0.61 \times \%\text{Opal2}) \qquad \text{Equation 3.1}$$

Where %Opal2 is the percentage of opal taken into solution during the second extraction cycle as a percentage of the opal taken into solution in both cycles. While this relationship does not represent a precise correlation, it is able to identify trends in the composition of the siliceous microfossil assemblages without the need for detailed microscope examination.

## 3.5 ORGANIC CARBON AND CARBONATE DETERMINATION

The growth of mould (up to 5mm diameter) on the LDM sediments during storage precluded the production of a high resolution record (similar to that produced for biogenic silica) for organic carbon. Mould colonies do not fix carbon from the atmosphere but they do relocate available carbon with in the sediments, thus measurements of organic carbon will be altered on the scale of mould colonies (up to 10mm in diameter) smearing the high resolution record (C. Anthony, Dept Microbiology, University of Southampton, pers. comm.). The method detailed below was used to measure organic carbon levels in laminated sediments from other sites not affected by this problem.

### 3.5.1 METHODS IN USE

There are three groups of methods commonly used to determine carbonate and organic carbon content of sediments. The first group is based on wet-oxidation and direct determination of organic carbon (Duursma, 1961; Sims and Haby, 1971). The second group of methods uses the difference between total carbon before and after dry combustion (Krom and Berner, 1983; Manighetti, 1993). In the third group carbonate is removed by acid leaching before organic carbon measurement (Fröelich, 1980; Verado *et al.*, 1990; Nieuenhuize *et al.*, 1994). Many of these methods are subject to systematic errors both within and between laboratories and vary depending on the sediment composition (King *et al.*, in press).

#### 3.5.1.1 Wet oxidation techniques

Wet oxidation techniques measure only organic carbon. They are based on the oxidation of organic carbon to $CO_2$ using dichromate ($K_2Cr_2O_7$). The $CO_2$ evolved can be measured using a variety of techniques, usually titrimetric (Duursma, 1961) or colorimetric (Sims and Haby, 1971). Organic carbon measurements can represent significant over-estimates if reduced species other than carbon (e.g. sulphides) are oxidized (Fröelich, 1980). Under-estimates are also possible if refractory organic compounds are not completely oxidized by the oxidant used (Fröelich, 1980).

### 3.5.1.2 Differential combustion techniques

These techniques are based on the assumption that organic carbon and calcium carbonate decompose at different temperatures. Some authors argue that most organic matter is decomposed to $CO_2$ by heating to 500°C (Dean, 1974; Hirota and Spyzer, 1975) whereas carbonate does not decompose below about 800°C (Fröelich, 1980). There is much dispute over the exact temperature required to achieve complete removal of the organic phases, the temperature used varies between 400 and 1300°C (Pella and Columbo, 1973; Gibbs, 1977; Manighetti, 1993). Moreover, the thermal decomposition ranges of naturally occurring organic and inorganic carbon in modern sediments have been shown to overlap (Fröelich, 1980). The presence of high Mg-calcite which decomposes at temperatures below 400°C (Walsh *et al.*, 1991) and/or refractory organic matter which may not be completely oxidised below 1050°C (Gibbs, 1977) also creates potential inaccuracies in these methods.

Thorough tests (Manighetti, 1993) and recent inter-laboratory calibrations (King *et al.*, in press) suggest that combustion at 400°C for three hours gives consistent and comparable results. However, it has been suggested that these methods systematically underestimate the organic carbon content (King *et al.*, in press). Another problem with these methods is obtaining a small difference between two large numbers (total and carbonate values) each of which has an associated error, with sufficient precision to achieve a meaningful result.

### 3.5.1.3 Acidification methods

These methods measure organic carbon, following acid dissolution of calcium carbonate. The inorganic carbon is lost as $CO_2$ leaving only organic carbon in the sample. Inorganic carbon is then calculated by subtraction of organic carbon measurements from total carbon values. The main criticism of these methods is the possibility of hydrolysation of organic matter by the acid which may be lost if the particulate residue is separated from the spent acid (Fröelich, 1980; Karl and group, 1991). Over 40% of the organic carbon in modern sediments can be soluble in acid (Roberts *et al.*, 1973). Attempts have been made to overcome this problem by:

(1) Analysis of the carbon content in both spent acid and residue (Fröelich, 1980).
(2) Determining sequentially and directly the $CO_2$ yield of inorganic carbon by acidification and organic carbon by wet-oxidation (Weliky *et al.*, 1983).
(3) Using an acid vapour procedure to remove inorganic carbon (Hedges and Stern, 1984).
(4) Evaporation of spent acid to conserve the organic carbon taken into solution and correction for hygroscopic salts (Hedges and Stern, 1984).
(5) Addition of the acid to samples already weighed out into sample cups (Verado *et al.*, 1990; Nieuenhuize *et al.*, 1994)
(6) Measuring the dissolved calcium in the spent acid (Dean, 1974; Tsunogai and Noriki, 1991).

These procedures provide significant improvements in accuracy. However, the first two ot these methods require relatively large (50-200mg) samples and cannot be easily automated. Also, the phosphoric acid used in these methods may have a significant carbon content resulting in a systematic over-estimation of the organic carbon (P. King, pers. comm.). Fröelich's (1980) procedure requires a dissolved and a solid phase carbon analyzer while Weliky's (1983) method provides no nitrogen data. Fuming with HCl vapour eliminates the need for reweighing but can fail to remove all traces of carbonate material (Hedges and Stern, 1984). In situ acidification removes the need to consider hygroscopic salts (Nieuenhuize *et al.*, 1994) and also eliminates reweighing procedures (Verado *et al.*, 1990; Cutter and Radford-Knoery, 1991). Moreover, the in situ methods avoid the loss of acid soluble organic matter and consume only 10-20mg of sediment per analysis (Verado *et al.*, 1990; Cutter and Radford-Knoery, 1991; Nieuenhuize *et al.*, 1994).

Apart from methods which measure calcium directly, in all the above methods artifacts may arise if some of the organic matter is volatilised with the carbonate (Karl and group, 1991), although methods measuring $CO_2$ would only show inaccuracies if the acid oxidised organic carbon to $CO_2$ (King *et al.*, in press). There is also the possibility of incomplete removal of carbonate due either to incomplete acid reactions (Hedges and Stern, 1984; Nieuenhuize *et al.*, 1994), or to the protection of carbonate grains by clay coatings (Chave, 1965; Feistner, 1992). Carbonate residues resulting from incomplete acid reactions are reduced by repeating acid additions until there is no sign of effervescence (Nieuenhuize *et al.*, 1994).

Acids commonly used for carbonate removal include sulphurous (Verado *et al.*, 1990), hydrochloric (Hedges and Stern, 1984; Nieuenhuize *et al.*, 1994) and phosphoric (Fröelich, 1980; Weliky *et al.*, 1983) in various concentrations. The type of acid used is governed, to some extent, by the cups used for analysis. Tin cups are preferred by the manufactures of the CN analyzers since it oxides at 1700°C in the reaction chamber leaving a residual ash which is completely carbon free (Pella and Columbo, 1973). However, tin is heavily corroded by strong acids. Silver capsules are not so prone to acid dissolution but, in the CN analyzer, they melt and oxidize meaning that some carbon may be trapped in the centre of the silver globule and not be fully oxidized. Aluminium, is also attacked by acid and becomes brittle after acidification resulting in the possibility of sample loss through damages cups (Nieuenhuize *et al.*, 1994).

### 3.5.2 Choice of method

Due to available equipment an acidification method was chosen, using tin cups with a low concentration of HCl (10%), in situ acid additions and evaporation of the acidified slurry (see Appendix A2 for full details). This is essentially the method of Cutter and Radford-Knoery

(1991) modified to use sediment rather than filter samples. In order to ensure total removal of inorganic carbon the acid addition was repeated until there is no detectable effervescence. Sample loss though explosive effervescence was minimized by using low acid concentration, high sided cups and by damping the sediment with MilliQ before the acid addition. The low concentration of HCl minimized dissolution of the tin cups (P. King, pers. comm.) and the loss of organic carbon due to volatilisation of organic matter (King *et al.*, in press).

The operation of the CN analyzer is based on 'flash combustion' of the sample introduced into a high temperature column reactor by an autosampler. The combustion column contains stationary phases composed of a porous layer of oxidation catalyst of chromium trioxide ($Cr_2O_3$) overlying silver cobalt oxide granules ($Co_3O_4$+Ag) maintained at 1050°C. At these temperatures Verado *et al.* (1990) were able to achieve >99% recovery of carbon from graphite. The sample and container are oxidized in a burst of high purity oxygen. The combustion products, a mixture of $CO_2$, $NO_x$ and $H_2O$, are then swept through the combustion column by a high purity helium carrier gas into the reduction column. The reduction column, a U-shaped tube packed with metallic copper granules, is maintained at 650°C, and removes excess oxygen and reduces the nitrogenous oxides to $N_2$. The $N_2$, $CO_2$ and $H_2O$ are then carried through a water absorbing filter containing magnesium perchlorate, $Mg(ClO_4)_2$. The remaining $N_2$ and $CO_2$ is carried on to a 2m chromatographic column at 54°C, where detection is by thermal conductivity.

## 3.5 CHAPTER SUMMARY

This chapter describes the methods used in this study to investigate the sedimentology and chemical composition of LDM deposits. Optical methods and carbon determination techniques used are similar to those found in the literature. However, the unusually high levels of biogenic opal combined with negligible lithogenic content allowed the modification of the published MF method to enable the measurement of 4-5mg sample weight (compared to 15-25mg used in the MF method) without significant loss of accuracy. Other modifications to the MF method exploited the negligible lithogenic content to ensure the complete dissolution of biogenic material and enabled the estimation of biosiliceous frustule assemblage in LDM deposits from the chemical data without the used of time-consuming, optical methods.

SEM and BSEI methods are used in Chapter 4 to investigate the sedimentology of LDM sections on scales of millimetres to microns. This high-resolution sedimentology is used to separate individual depositional events and investigate the periodicity of these events. Results of these BSEI studies are also used in Chapter 5 calculate a lamina-based sedimentation rate. High-resolution biogenic opal measurements are used in Chapter 6 to

compare the depositional regime through the basal unit of the '4.4Ma' LDM depositional event at site 847 and 850 (over 2000km apart) and to identify periodicities within the records of sedimentary opal content. Chapter 7 uses the mean biogenic opal content of the '4.4Ma' LDM depositional event basal unit combined with the estimated areal extent of LDM deposits to calculate biogenic silica fluxes associated with LDM accumulation. These flux estimates are also used to estimate the flux of organic carbon associated with the deposition of LDM material. Estimates of organic carbon fluxes are compared with measurements of organic carbon from diatomaceous material from the Mediterranean sapropel, S-5.

In the literature, biogenic opal contents and silica fluxes are quoted in a range of forms. In this study sedimentary biogenic silica contents are generally quoted as wt%OPAL, i.e. the proportion of sediment consisting of biosiliceous frustules by weight. This figure includes the water and oxygen content of biogenic material and enables direct comparison of opal measurements with other sediment components. Where sediment compositions are used in the calculation of chemical fluxes, sedimentary biogenic silica contents are also given as the weight of silicon atoms as a proportion of the sediment, wt%BSi. To avoid confusion between different forms of biogenic silica (Si, $SiO_2$ and $SiO_2.nH_2O$), fluxes are quoted in mols/unit volume rather than weight/unit volume.

# CHAPTER 4: SEDIMENTOLOGY AND COMPOSITION OF LAMINATED DIATOM MAT DEPOSITS

## 4.1 INTRODUCTION

Extensive LDM deposits were cored in the eastern Equatorial Pacific during ODP Leg 138 (Mayer *et al.*, 1992; Kemp and Baldauf, 1993). Comparable sediments, composed of the same diatom group and deposited over similar time periods, have since been identified in the cores taken from more westerly sites in the same region (135-110°W) retrieved during DSDP Leg 85 (Kemp and Baldauf, 1993). In other ocean regions similar laminated sediments have been found, although the diatom species making up the mats can vary (e.g. Jordan *et al.*, 1991; Bodén and Backman, 1995; Dickens and Barron, 1997). A 2cm thick LDM layer from the North Atlantic cored at 56.3°N, 27.8°W during NEAPACC cruise CD88, July 1995, is also examined in this study (McCave and Shipboard Scientific Party, 1994).

This study focuses on the '4.4Ma' LDM deposits. Macroscopic descriptions are based on direct observation of the archive sections of Leg 138 cores held at the ODP Gulf Coast Repository, College Station, Texas. High resolution investigations were concentrated on the basal unit of the '4.4Ma' LDM event. This unit consists of a 60cm thick bed of continuously laminated sediments and is characteristic of all four sites (DSDP Site 572 and ODP Sites 847, 849 and 850) containing '4.4Ma' LDM deposits.

This chapter examines the sedimentary structures of LDM deposits using both macroscopic core observations and high resolution SEM studies of polished thin sections, taken from the basal unit of the '4.4Ma' LDM event in the eastern Equatorial Pacific. Dissolution levels are quantified using a frustule preservation index method.

## 4.2 SEDIMENT DESCRIPTION AND BACKGROUND OF EASTERN EQUATORIAL PACIFIC LDM DEPOSITS

### 4.2.1 Regional occurrence and sediment description

LDM deposits are typically concentrated in packets from a few metres to around 20m thick, within which laminated beds alternate with foram-diatom-nannofossil ooze (F-NO) on a decimeter scale, see Figure 4.1. The laminated beds are typically 1-10cm thick, occupying 5-15% of the sediment packet. Exceptionally, laminated beds over 50cm thick are present.

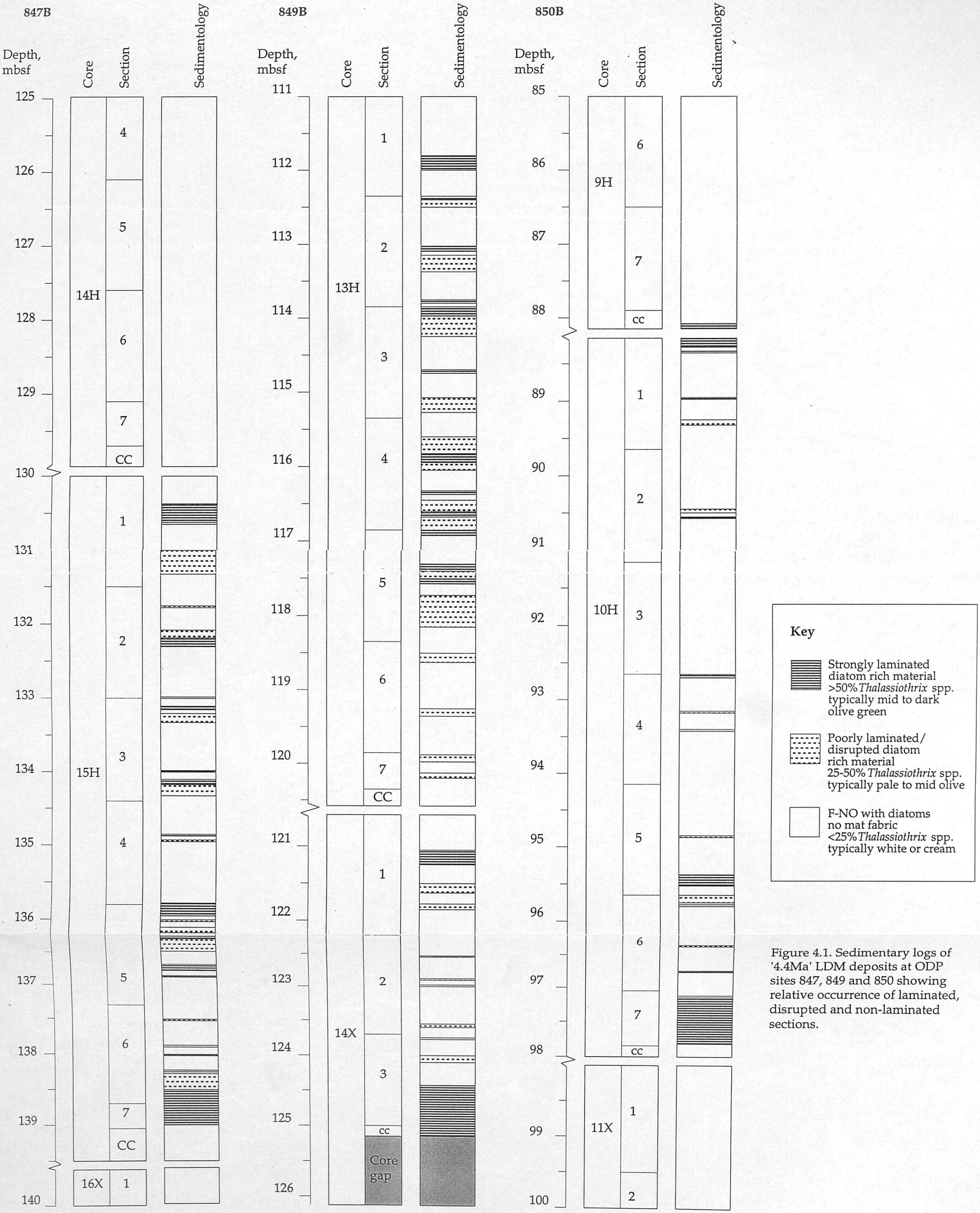


Figure 4.1. Sedimentary logs of '4.4Ma' LDM deposits at ODP sites 847, 849 and 850 showing relative occurrence of laminated, disrupted and non-laminated sections.

These thicker beds are typically found at the base of LDM sediment packets immediately overlying carbonate-rich sediments, indicating an abrupt change in deposition. Individual laminated beds can be correlated over distances as large as 2000km, between ODP drill sites.

Within the laminated beds there is a centimetre scale alternation between paler nannofossil-diatom ooze (N-DO) and the darker, purer diatom mats (Fig. 4.2). The diatom-mat laminae (100-300μm thick) have a strong glass fibre-like fabric due to the interweaving of the elongate *Thalassiothrix longissima* Group frustules into mats (individual mats are around 25μm thick), Figure 4.3a. The change in composition from diatom-rich to N-DO is paralleled by a loss of the matted structure in the paler nannofossil bearing sediment. Paler layers have an increasingly fragmentary fabric with a higher carbonate content, Figure 4.3b.

### 4.2.2 Bulk sediment composition

Bulk sediment biogenic silica measurements were made for all samples available during this project. These samples are spaced at 1-2m intervals from the '4.4Ma' LDM event at Sites 848, 849, 850 and 850 and from the '6.1-6.3Ma' event at Site 851. The results of these measurements are given in Figures 4.4 and 4.5 alongside the sedimentary logs (see Appendix A9 for data tables). These measurements give values ranging from 10 to 15 wt% opal for F-NO sediments below the LDM sections, compared to values of 20 to 30wt% for non-laminated beds within the LDM events. Laminated beds have opal contents of 40 to 80wt%.

### 4.2.3 GRAPE measurements as a proxy for sediment composition

GRAPE measurements represent a proxy for saturated bulk density. GRAPE measurements are routinely made at 2cm intervals for ODP cores. For a two component system (biogenic silica and carbonate) such as the eastern Equatorial Pacific sediments, changes in density result from the marked difference in grain density (about 1.8 and 2.7g/cm$^3$ for opal and carbonate respectively) and packing of the siliceous and carbonate components (Mayer, 1979). The intrinsic density contrast is enhanced by the more open, porous framework of the mat deposits.

Comparison between GRAPE records and measurements of biogenic opal shows a relationship of similar form to the algorithm published for the prediction of carbonate content from the GRAPE density measurements of sediments above depths of 150-200m (Fig. 4.6 and Mayer, 1991). Mayer (1991) related the second order form of this relationship to the linear relationship in grain density as sediment composition ranges from 0% to 100% of each component (~10% of the signal), and a non-linear packing factor related to the spinose structure of radiolarians (data from Hamilton, 1976; Mayer, 1979). The less spinose structure of the diatoms which dominate the sediments used in this study may in part explain the poor agreement been the measured data and the theoretical curve. This poor relationship is especially pronounced in samples containing over 50% biogenic opal. Improved packing of


Figure 4.2. Core photograph of '4.4Ma' LDM basal unit from Hole 850B (138-850B-10H-7, 39-81cm) showing centimetre-scale alternations between dark olive, strongly laminated sections and paler, poorly laminated sections.

a)


b)


Figure 4.3. SEM images of material from '4.4' Ma LDM basal unit. a) high opal/well laminated section showing dominance of *T. longissima* Group frustules and strongmat structure. Coccoliths, centric diatoms and radiolarian frustules are rare and occur between individual mats; b) low opal/poorly laminated material with mixed assemblage. Carbonate fraction dominated by coccoliths, accounts for around 60% the sediment. Diatoms are typically fragmented centric species and radiolarians are common. Relict mat fabric is clearly visible, but layers are not laterally continuous.

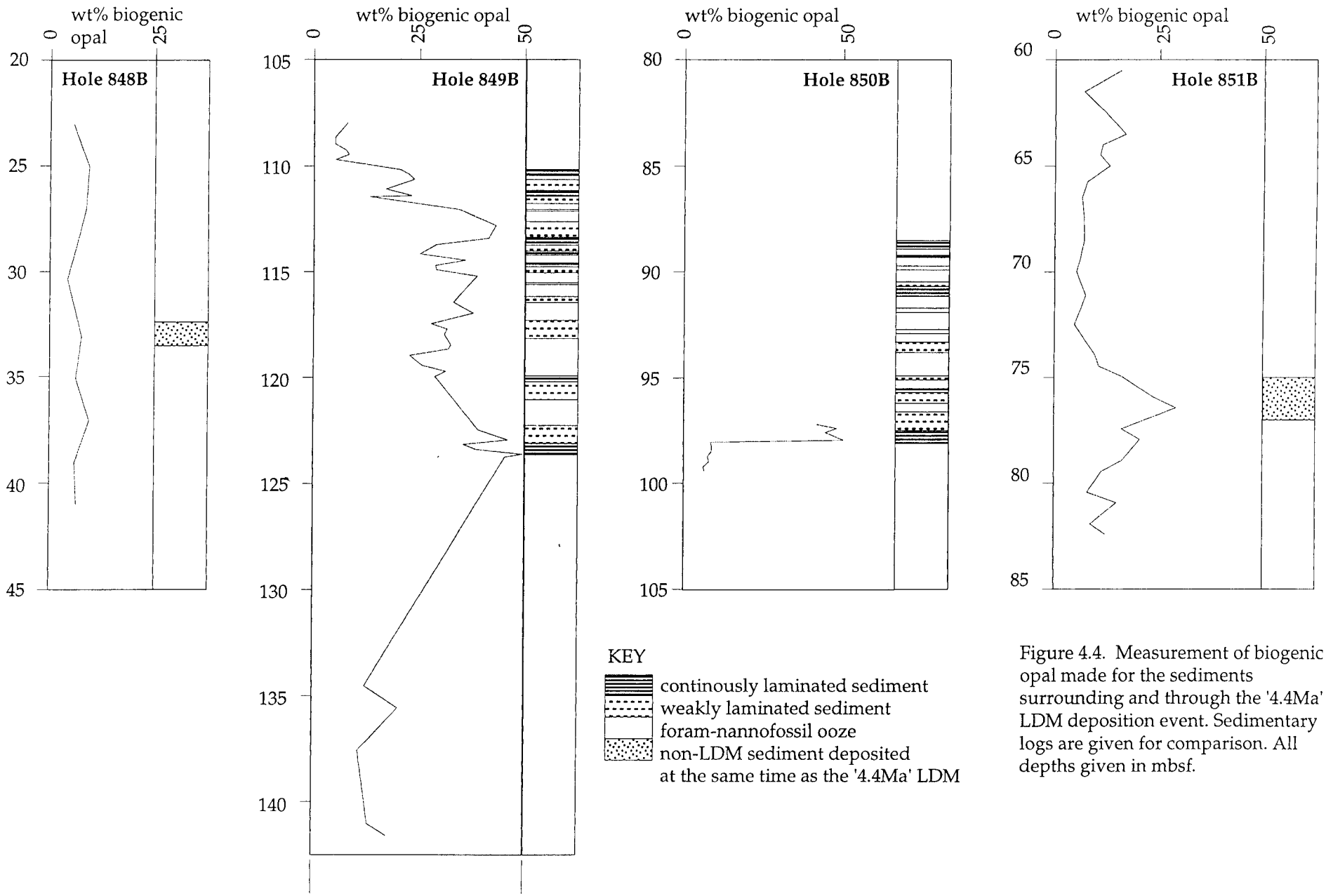


Figure 4.4. Measurement of biogenic opal made for the sediments surrounding and through the '4.4Ma' LDM deposition event. Sedimentary logs are given for comparison. All depths given in mbsf.

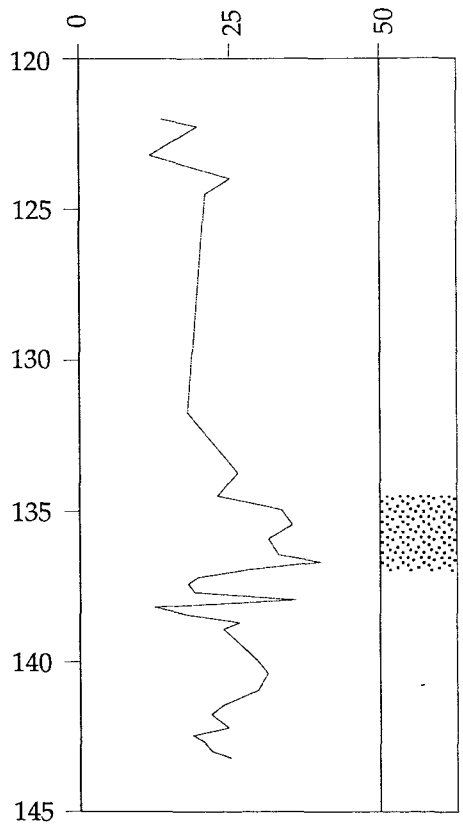


Figure 4.5. Coarse resolution biogenic opal measurements through non-LDM sediment deposited at the same time as the '6.1-6.3Ma' LDM event (Hole 851E-13H to 16X). Schematic sedimentary log shows location of sediment equivalent to LDM located using GRAPE comparison with Site 847, 849 and 850.

KEY

F-NO
non-laminated sediment equivalent to LDM

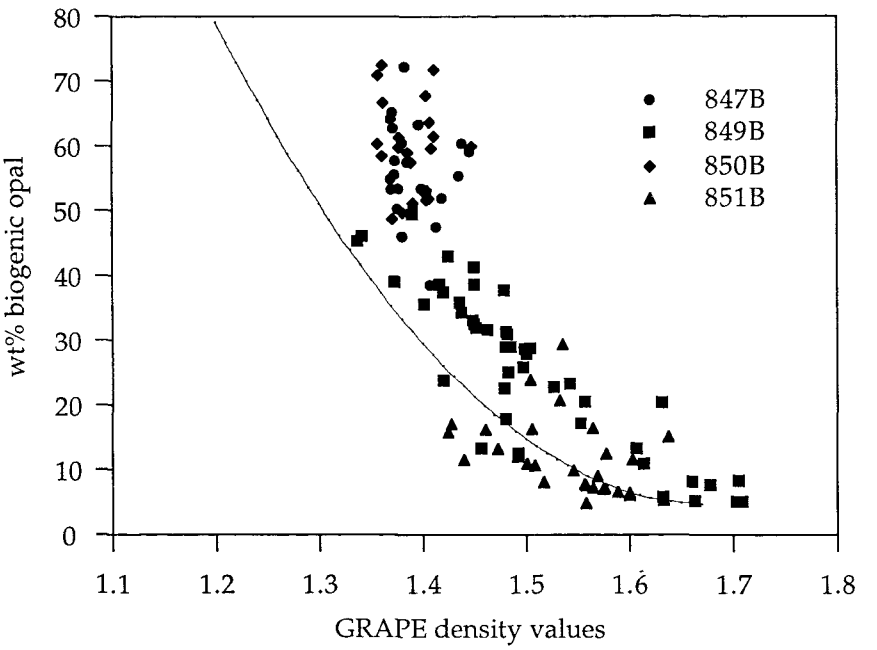


Figure 4.6. Relationship between measured biogenic opal values and GRAPE measurements for sediments containing laminated and non-laminated sections of the '4.4' Ma LDM deposits. Symbol shape denotes the site for which individual samples were taken from. From the plot it is clear that the non-laminated sediments from Site 851 (triangles) have a similar relationship between biogenic opal and GRAPE values to the laminated sediments at other sites. The solid line shows the theoretical relationship predicted by Mayer (1991) for near-surface sediments (less than 150-200m below the surface). See text for further discussion.

frustules within the sediment would increase density over the predicted values, as seen in the LDM samples.

#### 4.2.4 LDM FABRIC PRESERVATION

The preservation of lamination in deep sea sediments is generally interpreted as the suppression of benthic activity by low concentrations of oxygen, either in a silled basin or beneath zones of strong upwelling, where the oxygen minimum zone intersects the shelf or slope (Kemp and Baldauf, 1993). Benthic foraminifer studies show no evidence for a decrease in oxygenation (King *et al.*, 1995); instead they show a decrease in cylindrical and infaunal forms attesting to the impenetrability of the meshwork (Kemp and Baldauf, 1993; King *et al.*, 1995). A few burrows are found between mats, but vertical burrows are absent (Fig. 4.7). The lack of macroscopic burrows with diametres of less than 1cm in matted section suggests that the fauna creating burrows on this scale were unable to break through matted layers, promoting the preservation of the sediment fabric. The matted fabric results in a marked increase in the bedding parallel tensile strength of the sediment. This is demonstrated by individual laminae being partially pulled out of the core during piston coring, or by the wire during core splitting. We interpret these laminae to represent compacted stacks of diatom mats. Wire splitting of the cores also caused deformation of laminated intervals (Kemp *et al.*, 1995). Thus, the dense mesh-work of the diatom mats appears to have been of sufficient impenetrability and tensile strength to suppress benthic activity. The same characteristics of dense meshwork and high tensile strength also enable accurate dissection of the samples for geochemical analysis, matted layers, 0.5-1.0mm thick, were peeled away from the sample along mat boundaries.

#### 4.2.5 THE IMPORTANCE OF DIATOM MATS IN BURROW FILLS

Burrow fills found in many of the Leg 138 cores especially through LDM units vary in both colour and composition from the surrounding sediment. Burrows are typically mid- to dark-olive compared to the pale cream or white of the surrounding F-NO, see Figure 4.8. Compositionally, burrow fills resemble the composition of laminated intervals although frustules are broken into much shorter lengths. In some cases there is evidence of relict laminated fabrics. The lack of disturbance of these burrows indicates that these burrows represent the last imposed burrows beneath the mixed layer.

The occurrence of mat fragments in burrow fills has been related to the activity of deep burrowers (Kemp, 1995). These animals are thought to have dragged the organic-rich, diatom mats from the sediment surface into burrows below the surface mixed layer (8-11cm; Gage and Tyler, 1991). The material contained in deep burrows is removed from the surface mixing and dilution processes and represents a near-end-member of originally deposited sediment composition, recording short-lived depositional events within the F-NO units, see Figure 4.9.

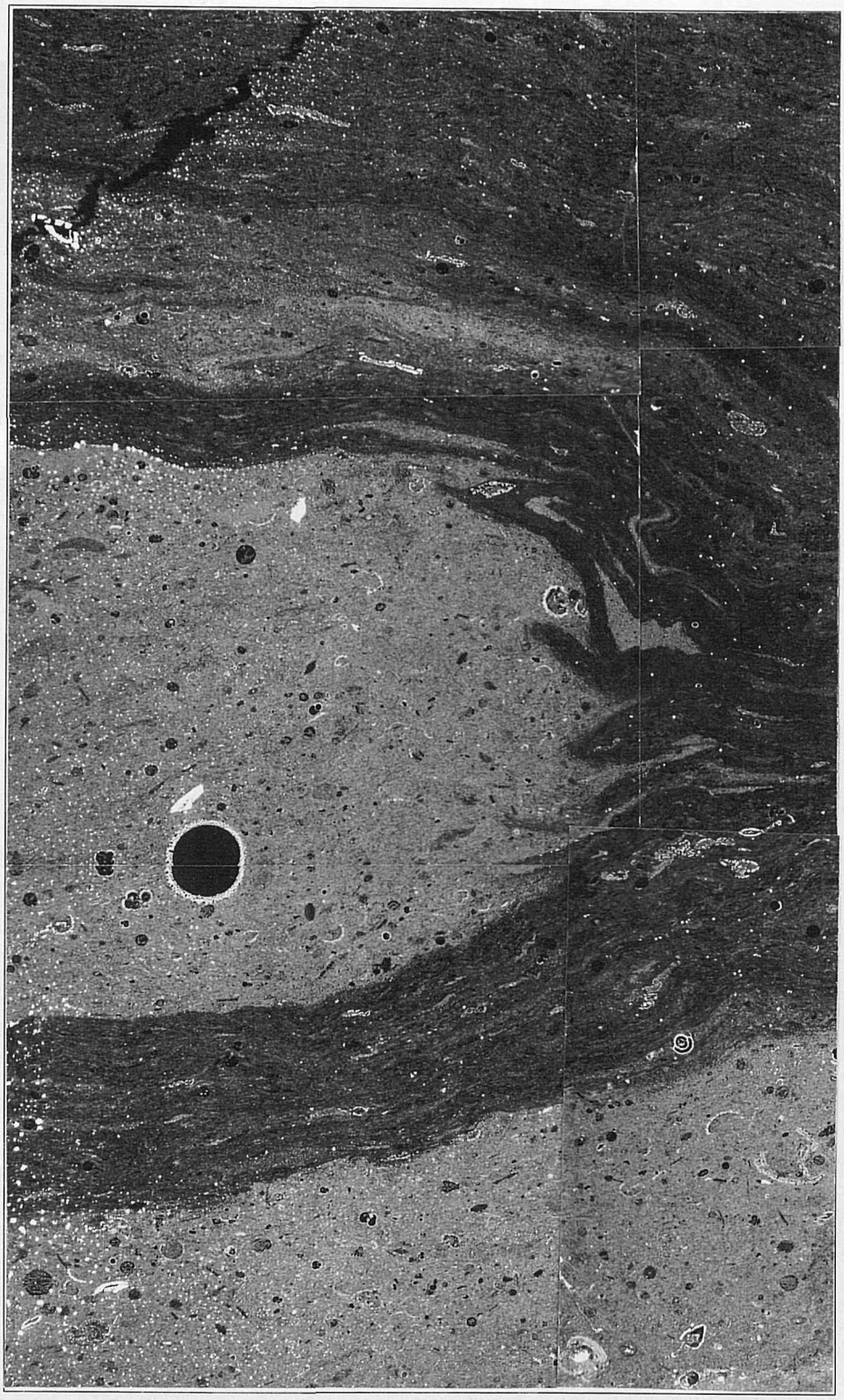


Figure 4.7. BSEI photomosaic showing large burrow forced between mats at the bottom of the '4.4Ma' LDM basal unit from Site 850. The burrow fill is of similar composition to the underlying F-NO.


Figure 4.8. Core photo (138-850B-10H-7, 16-36cm) illustrating the occurrence of LDM-filled burrows in the non-laminated section of the '4.4Ma' LDM deposits.

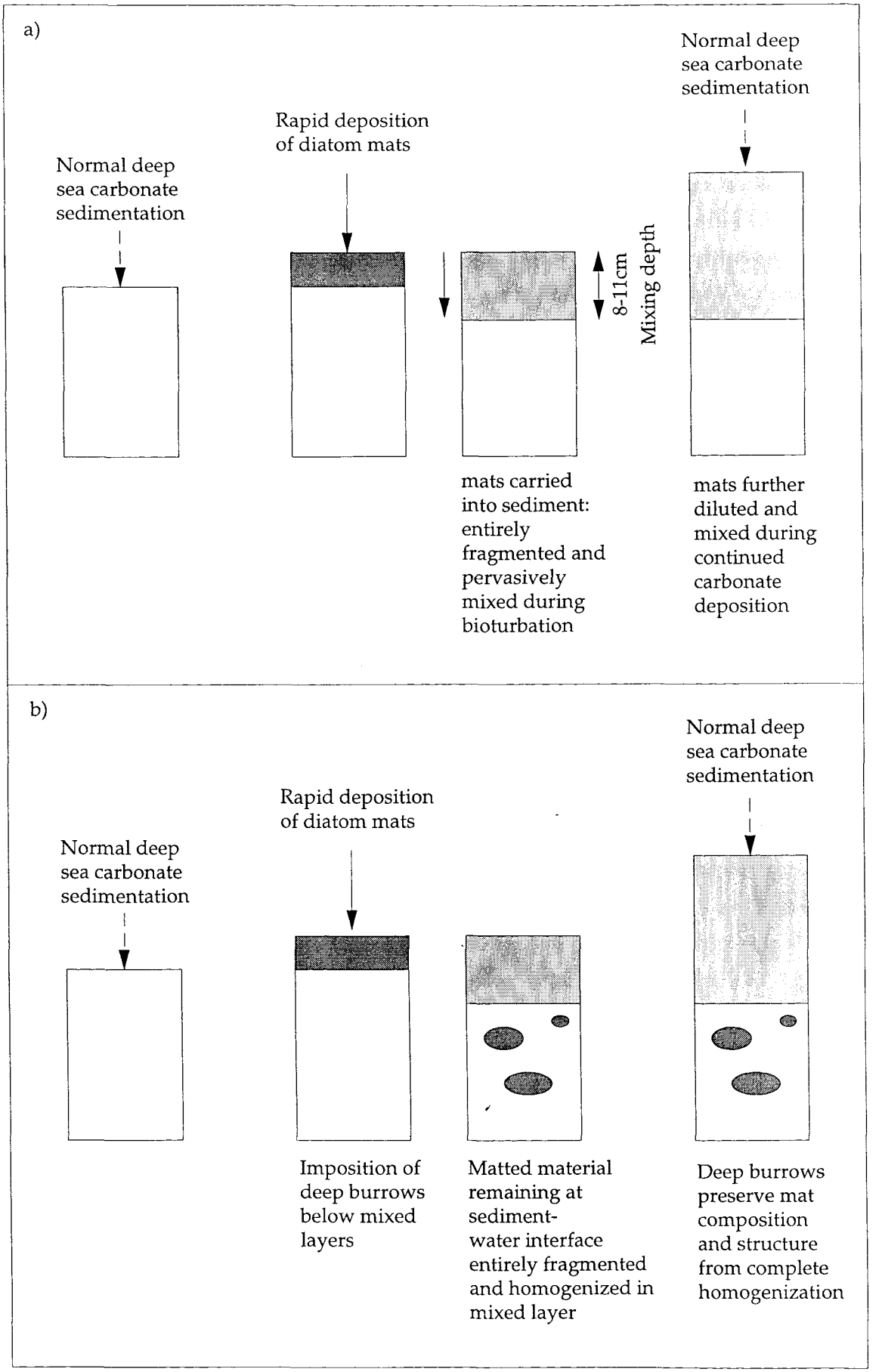


Figure 4.9. Deep burrow preservation of near-end-member sediment composition from complete homogenization in surface mixed layer; a) mixing and diluting effects of bioturbation on a diatom mat layer deposited over sediment of a different composition; b) the effect of deep burrowers rapidly removing sections of the diatom mat layer to below the mixed layer, resulting in the preservation of material close to the original diatom layer composition, after Kemp (1995).

Similar observations of deep burrows enriched with diatom deposits were made from box and piston cores following the mass sinking of *Rhizosolenia* mats observed by the JGOFS Fall '92 Survey (Smith *et al.*, 1996). Here, the burrows occurred between sediment depths of 17-27cm and occupied around 0.2% of the total sediment volume. Smith *et al.* (1996) concluded that even if similar depositional events occurred only once every ten years, the caching of this material in burrows could result in these depositional events 'playing a disproportionately large role, relative to their contribution to total organic-carbon flux, in the formation of the equatorial Pacific sedimentary record' (Smith *et al.*, 1996).

The frequent occurrence of diatom-mats within burrow fills (around 40% of non-laminated sediment contained in LDM packets contains such burrows), indicates that diatom mats formed an important sediment component even outside periods of intense LDM deposition. Laminated sediments appear to represent periods of particularly intense diatom export flux. During periods of less intense mat flux, the benthos could utilize the biogenic material, leaving only mat fragments preserved in some burrow fills and elevated levels of silica in the sediment.

## 4.3 LAMINAE COUPLETS

Sub-millimetre scale variations in both composition and structure are clearly visible in BSEI photomosaics of eastern Equatorial Pacific laminated sediments (Figs. 4.10 and 5.6), and can also be seen directly in the edges of coated stub samples, see Figure 4.11. Typically, laminated regions show a 100-200μm-scale alternations between near-monospecific *Thalassiothrix* mats and layers with a more mixed diatom assemblage. These laminae couplets are common throughout the '4.4Ma' basal unit and have also been recorded through other LDM events in the eastern Equatorial Pacific (Pearce *et al.*, 1995). Measurements of 276 couplets from the basal unit of the '4.4Ma' LDM deposits give a mean couplet thickness of 390μm (with a standard deviation of 290μm).

The mixed assemblage laminae are less porous with a higher carbonate content and appear brighter in BSEI photomosaics. In contrast, the more porous *Thalassiothrix* spp. dominated layers appear darker. The characteristics of *Thalassiothrix* spp. frustules occurring in *Thalassiothrix*-rich and mixed assemblage laminae are summarized in Table 4.1 and discussed in more detail in the following sections.

Measurements of *Thalassiothrix* spp. frustule width were made from x1000 BSEI images of a single lamina couplet, see Figure 4.11 (b and c). Comparison of the mean widths of frustules in the *Thalassiothrix*-rich and mixed assemblage laminae show a strong statistical difference.

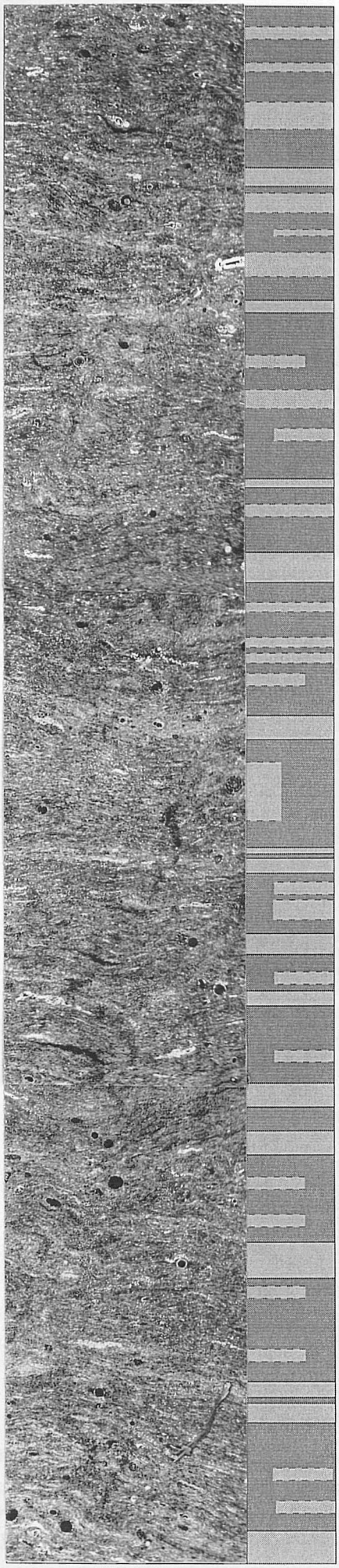

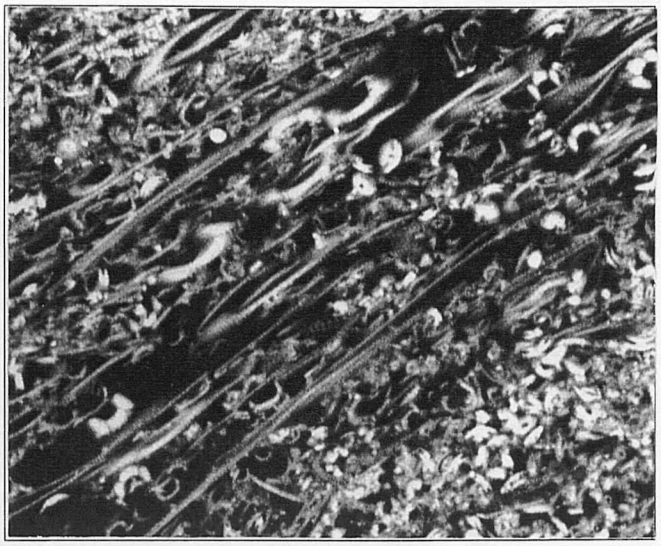

a)

0 20µm

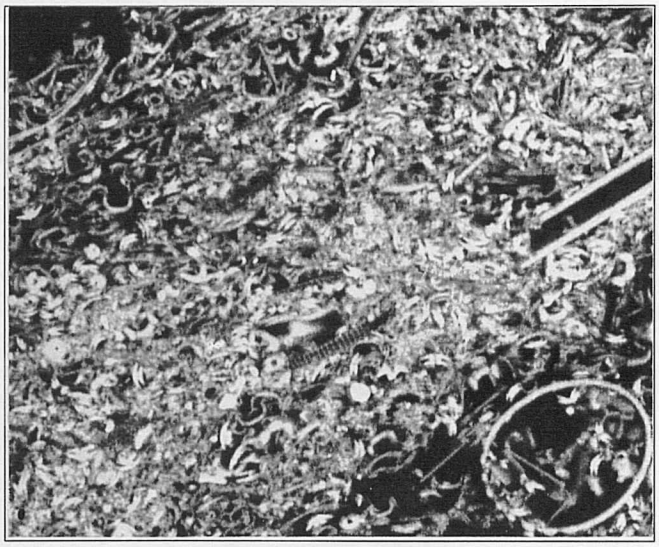

b)

0 20µm

Figure 4.10. x50 BSEI photomosaic (138-847B-15H-7, 20-26cm) with explanatory sedimentary log showing occurrence of laminae couplets, with high magnification example of a) *Thalassiothrix*-rich and b) mixed assemblage lamina. Dashed lines in the sedimentary log indicate weakly developed lamina boundaries.

0

500µm

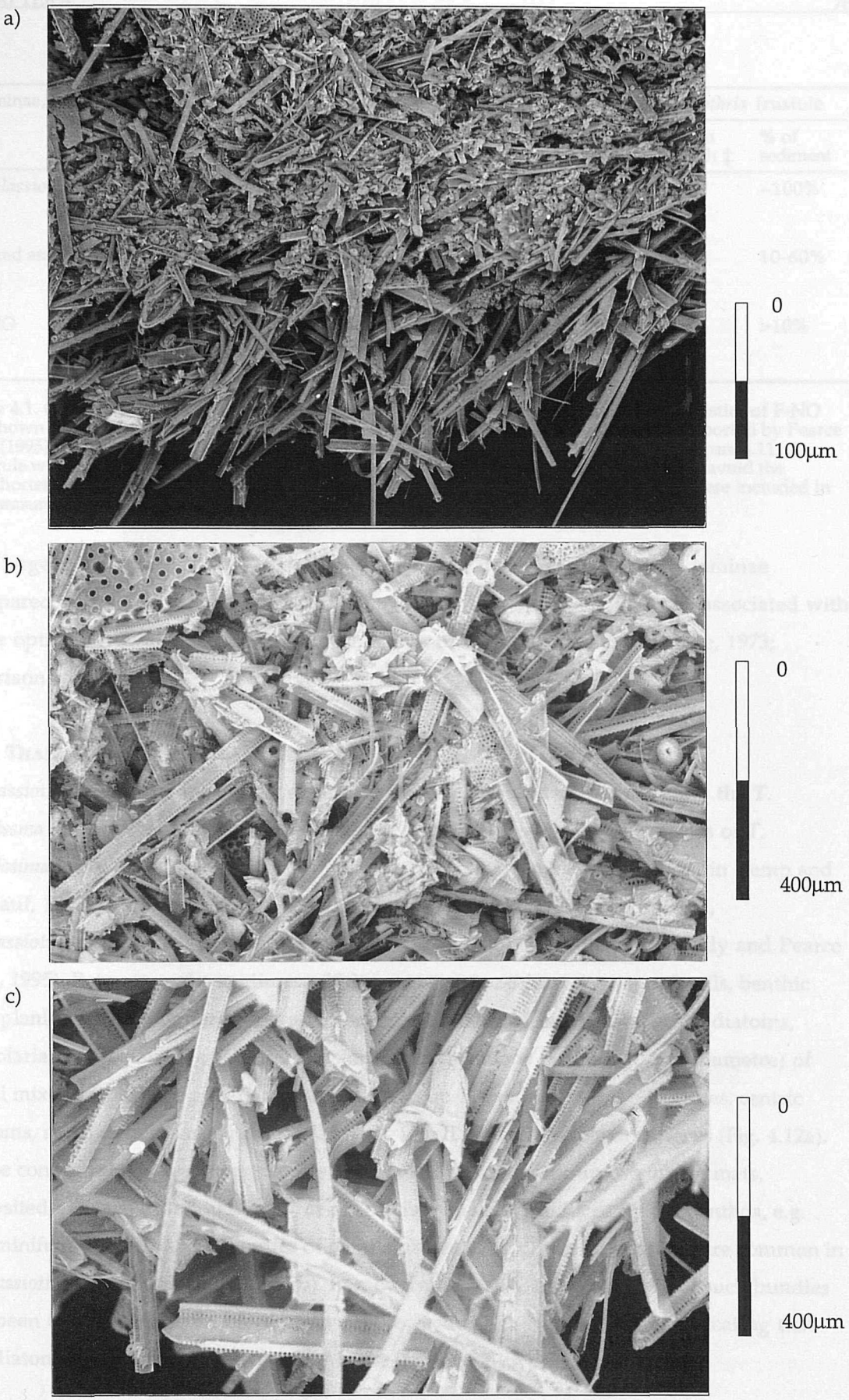


Figure 4.11. BSEI images of a single lamina couplet; a) complete couplet with mixed assemblage laminae on the top surface; b) Detail showing mixed composition and poor mat structure; c) Detail of *Thalassiothrix*-rich laminae showing near mono-specific composition, strong mat structure and larger mean frustule size.

| Laminae/sediment type | Appearance in BSEI photomosaic | Dominant fabrics | Typical *Thalassiothrix* frustule | | |
|---|---|---|---|---|---|
| | | | Typical length | Mean width ‡ | % of sediment |
| *Thalassiothrix*-rich | Dark | • Pervasive mat structure<br>• Parallel frustule bundles | >100µm | 4.8 | ~100% |
| Mixed assemblage | Intermediate | • Fragmented mat structure<br>• Silt aggregates | <100µm | 3.4 | 10-60% |
| F-NO | Bright | • Homogenous structure<br>• Disrupted mat structure in burrow fills | <50µm | n.d. | >10% |

Table 4.1. Characteristics of *Thalassiothrix*-rich and mixed assemblage laminae. Characteristics of F-NO are shown for comparison. Data from SEM stubs samples and BSEI photomosaics and supported by Pearce *et al.* (1995). ‡measured for one lamina couplet from Sample 138-850B-10H-7, 71cm , see Figure 4.11. Frustule width is measured perpendicular to length from the outer edge of the side bars. To avoid the foreshortening effects of tilted frustules, only frustules with both lines of areolae visible were included in the measurements.

The larger *Thalassiothrix* spp. frustule widths found in *Thalassiothrix*-rich laminae compared to the mixed assemblage laminae suggests that these laminae were associated with more optimal growing conditions, such as higher nutrient availability (Paasche, 1973; Harrison *et al.*, 1977).

### 4.3.1 *THALASSIOTHRIX*-RICH LAMINAE

*Thalassiothrix*-rich laminae consist of stacks of mats composed of diatoms from the *T. longissma* Group. Preliminary studies indicate that several varieties/subspecies of *T. longissima* make up between 95% and 100% of the fossil assemblage (J. Baldauf in Kemp and Baldauf, 1993; Pearce *et al.*, 1995). Individual mats range from 15 to 20µm thick, *Thalassiothrix*-rich layers are composed of around 25-30 of these mats (this study and Pearce *et al.*, 1995). Between and sometimes within mats are rare calcareous nannofossils, benthic and planktonic foraminiferas and non-*Thalassiothrix* spp. biosiliceous species (diatoms, radiolarians and silicoflagellates). Occasional concentrations (around 100µm diametre) of small mixed assemblage material (such as broken up *T. longissima* Group frustules, centric diatoms, small radiolarians and coccoliths) are found on or close to mat surfaces (Fig. 4.12a). These concentrations are interpreted as relict faecal pellets swept up by sinking mats, deposited between individual mats, or alternatively pellets produced by the benthos, e.g. foraminifera (Section 4.3.2). Bundles of parallel frustules of similar dimensions are common in *Thalassiothrix*-rich laminae (Fig. 4.12b). In modern net hauls, the occurrence of such bundles has been taken as evidence of vegetative reproduction (Hallegraeff, 1986), indicating that the diatoms were growing actively within the mat structure before deposition.

a)

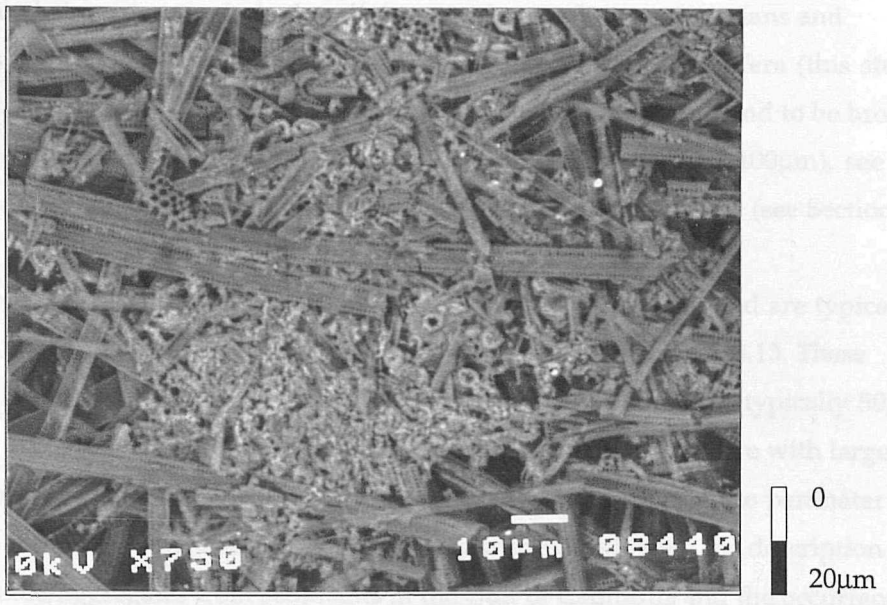


b)

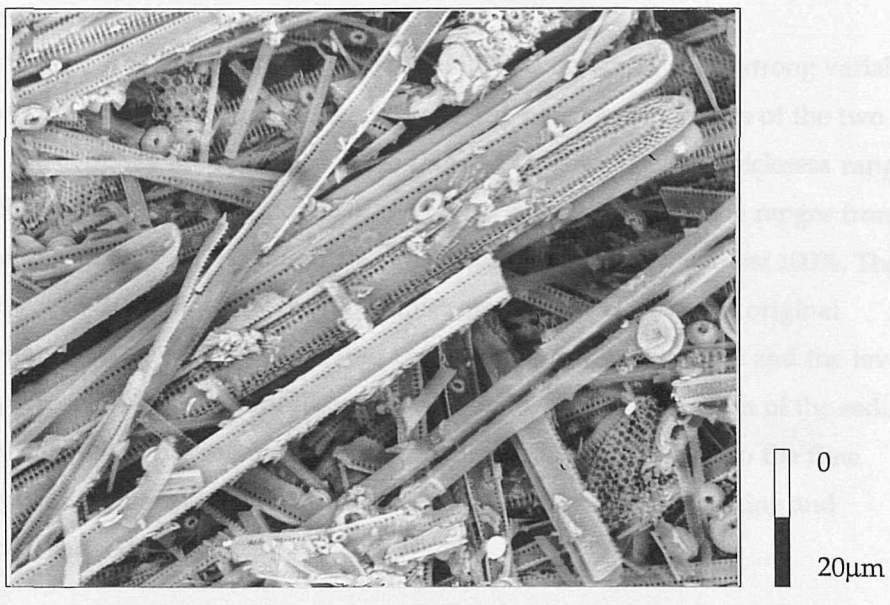


Figure 4.12. Characteristic structures in *Thalassiothrix* -rich layers
a) Concentration of fine-grained material ~60% carbonate containing fragmented diatom and radiolarian frustules, interpreted as relict faecal pellet; b) bundle of parallel *T. longissima* Group frustules of similar dimensions interpreted as evidence of vegetative reproduction within the mat structure.

### 4.3.2 MIXED ASSEMBLAGE LAMINAE

Mixed assemblage laminae contain 10-60% *T. longissima* Group frustules with the remaining sediment fraction being composed of other diatom species (10-50%), radiolarians and silicoflagellates (1-10%), calcareous nannofossils (0-80%) and rare foraminifera (this study and Pearce *et al.*, 1995). The *T. longissima* Group frustules are narrower and tend to be broken into shorter lengths than in *Thalassiothrix*-rich layers (generally less than 100μm), see Table 4.1. Mixed assemblage layers show varied frustule preservation levels (see Section 4.4).

Aggregates of silt-sized particles occur throughout the '4.4Ma' basal unit and are typically associated with the upper boundary of mixed assemblage layers, see Figure 4.13. These aggregates are lensoid with long axes parallel to lamina structure, they are typically 50μm thick and up to 1000μm across. These aggregates tend to have a clear structure with larger particles, typically carbonate grains, closely and regularly spaced around the perimeter surrounding an inner core of smaller, densely packed particles. Following the description of similarly structured aggregates from sediments in the Gulf of California and the occurrence of crushed carbonate foram tests these aggregates are interpreted as the crushed remains of agglutinating foraminifera tests (Pike, 1996).

### 4.3.3 OCCURRENCE OF LAMINAE COUPLETS

Laminae couplets cannot be defined throughout the LDM sections and show strong variability where they do occur. Both total couplet thickness and the ratio of thicknesses of the two laminae within the couplets are highly variable (Fig. 4.14). Total couplet thickness ranges from 30μm to 850μm. The relative thickness of the mixed assemblage laminae ranges from discontinuous lenses making up less than 10% of the couplet thickness to almost 100%. The relative thicknesses of the laminae within a couplet are related to both the original thickness of diatom mats deposited, the period between depositional events, and the level of bioturbation experienced between depositional events. Increasing bioturbation of the sediment surface by surface dwelling microfauna such as foraminifera (again related to the time between depositional events and faunal abundance) results in progressive mixing and homogenization of matted layers.

### 4.3.4 THE FRONTAL DEPOSITION MODEL: EVIDENCE FROM LAMINAE COUPLETS

The alternation between mixed assemblage and *Thalassiothrix*-rich laminae is interpreted as evidence for episodic deposition (Kemp *et al.*, 1995; Pearce *et al.*, 1995). Crushed foraminiferal (carbonate and agglutinating) tests are typically found at the top of mixed assemblage layers, directly below the overlying matted layer (Fig. 4.13). This relationship suggests that foraminifera colonized the organic-rich diatom mat deposits, breaking down the matted structure of the sediment surface. Material accumulated between depositional events would be assimilated into this broken up surface layer resulting in the mixed

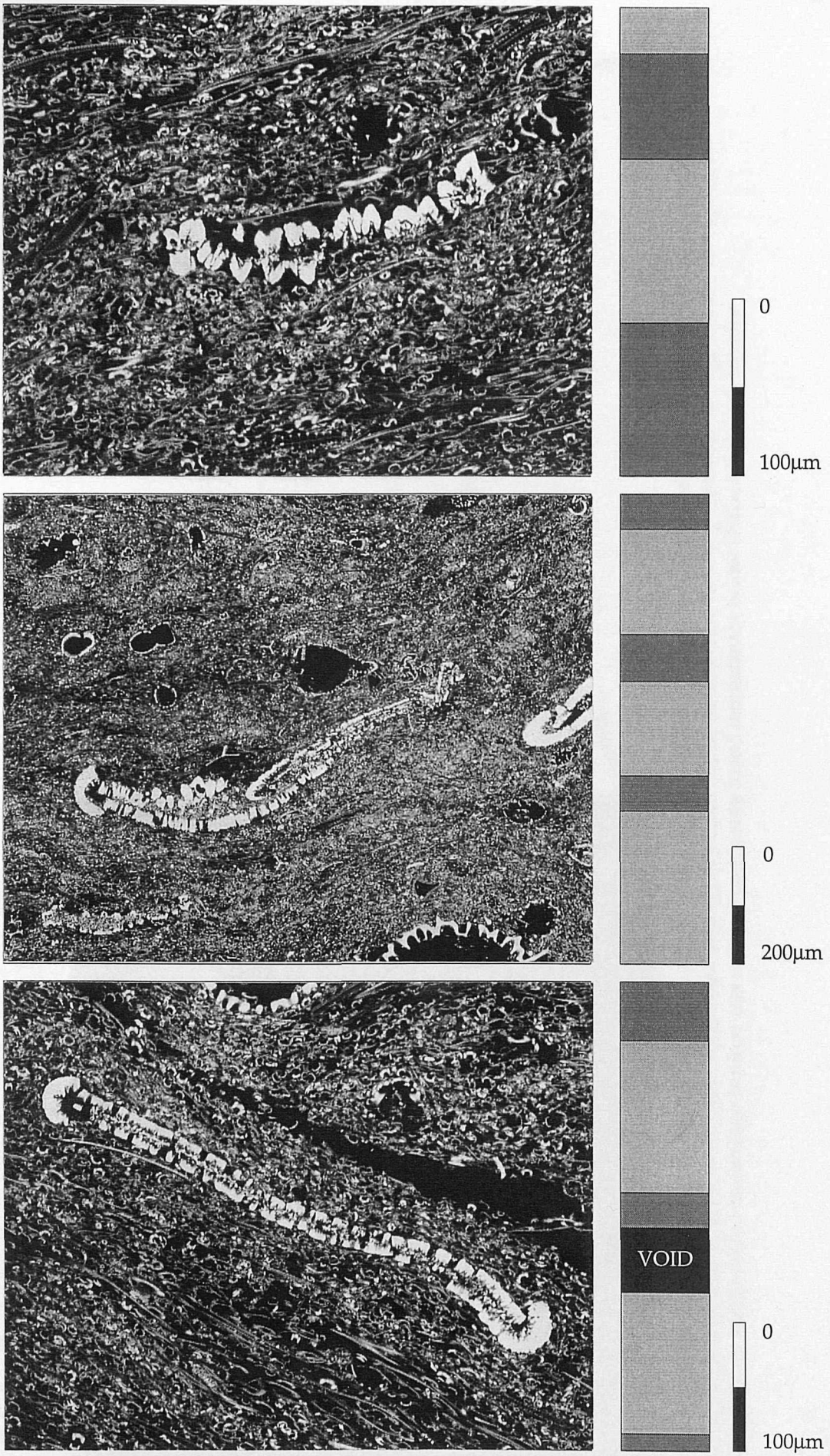


Figure 4.13. Examples of occurrence of silt aggregates and crushed carbonate foraminifera relative to laminae couplets. Sedimentary logs shown for reference; a) and b) directly beneath diatom-rich lamina; and, c) in lower part of mixed assemblage lamina.

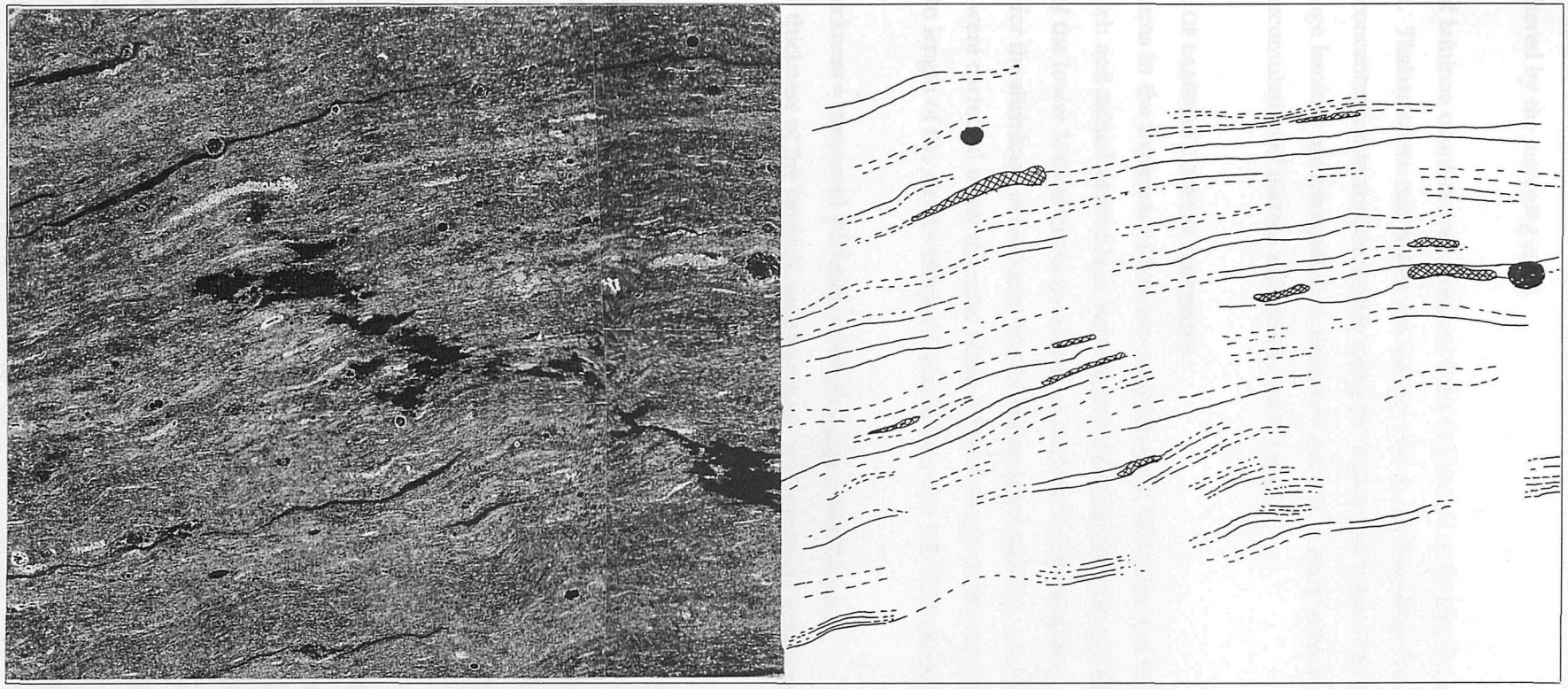


Figure 4.14. BSEI photomosaic of 138-850B-10H-7, 73-74cm with schematic overlay showing lateral impersistence of laminae and the occurrence of silt aggregates relative to laminae couplets. Solid areas denote radiolarian frustules and cross-hatching represents silt aggregates. Silt aggregates tend to occur within mixed assemblage laminae and are most commonly found immediately below *Thalassiothrix*-rich laminae.

assemblage laminae. The occurrence of foramineral remains directly below the overlying matted layer suggests that they were active immediately prior to the mat deposition event, and were smothered by the incoming mats.

Observations of laminae couplets are consistent with the frontal depositional model discussed in Section 2.4.2. *Thalassiothrix*-rich layers are interpreted as representing flux from periods of diatom mat concentration in surface waters along the Equatorial Front. The intervening mixed assemblage laminae are interpreted to represent periods of more normal deposition with reduced accumulation of diatom mats in the frontal region.

#### 4.3.5 CYCLICITY OF LAMINAE COUPLET THICKNESS

To test for patterns in the thickness of laminae couplets, total thickness and thickness of *Thalassiothrix*-rich and mixed assemblage laminae were measured from x20 BSEI photomosaics of the lower 104mm of the basal unit in Hole 847B (276 couplets), see Appendix A5. To account for the shrinkage of sediment blocks during impregnation, couplet thickness measurements were corrected using the ratio of the original length of the sample block ($length_{original}$) to length of the sample block measured from the x20 BSEI photomosaic ($length_{mosaic}$).

$$\text{True thickness} = \text{measured thickness} \times (length_{original} / length_{mosaic}) \qquad \text{Equation 4.1}$$

The cumulative thickness of the laminae couplet record was measured to the centre of each couplet.

This record of couplet thickness was tested for cyclic variations using spectral analysis. By using the Lomb method for the calculation of power spectra (Press *et al.*, 1992), the records of couplet thickness did not have to be interpolated to give evenly spaced data points. This use of unevenly spaced data points reduces computational error and problems associated with the aliasing effect below the sampling frequency (see Appendix A3 for full details of method).

#### 4.3.6 INTERPRETATION OF COUPLET THICKNESS CYCLICITIES

A strong periodicity (significant at the 95% level, Fig. 4.15c) was found in the records of total couplet thickness with a frequency of $0.38mm^{-1}$, this is equivalent to a wavelength of 2.63mm (wavelength=1/frequency). Using the mean couplet thickness (~390μm) this wavelength is calculated as representing approximately 6-7 laminae couplets or depositional events. Similar peaks are found in the power spectra calculated for both *Thalassiothrix*-rich and mixed assemblage laminae thickness (just above and below the 50% significance level respectively, Fig. 4.15a,b). A second peak in the power spectra for total couplet thickness is found at $0.12mm^{-1}$ (at the 90% significance level, Fig. 4.15c), this peak is also found in the power spectra for *Thalassiothrix*-rich layers. Using the mean couplet thickness gives an approximate cyclicity of 21 couplets.

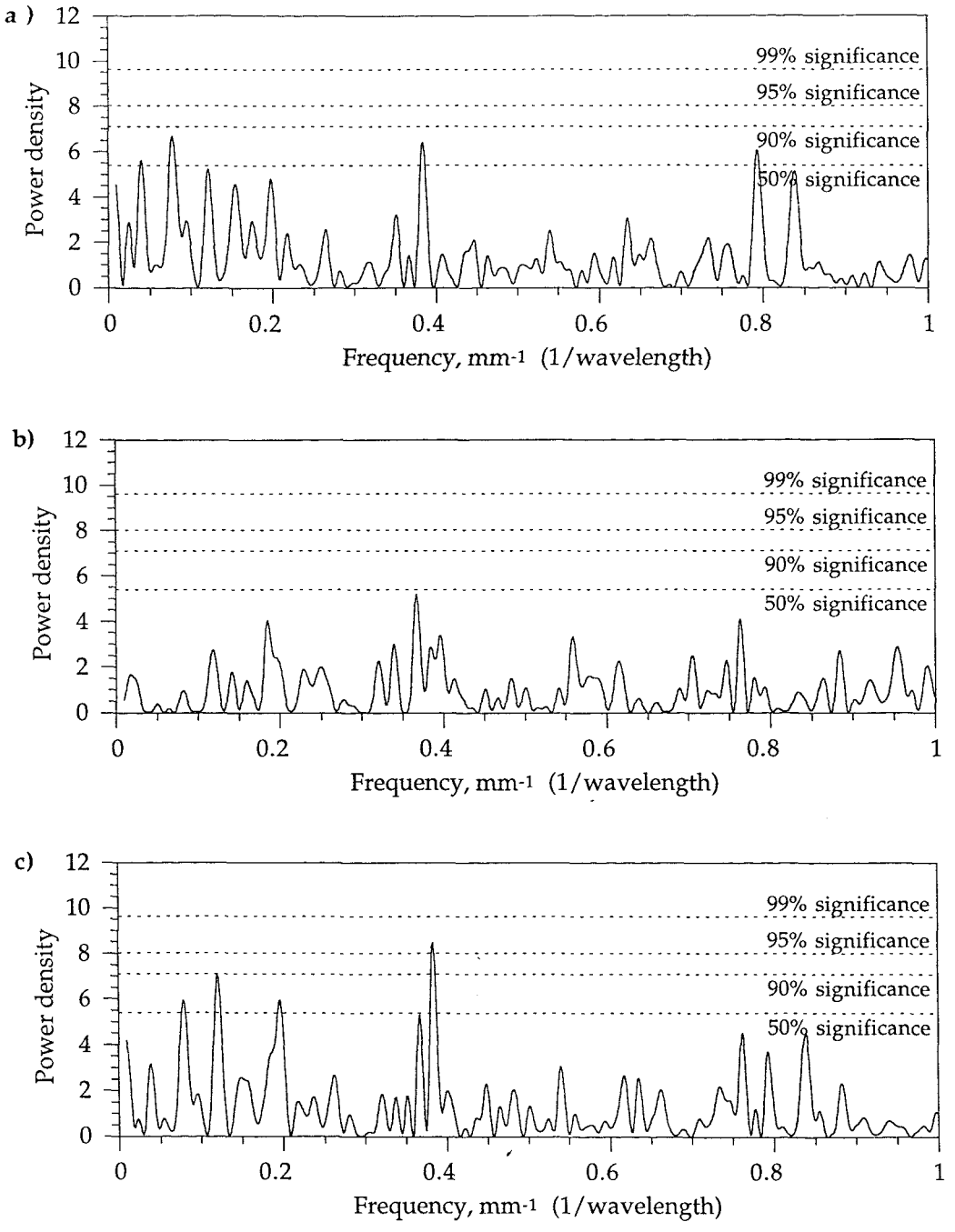


Figure 4.15. Power spectra for variation in lamina couplet thickness with cummulative thickness; a) Thalassiothrix-rich layers; b) mixed assemblage layers, and; c) total couplet thickness.

Interpretation of the controls on these cyclicities is dependant on the periodicity of laminae couplet deposition, i.e. mat flux events. With reference to the discussion of sedimentation rates in Chapter 5 (5.3 and 5.6), I assume that laminae couplets were deposited on a quasi-annual basis (implying sedimentation rates of around 390m/Ma, see Section 5.4). This assumption results in the 0.38 and 0.12 $mm^{-1}$ frequency peaks giving periodicities of around 6-7 and 21 years respectively (within a total time series of 276years).

The greatest variability in thickness is seen in the *Thalassiothrix*-rich laminae, suggesting that this is the principal control on couplet thickness. The thickness of the *Thalassiothrix*-rich couplets is controlled by the accumulation and sedimentation of buoyant diatom mats along the Equatorial Front (see Section 4.3.4). Less pronounced peaks in the mixed assemblage layers at the same 6-7 and 21 couplet periods (below the 50% significance level, see Figure 4.15b) suggest that periods with enhanced diatom mat accumulation also showed slightly elevated sedimentation rates between depositional events. A summary of climate and climate proxy records with periodicities similar to those found in the laminae couplet thickness record is given in Table 4.2.

| Reference | Record | Periodicity |
|---|---|---|
| Cane, 1983 | Modern El Niño events | 2-9 years |
| Weinheimer *et al.*, 1986 | El Niño event periodicity from Monterey Formation laminated sediments | 6Ma - 21 years<br>8Ma - 4 years |
| Enfield and Cid, 1991 | recurrence of strong/very strong El Niño events (using data from Quinn et al., 1987) | 9-12 years |
| Pike and Kemp, 1997 | occurrence of *Thalassiothrix* mats in Gulf of California | 11 years |
| Ripepe *et al.*, 1991 | varved oil shales | 11 years |
| Thurow and Schaaf, 1995 | laminated sediments, Gulf of California | 11 years |
| Labitzke and van Loon, 1990 | QBO-like oscillations in the atmosphere | 11 years |
| Anderson *et al.*, 1990 | bioturbation in laminated sediments off coast of northern and central California (late Pleistocene) | ~20 years |
| Lange et al., 1990 | biological productivity recorded in Santa Barbara Basin sediments | ~20 years |
| Pike and Kemp, 1997 | occurrence of *Thalassiothrix* mats in Gulf of California | 22-24 years |
| Mitchell Jr. *et al.*, 1992; Meko, 1992 | tree rings/ drought in western USA (Holocene) | 22 years |
| Anderson, 1992a; Quinn, 1992 | Nile floods (Holocene) | ~22 years |
| Anderson, 1992b | laminated sediments, Elk Lake - Minnesota (Holocene) | 20-25 years |
| Halfman and Johnson, 1988 | laminated sediments, Lake Turkana | 25 years |

Table 4.2. A selection of climate and climate proxy records with periodicities close to those found in the laminae couplet thickness record from the eastern Equatorial Pacific, modified from Pike and Kemp (1997).

#### 4.3.6.1 Recognized climate cycles with periodicities of less than 25 years

The modern El Niño cycle has a periodicity of 2-9 years (Cane, 1983), but there is strong evidence suggesting that this periodicity has varied over time. For example, laminated sediments from the Monterey Formation suggest periodicities of 21 and 4 years calculated for sediments from 6Ma and 8Ma respectively, see Section 2.3.2 (Weinheimer *et al.*, 1986); and, in the early Holocene records of fire, precipitation and pollen type suggest less frequent strong El Niño cycles (McGlone and Kershaw, 1992). Evidence for palaeo-circulation patterns (related to the closure of the Panama Seaway) suggests that the modern circulation patterns were not fully developed until after 5.5Ma, see Section 2.3.2. Prior to this El Niño-type events observed in the radiolarian record are not completely analogous to modern El Niño events (Casey *et al.*, 1989). Records of variability in the strength of El Niño events have been inferred from proxy data for precipitation (e.g. tree-rings Meko, 1992) and SST (e.g. coral Dunbar *et al.*, 1994). Both these ancient and historical records show strong and very strong events occur with a periodicity of 9-12 years (Enfield and Cid, 1991).

Solar modulation of El Niño events has been suggested as a cause for the occurrence of decadal periodicities in the late Pleistocene varve/bioturbation cycle off the California coast (Anderson *et al.*, 1990). Decadal-scale variations in the modern Pacific Ocean have been identified in ocean circulation. Spectral analysis of circulation indices shows several peaks between 2 and 6 years associated with El Niño events and a broad spectral peak with periods above 20 years (Trenberth and Hurrell, 1994). This peak is interpreted as the result of periodic deepening of the Aleutian low pressure cell. As the Aleutian Low expands and shifts southwards zonal winds are weakened (as in an El Niño event), consequently, upwelling is reduced, SST rises by 0.75°-1.0°C and the thermocline is deepened (although to a lesser degree than during El Niño events). In effect, this shift in atmospheric circulation results in the background state of the ocean-atmosphere system resembling the changes associated with weaker El Niño events (Graham, 1994; Norton and McLain, 1994; Trenberth and Hurrell, 1994).

#### 4.3.6.2 Controls on the periodicity observed in the laminae couplet thickness record

Using the frontal model for the generation of mat fluxes, the periodicities observed in laminae thickness are interpreted to reflect the occurrence and relative strength of El Niño/La Niña-type events: increased couplet thickness (especially in the record of *Thalassiothrix*-rich lamina thickness) associated with nutrient-rich waters and strong convergence during the return to cold tongue conditions; and decreased couplet thickness associated with nutrient-poor El Niño periods, when the Equatorial Front is weakly developed.

The 0.38mm$^{-1}$ frequency suggests an El Niño/La Niña-type event periodicity of 6-7 years, well within the range suggested by Cane (1983, 2-9 years). The 0.12mm$^{-1}$ frequency suggests variations in strength of these El Niño/La Niña-type events with a periodicity of around 21 years, similar to that observed in modern records. Alternatively, this periodicity could reflect the influence of the Aleutian Low during the deposition of these sediments. A weakening of the Aleutian Low results in conditions similar to those observed during El Niño events and might be assumed to control depositional patterns in the same way.

## 4.4 DISSOLUTION LEVELS

The sediments examined in this study are unusual as the frustules they contain are exceptionally well preserved. This section examines controls on dissolution levels observed in the sediments. Levels of dissolution are quantified using a new index of diatom dissolution developed from a similar but qualitative method used to investigate water column dissolution in radiolarians (Erez *et al.*, 1982). The results of these analyses are discussed in the context of mechanisms controlling the dissolution levels observed in these sediments.

### 4.4.1 CURRENT UNDERSTANDING OF BIOSILICEOUS FRUSTULE DISSOLUTION

Levels of frustule dissolution observed in sediments are primarily controlled by; (1) the initial level of silicification; (2) the period the frustule is in contact with strongly under saturated sea water (sinking and burial rates); (3) the level of protection from sea water resulting from organic coatings; (4) levels of pore water dissolution; and, (5) impurities in the biogenic silica inhibiting dissolution (Fig. 4.16). ICP measurements indicate negligible levels of frustule impurities (see Appendix A7) in the sediment examined in this study. These factors are discussed in more detail in the following section.

#### 4.4.1.1 Controls on silicification

Within species, levels of silicification are related to the availability of dissolved silica and the growth rates. Laboratory experiments show that cells grown in silica-deficient growth mediums tend to be more lightly silicified than cells of the same species grown in silica replete conditions. Levels of silica per cell can decrease by a factor of 2-3 (Paasche, 1973; Harrison *et al.*, 1977; Booth and Harrison, 1979). Growth rates can also control silicification levels, for example; in experiments using nutrient-depleted but silica replete growth mediums cell growth rate was slowed; however the availability of silica resulted in heavy silicification of the cells (Lewin, 1957).

The effect of silica availability during frustule formation as a factor in levels of frustule preservation is currently being discussed (D. DeMaster and D. Nelson pers. comm.). If silica is

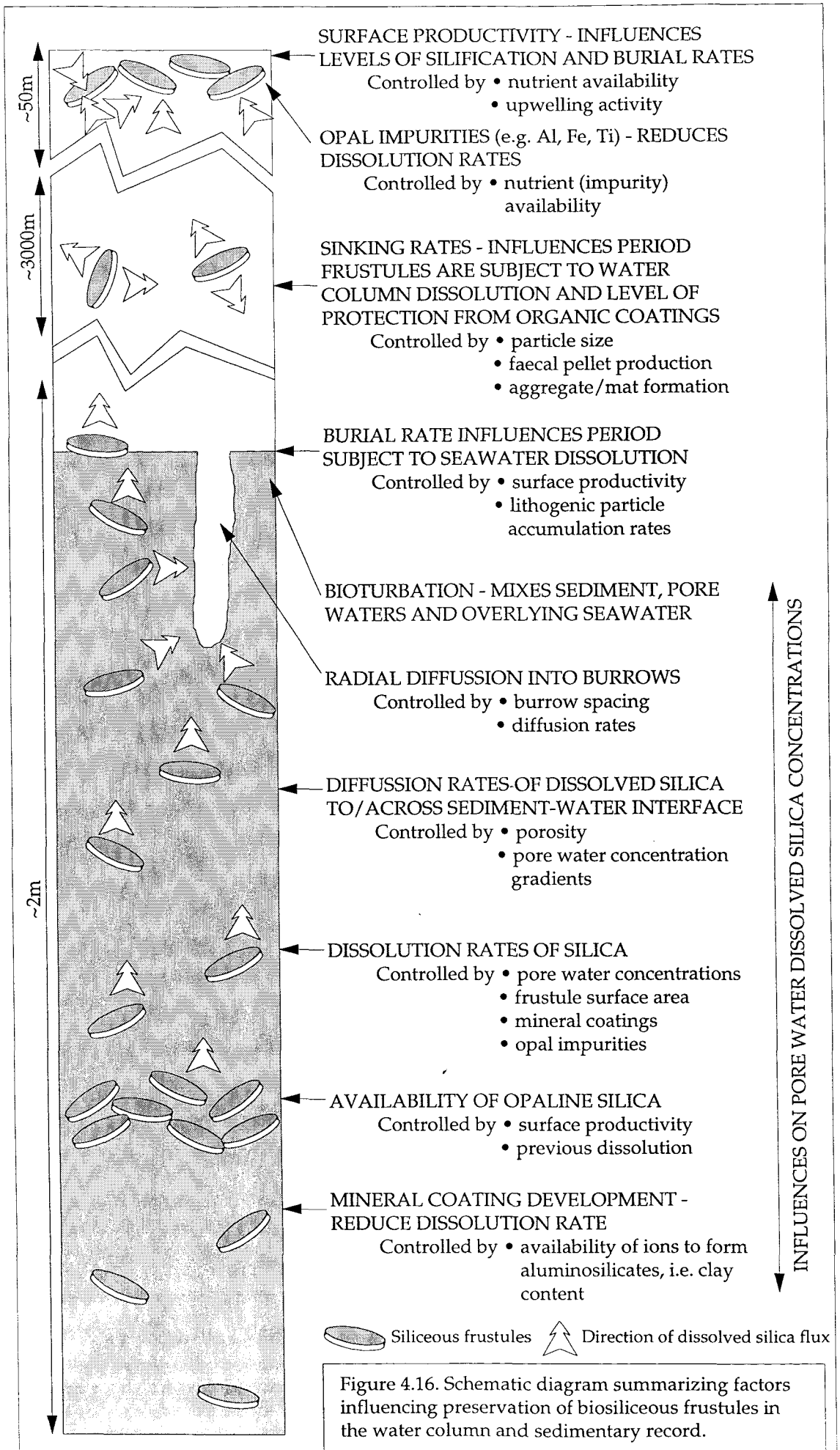


Figure 4.16. Schematic diagram summarizing factors influencing preservation of biosiliceous frustules in the water column and sedimentary record.

readily available in the surface waters, frustules will tend to be more heavily silicified (and thus dissolve slower) than frustules formed in silica-poor surface waters. Morphological changes related to silica deficiency during growth such as thinning of cell walls and suppression of specialized silica structures (the areolae cross walls in *Thalassiosira* or spines in *Chaetoceros*) are well documented (Paasche, 1973; Harrison *et al.*, 1976; Harrison *et al.*, 1977), but the effects of these changes on frustule preservation have yet to be investigated.

#### 4.4.1.2 Sinking rates

Larger particles, such as diatom mats, sink up to 50 times faster than individual frustules. The relationship between aggregate size and sinking rate established by Alldredge and Gotschalk (1989) suggests that mats with a diametre of 2cm should sink at around 150m/day (Section 2.5.2). This means that the frustules in LDM deposits would have been exposed to the strongly undersaturated seawater for significantly shorter periods than cells sinking individually, resulting in reduced levels of dissolution.

#### 4.4.1.3 Influence of organic coatings

Dissolution of diatom frustules by undersaturated surface waters during life is prevented by the organic material coating the siliceous skeleton. Recent deposits of *Rhizosolenia* aggregates reaching the sea floor following accumulation along the Equatorial Front had organic carbon levels of 1-12.5% by weight, 5-39 times higher than in associated sediments (Smith *et al.*, 1996). Assuming that *Thalassiothrix* mats accumulated in the same way, and arrived at the sea floor with similar organic carbon levels, the laminae with higher *Thalassiothrix* contents would also have higher levels of associated organic carbon. These coatings would contribute to the low levels of dissolution observed in LDM material.

#### 4.4.1.4 Pore water dissolution and burial

Opal dissolution within sediments is primarily controlled by the concentration of dissolved silica in pore waters, but pore water concentrations themselves are influenced by the availability of biogenic silica within the sediment. Low pore water concentrations drive opal dissolution. As more opal is dissolved the pore-water concentrations increase and dissolution is reduced. Pore water silica concentrations vary between oceanographic regions and do not approach a common concentration (Willey and Spivack, 1997).

Pore water concentrations are reduced by the diffusion of dissolved silica along concentration gradients towards the sediment-water interface. This combination of dissolution and diffusion processes results in an asymptotic profile of pore water concentration with depth below the sediment-water interface (Schink *et al.*, 1974; Schink *et al.*, 1975). The exact shape of these profiles is dependant on the interplay between the controls on these two processes, and the flux of biogenic silica to the sediments. The huge range of reported asymptotic silica

concentrations (220 to 850μM in the deep Atlantic and Pacific, data from Archer *et al.*, 1993) suggests that the solubility of silica may not be constant (Schink *et al.*, 1974; Archer *et al.*, 1993; Willey and Spivack, 1997).

Gradients in pore water are driven by the difference in concentration between overlying seawater and sediment, and are also influenced by the level of bioturbation. Bioturbation acts as a quasi-diffusive process affecting both pore-waters and sediment particles. Radial diffusion of pore water into deep burrows expands the influence of sea water to frustules below the asymptotic silica concentration predicted by diffusion models (Aller, 1978; Aller, 1980).

Mathematical models of pore-water concentrations without the influence of bioturbation have not been published. Models examining the effect of bioturbation levels imply that at low bioturbation rates, the asymptotic silica concentration is reached within the top 5cm of the sediment (Figure 7-6 in Berner, 1980). Beneath that depth, pore water concentrations are controlled solely by dissolution rates and availability of biogenic silica. Using the sedimentation rates estimated for laminated sediments in Chapter 5 (204m/Ma to 410m/Ma), would mean that, for these sections, biogenic opal would have been removed from the influence of seawater (buried below 5cm deep) over periods of 120 years to 270 years.

#### 4.4.2 CALCULATION OF DISSOLUTION INDEX

Numerical modelling, laboratory and *in situ* experiments relate silica dissolution kinetics to the volume of silica released into pore waters rather than to the level of silica remaining in the sediments (Boudreau, 1990 and references therein). Dissolution has been quantified in Southern Ocean sediments using transfer functions that relate surface species assemblages to those found at the sediment surface (Pichon *et al.*, 1992), but this method is not applicable to near-monospecific equatorial sediments. Berger (1968) and Erez (1982) demonstrated that dissolution (measured by weight loss) resulted in structural changes in radiolarian frustules, such as the enlargement of areolae and loss of delicate structures (such as spines). The following method for quantification of dissolution in diatom frustules was initially based on these studies.

In order to investigate the controls on dissolution in individual laminae, preservation of individual frustules was examined using SEM techniques. Quantification of frustule dissolution in LDM sediments was based on the level of preservation of *T. longissima* Group frustules using a number of observational criteria (Table 4.3 and Fig. 4.17.). The mean dissolution level for each sample was calculated from 500 individual frustules along a single section line of a strew mount. These strew mounts (carbonate and organic carbon free and gold coated) were examined under x3500 magnification using the SEM (Jeol SEM-6400). The index criteria were initially chosen on the basis of easy and unambiguous identification, rather

a)

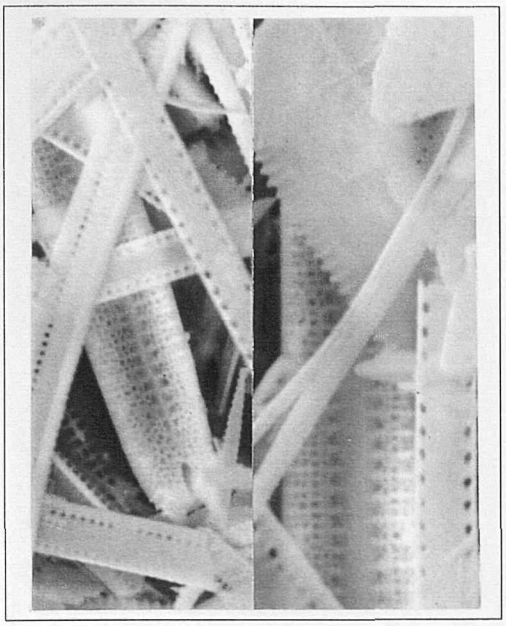

b)

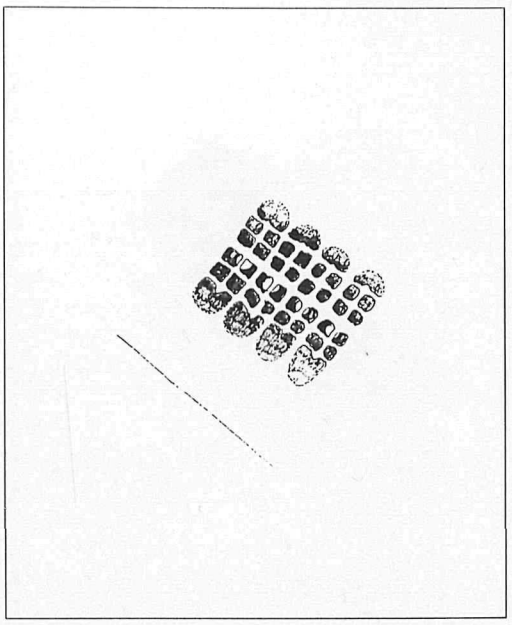

c)

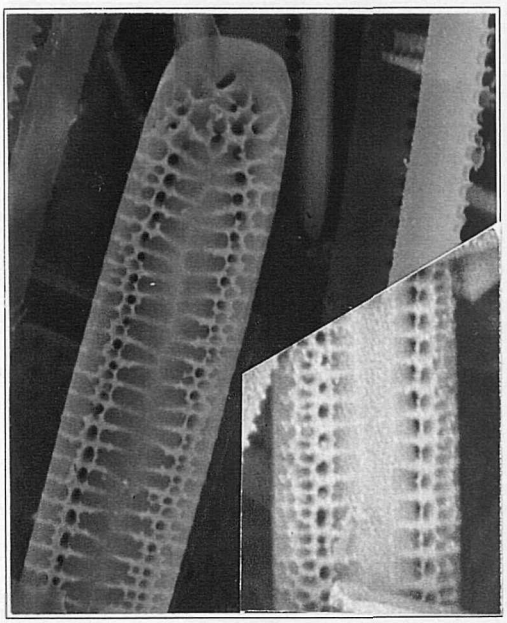

d)

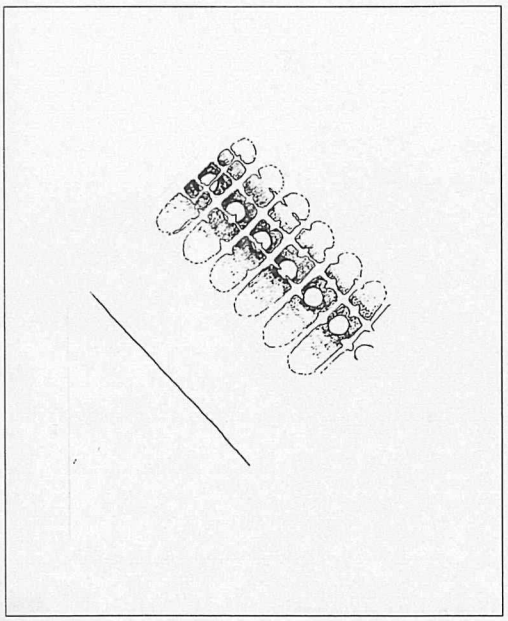

e)

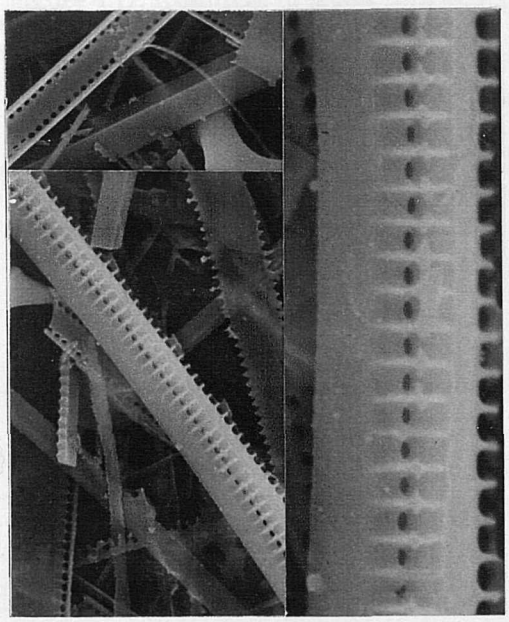

f)

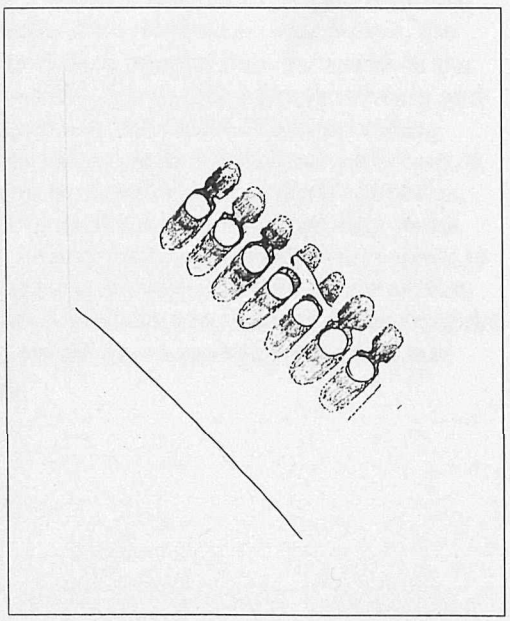

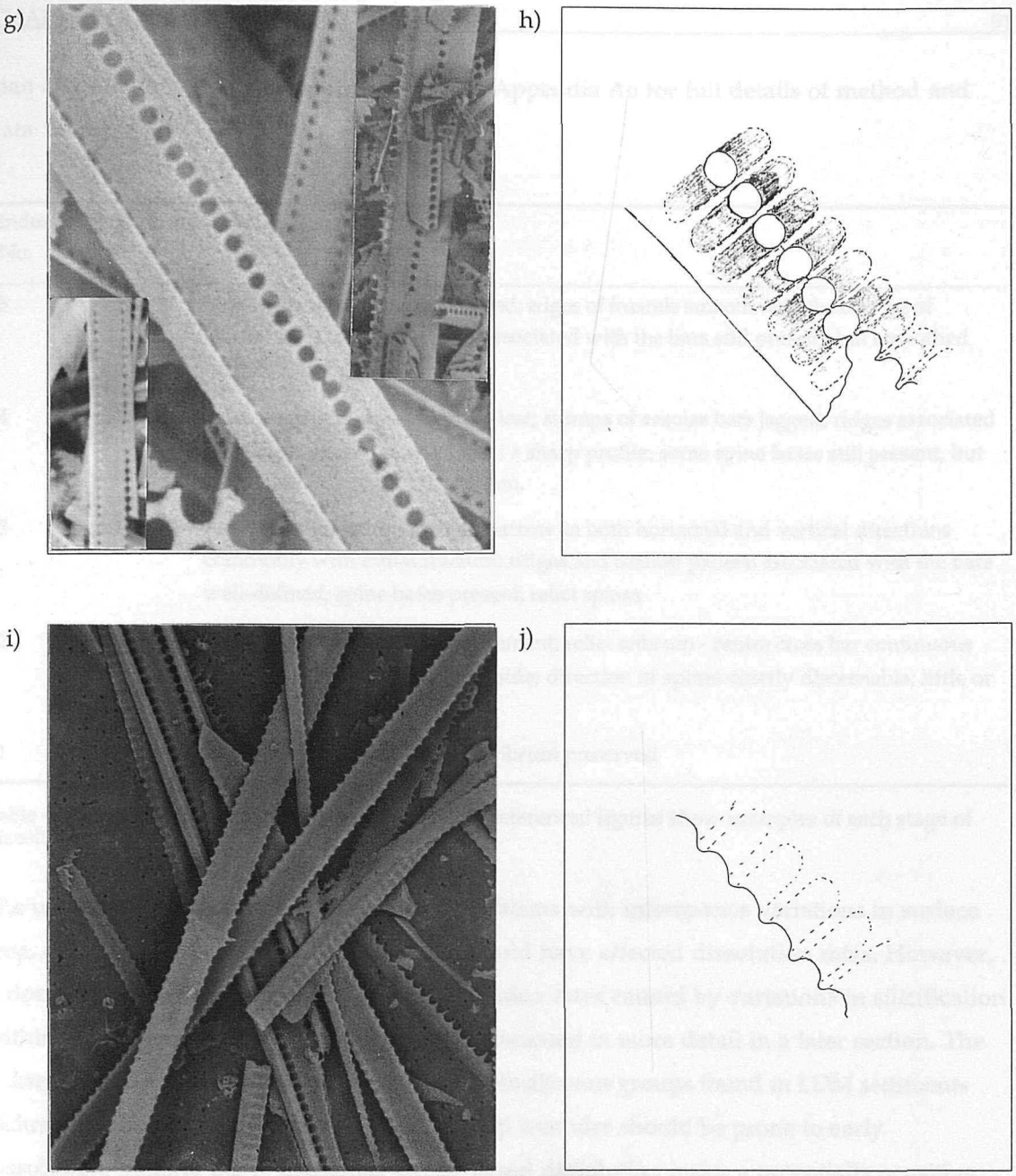


Figure 4.17. Examples of levels of dissolution observed in *T. longissima* Group frustules with reference to dissolution index. Index 1 frustules show little or no dissolution, the porate cribrum is entire and the diametre of the areolae is smaller than the width of the silica struts separating them (a and b). Index 2 frustules have a relict porate cribrum and enlarged areolae, the diametre of the areolae is similar to the width of the separating struts (c and d). More advanced dissolution removes the remaining delicate structure of the cribrum leaving only spine bases and relict spines. Areolae enlargement continues, resulting in areolae which have diametres greater than the width the separating struts (Index 3, e and f). Continued enlargement of the areolae narrows the separating struts to the point at which they fracture and the side sections pull away from the centre section (Index 4, g and h). Only the centre section of Index 5 frustules are counted, these frustules have no side section and the stumps of the fractures struts are smoothed, the frustule surfaces show heavy pitting and etching (i and j).

than any relationship to dissolution rates (see Appendix A6 for full details of method and data tables).

| Index No. | Figure No. | Index criteria |
|---|---|---|
| 5 | 4.17a, b | Side sections completely removed; edges of frustule smooth with the stumps of areolae bars rounded; ridges associated with the bars still present, but smoothed profile; surface pitted |
| 4 | 4.17c, d | Sides coming away or recently lost; stumps of areolae bars jagged; ridges associated with the bars well-defined with a sharp profile; some spine bases still present, but no evidence of the porate cribrum. |
| 3 | 4.17e, f | Areolae holes enlarged; bars narrow in both horizonal and vertical directions commonly with initial fracture; ridges and scallop pattern associated with the bars well-defined; spine bases present; relict spines |
| 2 | 4.17g, h | Little or no areolae hole enlargement; relict cribrum - centre cross bar continuous with relict cross bars to either side; direction of spines clearly discernable; little or no surface etching. |
| 1 | 4.17i, j | Intact frustules; entire porate cribrum preserved |

Table 4.3. Index criteria of *Thalassiothrix* dissolution, referenced figures show examples of each stage of dissolution.

The use of single species avoided potential problems with interspecies variations in surface area, opal structure or impurity uptake that could have affected dissolution rates. However, it does not however avoid variations in dissolution rates caused by variations in silicification within the chosen species. This effect will be discussed in more detail in a later section. The *T. longissima* Group is one of the least resistant biosiliceous groups found in LDM sediments (Schrader, 1971). This means *T. longissima* Group frustules should be prone to early dissolution, making the *T. longissima* Group based dissolution index a potentially sensitive indicator of sediment dissolution levels.

### 4.4.3 USING THE DISSOLUTION INDEX TO INVESTIGATE FACTORS INFLUENCING DISSOLUTION

Analysis of sediments dissolved experimentally in 2M $Na_2CO_3$ over 0.5 hour to 6 hour periods show that the dissolution index increases with an approximate parabolic relationship to dissolution period (Fig. 4.18). This is consistent with published studies of dissolution kinetics (Erez *et al.*, 1982; Kamatani *et al.*, 1988) in which delicate structures were destroyed rapidly in the early stages of dissolution. During this period of rapid silica release, the surface area of frustules is greatly reduced (Erez *et al.*, 1982; Kamatani *et al.*, 1988) resulting in a rapid reduction in dissolution rates. Reduction in dissolution rates reduces rates of structural change (measured by the dissolution index) resulting in the observed parabolic relationship between dissolution period, silica released and dissolution index.

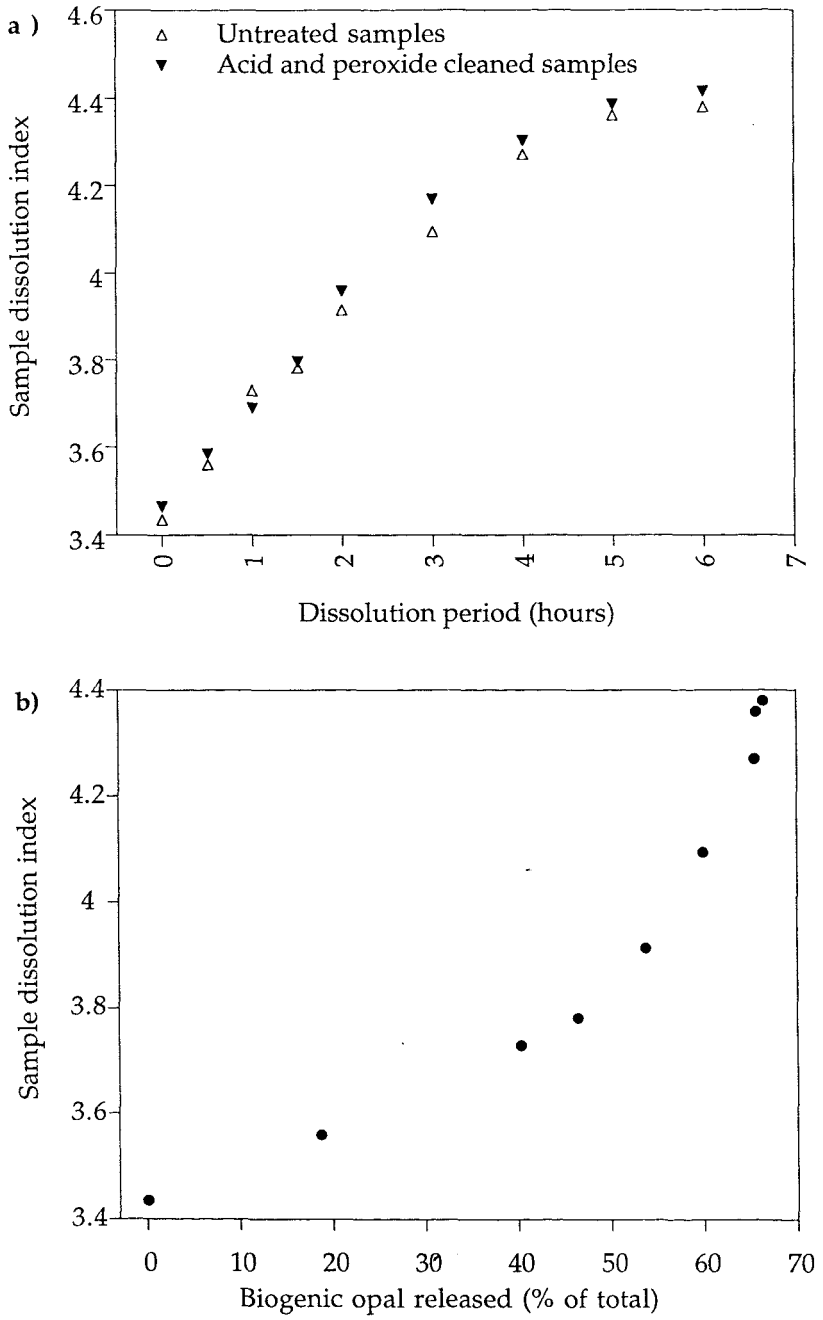


Figure 4.18. Experimental validation of sample dissolution index measurements; relationship to a) experimental dissolution period for both clean and uncleaned samples; and, b) opal released during experimental dissolution.

Following the results of Kamatani *et al.* (1988) which demonstrated the importance of mineral coatings developing over time in frustule dissolution rates, experimental dissolution was carried out using both cleaned (10%HCl and 10%$H_2O_2$) and untreated sediment samples to test for the effect of surface coatings. Measurements of silica released and comparison of the two dissolution index curves indicates that there is no significant difference between the two dissolution experiments. This suggests that surface coatings do not form a significant control in the dissolution kinetics of these sediments. Since clays are thought to form the major source of Mg and Al ions utilised in mineral coatings, this result is consistent with the low clay content of these sediments.

#### 4.4.4 LEVELS OF DISSOLUTION IN LDM MATERIAL

Two experiments were designed to investigate (1) the difference in dissolution levels between laminated and non-laminated samples in LDM sediments packets compared to the surrounding F-NO; and, (2) the difference between mixed assemblage and *Thalassiothrix* -rich layers.

EXPERIMENT 1: Strew-mounts were made from 31 laminated and non-laminated samples to test the difference in dissolution levels between the two end-member compositions contained in LDM sediment packets. Mean dissolution index results demonstrate a statistically significant difference in the levels of frustule preservation between laminated and non-laminated sediments (at the 95% significance level). Within the '4.4Ma' LDM deposits the laminated sections have a lower mean dissolution index than the non-laminated sections although there is a much higher degree of variability (given by the standard deviation), see Table 4.4 and Figure 4.19. The levels of dissolution observed in F-NO from sediment below the event at Sites 849 and 850 and from Site 848 which does not contain the LDM material, shows similar levels of dissolution to those in the non-laminated sections of the '4.4Ma' LDM deposits.

| Sediment type | Mean dissolution index | Number of samples | Standard deviation |
|---|---|---|---|
| LDM event - laminated | 3.65 | 41 | 0.32 |
| LDM event - non-laminated | 3.82 | 11 | 0.11 |
| F-NO (below LDM) | 3.81 | 22 | 0.11 |

Table 4.4. Comparison of dissolution level in LDM and normal marine sediments using mean dissolution index.

EXPERIMENT 2: This experiment was designed to further investigate the observational evidence of differences between mixed assemblage and *Thalassiothrix*-rich layers (for example differences in frustule size and sediment fabric, see Section 4.3). Since sample size makes it impractical to use samples of individual laminae, this experiment uses measurements of opal released in the first dissolution stage to quantify the proportion of

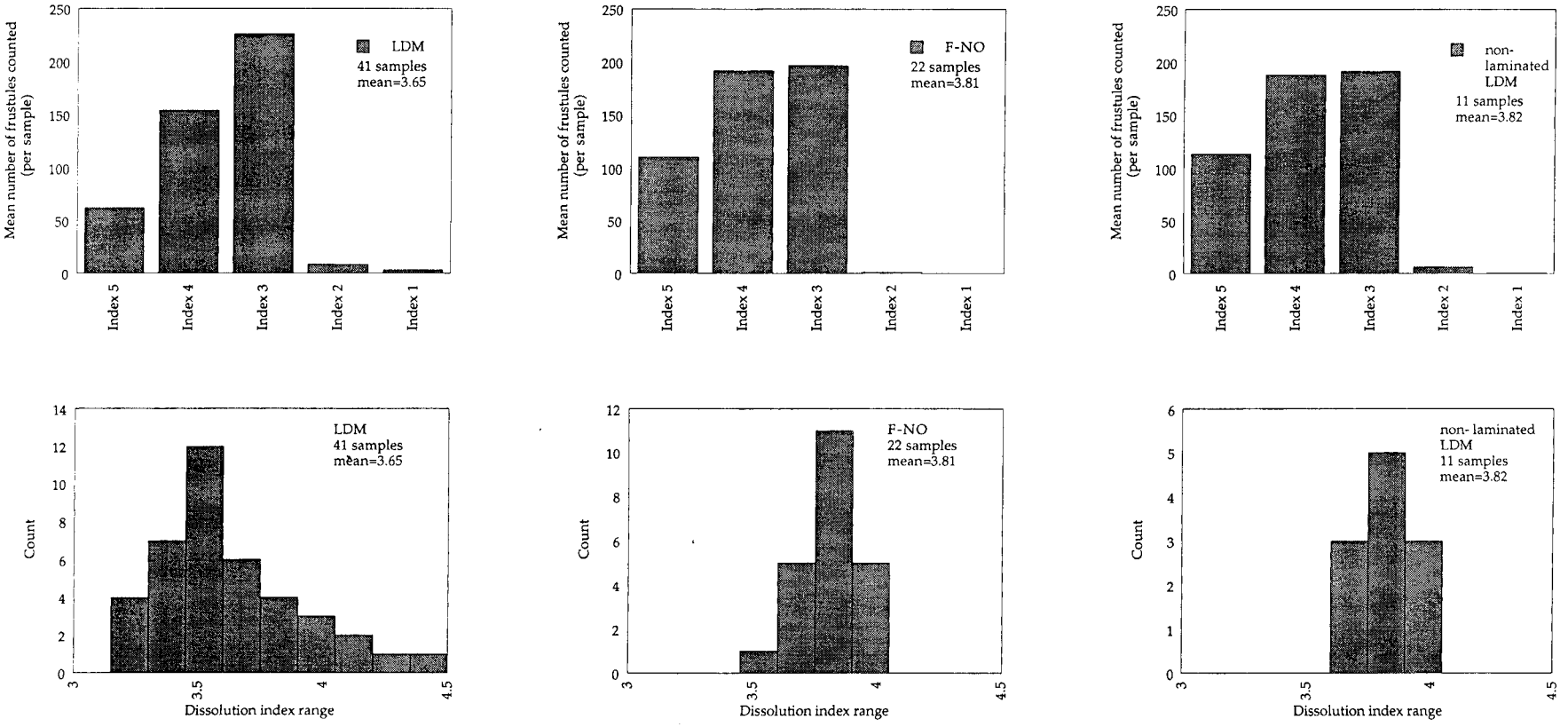


Figure 4.19. Comparision of mean dissolution index distribution for individual frustules and whole samples in LDM, non-laminated LDM and F-NO samples measured during Experiment 1 (see text for further details)

*T. longissima* Group frustules (see Section 3.4.3). Mean dissolution index results for 40 laminated samples were compared with the estimated *T. longissima* Group content.

Plots of opal content (first and second extraction and total) with sample dissolution index (Figure 4.20 a-c) show that as the relative proportion of opal increases, the level of preservation also increases (recorded by a decreasing dissolution index). This relationship is strongest in the first extraction opal (*T. longissima* Group related) where the correlation coefficient, $r^2$ , is 0.675. This value compares to $r^2$ of 0.670 for the relationship between total opal content and sample dissolution index (significant at the 99.9% level, Fig. 4.20a, b). This comparision and the lack of relationship between dissolution index and second extraction opal, non-*Thalassiothrix* spp. opal (Figure 4.20c) demonstrates that the availability of *T. longissima* Group frustules exerts a strong control on the sample dissolution index. Since the dissolution index measures only the dissolution of *Thalassiothrix* spp. frustules, this result is consistent with *T. longissima* Group frustules being more readily dissolved than other biosiliceous components of the sediment, e.g. radiolarians and centric diatoms (c.f. Schrader, 1971). Dissolved silica derived from *T. longissima* Group frustules would rapidly increase pore water silica concentrations and decrease the level of dissolution of other biosiliceous material.

#### 4.4.5 Implications of dissolution index for deposition of LDM material

The dissolution index results identify two trends in the preservation of siliceous frustules in LDM deposits (1) preservation levels within laminated sections of LDM deposits were statistically higher than those observed in non-laminated sections of LDM deposits, and; (2) within the laminated sections, preservation levels increased with increasing *T. longissima* Group content. Factors likely to control these trends include sinking and burial rates, pore water concentration levels and degree of initial silicification. These factors and their implications for LDM deposition are discussed in more detail in the following section.

The formation of diatom mats increases the sinking and burial rates, reducing the time period a frustule is subject to dissolution by the strongly undersaturated seawater. Variations in frustule preservation within LDM material are linked to the *T. longissima* Group content of individual samples. If reduced *T. longissima* Group content resulted from weakened mat forming events, lower burial and sinking rates would be expected, consistent with the observed decrease in frustule preservation levels. Increased sinking and burial rates also reduce the time for remineralization of organic coatings which also reduces the impact of seawater dissolution. Models of organic carbon remineralization suggest that these coating will be destroyed over periods of 30-400 years, this is comparable with the period estimated for the removal of a frustule in LDM deposits to be buried to a depth 5cm (120-270years), below the direct influence of strongly undersaturated sea water. BSEI photomosaics show evidence for

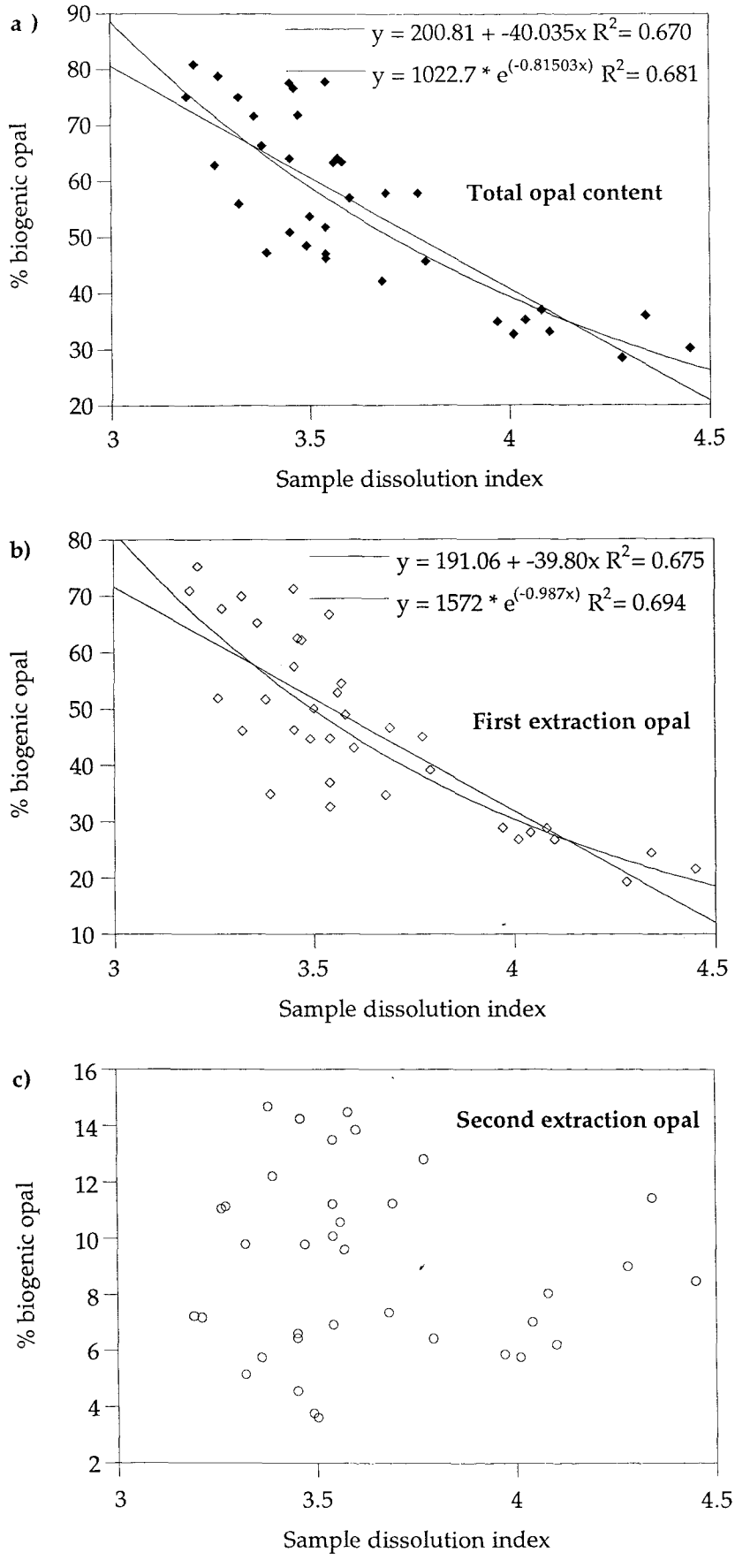


Figure 4.20. Relationship between sample dissolution index and opal content showing both linear and exponential best fit lines; a) total opal content, b) first extraction opal content, and c) second extraction opal content.

foraminifera colonizing the sediment, grazing by organisms would result in the removal of organic coatings from frustules at the sediment surface, this is consistent with the decrease in preservation observed in sediment compositions typical of mixed assemblage laminae.

Once a frustule has been buried, the high levels of silica within the LDM deposits should result in pore water saturation being reached with proportionately less dissolution of individual frustules than in sediments with lower silica contents. The lack of large scale bioturbation in LDM compared to F-NO sections would remove the effect of radial diffusion of pore water into deep burrows. This also reduces the level of dissolution in LDM deposits, consistent with the observed difference between laminated and non-laminated sediments.

It is also possible the trends of increased preservation both between LDM and F-NO and within LDM sediments is a consequence of increased levels of silicification during growth. Levels of silicification are controlled by the availability of dissolved silica in the surface waters. The trends in preservation observed in these sediments suggest that mat flux could be associated with periods of increased dissolved silica. This is consistent with the observed increase in *T. longissima* Group frustule dimensions observed in *Thalassiothrix*-rich laminae compared to mixed assemblage laminae (described in Section 4.3 and Table 4.2) which also suggest that mat flux events were associated with periods of improved growing conditions (Paasche, 1973; Harrison *et al.*, 1977).

Such an improvement in growth conditions combined with the occurrence of enhanced surface concentrations of diatom mats, could be achieved by an increase in equatorial upwelling. A temporary increase in upwelling should (1) increase convergence rates along the Equatorial Front, increasing the rate of diatom mat accumulation at the surface; and (2) increase the availability of nutrients in the surface waters, improving growing conditions which should increase the frustule size of diatoms accumulating in the frontal region. Observations of modern ocean processes suggest such a change could be achieved by either changes in circulation, or interannual changes related to the return to cold-tongue conditions following an El Niño event. Possible controls on the occurrence of mat forming events are discussed in later chapters.

## 4.5 CHAPTER SUMMARY

Measurement of bulk opal contents below and through LDM intervals gives values ranging from 10 to 15 wt% opal for F-NO sediments below the LDM sections, compared to values of 20 to 30wt% for non-laminated beds with the LDM events. Laminated beds have opal contents of 40 to 80wt%. Comparison between GRAPE records and measurements of biogenic opal shows a

relationship of similar form to the algorithm published by Mayer (1991). The relationship allows the identification of silica rich intervals and estimation of sediment silica content from GRAPE records.

The dense meshwork of the *T. longissima* diatom mats results in the preservation of lamina couplets. These couplets are interpreted as episodic mat flux events, similar to that observed in the eastern equatorial Pacific by the JGOFS Fall '92 survey (Barber, 1992), separated by more normal deep sea sedimentation patterns. Sedimentation rates suggest these depositional events occurred on a quasi-annual basis.

Spectral analysis of lamina couplet thickness records identified two significant periodicities of 6-7 and 21 years. The 6-7 year periodicity is consistent with an El Niño-type regime, and the 21 year periodicity could either be related to variation in the relative strength of these El Niño-type events, or to fluctuation in the Aleutian low pressure system modulated by variations in the solar-cycle.

A new method of quantifying diatom frustule dissolution within deep sea sediments has been developed and tested. Although the method is currently limited to using *Thalassiothrix* spp., it would be entirely possible to extend it to use other diatom species. This method allowed the detection and quantification of the trend of increasing diatom frustule preservation levels with increasing sedimentary opal content.

Frustule preservation levels are significantly higher in LDM sediments compared with those from F-NO both within and below the '4.4Ma' LDM deposition event. Also, within LDM intervals frustule preservation increases with increasing *T. longissima* Group content. These trends in frustule preservation are related to a combination of factors including relative sinking and burial rates. Another possible trend of increased frustule size within *Thalassiothrix*-rich layers was isolated, suggesting that variation in preservation with LDM sediments may also be related to increased silica availability (from the larger frustules) during mat forming events. The mechanism for this size increase is unclear.

# CHAPTER 5: TIMESCALES, CORRELATION AND SEDIMENTATION RATES

## 5.1 INTRODUCTION

To constrain sedimentation rates during LDM depositional periods four separate methods for calculating sedimentation rates are examined in this chapter: (1) Traditionally sedimentation rates are calculated between datums (geomagnetic or biostratigraphic) within the sedimentary column. Recent advances using climate controlled fluctuation of stable isotope and GRAPE records have allowed the construction of orbitally tuned timescales (Shackleton *et al.*, 1995 and references therein); (2) In this study the use of high resolution BSEI has identified laminae couplets (see Section 4.2). Assuming these couplets represent periodic depositional events, they provide a second and independent method of estimating sedimentation rates; (3) Comparison of GRAPE records between sites with and without LDM material allows the deposition period of the LDM to be estimated from the thickness of the equivalent non-laminated sediment; (4) Finally, sediment $^{3}He$ concentrations (derived from cosmic dust) in combination with an assumed $^{3}He$ flux is another recent method of sedimentation rate estimation.

The results of the different methods are compared and their relative merits examined. Implications for depositional event periodicities based on observations of lamina couplets and sedimentation rates used in regional flux calculations are also discussed.

## 5.2 DATUM-BASED SEDIMENTATION RATES

Published sedimentation rates for ODP sites are calculated on the basis of micropalaeontological and palaeomagnetic datums. Since these rates were calculated, the Berggren time scale (Berggren *et al.*, 1985; Berggren *et al.*, 1985) used for datum calibration has been superseded by a new time scale (Berggren *et al.*, 1995) based on the magnetic reversal ages of Cande and Kent (1992). Biostratigraphic datums based on this new timescale have been calculated using the Ceara Rise sediments, ODP Site 926 (Backman and Raffi, in press). A second timescale is based on orbital tuning of the GRAPE record from Leg 138 sites (Shackleton *et al.*, 1995). The following section examines these timescales in more detail. The biostratigraphic datums used in this study are presented alongside the resulting sedimentation rates.

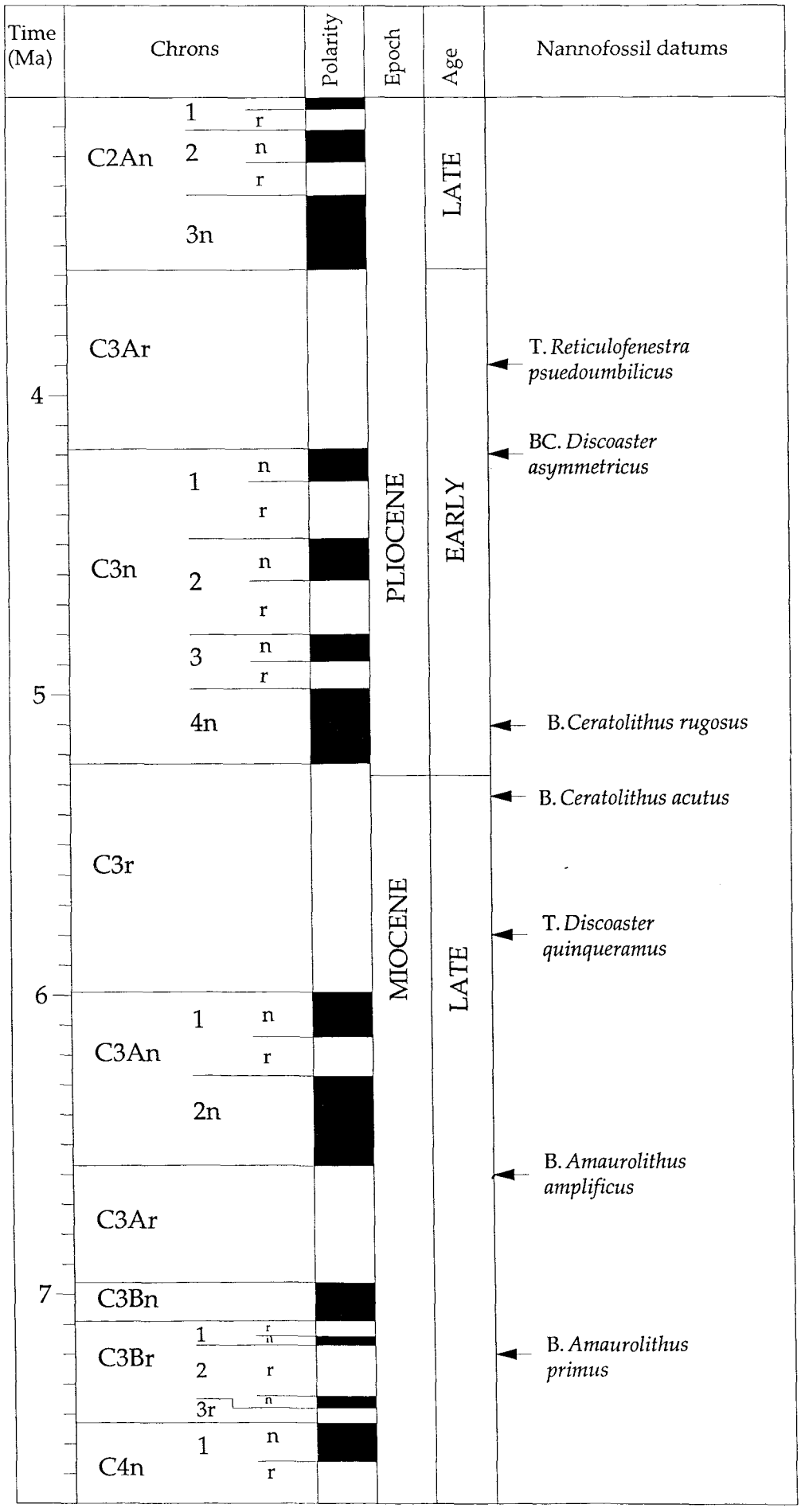


Figure 5.1. Geomagnetic polarity timescale for late Miocene and Pliocene showing relationship to calcareous nannofossil datums used in this study. Modified from Berggren *et al.* (1995).

### 5.2.1 THE GEOMAGNETIC POLARITY TIMESCALE (GPTS)

The ages of biostratigraphic datums (first and last occurrences of microfossil species) used in sedimentation rate calculations are calculated from the geomagnetic polarity timescale (GPTS). The first GPTS for the Cenozoic was based on a single magnetic anomaly profile from the South Atlantic (Heirtzler *et al.*, 1968). This record was calibrated using radiometric ages for younger sections (e.g. Cox *et al.*, 1964). Ages of older reversals were estimated by extrapolating from the older end of Anomaly 2A (~3.4Ma) assuming a constant rate of sea-floor spreading. Subsequent revisions of the reversal sequence (Talwani *et al.*, 1971; Blakely, 1974; Klitgord *et al.*, 1975; Cande and Kristofferson, 1977) were incorporated in the revised timescale of LaBreque *et al.* (1977). Since this compilation, work on the GPTS has been focused on age calibration. Studies have included more detailed work on spreading rates in the South Atlantic (e.g. Ness *et al.*, 1980; Lowrie and Alvarez, 1981; Berggren *et al.*, 1985; Haq *et al.*, 1987; Haq *et al.*, 1988); radioisotope dating of the most recent 5 m.y. of the record using high precision $^{40}Ar/^{39}Ar$ dating (e.g. Baksi *et al.*, 1992; Tauxe *et al.*, 1992; Walter *et al.*, 1992; Renne *et al.*, 1993); and astrochronological timescales of stable isotope and GRAPE record (see Section 5.2.3, below).

Although many Miocene sections have been cored by DSDP and ODP, few have yielded magnetobiostratigraphic records of sufficient quality to derive reliable biochronology (Berggren *et al.*, 1995). The quality of the magnetostratigraphic record from ODP Leg 138 (Sites 844, 845, 848, 852, and 853) is of exceptionally good quality (Mayer *et al.*, 1992; Schneider, 1995) allowing precise ties between biostratigraphic datums and magnetostratigraphic events in the eastern Equatorial Pacific (Raffi and Flores, 1995; Raffi *et al.*, 1995). Inconsistencies remain between the correlations established in this area and those in other sections (e.g. B. *C. rugosus*, see Table 5.1). The relationship of calcareous nannofossil datums used in this study to the GPTS is given in Table 5.1 and Figure 5.1.

### 5.2.2 ORBITALLY TUNED TIMESCALES

Age calibration of biostratigraphic datums is based on linear interpolation between observed geomagnetic reversals. This interpolation can be improve by matching peaks and troughs in the climate controlled $\delta^{18}O$ stable isotope record with those of the orbitally controlled insolation cycle (e.g. Pisias and Moore, 1981; Ruddiman *et al.*, 1986; Shackleton *et al.*, 1990; Hilgen, 1991). Temporal changes in the calcium carbonate content of deep sea sediments have been linked to the glacial cycle since they were first identified by Arrhenius (1952) in sediments from the East Pacific Rise. During glacial periods sediment deposition is dominated by carbonate, whereas sediments accumulated during interglacials have a higher silica content.

| Datum | Palaeomagnetic Chron | Age in Ma (linear interpolation) | Reference | Remarks |
|---|---|---|---|---|
| T. *R pseudoumbilicus* | Upper Chron C2Ar | 3.75 | 1 | Tied to upper section of C2Ar at Site 397 |
| BC. *D. asymmetricus* | Upper Subchron C3n.1n | 4.2 | 1 | Near to top of Subchron C3n.1n at Site 397 |
| B. *C rugosus* | Mid Subchron C3n.4n | 5.0-5.23 | 2,3 | Mid Subchron C3n.4n in Pacific Sites, near top of C3n.2n in Mediterranean |
| B. *C. acutus* | Upper Subchron C3r | 5.34 | 4, 5 | Tied to uppermost part of Upper Subchron C3r |
| *T. D. quinqueramus* | Mid Chron C3r | 5.6 | 4, 6, 7 | Tied to mid chron C3r at Sites 710 and 844 but late Chron |
| B. *A. amplificus* | Subchron C3 An.2n/Chron C3.Ar | 6.6 | 4, 7 | Tied to Subchron C3n.2n/Chron C3Ar boundary at Sites 844 and 853 |
| B. *A. primus* | Subchron 3Br.2r | 7.2 | 4, 7 | Tied to mid Subchron 3Br.2r at Sites 710, 844, 845 and 853. |

Table 5.1. Relationship of calcareous nannofossil datum levels to observed magnetic polarity stratigraphy, age estimates in Ma are derived from linear interpolation between the GPTS magnetic reversal ages of Cande and Kent (1992 and 1995) and Berggren et al (1995). Modified from Berggren *et al.* (1995a and 1995b). References are 1 - Mazzei *et al.* (1979), 2 - Haq and Takayama (1984), 3 - Rio *et al.* (1990), 4 - Raffi and Flores (1995), 5 - Berggren (1985a), 6 - Shackleton *et al.* (1995) and 7 - Raffi *et al.* (1995).

Controls on this cyclic variation in sediment composition are controversial, the three schools of thought on the dominant control are summarized below.

(1) Productivity hypothesis (e.g. Arrhenius, 1952). Increased strength of trade winds associated with glacial conditions results in increased upwelling. The increased nutrient availability results in increased productivity. Increased calcium carbonate productivity would also have the effect of lowering the lysocline reducing dissolution levels in the surface sediments. Changes in the supply of biogenic silica have also been shown to be an important factor in cyclic variations in the sedimentary composition of the Leg 138 sediments (Pisias and Prell, 1985).

(2) Dissolution hypothesis (Berger, 1992 and references therein). Changes in the chemical asymmetry of deep ocean, deriving from deep water production in the North Atlantic, affect the dissolution of carbonate in the deep ocean in the surface sediment. Increasing the asymmetry (by increasing deep water production) reduces dissolution in the Atlantic resulting in increased carbonate sedimentation and reducing the carbonate available in the Pacific.

(3) Dilution hypothesis (Berger, 1992). Changes in the dilution of carbonate material by siliceous and other non-carbonate particles would result in the variations in sediment composition.

These three factors are suggested to work simultaneously to generate the observed fluctuations in sediment composition. The very large ranges in carbonate supply required by the productivity hypothesis suggest that the direct effect of productivity is the least powerful of these controls, but productivity is the governing factor through its effect on ocean chemistry

(Berger, 1992). Regardless of the dominate control on cyclic variations the above arguments imply sediment composition is ultimately controlled by the glacial cycle and can be used in the same way as the $\delta^{18}O$ stable isotope record to improve age calibration between geomagnetic events (e.g. Ninkovitch and Shackleton, 1975; Keir and Berger, 1985; Le and Shackleton, 1992).

The above controls are based solely on changes in carbonate content and implicitly assume a constant silica sedimentation rate. In the eastern Equatorial Pacific sediments the dominant agent of carbonate-silica cyclicity in intervals with high datum-based sedimentation rates is the occurrence of diatom-rich interbeds (Kemp, 1995). In intervals with exceptionally high datum-based sedimentation rates (100-150m/Ma), the carbonate-silica variations controlled by diatom-rich interbeds occur on similar length scales to the carbonate/glacial cycle-controlled variations discussed above, see Fig. 5.2. This means that silica and especially diatom productivity is a regionally important control on carbonate-silica variations (Kemp and Baldauf, 1993; Kemp, 1995; Kemp *et al.*, 1995). Although the length-scales of these silica productivity controlled variations are similar to those controlled by carbonate/glacial cycles, the time scale of formation is at least an order of magnitude less (Kemp and Baldauf, 1993; Kemp, 1995; Kemp *et al.*, 1995). This silica-productivity control on variation means that care must be taken in the production of orbitally tuned time scales based on GRAPE data and can lead to errors in the generation of tuned timescales (e.g. that of Shackleton *et al*, 1995 and Kemp, 1995].

### 5.2.3 Orbital tuning of the GRAPE record

By matching peaks in the GRAPE record with the record of variations in the insolation cycle at 65°N calculated by Berger and Loutre (1991), ages of datums could be more accurately calculated between geomagnetic datums (Shackleton *et al.*, 1995; Herbert *et al.*, 1992 and references therein, Fig. 5.3). Comparison of the GRAPE records with the sedimentary logs for sites containing the '4.4Ma' LDM deposits shows that the some lows in the GRAPE record are associated with variations in silica productivity (recorded in LDM deposits) rather than carbonate cycle controls (Fig. 5.4). Initial tuning ignored this problem and treated the GRAPE lows related to LDM deposits as carbonate cycles (N. Shackleton, pers comm.). Comparing the GRAPE record to the orbital cycles used to tune the record shows the '4.4Ma' LDM deposits in Site 847 are tuned to occupy 245k.y. of the orbital record, see Figure 5.5. Sediments equivalent to the LDM sediments at Site 851 occupy around 59k.y. of the tuned timescale. Comparing these two records suggests that Shackleton's (1996) tuned timescale for Site 847 is offset by around 186k.y. (9-10 precession cycles) between the base of the '4.4' and top of the '6.1-6.3' Ma LDM deposits. A similar offset is found at Sites 849 and 850 which also contain the '4.4Ma

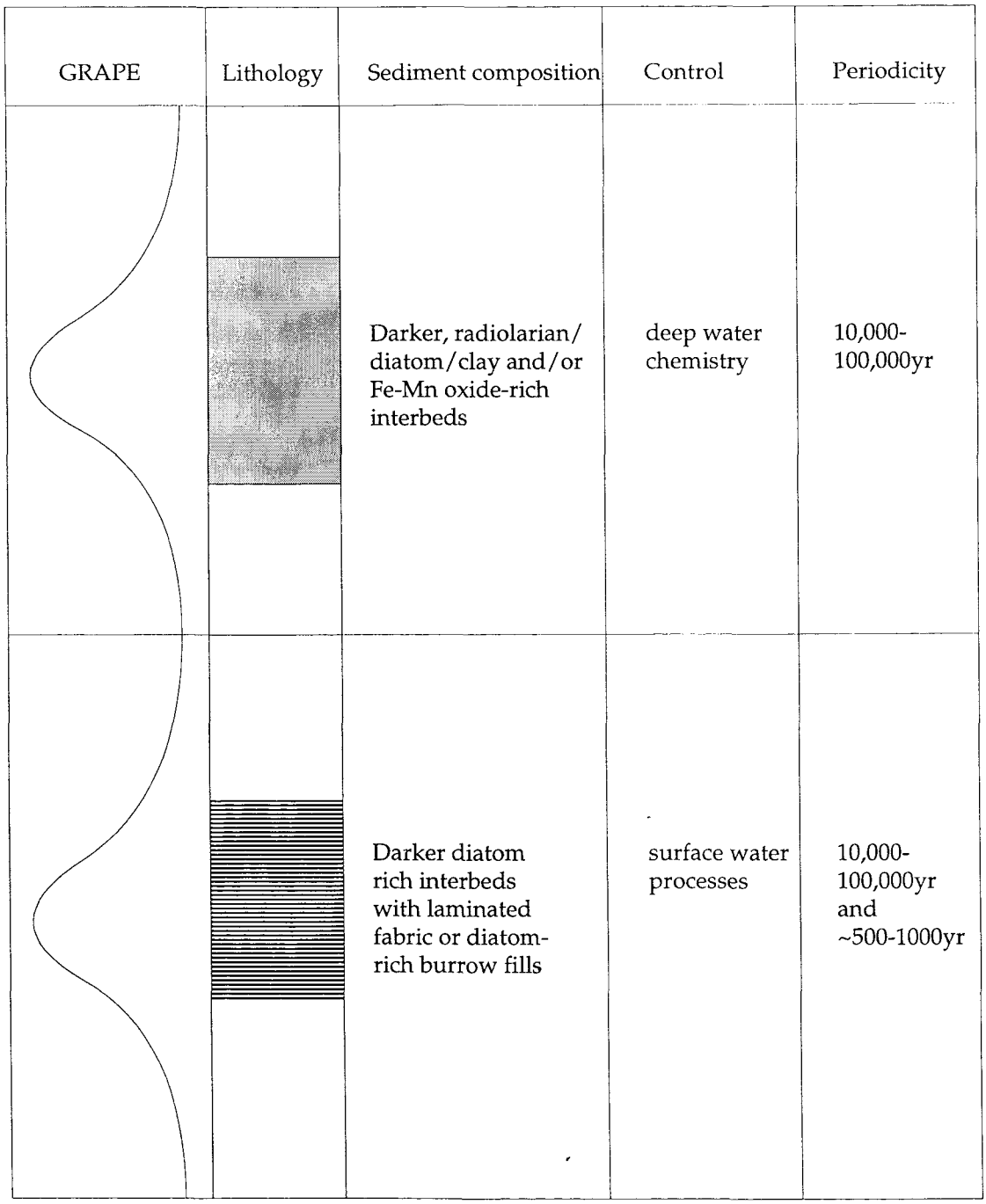


Figure 5.2. After Kemp (1995). The contrasting types and origins of high frequency variation in carbonate content in the equatorial Pacific Ocean cores recorded in both the lithology and GRAPE record. Decimetre- to metre-scale interbedding is caused by dissolution (top figure) resulting in beds lower in carbonate with some or all of the following features: increased proportions of radiolarians, diatoms, clays and/or Fe-Mn oxides. This style of variation is caused by variations in the dissolution of carbonate related to deep water chemistry and has periodicities of 10,000 to 100,000 years, within the Milankovitch band. The lower figure shows variation resulting from increased diatom flux, which may be at similar periodicities or, in the case of diatom mat deposits, one to two orders of magnitude faster.

Figure 5.3. Relationship between GRAPE record and insolation cycle at Site 851, the GRAPE record has been plotted in the time domain by matching peaks in the GRAPE record with peaks in the insolation curve. Age control points used by Shackleton *et al.* (1995) are shown for reference. Modified from Shackleton *et al.* (1995).

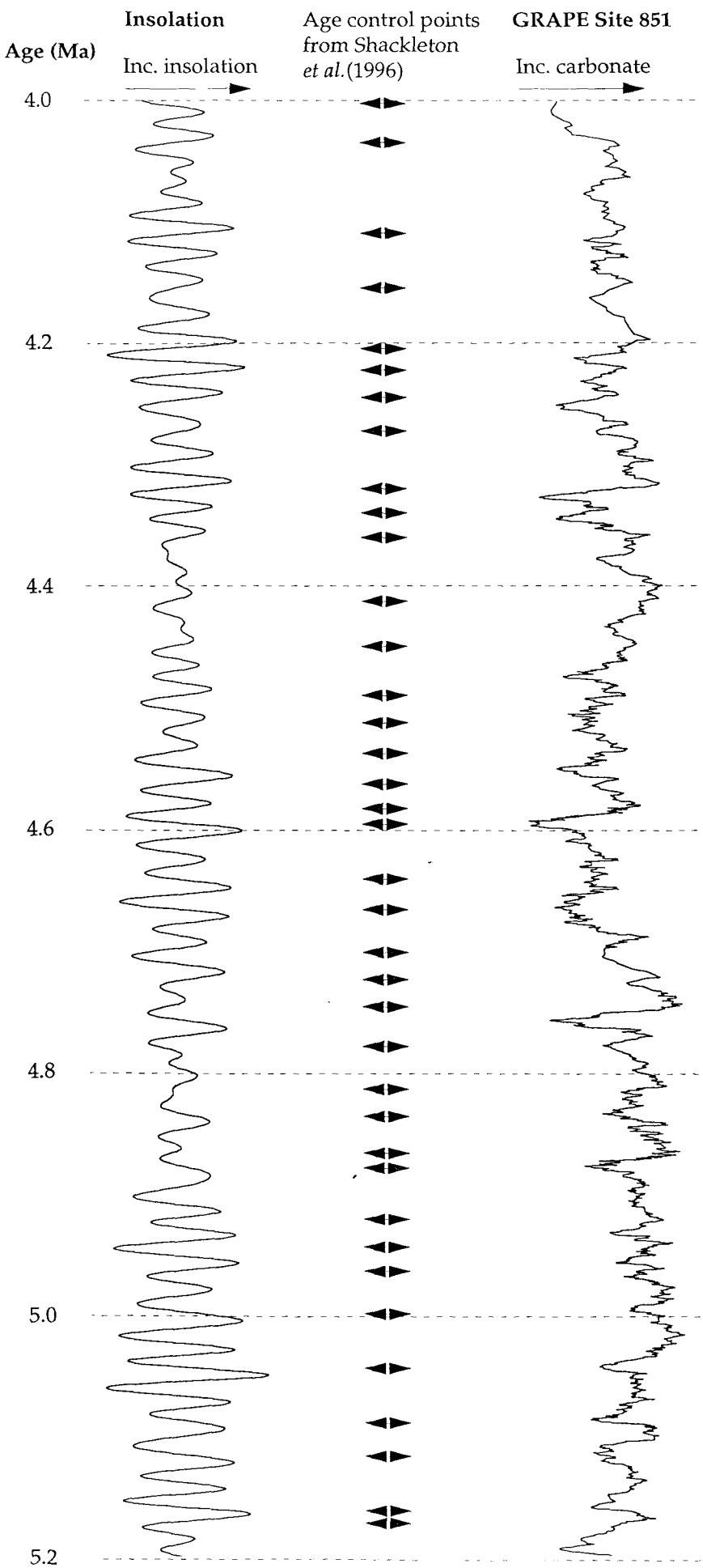
Insolation
Inc. insolation
Age control points from Shackleton *et al.*(1996)
GRAPE Site 851
Inc. carbonate
Age (Ma)
4.0
4.2
4.4
4.6
4.8
5.0
5.2

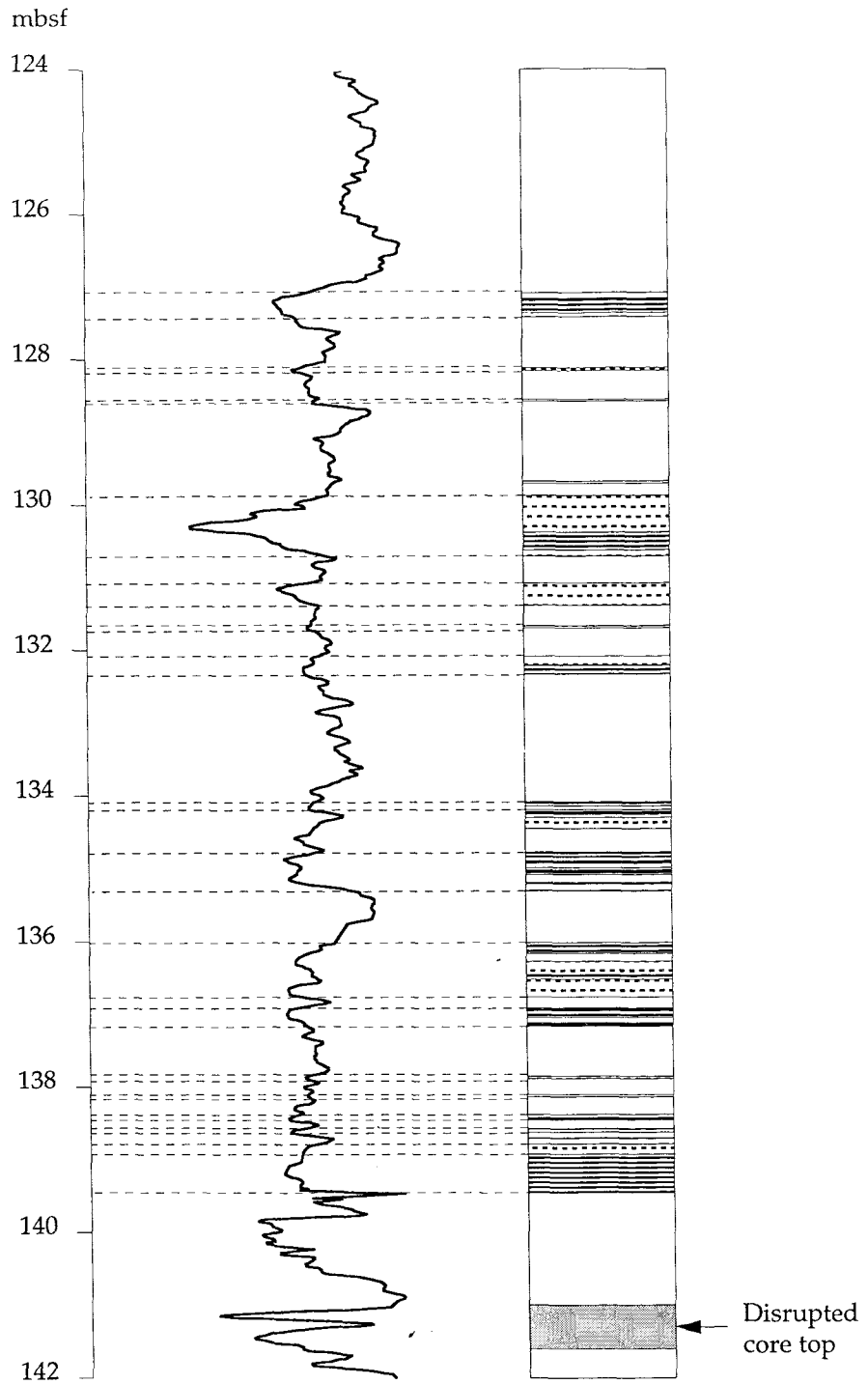


Figure 5.4. Comparision of GRAPE record for site 847 to the sedimentary log made through the '4.4Ma' LDM deposits showing the strong influence of sediment composition on the GRAPE value.

Figure 5.5. Composite GRAPE record from sites 847 and 851 showing offset relative to orbitally controlled insolation cycle related to presence of LDM deposits at Site 851. Correlations from Shackleton*et al.* (1995)

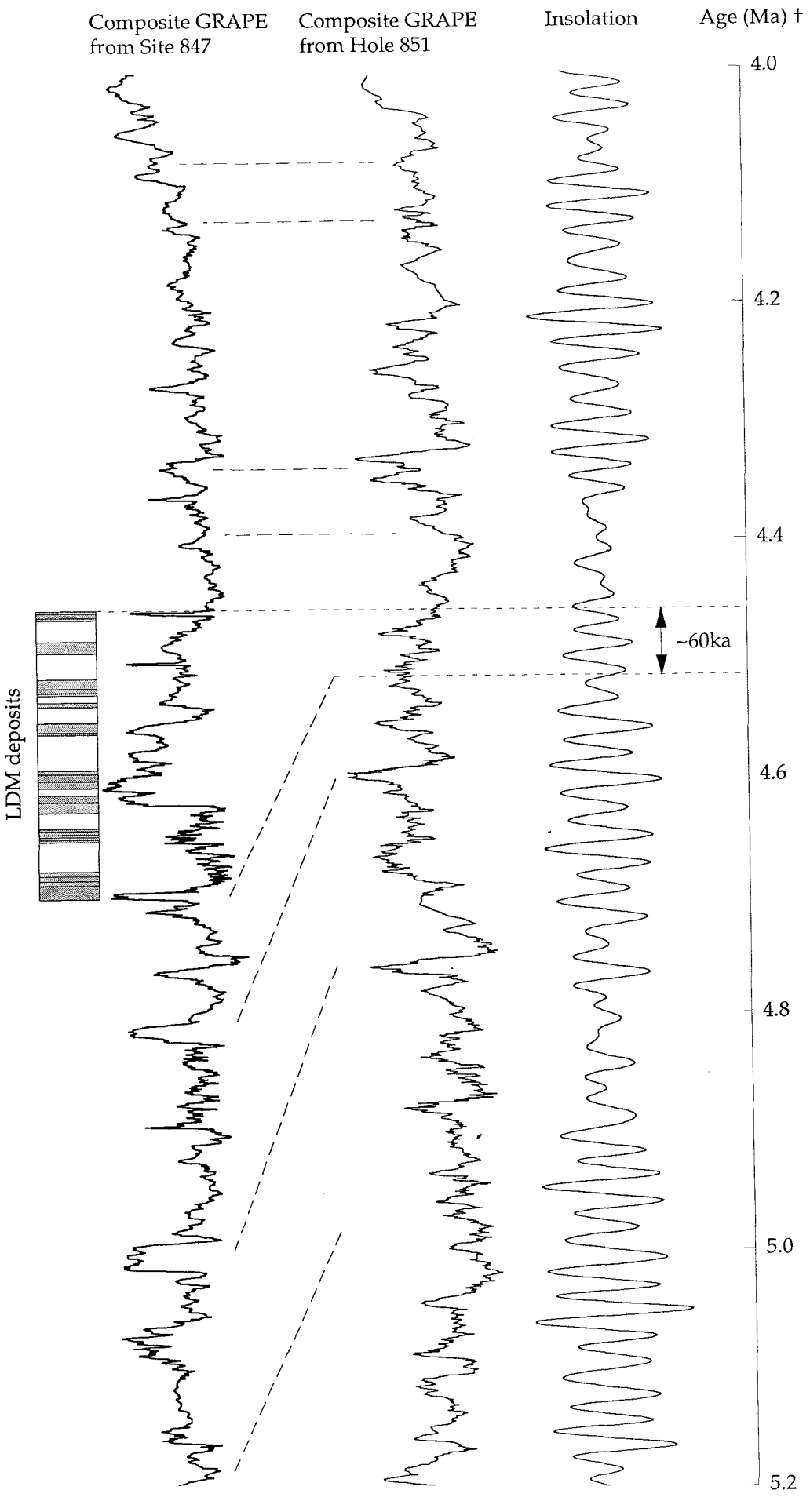
Composite GRAPE from Site 847
Composite GRAPE from Hole 851
Insolation
Age (Ma) †
4.0
4.2
4.4
4.6
4.8
5.0
5.2
~60ka
LDM deposits

LDM deposits. To avoid this offset, only datum ages calculated by Shackleton *et al.* (1995) above the LDM deposits are used in this study.

Age calibration for datums below the '4.4Ma' LDM deposits was carried out using the orbitally tuned age model established for the GRAPE record at Site 851 (Shackleton *et al.*, 1995) which does not contain '4.4Ma' LDM material. Ages for biostratigraphic datums were calculated assuming a constant sedimentation rate between age picks, see Table 5.2. The ages calculated in this way for Site 851 and those published by Shackleton *et al.* (1995) were calculated using an identical method so systematic errors should be consistent throughout the datum ages used in this study. Geochemical analysis of sediment from Hole 851B shows elevated levels of biogenic silica content in sediments equivalent to both the '4.4Ma' and '6.1-6.3Ma' LDM deposits (see Section 7.2.1). This change in sediment composition indicates that sedimentation rates may not have been constant at Site 851. If sedimentation rates were increased across the entire eastern equatorial region during the deposition of LDM material at the equatorial sites, the datum ages calculated for Site 851 in this section of the core would be affected. However, no datums fell in these sections.

### 5.2.4 Discussion of datum ages used in this study

The datum ages discussed above are summarized in Table 5.2 and Figure 5.1, datum ages used in this study are shown in bold in Table 5.2. Datum ages published for sediments cored over the Ceara Rise in the western Equatorial Atlantic, ODP Site 926 (Backman and Raffi, in press) are shown for comparison. This calibration is based on the new geomagnetic timescale (Cande and Kent, 1992) and are shown in Table 5.2 for comparison.

The poor agreement between ages calculated for the B. *Spongaster tetras* datum at Sites 851 and 849 can be explained by a diachronous event. At Site 849 this datum occurs within the range of the T. *Nitzchia cylindrica* datum. At Sites 847, 850 and 851 the B. *Spongaster tetras* datum range is around 1.5m above that of T. *Nitzchia cylindrica*. To test the variability of datum ages calculated in this way, the age of the B. *Spongaster tetras* datum was calculated using the Shackleton *et al.* (1995) age models at Sites 847 and 849 to 851, see Table 5.3. The similarity between the ages calculated for this datum at Sites 847 and 849 and Sites 850 and 851 suggest that the B. *Spongaster tetras* datum is truly diachronous within the eastern Equatorial Pacific region. The two pairs of ages suggest that Sites 847 and 849 were dominated by the NECC/NEC boundary whereas Site 851 was influenced by the warmer NEC (*S.tetras* a tropical species). The datum ages suggest that Site 850 was also strongly influenced by the NEC water mass. This is consistent with the observation that the thickness of the LDM unit at Hole 850B is less than that at both Site 847 and 849, suggesting that Site 850 was located on the edge of the LDM depositional region. Although the reduced thickness of the LDM at Site 850 may be due to a coring gap but this hypothesis cannot be confirmed as Site 850 was only

| Datum | Type | Datum ages (Ma) | | | | |
|---|---|---|---|---|---|---|
| | | Berggren *et al.* (1985) | Berggren *et al.* (1995a, b) | Backman and Raffi (in press) - Ceara Rise | Shackleton *et al.* (1995) - EEP Site 849 | Calculated from Shackleton *et al.* (1995) - EEP Site 851 (this study) |
| T. *Reticulofenestra pseudoumbilicus* | N | 3.56 | 3.75 | n.d. | **3.82±0.05** | 3.80±0.02 |
| Cochiti Subchron | G | 3.88 | 4.29 | n.d. | n.d. | **4.290(1)** |
| BC. *Discoaster asymmetricus* | N | 3.83 | 4.2 | n.d. | 4.13±0.09 | **4.49±0.012** |
| B. *Spongaster tetras* | R | 3.8±0.1 | n.d. | n.d. | **4.17±0.14** | 4.69±0.19 |
| T. *Didymocyrtis penultima* | R | n.d. | n.d. | n.d. | **4.20±0.14** | n.d. |
| T. *Nitzschia cylindrica* | D | 4.3 | n.d. | n.d. | **4.87±0.15** | 5.07±0.19 |
| T. *Amaurolithus primus* | N | 4.37 | **4.8** | n.d. | **4.56±0.10** | n.d. |
| | | | **'4.4Ma' LDM event** | | | |
| T. *Ceratolithus acutus* | N | 4.42 | n.d. | 5.046±0.002 | 4.99±0.06 | **n.d.** |
| B. *Ceratolithus rugosus* | N | 4.66 | 5.0-5.23 | 5.089±0.003 | 5.07±0.02 | **4.98±0.01** |
| B. *Ceratolithus acutus* | N | 4.85 | 5.34 | 5.372±0.003 | 5.34±0.02 | **5.37±0.01** |
| T. *Discoaster quinqueramus* | N | 4.98 | 5.6 | 5.537±0.05 | 5.55±0.02 | **5.563±0.014** |
| T. *Siphostichartus corona* | R | 5.15±0.15 | n.d | n.d. | 5.76±0.01 | **5.81±0.01** |
| T. *Nitzschia miocenica* | D | 5.55 | n.d | n.d. | 6.07±0.04 | **6.10±0.03** |
| T. *Thalassiosira praeconvexa* | D | 5.8 | n.d. | n.d. | 6.17±0.19 | **n.d.** |
| | | | **'5.8Ma' LDM event** | | | |
| T. *Stichocorys johnsoni* | R | 5.9±0.1 | n.d. | n.d. | n.d. | **6.26±0.02** |
| B. *Amaurolithus amplificus* | N | 6.02 | 6.6 | 5.993±0.002 | 6.50±0.02 | **6.48±0.02** |
| | | | **'6.1-6.3Ma' LDM Event** | | | |
| B. *Amaurolithus primus* | N | 6.42 | 7.2 | 7.392±0.004 | n.d. | **7.20±0.03** |
| B. *Nitzschia miocenica* | D | 6.75 | n.d. | n.d. | n.d. | **7.23±0.06** |

Table 5.2. Age datums used in this study in bold, showing both ages based on the Berggren timescales (1985a,b and 1995a,b) and those calculated for sediments from the Ceara Rise (Equatorial Atlantic) for comparison. Datum ages for ODP Site 851, in the eastern Equatorial Pacific (EEP) are calculated using the orbitally tuned age model and assuming constant sedimentation rates between age picks (following the method of Shackleton *et al.*, 1996). The age of the Cochiti Subchron (1) is taken from the geomagnetic timescale published by Cande and Kent (1992). Datum types are given for reference; D is diatom, N is nannofossil, R is radiolarian and G is geomagnetic. In Leg 138 cores the nannofossil datums are constrained to within 1.5m. (n.d. - no data).

cored once. The range of datum ages calculated across this region is consistent with other diachronous radiolarian events in the eastern Equatorial Pacific area. These events are used to suggest the Equatorial Front was a significant barrier to plankton migration and colonization (Moore *et al.*, 1993).

| | B. *Spongaster tetras* datum age (Ma) | Latitude at '4.4Ma' | Current System |
|---|---|---|---|
| 847B | 4.17±0.06 | 2°N | NECC/NEC |
| 849B | 4.17±0.14 | 2°S | NECC/NEC |
| 850B | 4.57±0.02 | 0° | NECC/NEC |
| 851B | 4.69±0.19 | 2°N | NEC |

Table 5.3. Age of the B. *Spongaster tetras* datum calculated using the Shackleton *et al.* (1995) orbitally tuned age model for each site. Site locations during the deposition of the '4.4Ma' LDM are estimated using the back-track model of van Andel *et al.*(1975). The presence or absence of LDM material at each site indicates the overlying current system.

Datum ages calculated for Ceara Rise sediments were not used to avoid problems with diachronous microfosssil and nannofossil events between the Equatorial and Atlantic Oceans. The close agreement between the Atlantic and Pacific datums ages, especially the B. *C. rugosus*, B. *C. acutus* and T. *D. quinqueramus* datums provides evidence for an open connection, with large scale circulation between the two oceans across the Panama Seaway at this time.

### 5.2.5 CALCULATION OF DATUM-BASED SEDIMENTATION RATE

The sedimentation rates published for Holes 847 and 849 to 851 have been recalculated from the datum ages shown in bold in Table 5.2. Since the nannofossil datums are best constrained within the cores (located to within 1.5m), these datums are used whenever possible. Recalculated sedimentation rates for the '4.4Ma' LDM event are given in Table 5.4, alongside deposition period and core length over which they were calculated. The wide spacing of datums (at least 0.34±0.11Ma) results in time-averaging of sedimentation rates over the depositional period, short-lived events of abnormally high or low sedimentation are averaged out.

| Site | Datums used | Datum based sedimentation rate (m/Ma) | Datum spacing (Ma) | Core length (m) | Percentage error |
|---|---|---|---|---|---|
| 847 | T. *A. primus* - B. *C. rugosus* | 65.68±20.77 | 0.34±0.11 | 29.17±1.5 | 31.62 |
| 849 | T. *D. penultima*- B. *C. rugosus* | 39.39±9.32 | 1.16±0.06 | 50.86±1.06 | 23.66 |
| 850 | B. *S. tetras* - T. *C. acutus* | 20.59±4.76 | 1.55±0.05 | 40.88±0.08 | 22.89 |
| 851 | Subchron C3n.1n - B. *C. rugosus* | 24.18±5.99 | 0.81±0.13 | 18.81±1.71 | 24.77 |

Table 5.4. Datum-based sedimentation rates for '4.4Ma' LDM deposits calculated using datum s immediately adjacent to LDM deposits (datum ages given in Table 5.2). Datums used, time spacing and core length used to calculate each sedimentation rate are given for reference.

Errors in these sedimentation rates are dependant on the spacing of samples used to constrain datum depths and in the uncertainty in assigning datum ages. These two error sources typically combine to give an estimated error of at least 2% to datum-based sedimentation rates. Error associated with the above sedimentation rate estimates is calculated as $100.y/x$ where the sedimentation rate is given as $x \pm y$ m/Ma. As the interval between datum ages decreases, the relative importance of datum age uncertainties becomes much larger (through a reciprocal relationship).

## 5.3 DEPOSITIONAL FABRICS RELATED TO SEDIMENTATION RATE

Scanning electron microscope examination using BSEI photomosaics of the '4.4Ma' LDM basal unit shows the existence of laminae couplets at Sites 847 and 850, see Section 4.2 (Figs. 4.7 and 4.11). In summary, these couplets consist of:
(1) pure diatom ooze with high porosity and low nannofossil content, consisting almost solely of *Thalassiothrix* frustules with around 5% comprising of nannofossils and radiolarians (estimated visually from SEM images). The *Thalassiothrix* frustules have a well defined mat structure. Using measurement from BSEI photomosaics, these laminae are typically 190μm thick (standard deviation of 110μm, n=276);
(2) mixed assemblage sediment with lower porosity and higher nannofossil content (around 20%), radiolarians and centric diatoms make up around 5% of these layers. The mat structure in the mixed assemblage layers is not as strongly developed as in the diatom ooze layers. Mean thickness of these laminae is 140μm (standard deviation of 100, n=276).

These couplets are interpreted as evidence for periods of massive *Thalassiothrix* mat export along the Equatorial Front (the diatom ooze laminae) separated by periods of more normal deposition with colonization of the sediment surface by microfauna such as forams (the mixed assemblage layers, Chapter 4), see Figure 5.6 (Kemp, 1995). A similar depositional regime exists in the modern eastern Equatorial Pacific. In this case, massive accumulations of diatom mats are observed during the return to cold tongue conditions following El Niño (Barber, 1992; Yoder *et al.*, 1994). These short-lived events are separated by periods of normal upwelling productivity and the suppressed productivity of actual El Niño event (Smith *et al.*, 1996). This modern depositional cycle is controlled by the El Niño cycle, which has a periodicity of 1-7 years (Cane, 1983).

Laminae couplets are not found continuously through the basal unit, around 30% of the basal unit thickness in Hole 847B has no clearly defined structure, see Figure 5.7. This could be due to disruption of the surface layers by benthic organisms between depositional events, or may reflect changes in the depositional regime. The presence of aggregates of silt-sized particles

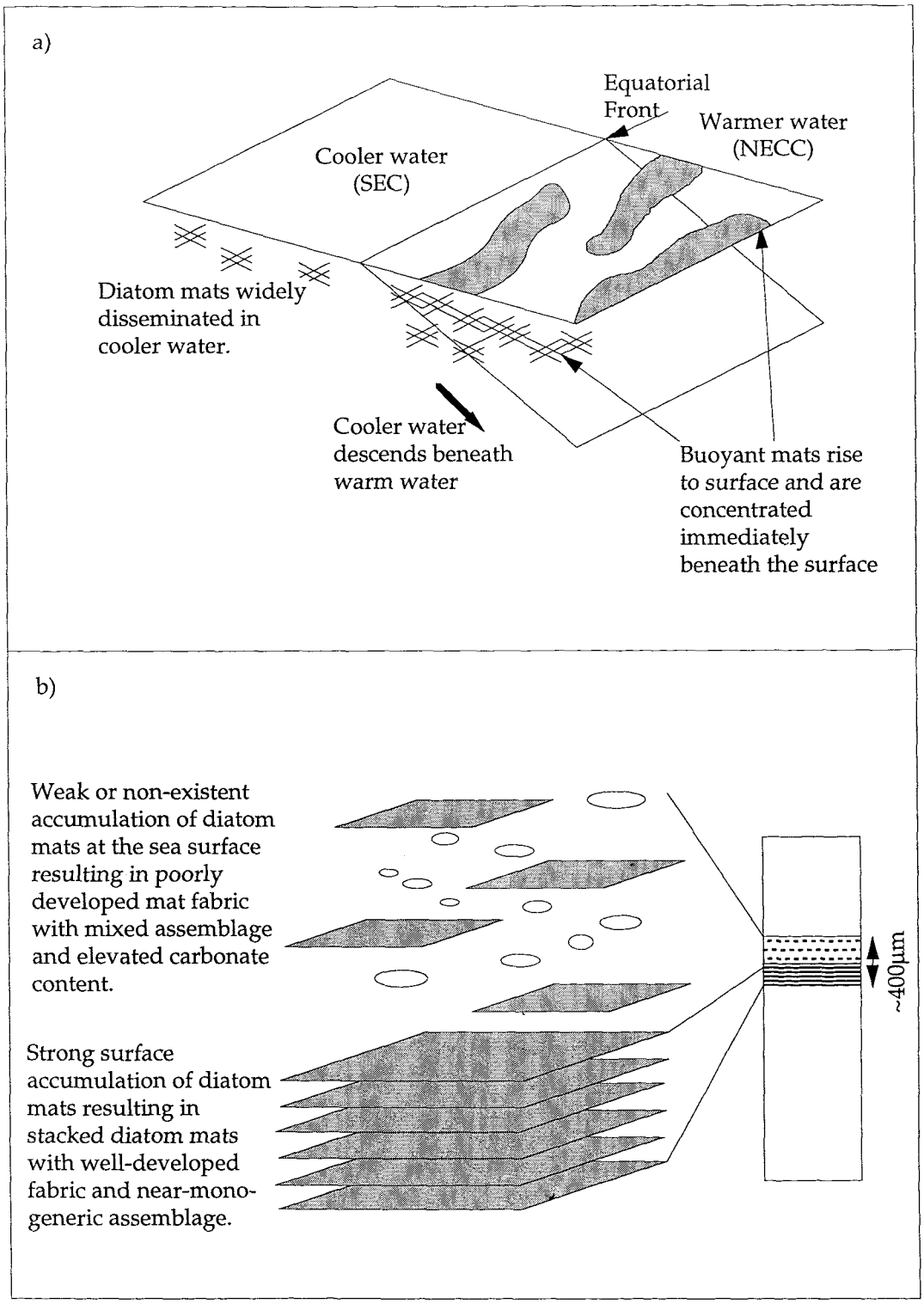


Figure 5.6. Schematic diagram showing influence of the frontal accumulation model in the formation of lamina couplets; a) schematic summary of frontal accumulation model, after Kemp *et al.* (1995) ; b) model for the formation of lamina couplets.

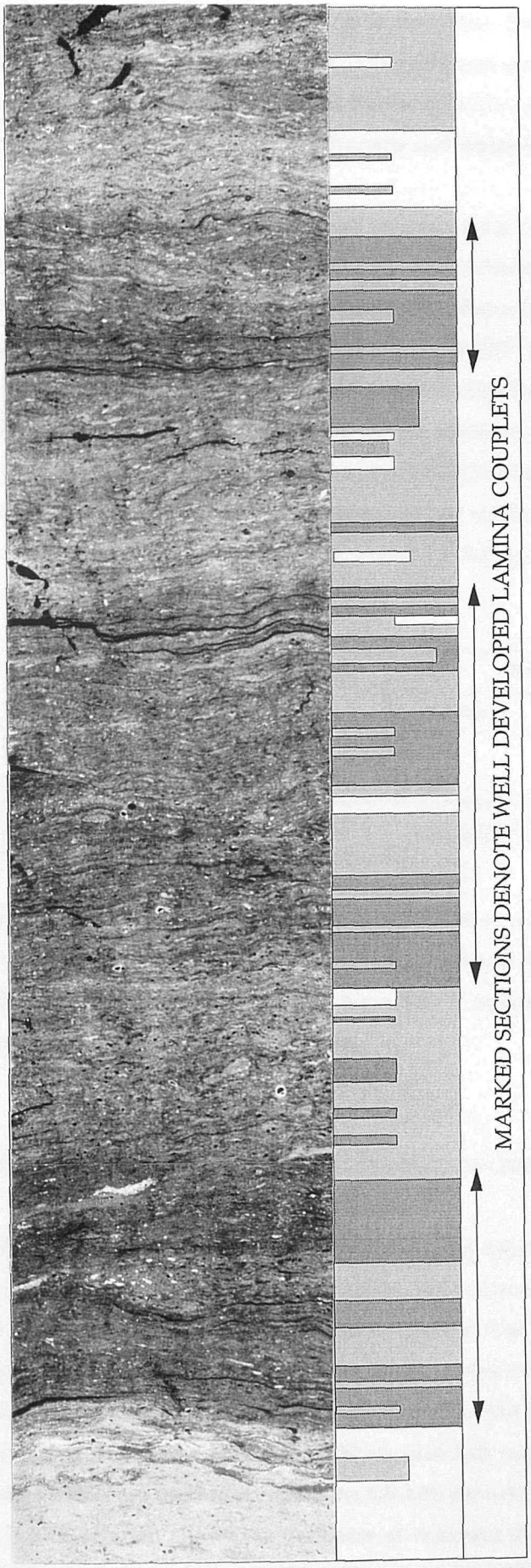


Figure 5.7. BSEI photomosaic of 847B-15H-7, 33-45cm with schematic sedimentary log showing the sporadic occurrence of lamina couplets within the '4.4Ma' LDM basal unit. Note the location of silt aggregates which tend to occur in mixed assemblage intervals.

**KEY**

F-NO (>50% carbonate)

mixed assemblage (50-80%*Thalasiothrix*)

*Thalasiothrix* - dominated (>80% *Thalasiothrix*)

2cm

1cm

0

indicating the presence of agglutinating forams (Pike, 1996) often coincide with structureless sections, see Section 4.3. Observations of the sediment surface following massive sinking of *Rhizosolenia* in the eastern Equatorial Pacific indicate rapid colonization by surface deposit-feeding fauna, such as holothurians and echurians (Smith *et al.*, 1996).

Assuming the mat-forming depositional regime prevailed throughout the depositional period (the non-laminated sections associated with faunal disruption) the mean couplet thickness can be used to estimate the sedimentation rate of this unit. Lamina-couplet thicknesses were measured from BSEI photomosaics for the entire '4.4Ma' LDM basal unit in Holes 847B and 850B. Calculations of the maximum sedimentation rate for LDM deposition assume an event periodicity of 1 year, with mat-forming events related to seasonal forcing such as the occurrence of tropical instability waves, see Table 5.5. Sedimentation rates are also calculated assuming a couplet depositional period similar to that of the modern, El Niño controlled regime. In this comparison, events resulting in the deposition of *Thalassiothrix* laminae are assumed to occur every 4 years.

| Site | Mean couplet thickness thickness, mm (±1SD) | Sedimentation rates (m/Ma) | |
|---|---|---|---|
| | | Annual events | 4 yearly events |
| 847 | 0.339 ± 0.163 | 339±163 | 86±41 |
| 850 | 0.315± 0.163 | 315±163 | 79±42 |

Table 5.5. Linear sedimentation rates calculated from laminae couplets, showing mean couplet thickness with estimated error of one standard deviation (1SD).

From Table 5.5 it is clear that 4 yearly depositional events would result in sedimentation rates lower than those predicted using the conventional datum-based method. This suggests that if the model for laminae couplet formation is correct, the periodicity of the depositional events is significantly less than 4 years.

## 5.4 COMPARATIVE GRAPE DERIVED SEDIMENTATION RATES

GRAPE records of sites containing the '4.4Ma' LDM deposits show strong similarities, see Figure 5.8. Comparison of GRAPE records between sites with the '4.4Ma' LDM and Site 851, which does not contain this event, allows the estimation of the length of the LDM depositional period. Site 851 is the closest site without laminated material to those containing the '4.4Ma' LDM sediments. Peaks in the GRAPE record and nannofossil datums to either side of the LDM event at Site 850 are matched with those at Site 851, see Figure 5.9. The same peaks are used to correlate the GRAPE records between the LDM-bearing sites (Fig. 5.8). This correlation allows the thickness of sediment deposited simultaneously with the LDM deposits to be calculated. Using the age-picks calculated by Shackleton *et al.* (1995) for

Figure 5.8. Comparision of GRAPE records through '4.4Ma' LDM event. Correlations made using characteristic peaks are shown with broken lines. Nannofossil datums used in initial correlation are shown with solid lines. In order to show exact correlation between lithology and GRAPE measurements the composite GRAPE records have not been used regardless of the large coring gaps.

KEY

continously laminated sediment
weakly laminated sediment
foram-nannofossil ooze
core break

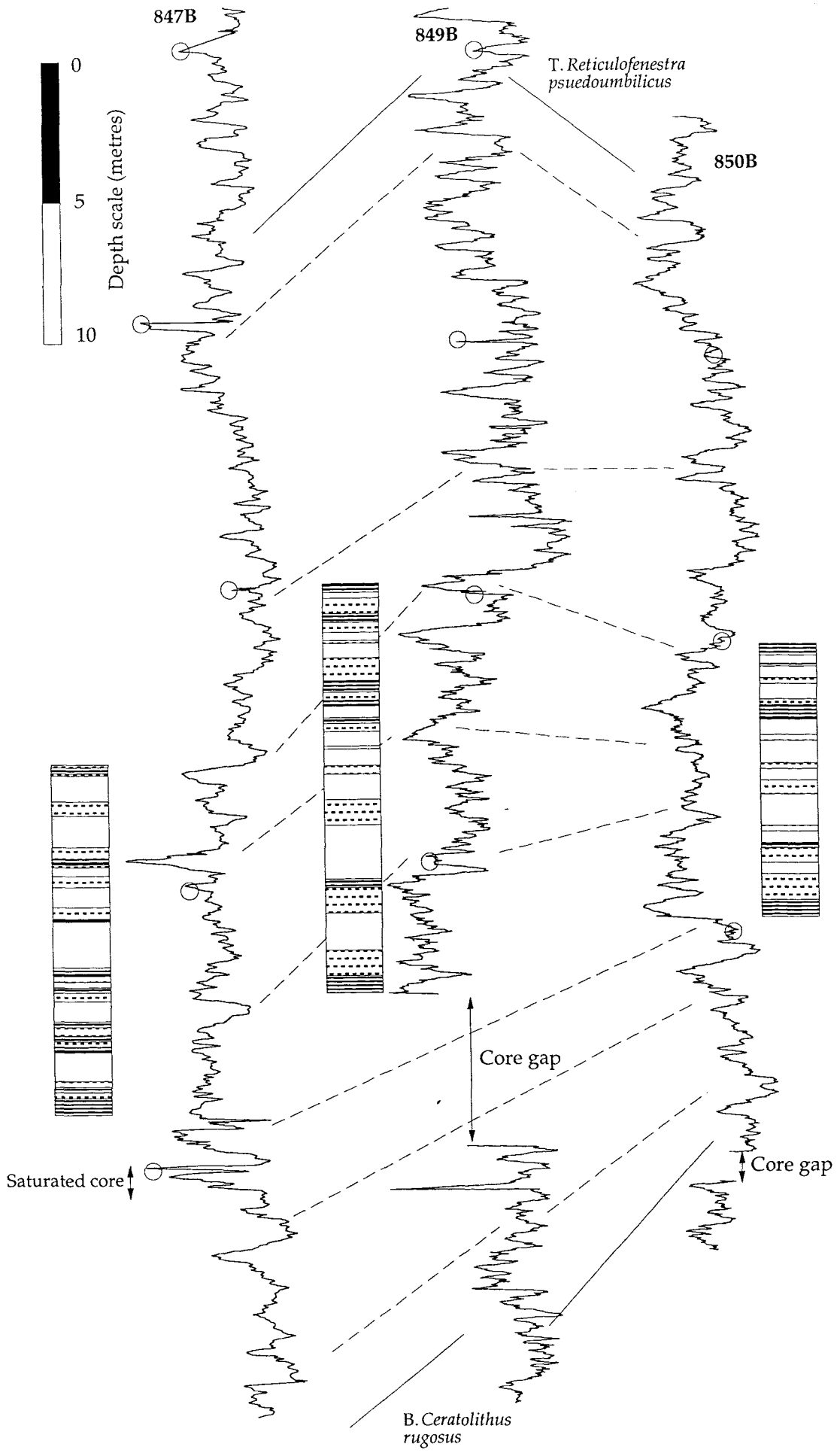
847B
849B
850B
T. Reticulofenestra psuedoumbilicus
0
5
10
Depth scale (metres)
Core gap
Saturated core
Core gap
B. Ceratolithus rugosus

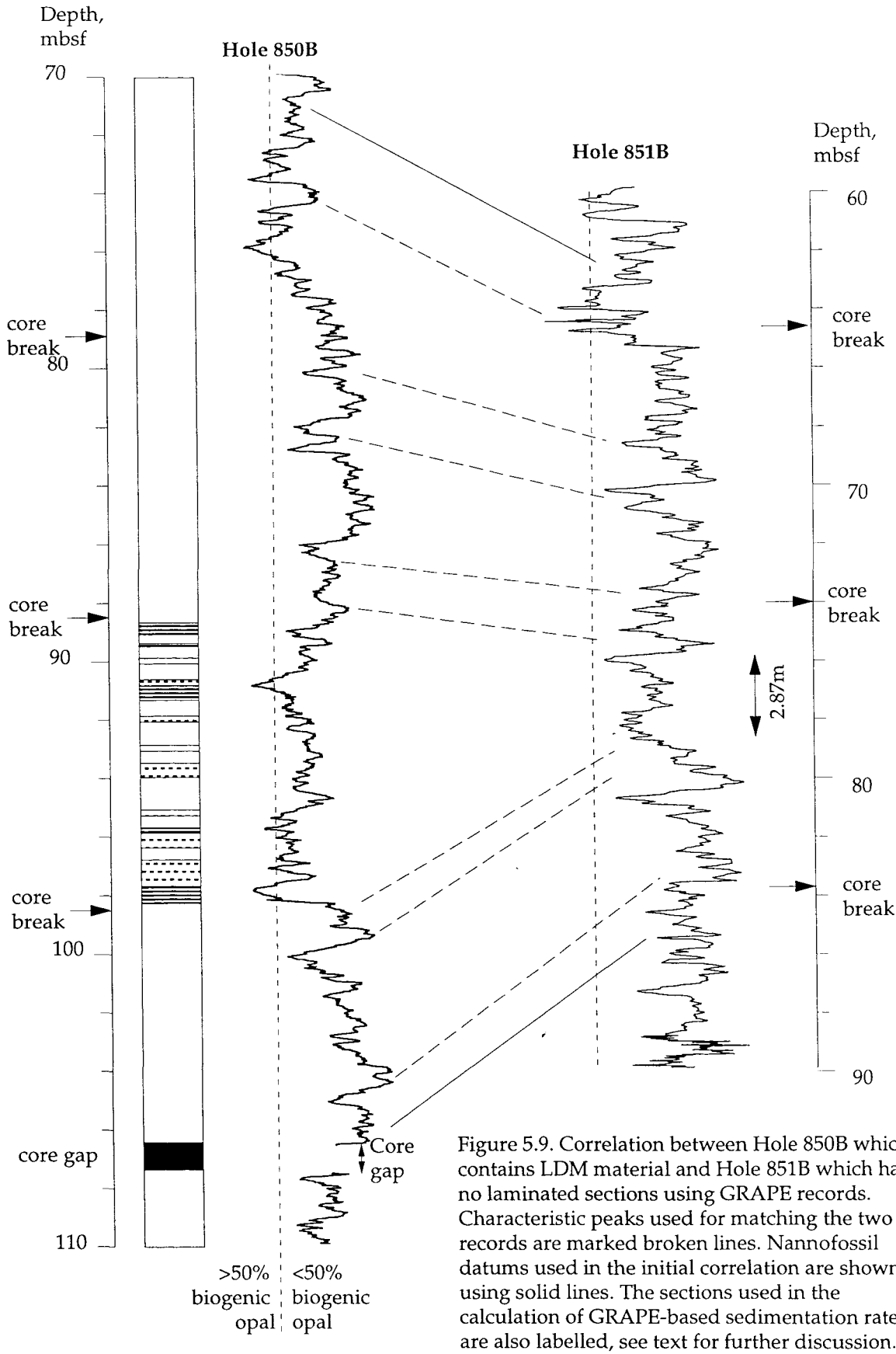


Figure 5.9. Correlation between Hole 850B which contains LDM material and Hole 851B which has no laminated sections using GRAPE records. Characteristic peaks used for matching the two records are marked broken lines. Nannofossil datums used in the initial correlation are shown using solid lines. The sections used in the calculation of GRAPE-based sedimentation rates are also labelled, see text for further discussion. The vertical dashed lines indicate the GRAPE value at ~50 wt% biogenic opal.

Site 851 and assuming constant sedimentation rate between them, the depositional period for LDM equivalent sediments at Site 851 can be estimated as 59.0ka. Sedimentation rates for the LDM units at each site are calculated by dividing the thickness of LDM deposits by this time period, see Table 5.6.

Like the datum-based sedimentation rates, GRAPE based sedimentation rates are calculated assuming a constant sedimentation rate between two points. This has the effect of averaging extremes in sedimentation rates over time, the calculated rates are 'time-averaged'. However the time-averaging effect in the GRAPE-based sedimentation rate should be much smaller that associated with the datum-based sedimentation rates. Assuming that laminated sections of the sediment were deposited more rapidly than non-laminated (based on dissolution levels and lack of bioturbation), the GRAPE-based rates represent underestimates for laminated sections and overestimates of the intervening, non-laminated sediments. On this basis, GRAPE-based sedimentation rates are taken as minimum and maximum rates for laminated and non-laminated sediments respectively.

| Site | Thickness of LDM interval (metres) | Estimated sedimentation rate (m/Ma) |
|---|---|---|
| 847 | 11.92 | 202.03 |
| 849 | 14.51 | 245.93 |
| 850 | 9.73 | 164.92 |

Table 5.6. Estimates of sedimentation rates for '4.4Ma' LDM based on comparison of GRAPE records with those of Site 851 (LDM free).

Errors in these estimates are related to inaccurate definition of the extent of LDM units and sediment equivalent to LDM units within the sediment cores. The base of LDM events is clearly defined by the 60cm thick basal unit but the upper boundary is more difficult to define. In the three Leg 138 sites containing the '4.4Ma' LDM event, the upper limit is defined as the top of the last clearly laminated section. It is entirely possible that these laminated sections defined at each site were not deposited by the same depositional event. This could have been caused by limited lateral extent of mat accumulation or heavy bioturbation of laminated material resulting in homogenization of previously laminated layers.

A second source of potential error is in the depositional period estimated for the equivalent non-laminated sediment. Geochemical and microscopic examination of the sediment equivalent to the '4.4Ma' LDM deposits at Site 851 indicate elevated levels of silica, caused by increased *Thalassiothrix* content during the LDM depositional period (see Sections and 5.2.3 and 7.2). This change in sediment composition may have resulted in low in the GRAPE record not related to changes in insolation, resulting in errors in the correlation of the insolation cycle to the GRAPE record. The change in sedimentary opal content could also have resulted in a short-term increase sedimentation rates at Site 851, such short-term variations

are not taken into account in the assignment of age-pick in the Shackleton *et al.* (1995) age model and could also result in errors in the assignment of age-picks to GRAPE peaks and troughs.

## 5.5 $^3$He-BASED SEDIMENTATION RATE ESTIMATION (carried out by F. Marcantoni - Yale University)

$^3$He falls to the surface of the Earth in cosmic dust at a relatively constant rate (Farley, 1995). The dust is incorporated into sediments forming at the time it reaches the sediment surface. Recent studies have suggested that sediment mass accumulation rates, MAR, can be estimated using the concentration of $^3$He in a sediment sample and an assumed flux of cosmic dust (F.Marcantoni, pers. comm.). Experimental accuracy in MAR estimated in this way are dependent on the measurements of $^3$He concentrations in sediments, and the assumed flux of cosmic dust. Reproducibility experiments of $^3$He concentrations give errors of 15 to 20%. Errors in the assumed flux are unknown since there is no independent, accurate measure of $^3$He accumulation (F.Marcantoni, pers. comm.). It is possible that the flux was 3-5 times lower during the Miocene and Pliocene, lowering the estimated MAR by this amount (Farley, 1995). This method also assumes that cosmic dust is incorporated into the sediment at a constant rate. In other methods based on the flux of cosmic dust, such as $^{231}$Pa/$^{230}$Th, the effect of scavenging by organic matter is an important factor (e.g. Rugers van der Loeff and Berger, 1993). It is possible that this mechanism for focussing of $^3$He should also be considered in these calculations.

### 5.5.1 CALCULATION OF $^3$He BASED SEDIMENTATION RATES

$^3$He-based mass accumulation rates were measured for a total of six samples from the lower boundary of the '4.4Ma' LDM event in Hole 847B. Three samples were taken from immediately below the boundary and three from above the boundary, see Figure 5.10. From Figure 5.10 it can be seen that Sample 2 contains a discontinuous layer of diatom rich material. Geochemical measurements of biogenic opal content indicate burrow fill material accounts for approximately 2% of the total sample volume. Sample 3 is taken from directly below the LDM boundary, from both the core photo and BSEI photomosaic it is clear that discontinuous layers of LDM material are common throughout this sample. Based on the area of laminated material visible on the core surface (Fig. 5.10), the laminated material is estimated to account for 10% of the sample volume. Given the 15-20% errors in $^3$He measurement, these differences in sediment composition should not affect the results significantly. Mass accumulation rates (MAR) for these samples are given in the second column of Table 5.7.

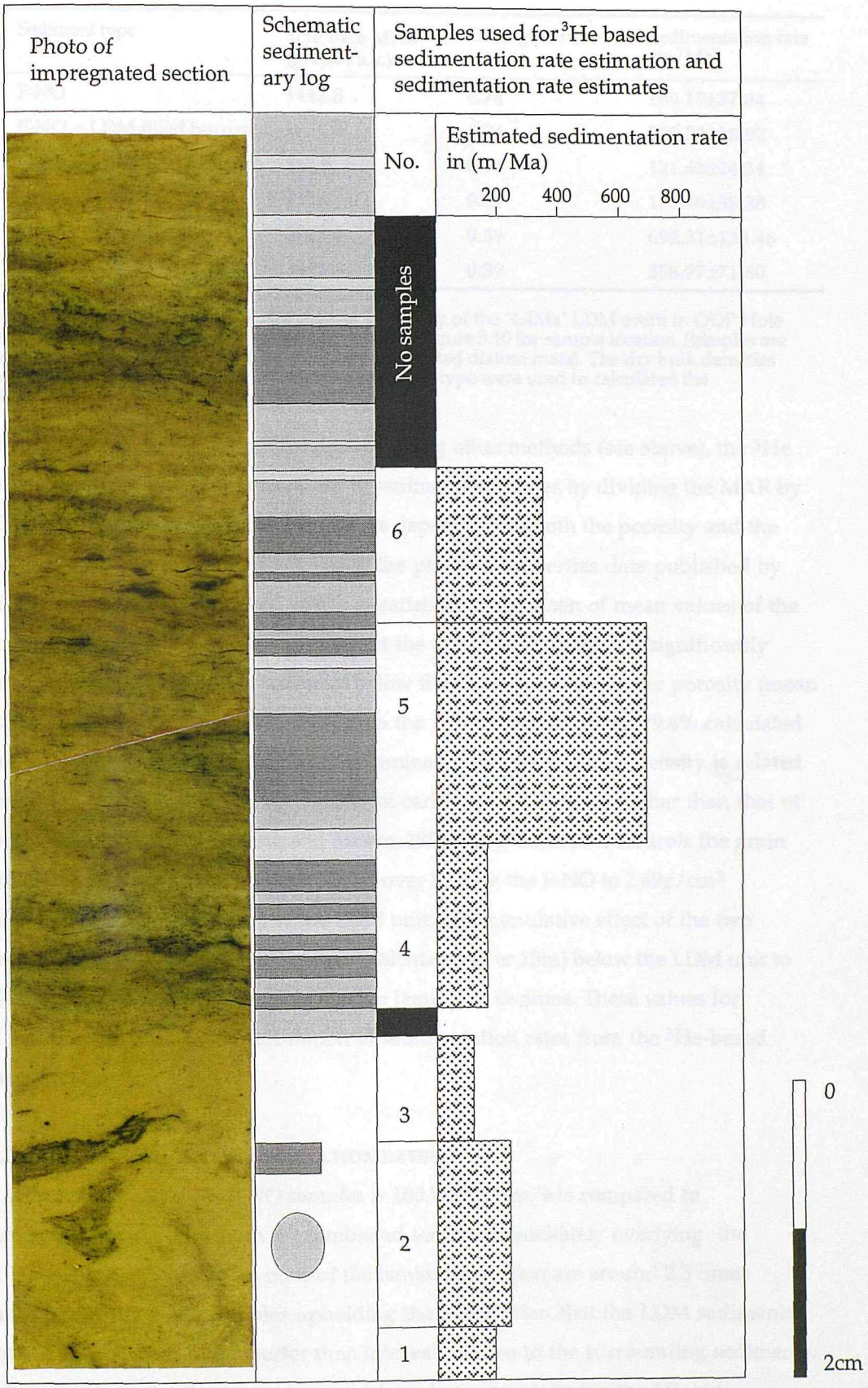


Figure 5.10. Photograph of impregnated Section 138-847B-10H-7, 39-49cm showing based of '4.4Ma' LDM deposits. Samples used to estimate $^3$He based sedimentation rates are given alongside the schematic sedimentary log. Note the LDM material filling burrows approximately 0.5cm below the base of the laminated section and falling into Sample 2.

| Sample Number | Sediment type | $^3$He base MAR (g/cm$^2$/k.y.) | DBD (g/cm$^3$) | Sedimentation rate (m/Ma) |
|---|---|---|---|---|
| 1 | F-NO | 14±2.8 | 0.74 | 189.19±37.84 |
| 2 | F-NO + LDM filled burrow | 17±1.4 | 0.74 | 229.72±18.92 |
| 3 | F-NO + discont. LDM layers | 9±1.8 | 0.74 | 121.62±24.34 |
| 4 | LDM | 7±1.4 | 0.39 | 179.49±35.88 |
| 5 | LDM | 27±5.4 | 0.39 | 692.31±138.46 |
| 6 | LDM | 14±2.8 | 0.39 | 358.97±71.80 |

Table 5.7. MAR for sediments either side of the basal boundary of the '4.4Ma' LDM event in ODP Hole 847B estimated using $^3$He concentration of the sediment, see Figure 5.10 for sample location. Samples are divided into F-NO (foram-nannofossil ooze) and LDM (laminated diatom mats). The dry bulk densities (DBD) calculated from ODP data for the appropriate sediment type were used to calculated the sedimentation rate of each sample, see text for detail.

For comparison with sedimentation rates derived using other methods (see above), the $^3$He based mass accumulation rates are converted to sedimentation rates by dividing the MAR by the dry bulk density (DBD), see Table 5.7. DBD is dependent on both the porosity and the grain density of the sediment (Fig. 5.11). Using the physical properties data published by ODP for these sediments (Mayer *et al.*, 1992), a statistical comparison of mean values of the two sediment types (F-NO and LDM) shows that the dry bulk densities are significantly different, see Figure 5.11. The F-NO sediment below the LDM unit has a lower porosity (mean 71.7% of total volume, calculated over 15m) than the LDM material (mean 79.4% calculated for the 13m thick LDM unit, rising to 84.1% in laminated intervals). Grain density is related to the mineralogy of the sediments, the density of carbonate is 1.2 times higher than that of biogenic opal (calculated from Becking and Moore, 1959). This difference controls the grain density, which drops from 2.62g/cm$^3$ (calculated over 15m) in the F-NO to 2.49g/cm$^3$ (calculated over 13m) across the base of the LDM unit. The cumulative effect of the two variables is to reduce the DBD from 0.74g/cm$^3$ (calculated over 15m) below the LDM unit to 0.52g/cm$^3$ within the unit, falling to 0.39g/cm$^3$ in laminated sections. These values for laminated sections are used in the calculation of sedimentation rates from the $^3$He-based MAR values.

### 5.5.2 Evaluation of $^3$He based sedimentation rates

The mean sedimentation rate for F-NO samples is 180.18±27.04m/Ma compared to 410.26±82.05m/Ma for samples from the laminated section immediately overlying the boundary. Hence, the sedimentation rates of the laminated section are around 2.3 times higher than those of the F-NO samples upholding the assumption that the LDM sediments were deposited over significantly shorter time interval relative to the surrounding sediments. While the flux of $^3$He to the Earth's surface may have been lower during the Miocene (reducing the calculated sedimentation rates), this ratio of sedimentation rates across the lower LDM boundary should be unaffected (providing the flux of $^3$He to the Earth's surface was constant during the deposition of these sediments).

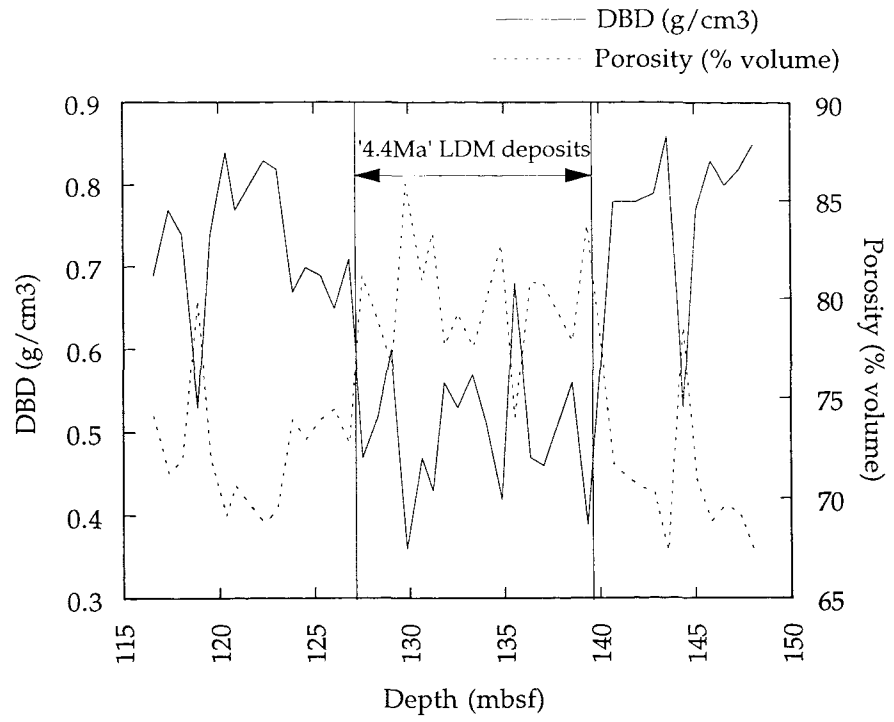


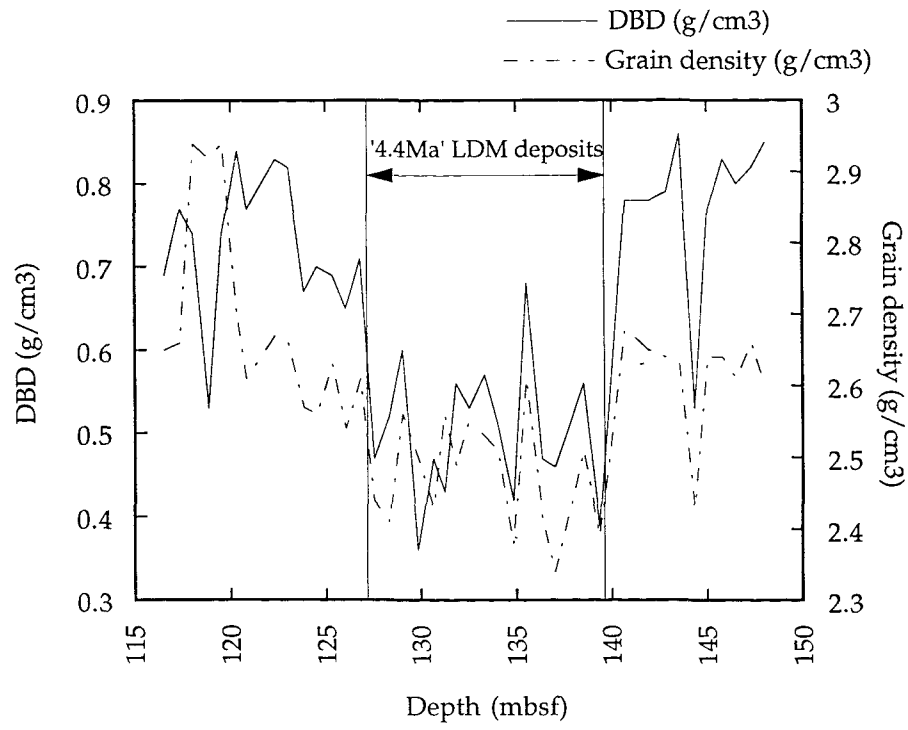


| | Below LDM material | LDM material | Above LDM material |
|---|---|---|---|
| Dry bulk density (g/cm$^3$) | 0.726 (0.085) | 0.520 (0.093) | 0.744 (0.127) |
| Grain density (g/cm$^3$) | 2.700 (0.143) | 2.491 (0.080) | 2.62 (0.082) |
| Porosity (%volume) | 75.56 (2.98) | 79.44 (3.34) | 71.66 (4.36) |

Figure 5.11. Variations in sediment physical properties through the '4.4Ma' LDM deposits (dry bulk density, grain density and porosity), data from Mayer *et al.* (1992, CD Rom). Mean and standard deviation (given in brackets) of measurements for each property are summarized in the table, and can be used to demonstrate statistical differnences between the LDM material and the sediment above and below the laminated section, see text for further details.

MARs estimated using the $^3$He method show very little difference between sediments from directly above and below the basal boundary of the '4.4Ma' LDM unit in Hole 847B, see Table 5.7. Sedimentation rates calculated using the mean DBD values for F-NO and laminated sections (see above) show a pronounced difference. These results demonstrate the importance of sedimentary physical properties in the calculation of sedimentation rates. In this case the majority of the variation in DBD was due to an increase in porosity, demonstrated by the strong negative correlation in Figure 5.11. The small increase in mean MAR across the boundary between F-NO and LDM material (13.3 to 16.0 /cm$^2$/k.y respectively, LDM material accumulating 1.2 times faster than F-NO) was enhanced by the change in physical properties to give a much larger difference in linear sedimentation rates (LDM thickness increases 2.3 times faster than F-NO).

## 5.6 COMPARISON OF SEDIMENTATION RATE ESTIMATES

The advantages and disadvantages of the four methods of sedimentation rate estimation discussed above are summarized in Table 5.8 alongside the estimates produced for the '4.4Ma' LDM deposits. Sedimentation rates and intervals over which they are calculated are compared schematically in Figure 5.12. From Table 5.8 and the above discussion it is clear that the most robust sedimentation rates for the laminated sections are those based on the GRAPE comparisons. Although these rates are time-averaged, it is over much shorter (around 40%) length scales than the datum-based sedimentation rates. Direct correlation of a compositional, climate based proxy between cores also minimizes problems with diachronous biostratigraphic events (related to ocean circulation patterns) found in the datum-based method. Errors in the GRAPE-based rates related to inaccuracy in the identification of the equivalent non-laminated sediment and estimation of depositional time period are small compared to those of the laminae couplet and $^3$He-based sedimentation rates.

Sedimentation rates calculated for both F-NO and laminated sections of the '4.4Ma' LDM depositional event in Hole 847B using both the comparative GRAPE method and $^3$He method are compared in Table 5.9. There is a remarkably good agreement between the lamina couplet-based sedimentation rate calculated assuming annual depositional events and the $^3$He-based estimates for laminated intervals. The maximum rate for F-NO sedimentation is given by the GRAPE-based method (202.03 m/Ma) is within the range estimated by the $^3$He- based method (180.18±27.04 m/Ma). The time-averaging effect results in GRAPE-based sedimentation rates representing maximum rates for F-NO sections of LDM deposits. Using the lamina-couplet based sedimentation rate for LDM deposition the GRAPE-based sedimentation rate for F-NO sections can be recalculated. Given LDM and F-NO thicknesses

| Method | Advantages | Disadvantages | Dominant sediment type through estimate region | Sedimentation rate estimates for individual sites (m/Ma) | | | |
|---|---|---|---|---|---|---|---|
| | | | | 847 | 849 | 850 | 851 |
| Datum based | • established method | • assumes constant sedimentation rates between age picks resulting in time- averaging across different sediment types<br>• many biostratigraphic events are diachronous | F-NO (around 90%) | 97.35±4.13 | 35.56±2.25 | 29.16±1.85 | 14.51±0.23 |
| Laminae couplets based | • independent of datum ages and constraints<br>• measures sedimentation rates of laminated material directly | • assumes the laminae couplets are related to depositional events.<br>• reliant on knowing the periodicity of depositional events<br>• no way to prove that laminae couplets originally existed throughout the laminated sections. | LDM | Annual events 339±163<br>Four yearly events 85±41 | n.d.<br>n.d. | Annual events 315±163<br>Four yearly events 79±42 | n/a |
| GRAPE based | • calculated over much shorter interval than datum based rates reducing time averaging problem<br>• does not require poorly constrained assumptions | • reliant on an accurate assignment of age-picks at site 851<br>• time-averaging results in minimum values for LDM sedimentation rates | F-NO (around 80%) | 113.32±11.38 | 132.84±13.34 | 89.05±8.94 | n/a |
| $He_3$ based | • relies on direct measurements and is therefore independent of datum ages and constraints | • assumes an $He_3$ flux that cannot be tested<br>• measurements of $He_3$ concentration have associated error of 15-20%<br>• this is a new method that has not been published<br>• similar to other methods based on cosmic dust, scavenging by organic material may result in spurious results | F-NO (100%)<br>LDM (100%) | 135.13±27.03<br>410.26±80.05 | n.d.<br>n.d. | n.d.<br>n.d. | n.d.<br>n.d. |

Table 5.8. Comparison of the four methods of sedimentation rate estimated used in this study showing advantages and disadvantages of each method and the rate estimates derived from each method. Dominant sediment type through the region each estimate is based on is also given for comparison. (n.d. - no data, n/a not applicable)

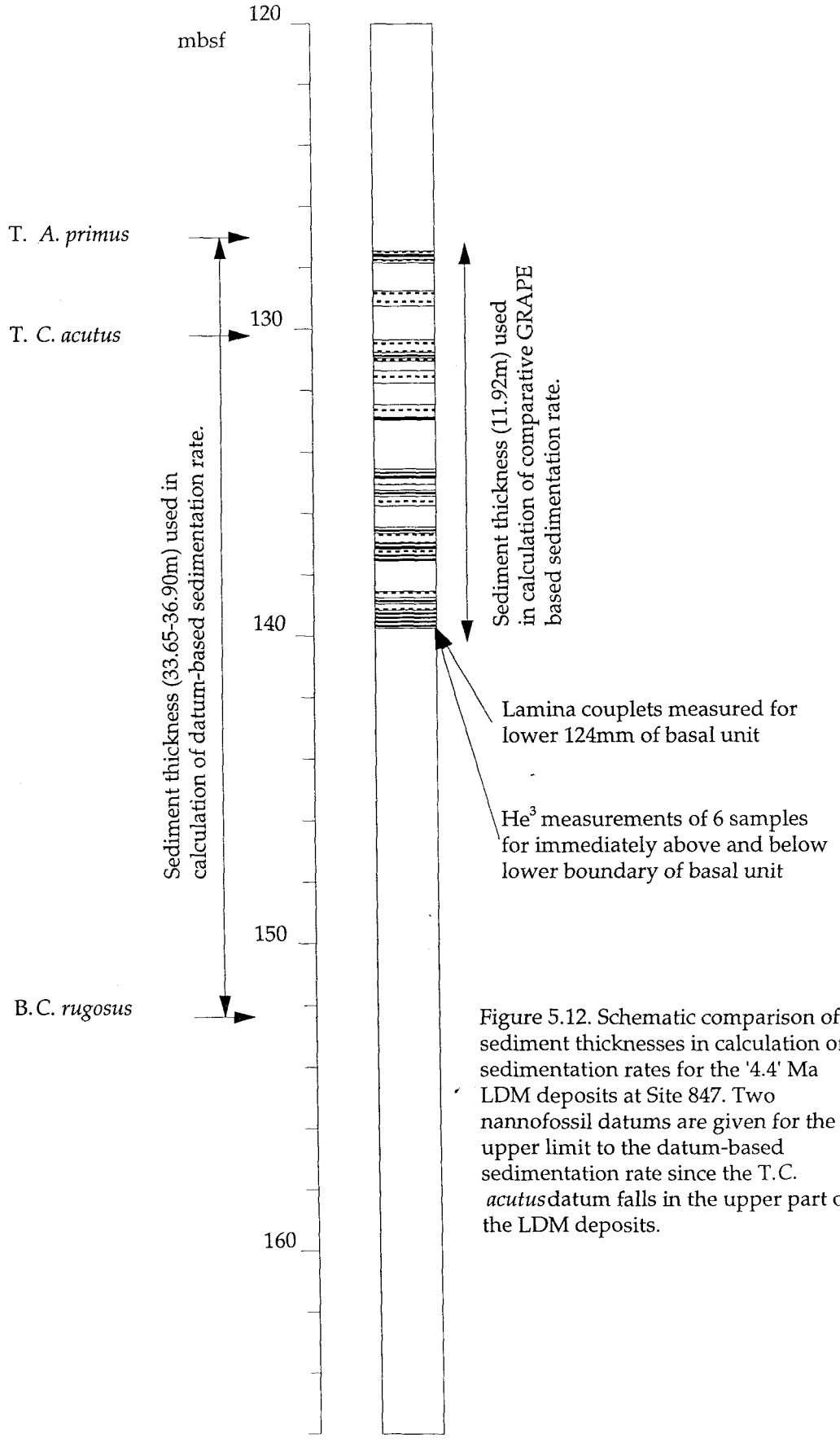


Figure 5.12. Schematic comparison of sediment thicknesses in calculation of sedimentation rates for the '4.4' Ma LDM deposits at Site 847. Two nannofossil datums are given for the upper limit to the datum-based sedimentation rate since the T.C. *acutus* datum falls in the upper part of the LDM deposits.

of 1.79-2.89m and 7.4-8.5m respectively, the GRAPE-based sedimentation rate for F-NO at Site 847 is 152.42±5.89m/Ma. This value falls well inside the limits for F-NO sedimentation through the '4.4Ma' LDM event estimated using datum-based and GRAPE-based data (91.99-202.03m/Ma).

| Method used to estimate sedimentation rate | F-NO sedimentation rate (m/Ma) | LDM sedimentation rate (m/Ma) |
|---|---|---|
| Lamina | n.d. | 339±163 |
| Comparative GRAPE | 202.03 (maximum) | 202.03 (minimum) |
| $^3$He content | 180.18±27.04 | 410.25±82.05 |

Table 5.9. Comparison of sedimentation rate calculated for F-NO and LDM sections of '4.4Ma' LDM depositional event.

### 5.6.1 Regional sedimentation rates used in this study

Approximate regional sedimentation rates are needed in order to calculate estimates of regional fluxes of biogenic silica and organic carbon to the deep ocean during the deposition of LDM material (Section 7.3). Based on the above discussion, minimum sedimentation rates for LDM deposits are taken as GRAPE-based sedimentation rates (Table 5.10). Given the possibility of an incomplete record of LDM deposits at the single-cored Site 850 (see Section 5.2.4), the minimum sedimentation rate is taken as the mean of the GRAPE-based sedimentation rates from Sites 847 and 849. Maximum sedimentation rates are taken from $^3$He-based rates. To account for experimental variability the mean of the measured rates is used. The $^3$He-based sedimentation rate is not scaled to account for possible reductions in cosmic $^3$He flux.

| Sedimentation rate limit | Minimum | Maximum |
|---|---|---|
| Estimation method | GRAPE-based | $^3$He- based |
| Regional sedimentation rate (m/Ma) | 202 | 410 |

Table 5.10. Minimum and maximum sedimentation rates for the laminated sections of the '4.4Ma' LDM depositional event used for regional calculations in eastern Equatorial Pacific area, showing estimation method. See text for discussion.

### 5.6.2 Estimation of depositional event periodicity

Limits on event periodicities can be calculated from the minimum and maximum sedimentation rates discussed above. Assuming that the mat-forming event depositional regime prevailed throughout the accumulation of the '4.4Ma' LDM basal unit, the maximum and minimum event periodicities can be calculated using the GRAPE- and $^3$He-based sedimentation rates respectively for each site. Dividing the mean laminae couplet thickness (339μm) by the sedimentation rate gives the depositional period for a single couplet. This equates to the mean periodicity of depositional events. Since the GRAPE-based sedimentation rate is assumed to represent minimum sedimentation rates, dividing this into the mean couplet thickness gives the maximum event periodicity. Using the $^3$He based

sedimentation rate, assumed to be the maximum rate gives the minimum periodicity (Table 5.11).

| Site | Event periodicity | |
|---|---|---|
| | Minimum | Maximum |
| 847 | 0.8 | 1.3 |
| 850 | n.d. | 1.5 |

Table 5.11. Maximum periodicity of deposition events calculated from GRAPE derived sedimentation rates.

The maximum event periodicities are comparable to those of the modern El Niño cycle, while the minimum values suggest annual events. Both of these results are consistent with the use of the frontal deposition model in both explaining the occurrence of laminae couplets and the deposition of LDM deposits.

## 5.7 CHAPTER SUMMARY

Sedimentation rates have been calculated for the '4.4Ma' LDM interval using four different methods. The two methods based solely on material from laminated sections (annual lamina couplet-based and $^{3}He$ -based) give comparable results significantly greater than those obtained using the traditional datum-based method and the GRAPE-based method. This demonstrates the magnitude of the difference between the sedimentation rates of the two sediment types, LDM and F-NO. Regardless of absolute rates the $^{3}He$-based method indicates a 2.3 fold increase in sedimentation rate related to the onset of LDM deposition.

The sedimentation rates calculated in this chapter also offer two lines of evidence supporting the assumption of annual deposition events resulting in the observed lamina couplets; (1) the lamina couplet-based sedimentation rates calculated using annual depositional events and the $^{3}He$-based sedimentation rates are similar within the calculated bands of error; and, (2) maximum frequencies calculated using GRAPE-based sedimentation rates suggest frequencies of less than 1.5 couplets per year.

The high levels of frustule preservation observed in laminated sections compared to non-laminated sections (see Section 4.4) suggests that sedimentation rates were not constant during periods of LDM deposition. Comparison of Gamma Ray Porosity Evaluator (GRAPE) records between sites with and without laminated sediments shows that periods of LDM deposition are associated with sediment thicknesses 5 to 6 times greater than equivalent non-laminated sediments.

# CHAPTER 6: HIGH RESOLUTION (MILLIMETRE-SCALE) ANALYSIS

## 6.1 INTRODUCTION

This chapter presents the results of ultra-high resolution measurements (0.5-2mm sampling interval) of biogenic opal from two sites in the eastern Equatorial Pacific, ODP Sites 847 and 850 (Fig. 6.1). The laminated nature of LDM material allowed the 60cm continuously laminated basal unit of the '4.4Ma' LDM depositional event to be analyzed at 0.5 to 2.0 mm intervals. Although the two sites are currently over 2000km apart, their opal records through the '4.4Ma' LDM event basal unit show remarkable similarities, demonstrated statistically using cross-correlation algorithms. These similarities were strongest on the lower 10cm of the records. Above this section, levels of correlation were maximized by mapping the records for Site 850 onto the same length scale as those of Site 847. This was achieved using characteristic sediment layers found in both sites as tie-points in the records of biogenic opal content. Strong cyclicities both within and between the two records were identified using spectral analysis methods. The palaeoceanographic significance of these results is discussed in the context of modern observations of ocean circulation patterns and processes.

## 6.2 SAMPLING METHODS

The unique matted structure and resulting horizontal tensile strength of LDM deposits (Kemp *et al.*, 1995) allows the separation of individual diatom mats (as little as 20μm thick) using a micro-scalpel (Martin 34-400-07) and flexible tweezers under a binocular microscope. In strongly laminated sections it is theoretically possible to sample at this level of resolution, but sample size and time constraints make this unrealistic. Sample weights would be at least an order of magnitude smaller than that required for a single analysis for opal content even following the modifications to the published method used in this study (see Chapter 2). Based on published dry bulk densities for LDM material (0.39g/cm3, data from Mayer *et al.*, 1992), a minimum sub-sample layer thickness of 0.85mm is needed to yield a dry sub-sample weight of 100mg from a $3cm^2$ sample cross-section (sufficient for accurate opal analysis, smear slide and SEM strew mount preparations and carbonate analysis). In cases where sedimentological changes made thinner sub-sample layers appropriate, sub-samples were analyzed for opal content with the remaining material used sparingly for other analyses.

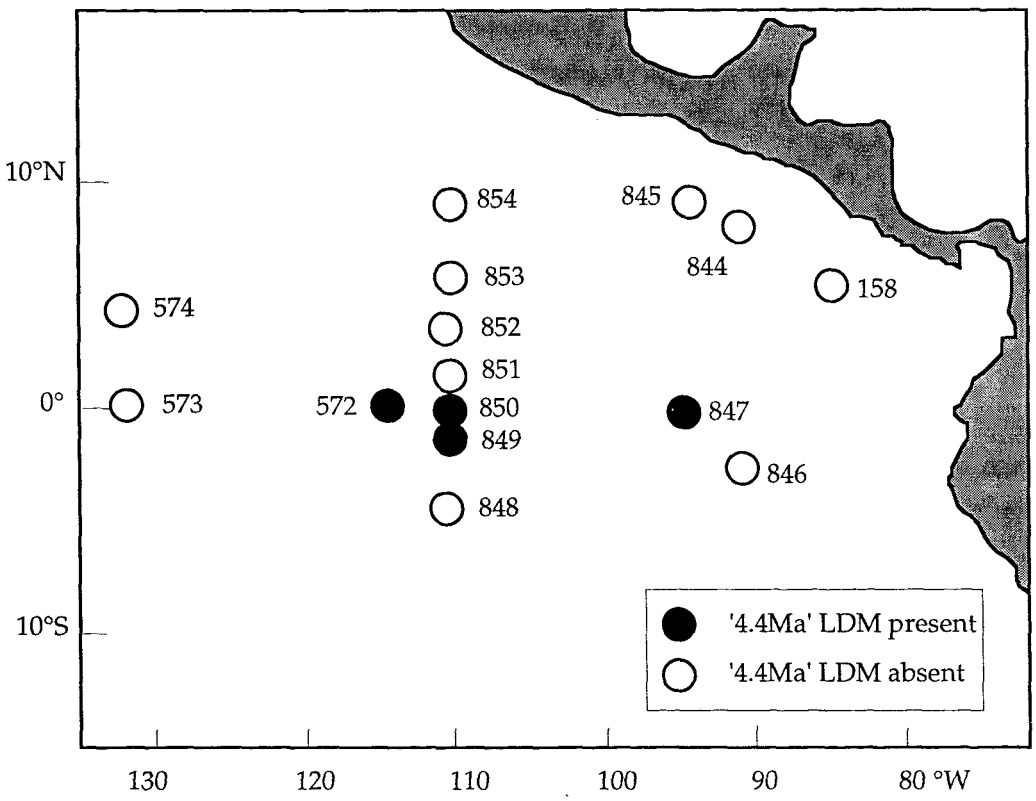


Figure 6.1. Location of ODP and DSDP drill sites in the eastern Equatorial Pacific area showing the occurrence of '4.4Ma' LDM deposits.

During the sampling process, the thickness of sub-sampled layers was constrained by a) the visual identification of layers within the samples; and b) the level of lamination within individual layers. Sub-samples were taken on the basis of laminae defined in x20 BSEI photomosaics; epoxy resin-impregnated blocks of sample remaining from the production of the polished thin section; and the sample itself. The sediment was divided into sub-samples on the basis of colour changes and changes in texture using identified in BSEI photomosaics (such as regions of well developed lamina couplets). In sections of homogeneous structure sub-samples were taken at 1.5-2.0mm intervals. The thickness of sub-sample layers was also constrained by the tensile strength of the individual sample intervals. Sections with strongly matted texture have a much higher tensile strength and can be peeled into much thinner layers than sections with a higher carbonate content and more fragmentary structure (minimum thicknesses of around 1.0-1.5mm for layers of around 50% carbonate).

## 6.3 RELATIONSHIP OF OPAL CONTENT TO SEDIMENT FABRIC

Ultra-high resolution measurements of biogenic opal content were used to identify the relationship between degree of lamination and opal content. Well laminated sections have much higher opal contents (up to 80 wt% biogenic opal) than more poorly laminated and disrupted layers (around 30-50 wt% biogenic opal), see Figure 6.2. Quantitative inspection of smear slides and SEM strew mounts (using point counts, see Appendix A9) made for the high opal/well laminated layers show that the biosiliceous assemblage is dominated by *Thalassiothrix* frustules. Radiolarian and centric frustules are rare (around 5% of the biosiliceous assemblage). The non-biosiliceous assemblage (up to about 40 wt%) is dominated by coccoliths, see Figure 6.3a.

In low opal/poorly laminated or disrupted sub-samples the *Thalassiothrix* frustules tend to me much more fragmented with frustule sections typically less than 40μm long with broken ends. The biosiliceous assemblage is also typically more mixed with an increased occurrence of centric diatoms and radiolarians (up to 15-20% of the biosiliceous assemblage), see Figure 6.3b. The carbonate fraction is again dominated by coccoliths although BSEI photomosaics suggest that foraminifer numbers should also increase in the more disrupted sections. The images in Figure 6.3 also illustrate the lower levels of dissolution associated with high opal/well laminated sub-samples relative to low opal/poorly laminated layers. This observation is consistent with the relationship established between dissolution level and opal content (increased levels of dissolution associated with lower biogenic opal contents, see Section 4.4).

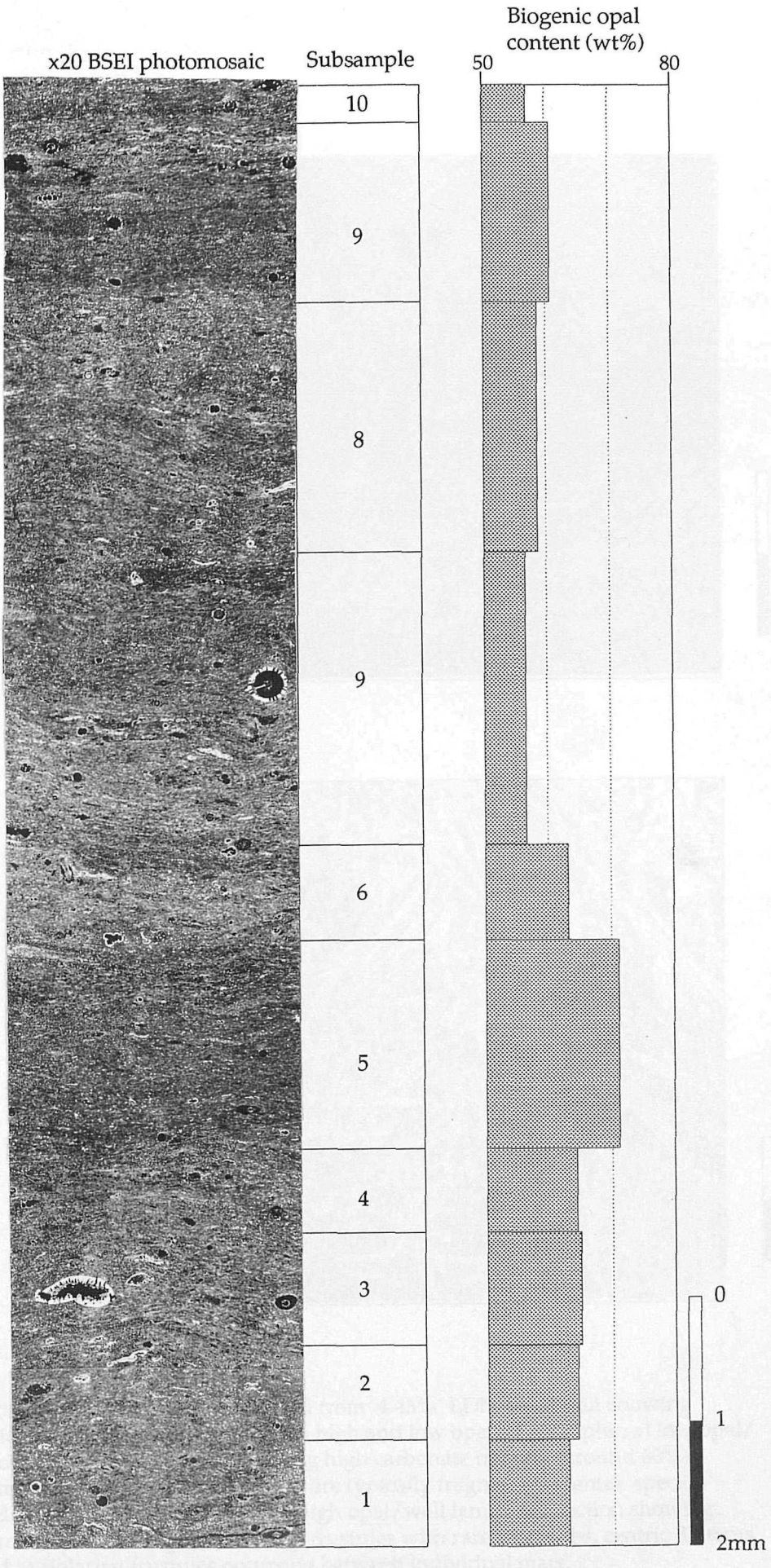


Figure 6.2. Comparison of sediment structure defined in x20 BSEI photomosaic with biogenic opal content in 850B-10H-7, 62-74cm. Note increased biogenic opal content in strongly laminated sections (e.g. Subsample 5).

a)

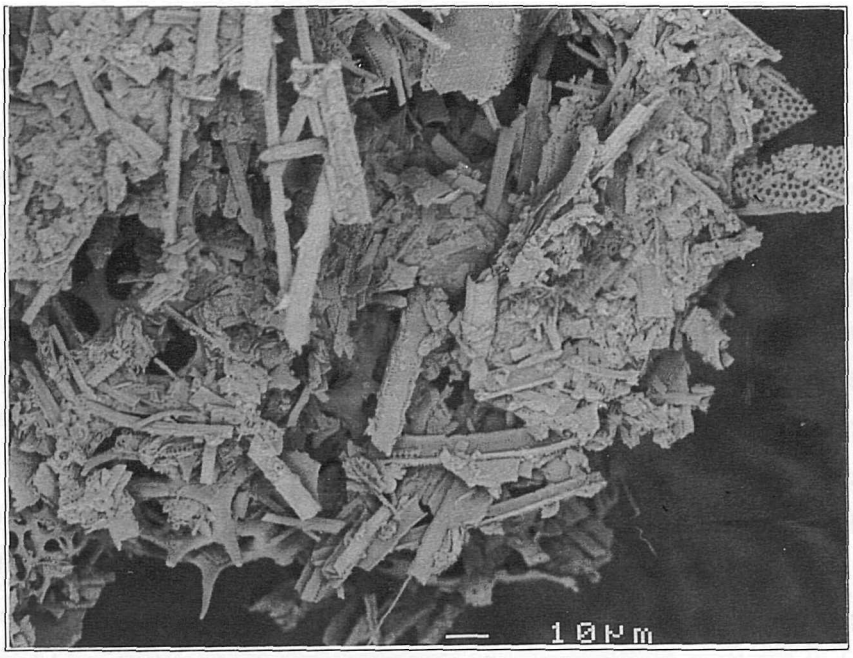


b)


Figure 6.3. SEM images of material from '4.4Ma' LDM basal unit showing difference in composition between high and low opal sub-samples; a) low opal/ poorly laminated material showing high carbonate fraction (around 60%) dominated by coccoliths. Diatoms are typically fragmented, centric species and radiolarians are common; b) high opal/well laminated section showing dominance of *T. longissima* Group frustules with rare coccoliths, centric diatoms and radiolarian frustules occurring between individual mats.

## 6.4 CORRELATION BETWEEN ODP SITES 847 AND 850 (for the '4.4Ma' LDM basal unit)

Visual inspection of records of the '4.4Ma' basal unit from Holes 847 and 850 show distinct similarities between both the opal records and sedimentology, see Figure 6.4 and 6.5. Individual layers can be clearly correlated using sediment colour, texture and opal content (Fig. 6.5 and Section 6.4.1) regardless of the fact that these two records were deposited around 2000km apart (Fig. 6.1). In order to test the level of correlation statistically the opal records from the two sites were compared using cross-correlation algorithms. The records were first fitted to the same 0.5mm incrementing length scale using linear interpolation. This provided a much closer fit with the original data than cubic spline or cubic interpolation. Initially, the two interpolated records were cross correlated using the base of the laminated section as the reference point in both record with no further manipulation of the data. This process produced a correlation coefficient of $r^2$=0.176. Given the number of original data points (around 420) in each data-set, this correlation coefficient is significant to above the 99.9% level. Statistically this value of $r^2$ indicates that around 18% of the observed variation in the two raw data-sets could be attributed to regional controls directly affecting the two sites in the same way.

Comparison of the opal records (henceforth referred to as OPAL847 and OPAL850 for records from Site 847 and 850 respectively, Fig. 6.4), shows that correlation between the two sites is strongest in the lower 13.2cm of the unit ($r^2$ = 0.553 for total opal content, at the 99.9% significance level). The base of Site 850 in these records is affected by a large foram-nannofossil ooze filled burrow 2-6mm above the lower boundary of the laminated material.Without this artifact, levels of statistical correlation would improve significantly. Above this interval the records appear to diverge, and it becomes unclear which peaks and troughs can be matched. The greater width of peaks and troughs in OPAL847 compared to the same peaks in OPAL850 suggests that the sedimentation rate over this interval at Site 847 was higher than that at Site 850. Independent tie-points linking the two records were sought to make statistical correlation meaningful. These tie-points were provided by characteristic patterns in the sedimentology, see following section.

### 6.4.1 CORRELATION USING TIE-POINT LAYERS

Characteristic layers within the basal unit were identified in BSEI photomosaics on the basis of sedimentary features such as changes in biogenic composition, sharp boundaries between sediment types, well developed lamina couplets or the occurrence of nannofossil rich pelloidal structures. In order to test the correlation of these characteristic layers, sediment 5-10mm above and below the layers was also compared. The characteristic layers were only used as tie-points if the less pronounced sedimentary features in the surrounding sediment also

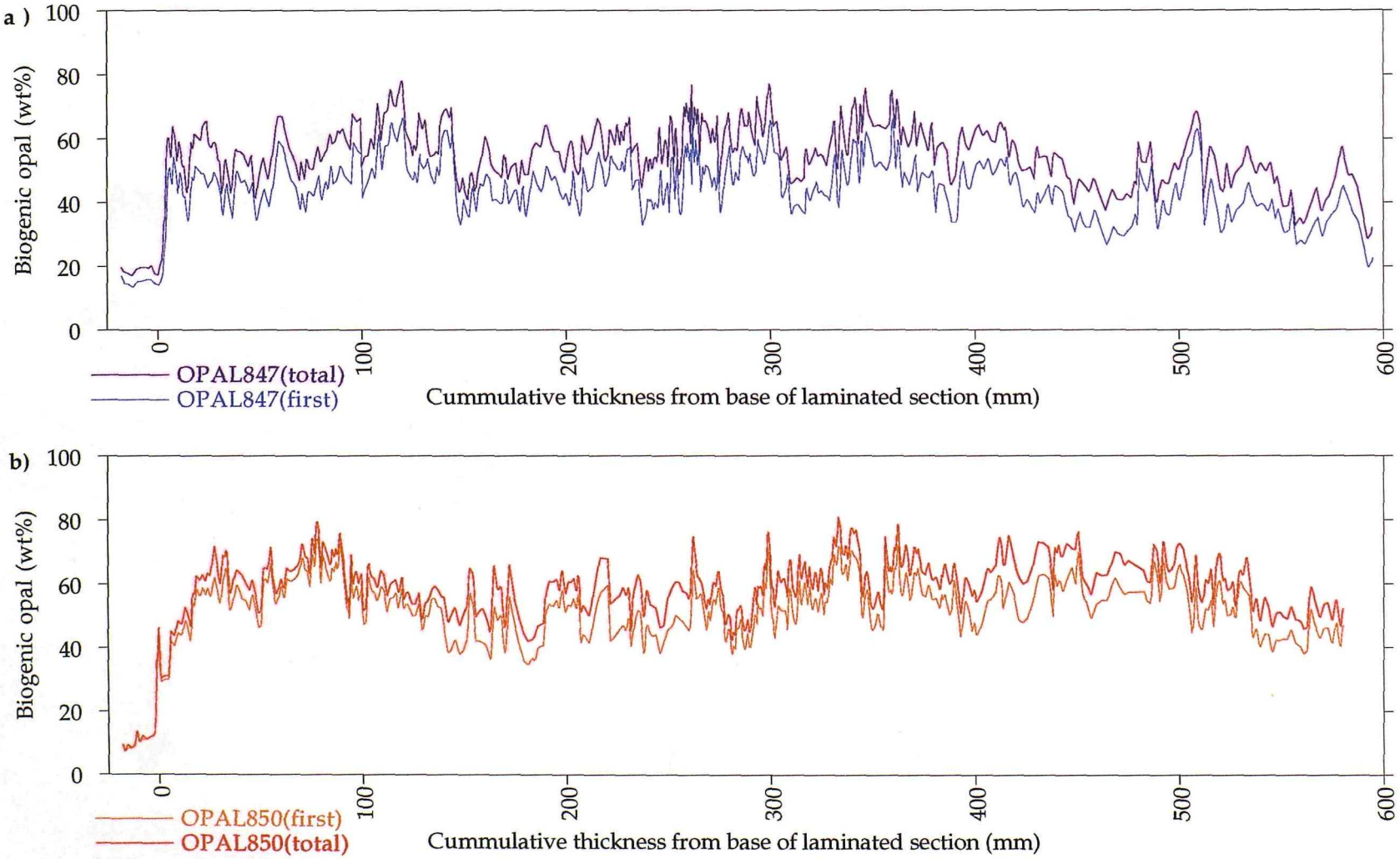


Figure 6.4. Comparison of high resolution opal measurements (total and Thalassiothrix-related opal) showing the similarity between variations in opal content at sites 847 and 850.

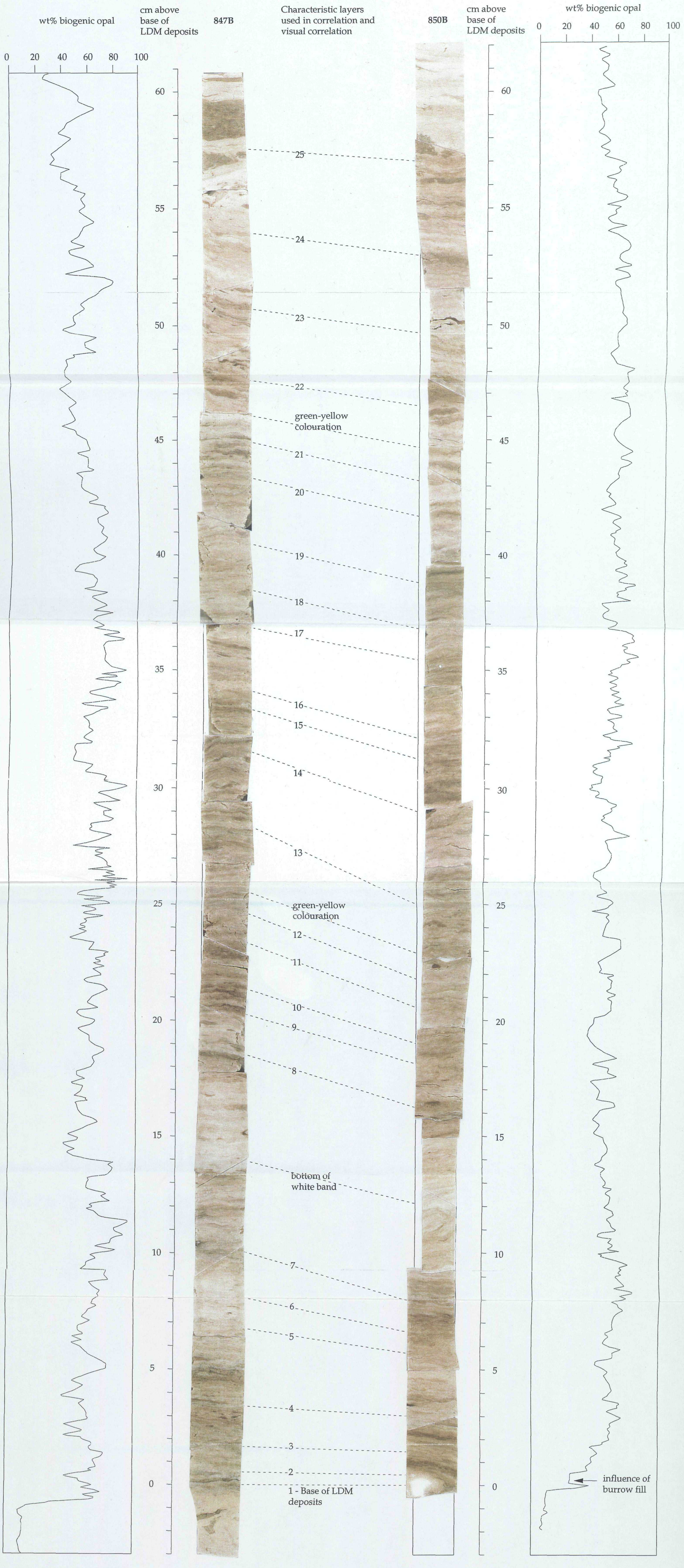


Figure 6.5. True scale comparison of resin impregnanted sediment and measured opal record of '4.4Ma' basal unit from Sites 847 and 850. Correlation between the two sites is based in the characteristic layers defined in Table 6.1 and macroscopic colour changes visible in the sample blocks.

correlated between the two sites as in Figure 6.6. A summary of the characteristics of each tie-point layer and its location above the base of the laminated section at the two sites is given in Table 6.1.

In a number of cases these layers could also be identified in the epoxy resin impregnated sample blocks. This macroscopic comparison of the two sedimentary records is based on colour changes from the dark olive green, strongly laminated, diatom rich layers to the white colouration associated with elevated carbonate contents, see Figure 6.5. Comparison of the sedimentary records in this way is complicated by the formation of lamina couplets in diatom rich layers. The nannofossil content of the mixed assemblage lamina results in the dilution of the dark olive green colouration to a pale or mid-olive colour depending on the relative thickness of the two lamina types. Although the existence of couplets is clearly visible in BSEI photomosaics, variation in couplet development between sites result in the correlation of sediments with different levels of colouration.

Holding OPAL847 constant, OPAL850 was stretched between the sedimentary tie-points (assuming a constant sedimentation rate). This process translated the OPAL850 onto the same time frame as that of OPAL847. The adjusted OPAL850 record ($OPAL850_{STRETCHED}$) was then interpolated onto the same 0.5mm spaced length scale as OPAL847 and the cross-correlation process repeated. This comparison of OPAL847 and $OPAL850_{STRETCHED}$ gives a correlation coefficient of $r^2=0.271$ for the total opal content records at the 99% significance level, see Figure 6.7. This indicates that around 27% of the variation in the two records can be attributed a regional controlling mechanism affecting both sites in the same way. Similar cross-correlation on the lower 132mm of the records gives a correlation coefficient of $r^2=0.691$ at the 99% significance level, compared to the values of $r^2=0.553$ calculated for OPAL850 before the recalculation of the time-frame.

### 6.4.2 Trends and relationships within the opal records

Comparison of the records of total opal and first extraction (*Thalassiothrix* spp. related) opal demonstrate a number of trends, both in similarities and differences between the two sets of records. The records can be divided into 10 sections on the basis of similarities and differences between opal records from the two, see Figure 6.8. This division is made clearer by plotting the difference between the records at the two sites, see Figure 6.9. In these plots the difference between the opal records (DIFFOPAL) is calculated as OPAL847 minus $OPAL850_{STRETCHED}$. Thus, positive values indicate higher opal contents in OPAL847 records and negative values, higher opal contents at Site 850. The characteristics used to define these sections are given in Table 6.2. Mean biogenic opal contents of each zone are compared in Figure 6.10.

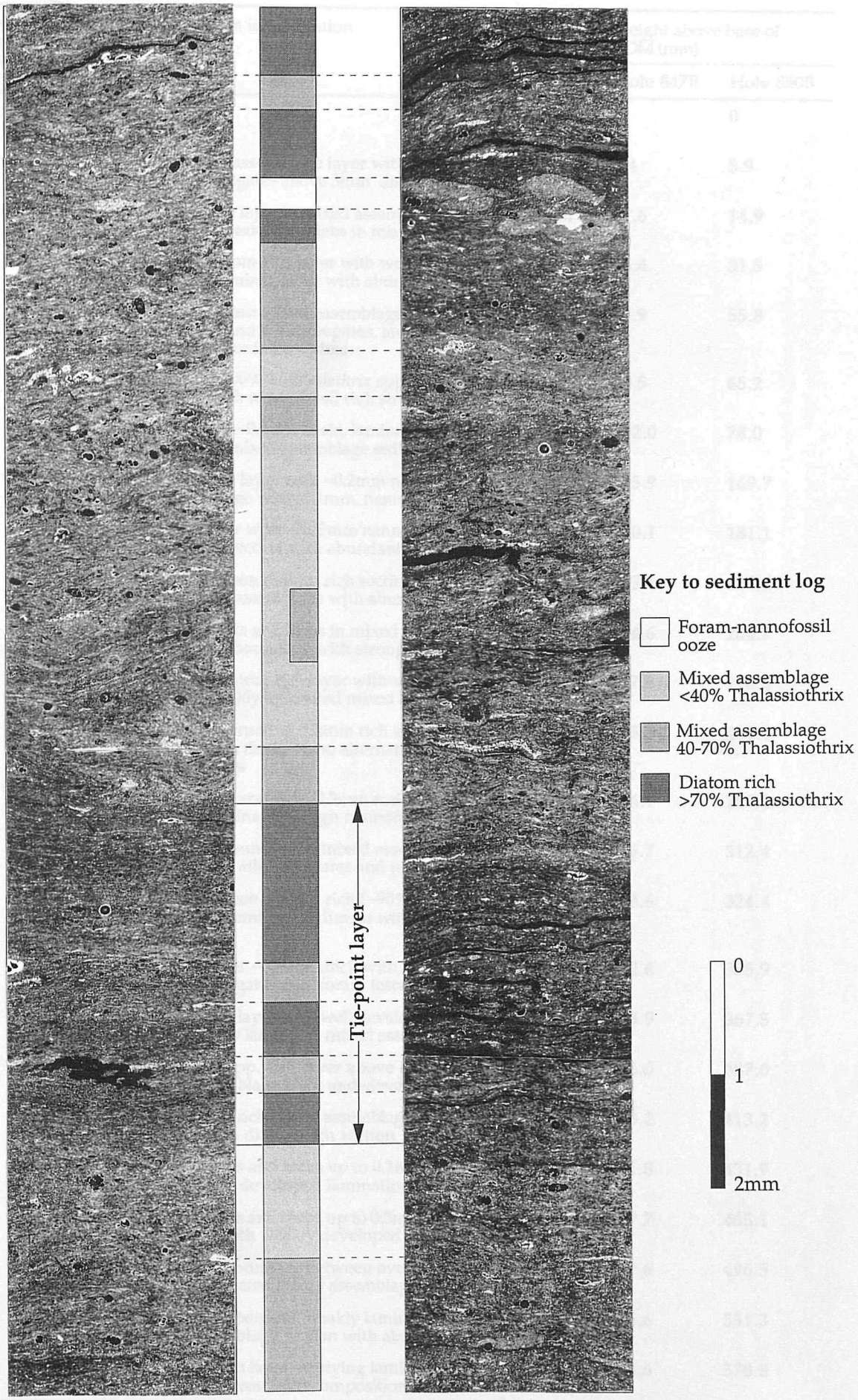


Figure 6.6. Example of tie-point layer showing characteristic layer (Tie-point 4: 2mm thick diatom rich layer with lamina couplets) and the correlation of more weakly developed sedimentary features to either side of this layer which allow its use as a tie-point. Schematic sedimentary log shown for reference

| Tie-point layer number | Characteristics used in identification | Height above base of LDM (mm) | |
|---|---|---|---|
| | | Hole 847B | Hole 850B |
| 1 | Base of LDM unit | 0 | 0 |
| 2 | Lower edge of mixed assemblage layer with rare radiolarian frustules and silt aggregates above 3mm diatom-rich layer | 6.4 | 5.9 |
| 3 | 1mm thick diatom rich layer in mixed assemblage section, overlain by nannofossil rich streaks and blebs in mixed assemblage matrix | 17.6 | 14.9 |
| 4 | Top of 2mm thick diatom-rich layer with well developed lamina couplets, above more mixed layer with abundant silt aggregates | 35.4 | 31.5 |
| 5 | Sharp boundary between mixed assemblage layer with abundant radiolarian frustules and silt aggregates, and diatom rich layer with well developed lamina couplets | 67.9 | 55.8 |
| 6 | Diatom rich layer (~100% *Thalassiothrix* spp.) overlying mixed assemblage layers with nannofossil rich streaks and blebs | 80.5 | 65.2 |
| 7 | Diatom rich layer with~0.5mm scale, lamina couplets below a gradational change to mixed assemblage sediments | 102.0 | 78.0 |
| 8 | 1mm thick diatom rich layer with ~0.2mm nannofossil rich layer above mixed assemblage with<0.1mm, nannofossil rich streaks | 185.9 | 169.7 |
| 9 | 1mm diatom rich layer with ~0.25mm nannofossil rich layer at base in mixed assemblage section with abundant radiolarians | 200.1 | 181.1 |
| 10 | Sharp boundary between diatom rich section with rare silt aggregates and mixed assemblage with abundant radiolarians | 213.1 | 188.6 |
| 11 | Nannofossil rich streaks and blebs in mixed assemblage matrix overlying gradational boundary with strong lamina couplets | 234.6 | 204.9 |
| 12 | Upper boundary of diatom rich layer with well developed laminations under weakly laminated mixed assemblage material | 247.6 | 216.4 |
| 13 | 5mm thick layer of alternating diatom rich and nannofossil rich laminae around 0.5mm thick. These alternations were also noted in sediment colour changes | 285.3 | 249.4 |
| 14 | Well developed lamina couplets (0.3mm scale) in diatom rich layer. Mixed assemblage lamina with high nannofossil content. | 316.1 | 289.2 |
| 15 | Lower (gradational) boundary of mixed assemblage layer with many radiolarians and silt aggregates and high carbonate content | 333.7 | 312.4 |
| 16 | Sharp boundary between diatom rich (~90% *Thalassiothrix* spp.) material and mixed assemblage sediment with abundant radiolarians | 343.6 | 324.4 |
| 17 | Mixed assemblage layer ~0.5mm thick with abundant radiolarian frustules and silt aggregates also, foram tests in diatom-rich region | 372.6 | 355.9 |
| 18 | 2mm thick diatom rich layer with well developed lamina couplets (0.5mm scale) in weakly laminated mixed assemblage region | 383.9 | 367.5 |
| 19 | ~100% *Thalassiothrix* spp. rich layer above diatom-rich layer with abundant mixed assemblage blebs and elevated radiolarian content | 406.0 | 387.0 |
| 20 | 1mm thick nannofossil rich mixed assemblage layer with abundant radiolarian frustules in diatom rich section | 433.2 | 413.2 |
| 21 | Nannofossil rich streaks and blebs up to 0.2mm thick within diatom rich material with well developed lamination | 451.8 | 431.9 |
| 22 | Nannofossil rich streaks and blebs up to 0.3mm thick with mixed assemblage material with weakly developed lamination | 477.7 | 465.1 |
| 23 | Strongly gradational boundary between overlying nannofossil rich layer and weakly laminated mixed assemblage material | 507.6 | 496.5 |
| 24 | 1mm diatom-rich layer between weakly laminated mixed assemblage layer and mixed assemblage section with abundant radiolarians | 555.6 | 531.3 |
| 25 | 3-4mm thick diatom rich layer overlying lamina couplets of mixed assemblage and nannofossil rich composition. | 574.6 | 570.8 |

Table 6.1. Defining characteristics of tie-point layers identified in BSEI photomosaics used to correlate between '4.4Ma' LDM basal unit deposits at Sites 847 and 850.

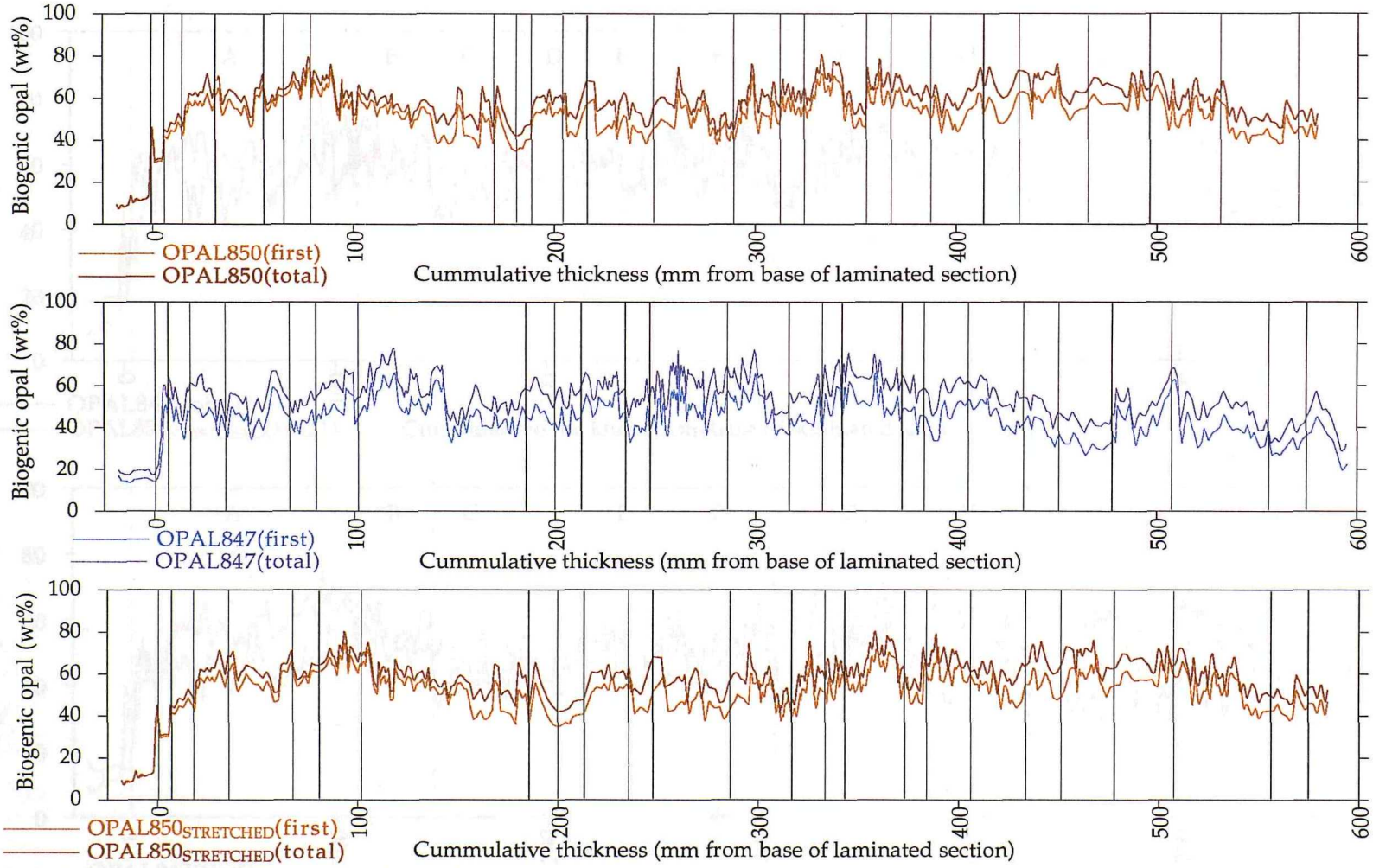


Figure 6.7. Total and first extraction opal records of the '4.4Ma' basal unit showing the location of tie-points used in the correlation; a) OPAL850 with no adjustment; b) OPAL847, and; c) $OPAL850_{STRETCHED}$. Note the increase in similarity in the two records after correlating the OPAL850 onto the OPAL847 length scale

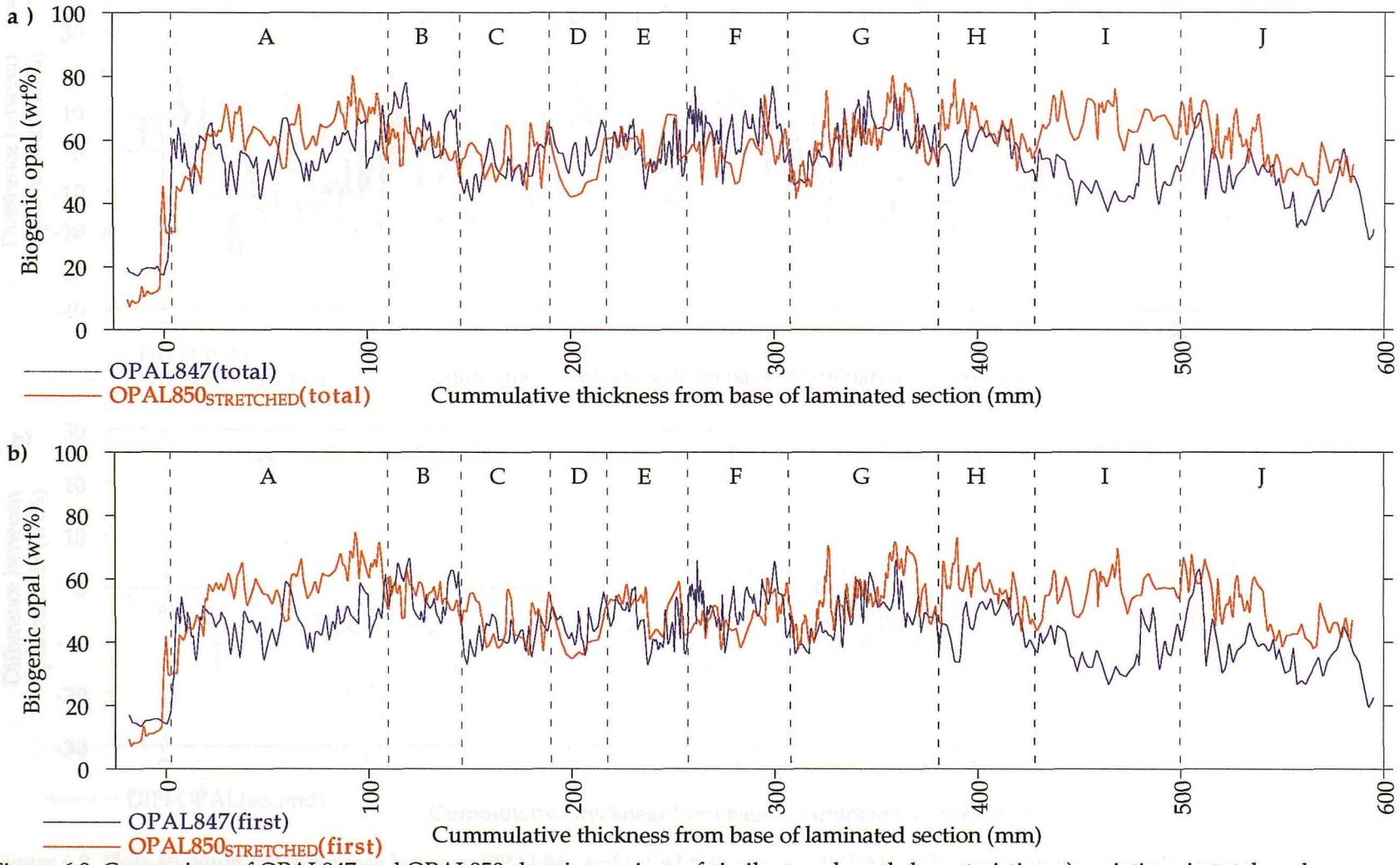


Figure 6.8. Comparison of OPAL847 and OPAL850 showing regions of similar trends and characteristics; a) variations in total opal; b) variations in first extraction opal (T. longissima Group opal).

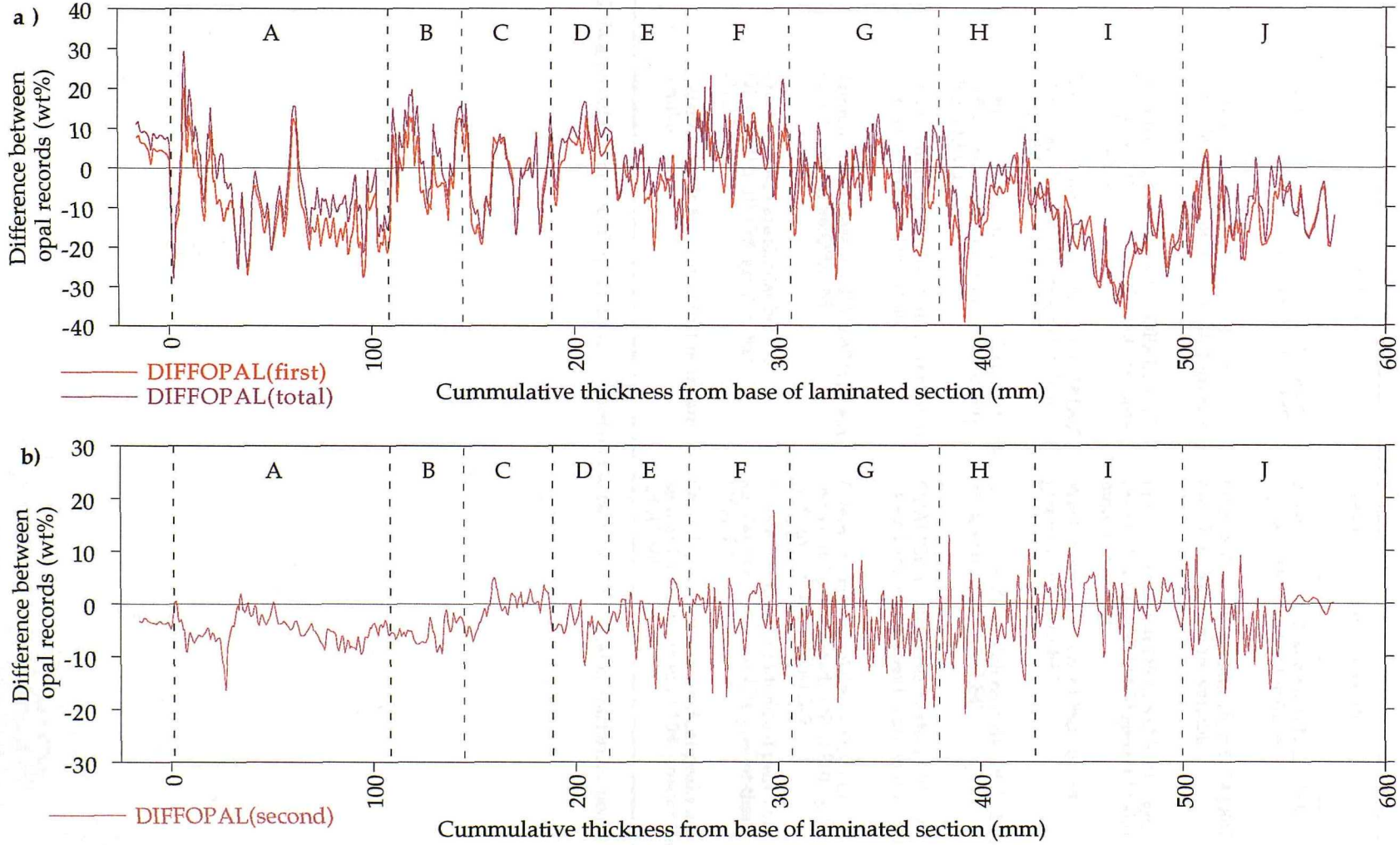


Figure 6.9. Plots showing the difference between OPAL847 and OPAL850$_{\text{STRETCHED}}$ (OPALDIFF) with regions of similar trends and characteristics; a) OPALDIFF(total) and OPALDIFF(first); b) OPALDIFF (second).

| Section number | Trends in total opal records | Trends in first opal records |
|---|---|---|
| A | Similar trends in both records, OPAL850 typically 5-10% greater than OPAL847 | Levels in OPAL850 generally 20-25% greater than those in OPAL847 |
| B | Similar lower values but peaks in OPAL847 (~10mm thick) 15-20% greater than values in OPAL850 | OPAL850 5-10% greater than OPAL847, but OPAL847 is more variable |
| C | Broadly similar trends but OPAL850 15-20% lower than OPAL847, both records highly variable | Similar trends but OPAL850 5-20% greater then OPAL847, OPAL850 generally shows more variability |
| D | Broadly similar overall trends, OPAL847 more variable and 5-10% greater than OPAL850 | Weak correlation OPAL850 10-15% greater than OPAL847 |
| E | Trends broadly similar but OPAL847 is 20-25% greater and shows more variability than OPAL850. | Similar trends in both records, OPAL850 2-5% greater than OPAL847 |
| F | Overall trends broadly similar both minor peaks do not correlate strongly | OPAL850 15-20% greater than OPAL847, overall and minor trends correlate weakly |
| G | Trends match closely, OPAL847 typically ~5% greater than OPAL850 | Overall trends correlate weakly but individual peaks match. OPAL850 up to 30% greater than OPAL847 |
| H | Overall trends are similar but the OPAL850 is 10-15% greater than OPAL847 | Overall trends and individual peaks are similar but OPAL850 40% greater than OPAL847 |
| I | Overall trends and individual peaks are similar | Overall trends and individual peaks are similar OPAL850 around 15% greater than OPAL847 |

Table 6.2. Regions of first and total opal records defined on the basis of trends and characteristic peaks.

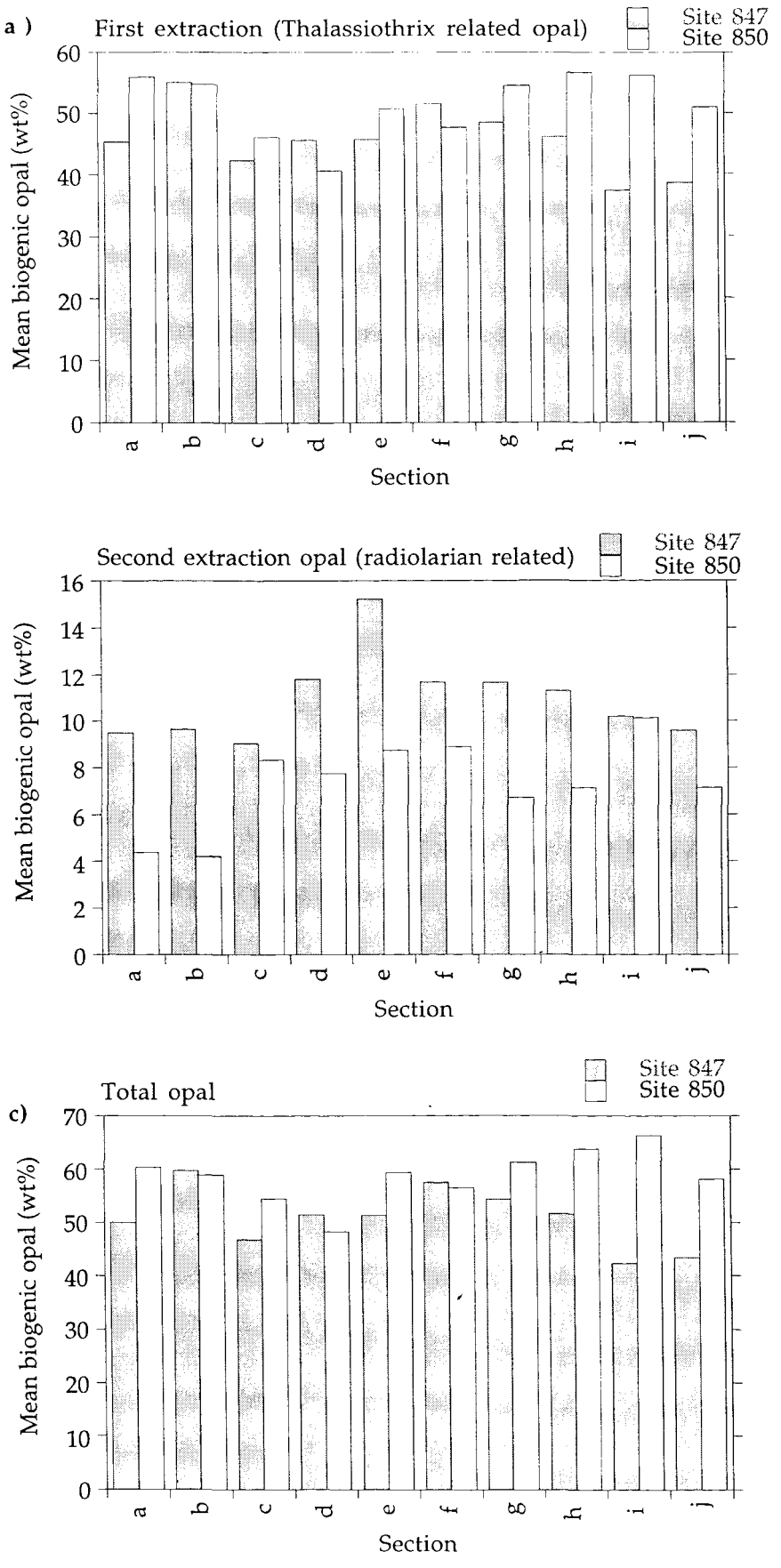


Figure 6.10. Plots of mean opal contents of OPAL847 and OPAL850$_{STRETCHED}$ for regions of similar trends and characteristics defined in Figures 6.8 and 6.8; a) first extraction; b) second extraction, and, c) total opal.

Total opal contents at Sites 847 and 850 are broadly similar through sections A to H but diverge in sections I and J the opal content at Site 850 rises up to 40% greater than values recorded at Site 847. Total opal contents at Site 850 also rise above those at Site 847 by around 10-20% in Sections A,C,E,G,H. The relationship between the first extraction (*Thalassiothrix* spp. related) opal records at the two sites is similar to that of the total opal records. Overall trends and minor peaks are again broadly similar, and total values of OPAL847 and $OPAL850_{STRETCHED}$ generally agree to within 5% in sections A-H. As with the total opal records, the records of first extraction opal diverge in sections I and J. The records of second extraction (radiolarian related opal) show the most consistent trend with $OPAL850_{STRETCHED}$ being around 5% greater than OPAL847 throughout the record.

This pattern of higher second extraction opal in OPAL850 compared to OPAL847 indicates that radiolarians form a consistently higher proportion of the export flux at Site 847 than in the more western area of the study region measured by Site 850. This pattern is enhanced by the generally higher silica contents measured at Site 850. Comparison of radiolarian occurrence per unit area of x20 BSEI photomosaics suggests that this pattern is the product of both increased numbers of radiolarian frustules in the sediments from Site 847 combined with a decrease in frustule dimensions at Site 850. The generally higher levels of *Thalassiothrix*. related opal measured at Site 850 can also be seen in the BSEI photomosaics. The sediments at Site 847 typically consist of mixed assemblage regions with thin layers of pure diatom mats (~90% *Thalassiothrix*). At Site 850 these layers of pure diatom mats are generally thicker and occur more frequently.

### 6.4.3 Patterns of radiolarian occurrence in the eastern Equatorial Pacific

Variations in upwelling intensity have been recorded both within and between sites in the eastern Equatorial Pacific using an 'upwelling radiolarian index' or URI (S. Haslett, pers. comm. and Haslett and Funnell, 1996). This index is calculated by quantifying the abundance of upwelling species relative to the entire radiolarian population and then summing the relative abundances (Nigrini and Caulet, 1992) and can be calibrated to thermocline depth (Haslett and Funnell, 1996). Between 1.79 and 1.9Ma, the URI values show that the thermocline at Site 847 was consistently shallower (~60m mean depth) than at Site 850 (~85m mean depth) indicating that upwelling was always stronger in the east of the region (Haslett and Funnell, 1996). The upwelling species are generally much larger than other species (S. Haslett, pers. comm) resulting in typically higher radiolarian related opal export at Site 847 compared to Site 850. This pattern of reduced radiolarian size in more western sites is consistent with reduction in radiolarian related opal between Site 847 and 850 identified in the high-resolution records of the '4.4Ma' LDM basal unit. This implies that the upwelling regime and longitudinal variation in thermocline depth during the deposition of the '4.4Ma'

LDM material were similar to the modern patterns, with both upwelling and thermocline depth decrease towards the west.

### 6.4.4 IMPLICATIONS FOR SEDIMENTATION RATES

The difference in spacing between the tie-point layers between the two sites indicates that the sedimentation rates at the two sites did not remain constant, although during the calculation of $OPAL850_{STRETCHED}$ the length-scale of OPAL847 was held constant. Comparison of the spacing of the tie-point layers indicates that the in the lower 250mm the sedimentation rate at Site 850 was generally lower than at Site 847 (Sections A-E). This consistent with results of lamina couplet measurements in the lower 100mm of the two records which show thicker couplets at Site 847, resulting in higher sedimentation rates of both *Thalassiothrix*-dominated and mixed assemblage than at Site 850 (see Section 5.3). In the upper 250mm of the basal unit, the sedimentation rate at Site 850 was generally higher than that at Site 847.

In this upper interval, the region with the largest differences in tie-point layer spacing (450-500mm above the base of the laminated material) coincides with Sections I and J (tie-points 21-25). This section is define by a strong increase in first extraction and total opal record of $OPAL850_{STRETCHED}$ over OPAL847 (values up to 40% greater). Conversely, between tie-points 18 and 19 where opal values are lower in $OPAL850_{STRETCHED}$ than OPAL847, the tie-point layer spacing denote a period with higher sedimentation rates at Site 847 relative to Site 850. Tie-points 16 and 18 have very similar spacing at the two sites (within 2mm), this region coincides with Section G which is characterised by closely matching opal records. The difference in relative opal content between individual tie-point layers is summarized in the final column of Table 6.3.

This relationship between relative opal content and relative sedimentation rate between the two sites suggests that variation in sedimentation rates of the upper 250mm of the basal unit were primarily controlled by opal flux. In contrast in the lower 250mm of the basal unit, the spacing of tie-point layers indicates that the sedimentation rate at Site 847 was consistently higher than at Site 850 although the latter had consistently higher opal contents. In the intervening region, 250-350mm above the base of the laminated section, there is no constant relationship.

## 6.5 CYCLICITIES WITHIN THE OPAL RECORDS

The opal records for the basal unit of the '4.4Ma' LDM depositional event from Sites 847 and 850 were tested individually for cyclic variations. To enable comparison of cycle frequencies

| Tie-point layer number (Defined in Table 6.1) | Height above base of LDM at Site 847 (in mm) | Tie-point layer spacing | | Relationship of sedimentation at Site 850 relative to Site 847 | Total opal content at Site 850 relative to Site 847 |
|---|---|---|---|---|---|
| | | Site 847 | Site 850 | | |
| 1 | 0 | | | | |
| 2 | 6.4 | 6.4 | 5.9 | similar | higher |
| 3 | 17.6 | 11.2 | 9.0 | lower | lower |
| 4 | 35.4 | 17.8 | 16.6 | similar | similar |
| 5 | 67.9 | 32.5 | 24.3 | lower | higher |
| 6 | 80.5 | 12.6 | 9.4 | lower | higher |
| 7 | 102.0 | 21.5 | 12.8 | lower | higher |
| 8 | 185.9 | 83.9 | 91.7 | higher | similar |
| 9 | 200.1 | 14.2 | 13.4 | similar | similar |
| 10 | 213.1 | 13.0 | 7.5 | lower | lower |
| 11 | 234.6 | 21.5 | 16.3 | lower | similar |
| 12 | 247.6 | 13.0 | 11.5 | lower | similar |
| 13 | 285.3 | 32.7 | 33.0 | similar | similar |
| 14 | 316.1 | 30.8 | 39.0 | higher | lower |
| 15 | 333.7 | 23.6 | 23.2 | similar | higher |
| 16 | 343.6 | 9.9 | 12.0 | higher | higher |
| 17 | 372.6 | 29.0 | 31.5 | similar | similar |
| 18 | 383.9 | 11.3 | 11.6 | similar | similar |
| 19 | 406.0 | 22.1 | 19.5 | lower | lower |
| 20 | 433.2 | 27.2 | 26.2 | similar | similar |
| 21 | 451.8 | 18.6 | 18.7 | similar | higher |
| 22 | 477.7 | 25.9 | 33.2 | higher | higher |
| 23 | 507.6 | 29.9 | 31.4 | higher | higher |
| 24 | 541.6 | 32.0 | 34.8 | higher | higher |
| 25 | 574.6 | 35.0 | 39.5 | higher | higher |

Table 6.3. Spacing of tie-point layers (defined in Table 6.1) located in BSEI photomosaics for basal unit of '4.4Ma' LDM deposits in ODP Sites 847 and 850. The effect of the difference in spacing on the relative sedimentation rate is given in the final column.

between sites, the power spectra must be calculated over similar length scales. This was achieved using $OPAL850_{STRETCHED}$ (defined by characteristic sediment layers, see Section 6.4.1). These results should be treated with caution since the interpretation of frequencies identified in the calculated power spectra assumes a constant sedimentation rate at Site 847 which cannot be proved. Correlation of characteristic sediment layers between Sites 847 and 850 identified relative changes in the sedimentation rates at the two sites (see Section 6.4.3), but could not isolate the actual changes at each site. The assumption of constant sedimentation at Site 847 is thought to be more realistic than assuming a constant sedimentation rate at Site 850 (the other possible option for simple interpretation) since upwelling is stronger at Site 847 and TIW activity decreases and becomes increasingly variable to the west (see Section 2.2.3). Site 850 also has a lower sediment thickness and hence lower calculated sedimentation rate for the overall '4.4Ma' LDM depositional period suggesting more variability between the sedimentation rates of diatom rich and nannofossil rich material (see Section 5.6).

At both sites the records of total opal, first and second extraction opal (measures of *Thalassiothrix* and non-*Thalassiothrix* related opal respectively, see Section 3.4.3) were tested separately, see Figure 6.11. Since the data points of the opal records are unevenly spaced, these records were analyzed using the Lomb Method for spectral analysis (Press *et al.*, 1992; see Appendix A3). This method both reduces potential errors related to interpolation processes and allows the identification of frequencies near and below the minimum sample frequency (Press *et al.*, 1992 and references therein). The dominant frequencies identified in each record and their statistical significance are summarized in Table 6.4. Frequencies are converted into core-length periodicities using the relationship frequency = 1/period.

### 6.5.1 Periodicities within high-resolution opal records

The power spectra for OPAL847 and $OPAL850_{STRETCHED}$ show strong peaks in the low frequency region below $0.03mm^{-1}$ (periodicities above ~30mm), see Figure 6.10 and Table 6.4, above this frequency there is only peak observed, at $\sim 0.9mm^{-1}$. This peak occurs at the 90% and 50% significance levels in Site 847 and weakly at Site 850 (see Figure 6.10) has a periodicity similar to that of the mean sample frequency. Although the Lomb method should allow the identification of such periodicities, sections of these data sets have relatively even spacing and it is likely that this peak is related to this artifact of the experimental process rather than an actual periodicity within the sediment. The relative weakness of this peak in $OPAL850_{STRETCHED}$ power spectra compared to those calculated from OPAL847 supports this conclusion. The original uneven spacing of the data points in OPAL850 was exaggerated during the calculation of $OPAL850_{STRETCHED}$, increasing the degree of

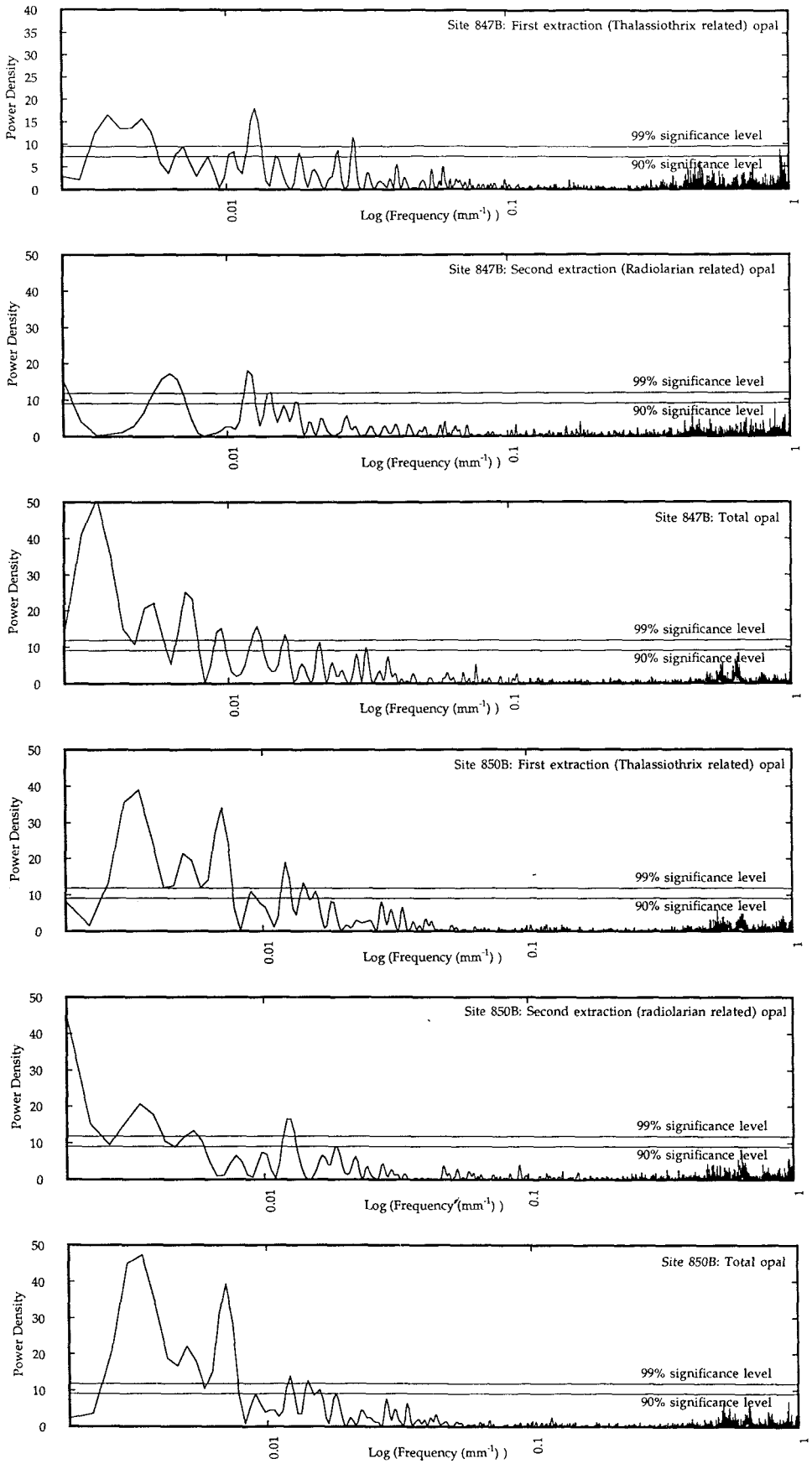


Figure 6.11. Power spectra with estimated significance levels for first, second and total opal records of OPAL847 and $OPAL850_{STRETCHED}$. Significant frequency peaks are summarized in Table 6.4.

| Frequency (mm-1) | Significance level | Opal record | Core-length periodicity (mm) |
|---|---|---|---|
| 0.0036-0.0037 | 99% | OPAL847(total) | 270-278 |
| | 99% | OPAL847(first) | |
| | 99% | OPAL850(total) | |
| | 99% | OPAL850(first) | |
| | 99% | OPAL850(second) | |
| 0.0052-0.0053 | 99% | OPAL847(total) | 188.7-192.3 |
| | 99% | OPAL847(first) | |
| | 99% | OPAL850(total) | |
| | 99% | OPAL850(first) | |
| | 99% | OPAL850(second) | |
| 0.0072-0.0074 | 99% | OPAL847(total) | 135.1-138.9 |
| | 99% | OPAL850(total) | |
| | 99% | OPAL850(first) | |
| 0.0092-0.0094 | 99% | OPAL847(total) | 106.4-108.7 |
| | 90% | OPAL850(total) | |
| | 50% | OPAL850(first) | |
| | 50% | OPAL850(second) | |
| 0.012-0.013 | 99% | All Records | 80.7-83.3 |
| 0.0142 | 99% | OPAL847(second) | 70.4 |
| | 95% | OPAL850(total) | |
| | 95% | OPAL850(first) | |
| 0.0158 | 99% | OPAL847(total) | 58.8-62.5 |
| | 95% | OPAL850(total) | |
| | 95% | OPAL850(first) | |
| 0.0282 | 50% | OPAL847(total) | 35.7 |
| | 99% | OPAL847(first) | |
| | 50% | OPAL850(total) | |
| | 50% | OPAL850(first) | |
| | 50% | OPAL850(second) | |
| 0.927-0.946 | 90% | OPAL847(total) | 1.1 |
| | 50% | OPAL847(first) | |

Table 6.4. Dominant frequencies identified in high- resolution measurements of opal content for the basal unit (600mm thick) of the '4.4Ma' LDM depositional event in ODP Holes 847B and 850B. The opal record in which each peak was identified is also given. Temporal periodicity calculated assuming a sedimentation rate of 390m/Ma, see text for discussion. See Figure 6.11 for power spectra with estimated significance levels.

randomization of the sample spacing and thus reducing the effect of the mean sample frequency.

There are three dominant frequencies clearly defined at both sites, 0.0036-0.037, 0.0052-0.0053 and 0.016-0.017mm$^{-1}$, see Figure 6.10. Of these frequencies only 0.012-0.013mm$^{-1}$ is found in all the records from both sites. No frequency is found at only one site although in some cases a frequency may be strong at one site but weak at the other (e.g. 0.0282mm$^{-1}$). The 0.0036-0.0037mm$^{-1}$ frequency has a core-length period of 270-278mm, i.e. the basal unit contains around two complete cycles. This pattern can be seen as the underlying trend to the total and first extraction opal records of OPAL847 and OPAL850$_{STRETCHED}$ seen in Figure 6.8. The lowest frequency peak occurs at 0.0282mm$^{-1}$ it is strongest in OPAL847(first) occurring at the 50% level in the power spectra for OPAL850$_{STRETCHED}$. This frequency has a length scale of ~36mm, similar to that of the region A-I defined on the basis of trends and differences between the opal records at the two sites (Section 6.4.2).

### 6.5.2 Investigating the difference between the two opal records

In order to further investigate the variation between the two opal records, the difference between OPAL847 and OPAL850$_{STRETCHED}$ was calculated (DIFFOPAL). The variation in DIFFOPAL was also tested for cyclic variations using spectral analysis. The dominant frequencies isolated in the DIFFOPAL records are summarized in Table 6.5. Core-length and temporal periodicities are also given. As in Table 6.4 temporal periodicities are estimated assuming a sedimentation rate of 390m/Ma.

| Frequency peak (mm$^{-1}$) | Significance level | Opal record | Periodicity (mm) |
|---|---|---|---|
| 0.0034 | | DIFFOPAL(second) | 294.1 |
| 0.0050 | | DIFFOPAL(total) | 200 |
| 0.0072-0.0074 | | All records | 135.1 |
| 0.0092-0.0094 | | All records | 102.0 |
| 0.0142 | | DIFFOPAL(total) | 70.4 |
| 0.0158 | | DIFFOPAL(second) | 64.9 |
| 0.0178 | | DIFFOPAL(second) | 56.2 |

Table 6.5. Summary of dominant cyclicities in power spectra of difference between total opal records for the '4.4Ma' LDM depositional event basal unit, see Figure 6.12. Temporal periodicity calculated assuming a sedimentation rate of 390m/Ma, see text for discussion.

The resulting power spectra identify strong cyclicities in the low frequency region of the power spectrum, periodicities are typically occur with core lengths of over 50mm, below this period the power spectra are consistently low. Dominant frequencies at 0.0072-0.0074 and 0.0092-0.0094mm$^{-1}$ are found in both the total opal (and also the first extraction opal) and second extraction opal records. These frequencies are similar to those found in OPAL847 and

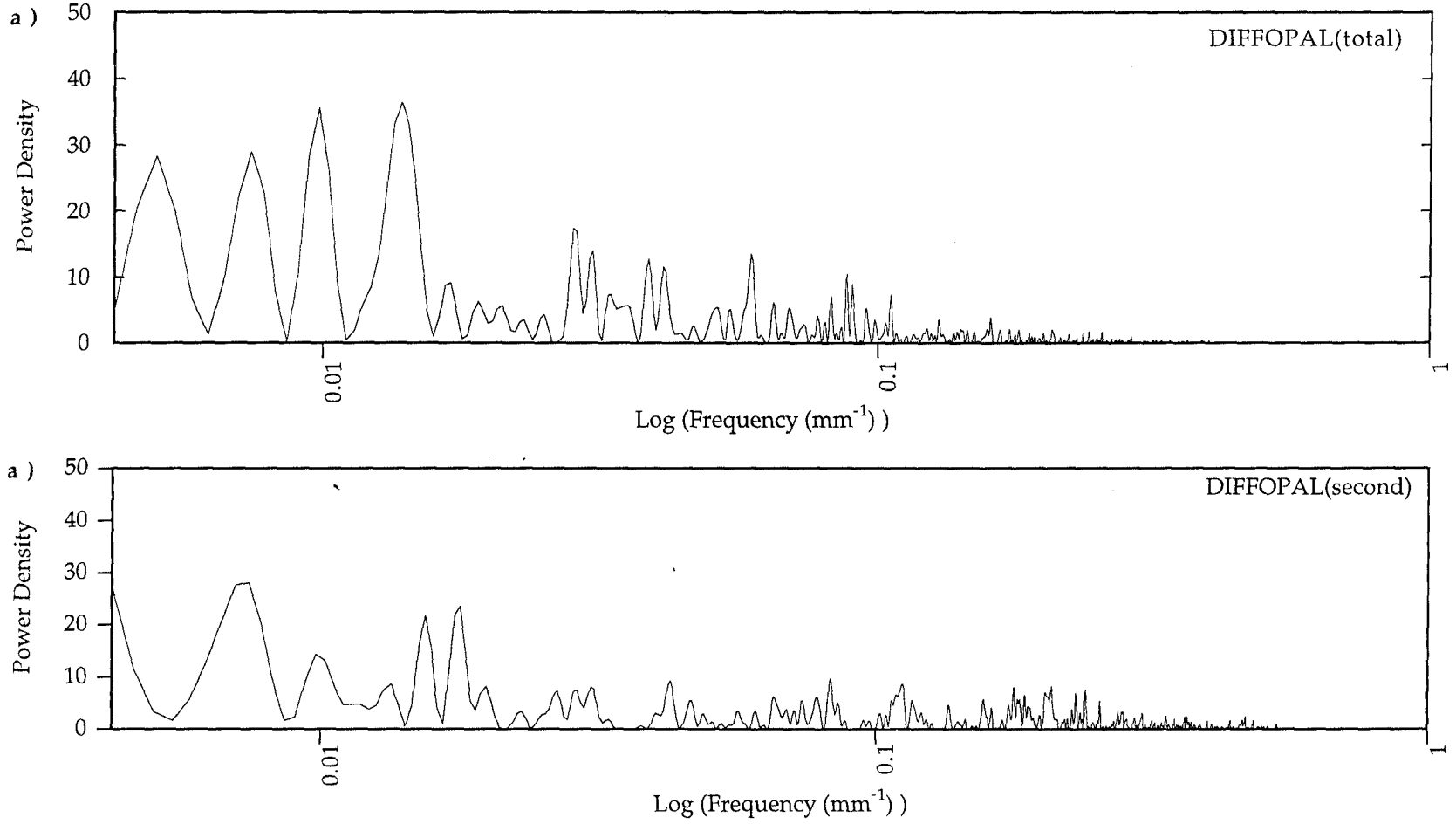


Figure 6.12. Power spectra of DIFFOPAL for a) total opal, and b) second extraction opal. As the record for DIFFOPAL(first) is effectively identical to DIFFOPAL(total) only the DIFFOPAL(total) power spectra is given here.

OPAL850. The 0.0072-0.0074mm$^{-1}$ frequency peak occurs strongly in all records of OPAL850 but only in the total opal record at Site 847. A similar pattern is associated with the 0.0092-0.0094 frequency which occurs strongly in OPAL847(total) but only at the 90% level in OPAL850(total). In the second extraction records the 0.0092-0.0094mm$^{-1}$ frequency occurs at the 95% level at Site 850 but below the 50% significance level at Site 847. In the power spectra of DIFFOPAL (second) this frequency is also weaker than in DIFFOPAL(total). Other frequencies in the DIFFOPAL power spectra are also related to frequency peaks occurring more strongly at one site than the other. Significance of the identified cyclicities will be discussed in more detail Section 6.6 alongside discussion of cyclicities identified in the opal records.

### 6.5.3 Estimation of temporal periodicities

Temporal periodicities are estimated from these core-length periodicities using an estimated sedimentation rate. Results of these calculations should be regarded as correct only to within an order of magnitude since the spacing of tie-point layers indicates relative sedimentation rates may vary by up to ~70% (for example between Tie-points 13 and 14). The use of a mean sedimentation rate is justified since the power spectra are calculated over the entire length of the opal records. To give a first-order estimate of the time-periods associated with identified core-length periodicities a sedimentation rate of 390m/Ma is used. This rate is based on lamina couplet measurements of the '4.4Ma' LDM basal unit at Sites 847 and 850, and sedimentary helium concentrations for the lower 50mm of the unit at Site 847 (see Section 5.6). The resulting estimates of temporal periodicities are given in Table 6.6

| Frequency (mm-1) | Core-length periodicity (mm) | Temporal periodicity (yrs) |
|---|---|---|
| 0.0034-0.0036 ‡ | 270-278 | 692-713 |
| 0.0052-0.0053 ‡ | 188.7-192.3 | 483.8-493.1 |
| 0.0072-0.0074 | 135.1-138.9 | 346.5-356.6 |
| 0.0092-0.0094 | 106.4-108.7 | 272.8-278.7 |
| 0.0124-0.0128 ‡ | 80.7-83.3 | 206.9-213.9 |
| 0.0142 | 70.4 | 180.6 |
| 0.0158 | 63.3 | 162.3 |
| 0.0178 | 56.2 | 144.1 |
| 0.0282 | 35.7 | 91.5 |

Table 6.6. Time periods associated with core-length periodicities identified using power spectra of OPAL847 and OPAL850STRETCHED. The strongest frequency peaks are denoted by '‡' in the frequency column.

These calculations estimate periodicities within the opal record with time-scale ranging from 90-700yrs, with the strongest periodicities as ~700 yrs, ~490yrs and ~210yrs.

### 6.5.4 CLIMATE CYCLES WITH PERIODS OF 90-700 YEARS

Climate cycles with periods of 90-700 years have been identified in a number of long term climate and natural proxy climate records, see Table 6.7. Climate variations on these scales are commonly attributed to sunspot cycles. In recent years, links between solar index and global weather patterns have been increasingly well documented but are still very poorly understood (e.g.Kerr, 1990). Temperature records from the last ~200 years correlate with the Gleissberg solar activity periods (80-90 year periods, Willet, 1987). Periods of minimal sunspot activity are reflected in periods of low terrestrial temperatures, whereas periods maximum temperature appear to precede periods of elevated sunspot activity (Willet, 1987).

Periods of minimal sunspot activity have been correlated with periods of maximum $^{14}C$ production (measured from tree-rings) and fluctuation in the $^{10}Be$ content of ice cores, these periods appear to correlate with periods of terrestrial climate cooling ( e.g. Sonett, 1984; Attolini *et al.*, 1988; Beer *et al.*, 1988; Stuvier and Braziunas, 1988; Stuvier and Braziunas, 1989). Spectral analysis of the Holocene $^{14}C$ record for tree rings and $^{10}Be$ from ice cores suggests quasi-periods at 50-70, 130, 140, 200-220 and 420 years (Beer *et al.*, 1988; Stuvier and Braziunas, 1989). Superimposed over the high frequency solar rhythms are prolonged minimums of sunspot activity also recorded in the $^{14}C$ records (e.g. Stuvier and Braziunas, 1988). These appear to be correlated to climate cooling phases (e.g. the Oort Minimum, AD 1010-1050; the Wolf Minimum, AD 1280-1340). These minima are neither evenly spaced nor uniformly long suggesting that they are not simple, periodic functions of solar activity (Stuvier and Grootes, 1980; Stuvier and Quay, 1980; Eddy, 1988).

There are also several planetary-solar relationships have periodicities within the 90-700 year time-scale which may force variation in global climate pattern; a 178 year 'King-Hele' cycle (or All Planet Synod); ~180 year Saturn-Jupiter repeat cycle; and, a 556 year progression for the lunar Perigee (Fairbridge, 1984). These orbital cycles affect the barycentre (centre of mass) of the solar system, forcing the Sun into an orbit around the mean barycentre. This solar orbit affects the position of individual planets relative to the sun, and thus the energy reaching them (Fairbridge, 1984). Periodicities of similar timescale to these extra-terrestrial forcing functions have been report from a number of lake deposits, but few studies have had enough control to test the correlation rigorously (Glenn and Kelts, 1991).

### 6.5.5 INTERPRETATION OF CYCLES IDENTIFIED IN HIGH-RESOLUTION OPAL RECORDS

The uncertainty in the temporal periodicities identified in the high-resolution opal records (related to the level of uncertainty in the sedimentation rates) mean that it is impossible to draw any firm conclusions as to the factors influencing silica exports. However, the periodicities in the opal records are of a similar order of magnitude to those associated with sun-spot cycles and solar-planetary periodicities. The strong ~210 year periodicity identified

| Reference | Record | Periodicity (years) |
|---|---|---|
| Halfman and Johnson (1988) | Recent laminated sediments in Lake Turkana, Kenya | 78 |
| Gleissberg (1958), Feynman (1982) | Gleissberg solar cycle | 80-90 |
| Anderson and Koopmans (1969) | Pleistocene laminated sediments in Lake Superior and Steep Rock Lake, Ontario | 80-90 |
| Stuvier and Braziunuas (1989) | C-14 in tree rings | 85 |
| Anderson and Kirkland (1970) | Jurassic laminations in Toldito Formation, Mexico | 85 |
| Fairbridge and Saunders (1987) and references therein | Lunar-Nodal Perihelion | 93 |
| Stuvier and Quay (1987), Schove (1983) | Sunspot cycle | 123 |
| Halfman and Johnson (1988) | Recent laminated sediments in Lake Turkana, Kenya | 100 |
| Stuvier and Braziunuas (1989) | C-14 in tree rings | 130 |
| Attolini et al. (1988) | Auroral | 130 |
| Sonett (1984), Stuvier and Braziunuas (1989) | C-14 in tree rings | 140 |
| Halfman and Johnson (1988) | Recent laminated sediments in Lake Turkana, Kenya | 165 |
| Anderson and Kirkland (1960) | Jurassic laminations in Toldito Formation, Mexico | 170 & 180 |
| Fairbridge and Saunders (1987) and references therein | King-Hele (All Planet Synod) and Saturn-Jupiter Repeat | 179 |
| Fairbridge and Saunders (1987) and references therein | Mauder Minimum-type interval of low sun-spot activity | 180 |
| Stuvier and Braziunuas (1989) | C-14 in tree rings | 180 |
| Sonett (1984) | C-14 in tree rings | 200 |
| Beer et al. (1988) | Be-10 in ice cores | ~200 |
| Schove (1983) | Sunspot cycle | 200 |
| Agterberg and Banerjee (1969) | U. Pleistocene laminated sediments in Lake Barlow-Ojibway, N. Ontario | 200 |
| Anderson (1986), Anderson and Kirland (1969a, b) | L. Pleistocene laminated sediments of Rita Blanca Formation, Texas | 200 |
| Walanus (1989) | Recent laminated sediments in Gosciaz Lake, Poland | 200 |
| Halfman and Johnson (1988) | Recent laminated sediments in Lake Turkana, Kenya | 200 |
| Fairbridge and Saunders (1987) and references therein | Spörer Minimum-type interval of low sun-spot activity | 220 |
| Stuvier and Braziunuas (1989) | C-14 in tree rings | 220 |
| Halfman and Johnson (1988) | Recent laminated sediments in Lake Turkana, Kenya | 270 |
| Stuvier and Braziunuas (1989) | C-14 in tree rings | 420 |
| Fairbridge and Saunders (1987) and references therein | Lunar Perigee | 556 |

Table 6.7 Compilation of potential external forcing frequencies in the range 70-900 years and examples of frequencies reported from climate proxies.

in the opal records correlates well with the 200 year sun-spot cycle identified in $^{14}C$ records and in a number of laminated lake sediments (see Table 6.7), while the weaker ~90 year cycle correlates with the 80-90 year periodicity of the Gleissberg cycle also identified in $^{14}C$ and lake sediments. Cycles of 130-140 years, similar to the ~140 periodicity in the opal records, have been found in the $^{14}C$ records and the ~180 year periodicity in the opal records correlates with the 179-180 solar-planetary cycles as well as $^{14}C$ and lake records, see Table 6.7.

## 6.6 SUMMARY OF HIGH-RESOLUTION RESULTS

The millimetre-scale sampling possible through LDM intervals enables the construction of quasi-annual resolution records silica fluxes to the deep ocean. Correlation of the records from the basal unit of the '4.4Ma' LDM depositional event at Sites 847 and 850 show a remarkable similarity indicating that the same depositional mechanism functioned along the Equatorial Front for lateral distances of over 2000km. Spectral analysis of the biogenic opal content records at the two sites also demonstrates the existence of cyclicities affecting this depositional mechanism with century-scale periods. Although no firm correlation with individual external forcing frequencies is possible (due to the uncertainties in sedimentation rates) the periodicities within the biogenic opal records have timescales that suggest the influence of extraterrestrial forcing mechanisms such as sun-spot variability and solar-planetary cycles.

# CHAPTER 7: IMPLICATIONS FOR GLOBAL BIOGEOCHEMICAL CYCLING

## 7.1 INTRODUCTION

In the modern oceans the distribution of silica in the different waters masses is governed by the biogeochemical silica cycle as illustrated in Figure 7.1. The majority of dissolved silica is derived from the products of chemical weathering of exposed rocks carried to the ocean surface via rivers. Other, much smaller additions are derived from dissolution of aeolian material reaching the surface ocean, and from hydrothermal fluids at mid-ocean ridges and weathering of submarine basalt. Biological uptake in the formation of siliceous skeletons of diatoms and radiolarians and subsequent sinking and burial, forms the most important sink in the global silica cycle. There is also some evidence of minor abiological uptake by clay alumino-silicates during the mixing of fresh and saline waters in estuarine environments (Burton *et al.*, 1970; Wollast and DeBroeu, 1971). Biogenic silica uptake is dominated by two planktonic types, the primary producers (diatoms, silicoflagellates and chrysophytes) and the protozoan radiolarians. Siliceous sponges are only locally important. Within these two groups, diatoms are the major silica users, comprising 70-90% of suspended biogenic silica in the world ocean (Lisitzin, 1972).

In this chapter, the fluxes of dissolved silica and organic carbon related to LDM deposits are estimated and compared to both modern fluxes and those associated with similar diatom rich-deposits from the Atlantic and Mediterranean. The effect of such fluxes on global silica cycling and possible sources of available silica are discussed. The laminated sediments found in the eastern Equatorial Pacific represent massive removal of silica and $CO_2$ from the world ocean over 100ka timescales (see Chapter 5). The calculated ocean residence time for both dissolved silica and organic carbon is by far exceeded by the removal represented by these sediments. Evidence is presented suggesting that the deposition of LDM material is associated with periods of increased dissolved silica availability.

## 7.2 BIOGENIC SILICA EXPORT FLUXES DURING LDM DEPOSITIONAL EVENTS

### 7.2.1 METHODS OF FLUX CALCULATION

Estimates for silica export fluxes are based on the bulk accumulation rate, derived from the regional sedimentation rate and sediment dry bulk density, and the relative proportion of

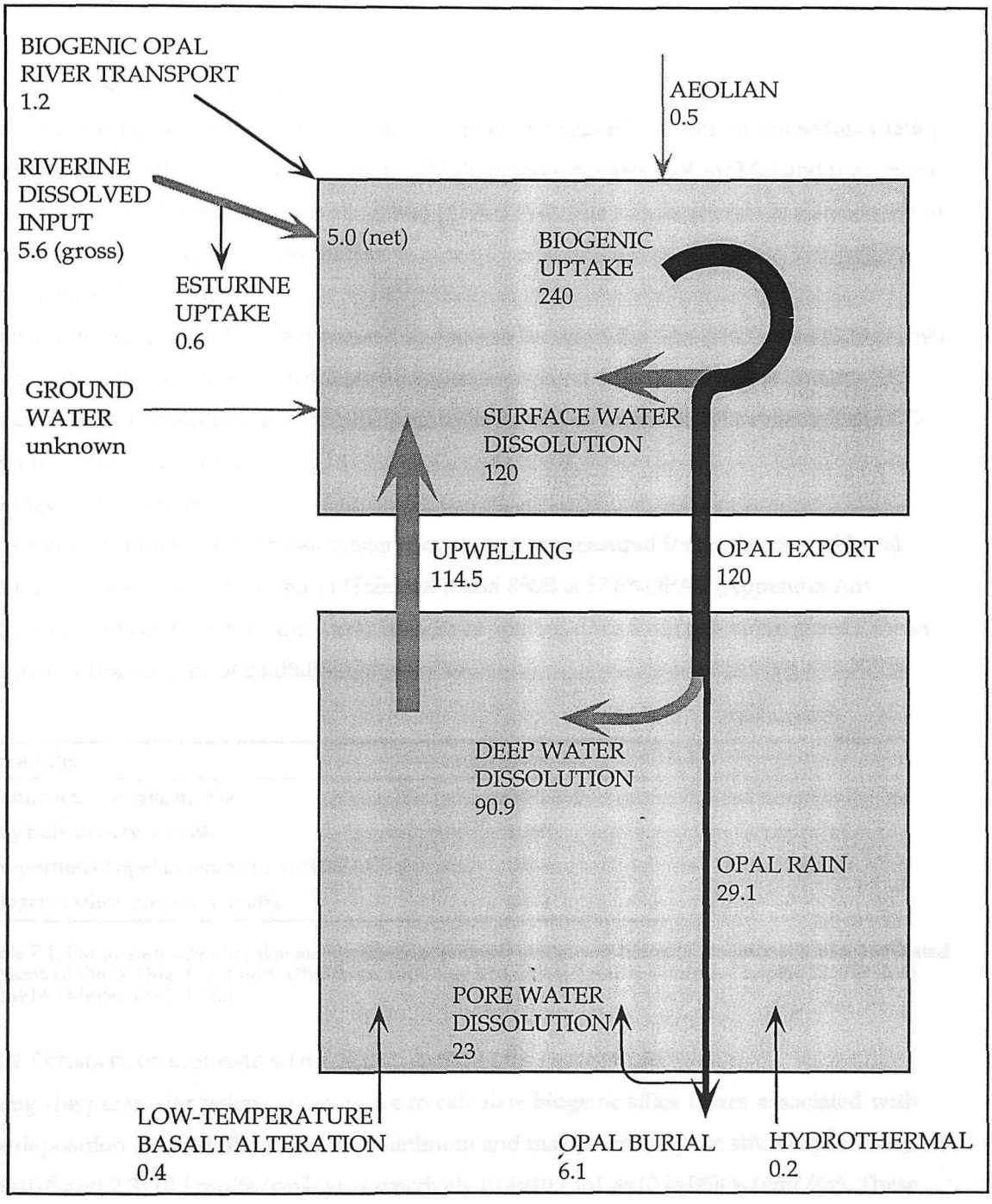


Figure 7.1. Tentative global silicon cycle (fluxes in Tmol Si/yr). Black lines indicate biogenic opal, grey lines dissolved silica. Modified from Tréguer et al (1995) with additional data from Tréguer et al (1996).

biogenic opal making up the sediment. The values for these parameters used in the following biogeochemical flux calculations are discussed below and summarized in Table 7.1.

a) Regional sedimentation rates

Estimates for regional sedimentation rates are given in Section 5.6.1. Minimum sedimentation rates for laminated sediments taken from GRAPE based estimates (204 m/Ma) and maximum rates from the $He^3$ based estimation method (410m/Ma). The maximum rate is also consistent with laminae couplet based estimates.

b) Dry bulk density (DBD)

Controls on sediment DBD are discussed in detail in Section 5.5.1. The DBD value (0.39g/$cm^3$) used in the calculation of biogeochemical fluxes associated with laminated sediments is taken from DBD measurements of laminated sections of the '4.4Ma' LDM deposits (from CD Rom in Mayer *et al.*, 1992).

c) Biogenic opal content

In laminated sediments the mean biogenic opal content measured for the laminated basal section of the '4.4Ma' LDM unit in Holes 847B and 850B is 57.6%OPAL (Appendix A8). Removing the correction for the water content of opaline silica from this value gives a mean biogenic silica content of 24.0%BSi.

| Parameter | Estimate |
|---|---|
| Sedimentation rate, m/Ma | 204-410 |
| Dry bulk density, g/$cm^3$ | 0.39 |
| Proportion of opal in sediment, wt%OPAL | 57.9 |
| Biogenic silica content, wt%BSi | 24.0 |

Table 7.1. Parameters used to calculate minimum and maximum export fluxes of biogenic silica for laminated sections of the '4.4Ma' LDM unit. DBD from ODP Leg 138, Initial Results Volume, Chapter 12, CD Rom Table14 (Mayer *et al.* 1992)

### 7.2.2 ESTIMATE OF BIOGENIC SILICA FLUX DURING LDM DEPOSITION

Using the parameter values given above to calculate biogenic silica fluxes associated with the deposition of LDM material, gives minimum and maximum biogenic silica export fluxes of $6.8x10^{-5}$ and $2.3x10^{-4}$ molSi/$cm^2$/yr respectively ($0.4x10^{-2}$ to$1.4x10^{-2}$g$BSiO_2$/$cm^2$/yr). These values do not include the component of biogenic silica removed from the surface waters but dissolved in the water column and surface sediments. Given the levels of dissolution observed in laminated sediments it can be estimated that this net flux represents around 60-80% of the gross (or original) flux (see Section 4.4.4). Correcting the flux estimates to include the dissolved fraction gives a total flux from the surface waters of 0.81-$3.8x10^{-4}$molSi/$cm^2$/yr (equivalent to 0.5-$2.3x10^{-2}$g$BSiO_2$/$cm^2$/yr), see Section 4.4.4.

These estimates exceed most biogenic silica flux estimates, measured using sediment traps, by one to three orders of magnitude (Table 7.2). Higher fluxes, comparable to those calculated for the LDM deposits, are measured in the Gulf of California (Thunell *et al.*, 1994), Bransfield Strait, Antarctica (Wefer, 1989), below the Polar Front in the Southern Ocean ($10^{-4}$molSi/ $cm^2$/yr, Rabouille *et al.* 1997) and the tropical Pacific (1-11°N, ~140°W, Dymond and Collier, 1988). The LDM sediments are exceptional in their preservation of these opal fluxes. Typically only about 20% of the biogenic material reaching the sea-floor accumulates in the sediments, the remainder returning to the water column through dissolution and diffusion (Tréguer *et al.*, 1995 and references therein). In LDM sediments the proportion of opal retained in the sediments is about 60-80%.

### 7.2.3 Areal extent of biogenic silica flux

The areal extent of LDM deposits in the eastern Equatorial Pacific is estimated using the locations of LDM bearing ODP and DSDP Sites. The '4.4Ma' LDM depositional event is found at Sites 572, 847, 849 and 850 where these sediments consistently 10-13m thick. There is also a 1.5cm thick layer of LDM at Site 574 deposited during time interval. This suggests that during the '4.4Ma LDM depositional event, Site 574 was situated as the edge of the LDM depositional area. The relative locations of sites containing the '4.4Ma' LDM deposits suggest that Site 574 was on both the northern and western edges of the LDM depositional area. Assuming that this 1.5cm thick layer represents the more westerly limit of the basal unit (60cm thick at the other sites), the minimum volume of LDM deposits accumulated in the basal unit can be estimated assuming a linear decrease in LDM sedimentation between Site 572 and Site 574 (Fig. 7.2). To take into account the movement of sites through sea floor spreading the site locations are backtracked to their positions during this period.

The maximum latitudinal extent is estimated using the lack of LDM deposits at ODP Sites 848 and 846 to either side of the LDM bearing sites (Fig. 7.2). To the west, sedimentation rates are assumed be consistently high, dropping sharply in sediments immediately adjacent to Site 574. To the east, LDM deposition is assumed to occur up to the Galapagos Islands at 98.5°W. To the east of the Galapagos Islands, the Equatorial Front has a different structure to that observed to the west. In the eastern section of the front, warmer water from the north is prevented from overriding the colder water by opposing wind patterns. Hence, the frontal deposition model (Section 2.4.2) would not function and LDM deposition should not occur in this region. The depositional areas discussed above are summarized in Table 7.3.

These estimated areas of LDM deposition are consistent with the modern extent of TIW activity in this region. TIW activity increases convergence rates across the Equatorial Front (Fig. 7.3 and Section 2.2.3.1). In the frontal deposition model, increased convergence rates

| Location | Trap depth (m) | Depth above seafloor (m) | Biogenic silica flux ($BSiO_2$) | | Reference |
|---|---|---|---|---|---|
| | | | (mol/cm2/yr) | g/cm2/yr | |
| **Eastern Equatorial Pacific, LDM sedimentation** | | | **0.49-2.0 x10-4** | **0.29-x1.2-2** | **This study** |
| **Mediterranean sapropel S-5** | | | **2.3x10-4** | **1.4 x10-2** | **This study** |
| South Pacific, Station P 50°N 145°W | 3800 | 520 | 3.2 x10-5 | 1.9 x10-3 | Honjo (1984) |
| Lofoten Basin, Arctic Ocean 69.5°N10°E | 2761 | 400 | 1.8 x10-6 | 1.1 x10-4 | Honjo *et al*, in Wefer (1989) |
| Bear Island, Arctic Ocean 75.9°N 11.5°E | 1700 | 418 | 3.3 x10-6 | 2.0 x10-4 | Honjo *et al.* (1987) |
| Norway Abyssal Plain 65.5°N 1°E | 2630 | 428 | 2.8 x10-6 | 1.7 x10-4 | Honjo *et al.* (1987) |
| W. Norwegian Sea 70°N 2.9°W | 2749 | 520 | 2.3 x10-6 | 1.4 x10-4 | Honjo *et al.* (1987) |
| Fram Strait 70.9°N 1.4°E | 2442 | 381 | 1.0x10-6 | 6.0 x10-5 | Honjo *et al.* (1987) |
| Greenland Basin 74.6° 6.7°W | 2823 | 622 | 4.3 x10-6 | 2.6 x10-4 | Honjo *et al.* (1987) |
| Bransfield Strait, Antarctica 62.2°S 34.7°W | 1588 | 364 | 6.5 x10-4 | 3.9 x10-2 | Wefer *et al.* (1988) |
| Weddell Sea 62.5°S 34.7°W | 863 | 3017 | 4.8 x10-7 | 2.9 x10-5 | Fischer *et al.* (1988) |
| Tropical Pacific, Site C 1°N 139°W | 3495 | n.d. | 1.2 x10-5 | 7.0 x10-4 | Dymond and Collier (1988) |
| Tropical Pacific, Site C 1°N 139°W | 2908 | n.d. | 2.7 x10-5 | 1.6 x10-3 | Dymond and Collier (1988) |
| Tropical Pacific, Site S 11°N 140°W | 3400 | n.d. | 6.5 x10-5 | 3.9 x10-4 | Dymond and Collier (1988) |
| Eastern Equatorial Pacific, 0° 140°W | 3618 | n.d. | 5.7 x10-6 | 3.4 x10-4 | Honjo *et al* (1996) |
| Gulf of California<br>Guaymas Basin<br>Carmen Basin | <br>n.d.<br>n.d. | <br>500<br>500 | <br>1.5 x10-4<br>1.2 x10-4 | <br>1.1 x10-2<br>9.1 x10-3 | Thunnell *et al.* (1994) |
| California Current, 42°N 126°W | n.d. | n.d. | 8.7x10-6 | 5.2x10-4 | Lyle *et al.* (1992) |
| California Current, 42°N 132°W | n.d. | n.d. | 3.0x10-6 | 1.8x10-4 | Lyle *et al.* (1992) |
| Bering Sea, 58°N 179°E | 3137 | n.d. | 2.8x10-5 | 1.7x10-3 | Honjo *et al.* (in preparation) |
| Sea of Okhotsk, 53°N 149°E | 1061 | n.d. | 2.0x10-5 | 1.2x10-3 | Honjo *et al.* (in preparation) |
| North Atlantic, 34°N 21°W | 1000<br>2000<br>n.d. | n.d.<br>n.d.<br>700 | 2.4 x10-6<br>3.0 x10-6<br>3.0 x10-6 | 1.4 x10-4<br>1.8 x10-4<br>1.8 x10-4 | Honjo and Manganini (1992) |
| North Atlantic, 48°N 21°W | 1000<br>2000<br>n.d. | n.d.<br>n.d.<br>700 | 5.3 x10-6<br>7.6 x10-6<br>8.3 x10-6 | 3.1 x10-4<br>4.6 x10-4<br>5.0 x10-4 | Honjo and Manganini (1992) |
| Sargasso Sea, Equatorial Atlantic | 150 | n.d. | 4.8 x10-6 | 2.8 x10-4 | Brzezinksi and Nelson (1995) |
| Sargasso Sea, Equatorial Atlantic | 3700 | n.d. | 2.2-5.4 x10-6 | 1.3-3.3 x10-4 | Deuser *et al.* (1995) |
| Santa Monica Basin | 100-135 | n.d. | 4.1 x10-5 | 2.5 x10-3 | Landry *et al.* (1992) |

Table 7.2 Biogenic silica fluxes measured using sediment traps compared to flux associated with LDM deposition in the eastern Equatorial Pacific and the Mediterranean sapropel S-5.

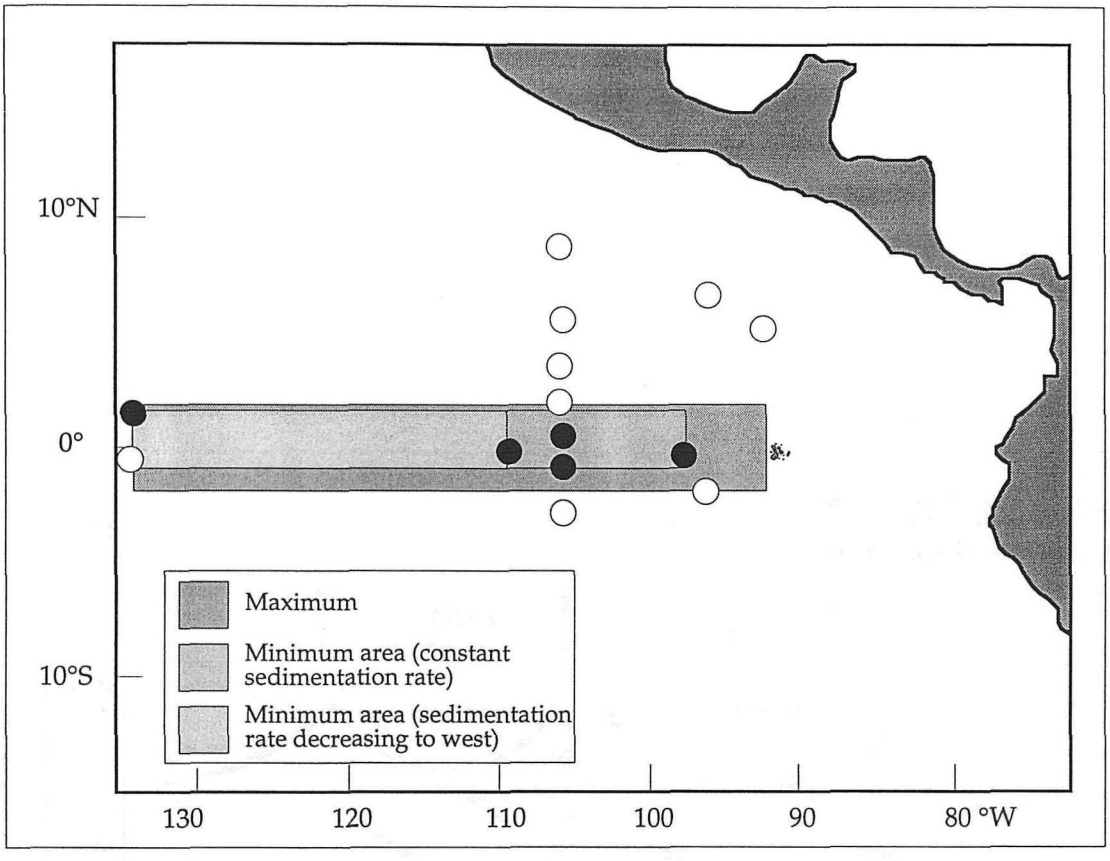


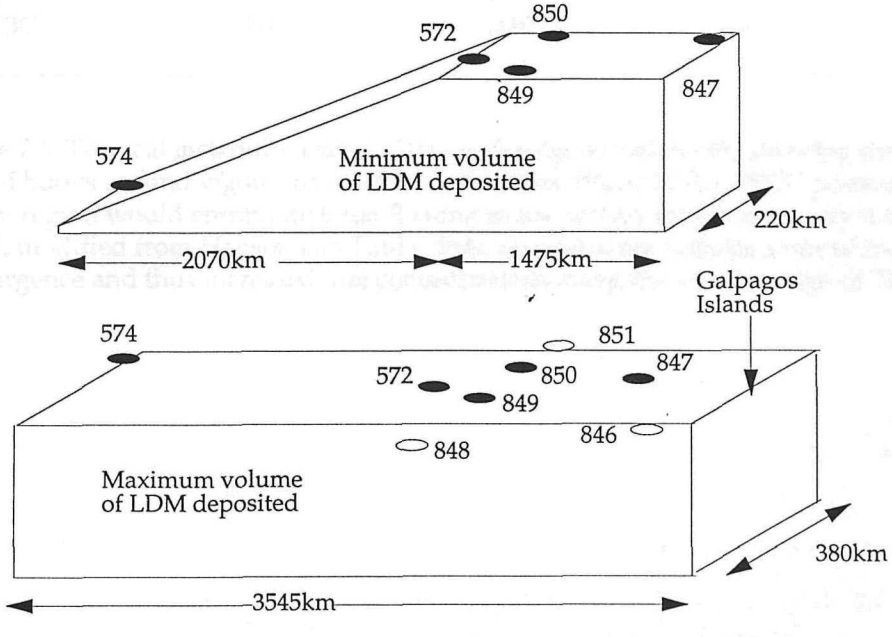


Figure 7.2. Estimated minimum and maximum areal extent of LDM material deposition, see text for rationale of limits to LDM deposition. Site locations are backtracked to their position during the '4.4Ma' depositional period following Duncan and Clague, 1985). Solid symbols denote sites containing '4.4Ma' LDM deposits.

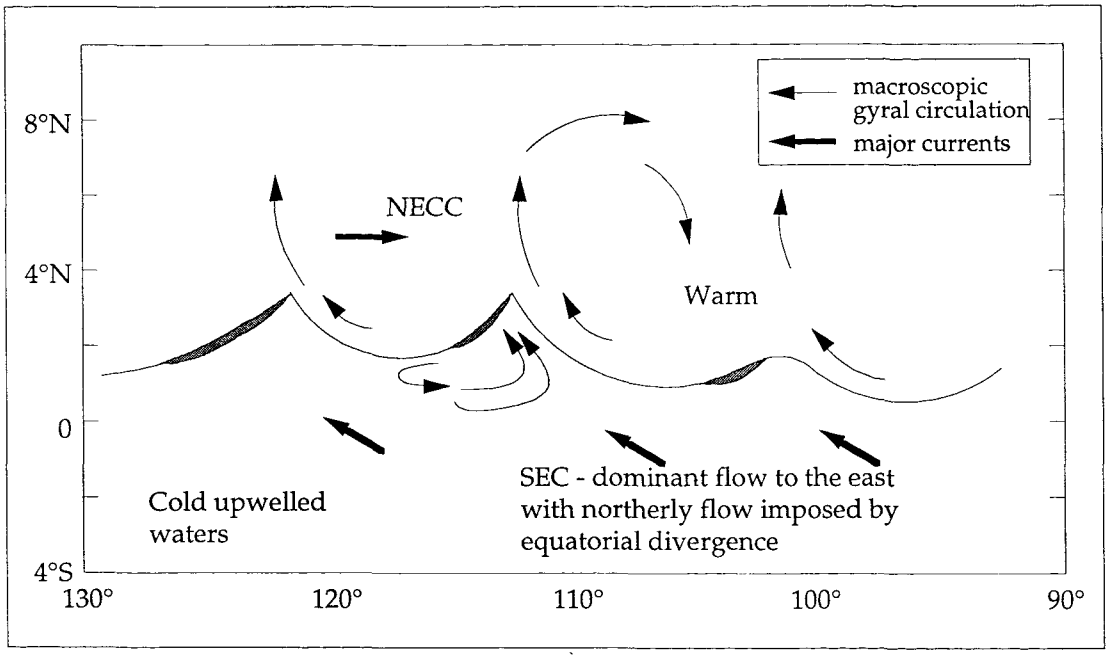


Figure 7.3. Tropical instability waves (TIW) in the Equatorial Pacific showing the direction of drift of buoys around vigourous macroscopic eddies. Water in the NECC passing along the frontal region would entrain material floating in the surface waters and carry it as far as 8-9°N, modified from Hanson and Paul (1984). Shaded areas indicate areas of increased convergence and thus increased mat concentrations along the western edge of TIW peaks.

result in increased concentrations of diatom mats in the surface waters. Currently TIWs typically occur between 90° and 130°W, occasionally reaching as far as 170°W (Legeckis *et al.*,1983; Perigaud, 1990). This westerly limit of frequent TIW activity is consistent with the minimal LDM deposits in DSDP Sites 573 and 574, at 130°W (Weinreich and Theyer, 1985). In the north-south direction TIW activity typically occurs over 3-4 degrees latitude (Legeckis *et al.*, 1983; Yoder *et al.*, 1994), coinciding with the lack of LDM deposits at ODP Sites 848 and 851 to either side of the LDM bearing Sites, see Figure 7.2. The effect of increased biosiliceous sedimentation in non-laminated sediments related to northerly advection of material from the frontal region (see Section 7.5.1) is not included in these calculations.

| | Minimum depositional area | Maximum depositional area |
|---|---|---|
| East-west extent (km) | Site 847to Site 572, constant LDM thickness - 1475km<br>Site 572 to Site 574, linear decrease in LDM thickness - 2070km | Site 574 to Galapagos Islands - 3545km |
| North-south extent (km) | Site 847 to Site 849 - 220km | Site 851 to Site 846 - 380km |
| Depositional area ($km^2$) | constant LDM thickness - $3.2x10^5$<br>LDM thickness decreasing to west - $4.6x10^5$ | $1.4x10^6$ |

Table 7.3. Minimum and maximum areal extent of LDM deposition during the '4.4Ma' LDM deposition event.

### 7.2.4 Duration of LDM deposition

The duration of LDM deposition can be estimated by comparing the GRAPE record of sites containing the '4.4Ma' LDM event with that of Site 851, which does not (Section 5.2.3). This comparison shows that these LDM sediment packets (10-13m thick) were deposited over around 59k.y. The '4.4Ma' event basal unit is 60cm thick and has an estimated sedimentation rate of between 204 and 410m/Ma (Section 5.6.1). These figures indicate that the basal unit was deposited over 1.46k.y. to 2.94k.y. Following this, LDM deposition continued episodically resulting in laminated sections typically 1-10cm thick. Using the sedimentation rate assumed for the basal unit, these episodic LDM deposition periods had durations of about 20-200years over the next 57k.y.

### 7.2.5 Regional estimates of LDM deposition

Regional biogenic silica flux associated with the '4.4Ma' LDM event for the maximum depositional area is calculated using the flux per unit area and regional extent given above (Sections 7.2.2 and 7.2.3). Since the minimum depositional area included a region of variable sedimentation rates, the minimum regional biogenic silica flux is calculated from the estimated volume of the '4.4Ma' LDM basal unit (Fig. 7.2). This unit is 60cm thick at Sites 572, 847, 849 and 850 and 1.5cm thick at Site 574. The minimum volume for the '4.4Ma' LDM basal unti can be calculated using these thicknesses. Dividing this volume by the minimum

area of LDM accumulation and depositional period for the basal unit gives regional sedimentation rates of 145.2-292.5m/Ma. Combining these sedimentation rates with mean biogenic silica content and DBD gives minimum regional biogenic silica flux of 0.38-0.76TmolSi/yr.

LDM volume = volume of constant thickness + volume of decreasing thickness area
$= 1.92 \times 10^{17} + (6.9 \times 10^{15} + 1.34 \times 10^{17})\ cm^2$
$= 3.3 \times 10^{17} cm^2$

Mean LDM thickness = volume/total area
$= 3.3 \times 10^{17} / 7.8 \times 10^{15}$
$= 42.7cm$

Mean sedimentation rate = mean thickness/deposition period
Deposition period for basal unit is 1.46-2.94k.y. (Section 7.2.4)

Minimum sedimentation rate = 0.427 /0.00294 m/Ma
$= 145.23m/Ma$
Maximum sedimentation rate = 0.427/0.00146 m/Ma
$= 292.47$ m/Ma

Text Box 7.1. Calculation of mean sedimentation rate for LDM over minimum depositional area

Estimation of maximum biogenic silica accumulation rates assumes a constant sedimentation rate over the maximum depositional area (given in Tables 7.1 and 7.3 respectively). The results of these calculations (for minimum and maximum flux per unit area and regional extent) are given in Table 7.4. These fluxes persisted over between 1.46k.y and 2.94k.y. and then episodically for shorter periods, around 20-200 years in duration, for the next 56-7.k.y. The '4.4Ma' LDM deposits contain about 3240-16850TmolSi (the minimum value is calculated assuming that LDM deposition after the basal unit only occurred in the area of constant sedimentation rate, delimited by Sites 572, 847, 849 and 850, see Fig. 7.2).

| | Minimum flux per unit area | Maximum flux per unit area |
|---|---|---|
| Minimum area | 0.38Tmol BSi/yr | 0.76Tmol BSi/yr |
| Maximum area | 0.95Tmol BSi/yr | 2.78Tmol BSi/yr |

Table 7.4. Estimates of regional biogenic silica flux calculated for minimum and maximum depositional extent and flux per unit area

Annual biogenic opaline silica accumulation is estimated using local opal accumulation rates combined with the area of deposition. The results of these studies have been summarized by Tréguer *et al.*, (1995, Table 7.5) and give an annual biogenic opal accumulation of 7.1TmolSi/yr. Comparison of regional flux estimates for the major global silica sinks demonstrates that during LDM deposition, the eastern Equatorial Pacific represented a sink at least three times the magnitude of the modern Antarctic shelf.

| Region | Silica removed (Tmol BSi/yr) | Reference |
|---|---|---|
| Antarctic shelf (including Ross Sea) | 0.12 | DeMaster (1996) |
| Gulf of California | 0.11-0.15 | Thunell *et al.* (1994) |
| Peru-Chile Coast | 0.1 | DeMaster (1983) |
| Walvis Bay | 0.18 | DeMaster (1983) |
| North American West Coast | 0.17 | DeMaster (1983) |
| Baltic Sea | 0.04 | Ledford-Hoffman *et al.* (1986) |
| LDM deposits in Equatorial Pacific | 0.57-4.83 | this study |

Table 7.5. Regional fluxes of silica to sediments in continental shelf regions and whole ocean fluxes compared to fluxes estimated for deposition of LDM deposits in eastern Equatorial Pacific, modified from Tréguer *et al.*, (1995). The value quoted to Antarctic shelf deposits is estimated using $^{14}C$ rate based sediment accumulation rates and is an order of magnitude smaller than that estimated using $^{210}Pb$ values (Ledford-Hoffman *et al.*, 1986). The $^{14}C$ accumulation rate is thought to be more accurate than $^{210}Pb$ rates for Holocene sediments so the lower value is used (DeMaster *et al.*, 1996).

### 7.2.6 Discussion of LDM biogenic silica flux

The values calculated in the above section should represent the absolute limits for biogenic silica flux associated with the '4.4Ma' LDM depositional event in the eastern Equatorial Pacific. It is likely that the actual sedimentation rate for LDM material falls into the upper section of the 204-410m/Ma range, since the GRAPE based sedimentation rate (which form the lower limit) is calculated assuming constant sedimentation rate over the ~13m core thickness of which only 2-3m (15-20%) is laminated. Thus, the actual silica fluxes should fall into the upper section of the calculated range (0.76-2.78TmolSi/yr).

In the above estimates deposition is assumed to be uniform or vary uniformly over the depositional area. The basal unit is uniformly around 60cm thick at Site 572, 847, 859 and 850, but this may be due to the relative proximity of these sites compared to the maximum extent of the estimated area. It is likely that annual sedimentation rates were lower at the edges of the area of LDM deposition. TIW activity is weaker towards the west, especially at the being and end of TIW seasons (typically May to November Legeckis *et al.*, 1983). Since accumulation of diatom mats at the surface appears to enhanced by TIW activity, this variation in TIW extent suggests that there should be a lateral gradient in the thickness of laminated deposits, with thicker accumulations in the east. The occurrence of LDM deposits 1.5cm thick at Site 574, suggests that the predicted pattern of decreasing LDM accumulation to the east existed. The relative location of Sites 574 and 851 suggests that Site 574 may have

been located on the north edge of LDM deposition, giving an alternative explanation for the small thickness of LDM observed at this site. Since there are no drill sites between Sites 572 and 574 there is no way of calculating the rate of decrease in LDM accumulation rates between the two sites. A linear decrease was assumed.

### 7.2.7 Evidence for increased silica availability during LDM depositional events

To test the hypothesis of increase silica availability, biogenic opal contents of non-laminated sediments deposited at the same time as the '4.4Ma' LDM deposits in the equatorial region were measured. Samples were taken from Sites 848 and 851, which are located 160km south and 220km north of the frontal region respectively. Geomagnetic and nannofossil datums (Fig. 7.4) and the GRAPE record (Fig. 5.6) were used to accurately locate the sediment equivalent to LDM events. Between the datums and GRAPE peaks (ages given in Shackleton *et al.*, 1995) the position of sediment equivalent to the LDM deposits is estimated assuming a constant sedimentation rate and a maximum age range of the '4.4Ma' LDM event as 4.78-4.58Ma (Section 1.4).

From Figure 7.5 it is clear that the '4.4Ma' LDM event is marked by a strong peak in the biogenic opal content at Site 851 (reflected by a trough in the GRAPE record, Fig. 7.6). Quantitative estimates of biosiliceous plankton groups were made from smear slides of the samples (Fig.7.6 and Appendix A9). These measurements clearly demonstrate that the majority of the biogenic opal increase during the '4.4Ma' LDM event is related to an increase in *Thalassiothrix* content, see Figure 7.6a,b. The biogenic opal measurements suggest that around 55% of the peak in opal content is due to the increase in *T. longissima* Group diatoms. This increase in *T. longissima* Group diatoms could be due to either; (1) increased productivity of these diatoms above Site 851, or (2) advection of diatom mats into this area from accumulations in the frontal region. Observations of *Rhizosolenia* material in sediment traps and at the sediment surface as far as 400km north of the surface accumulations seen during the JGOFS Fall '92 survey (Honjo *et al.*, 1995; Smith *et al.*, 1996) are consistent with the latter explanation.

There is a much smaller increase in the biogenic opal record in samples from Site 848, although this may be related to the spacing of available samples. This site has very low sedimentation rates, consequently only weak peak was expected. The sedimentation rate calculated between palaeomagnetic datums for this section (11.52m/Ma) gives a sediment thickness of 0.68m for the duration of the '4.4Ma' LDM event (59Ka). Samples are spaced at 1-2m intervals and only one sample fell into the region equivalent to the '4.4Ma' LDM event, meaning that any increase in opal content will not be recorded clearly by this sample suite. Similar to Site 851, the GRAPE record from Site 848 shows a trough coinciding with the predicted location of the LDM equivalent samples, see Figure 7.5. Using the relationship

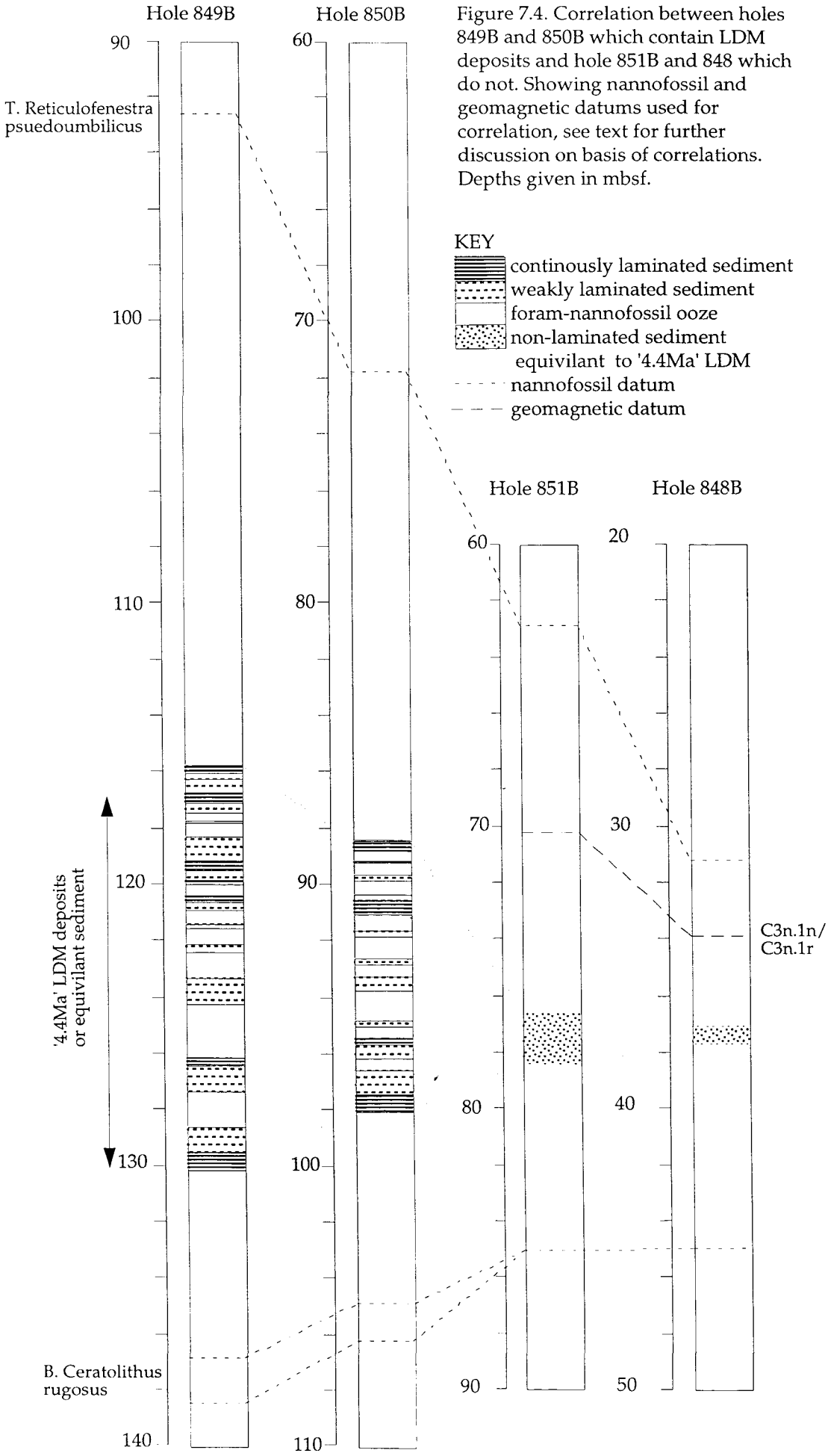


Figure 7.4. Correlation between holes 849B and 850B which contain LDM deposits and hole 851B and 848 which do not. Showing nannofossil and geomagnetic datums used for correlation, see text for further discussion on basis of correlations. Depths given in mbsf.

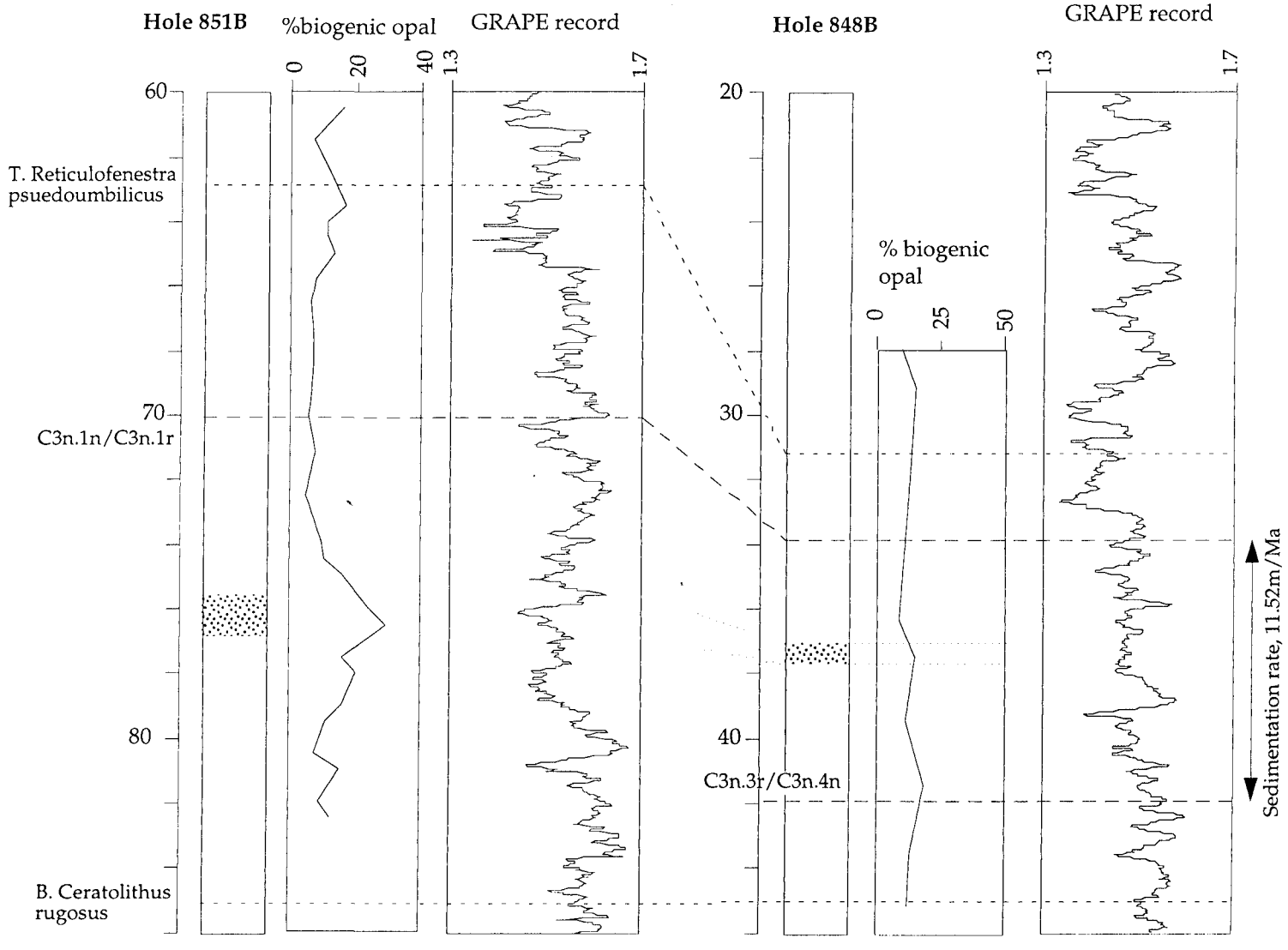


Figure 7.5. Biogenic opal content of non-laminated sediments equivalent to the '4.4Ma' LDM deposits in Holes 848B and 851B. Position of '4.4Ma' sediments in Hole848B calculated using sedimentation rates calculated between nannofossil/geomagnetic datums and event age of 4.78-4.58Ma and correlation between GRAPE records (see Figs. 4.4 and 5.3).

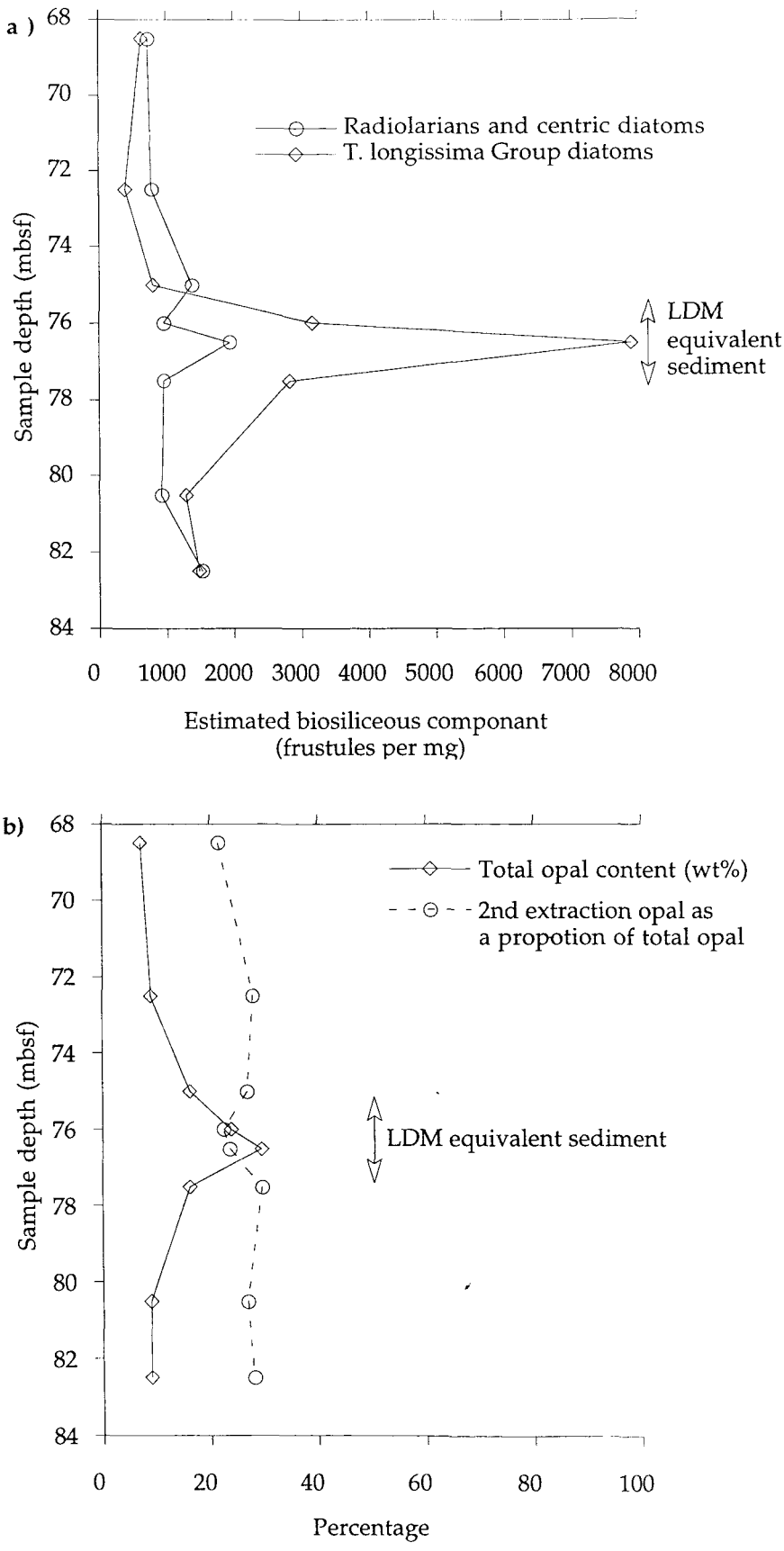


Figure 7.6. a) Sediment content of T. longissima Group and other biosiliceous frustules through the '4.4Ma' LDM event at Site 851. Note the marked increase in T. longissima Group frustules compared to the weaker increase in other biosiliceous material associated with the deposition of LDM material at the equatorial sites; b) total opal content and second extraction opal as a proportion of total opal. Note the relative decrease in radiolarian related opal in sediments equivalent to the LDM deposits

established between biogenic opal and GRAPE values for sediments from Sites 847 and 849-851 (Section 5.2.3) suggests a maximum biogenic opal content of 20%.

The massive increases in biogenic silica flux recorded by the LDM sediments suggests a major change in regional silica availability. This could be achieved through either (1) an increase in upwelling, or (2) an increase in dissolved silica input to the ocean system. The LDM sediments are composed almost solely of diatoms from the *T. longissima* Group. This group is typically found in low nutrient, stratified regions such as open ocean gyres (Beers *et al.*, 1975) and is not usually found in upwelling assemblages. It follows that the increase in silica flux is more likely to be related to an increase in dissolved silica availability, although the mechanism for this increase is still unclear.

Changes in the relative contributions of riverine, atmospheric and hydrothermal sources of both dissolved and particulate silica to the world ocean have been suggested by a number of authors (Shemesh *et al.*, 1989; Murnane and Stallard, 1990; Fröelich *et al.*, 1992). The main control on variations in silica supply is thought to be changes in weathering processes of terrestrial material altering the dissolved silica content of rivers (Shemesh *et al.*, 1989). The above evidence for increased deposition of biogenic silica during the '4.4Ma' LDM event at sites not affected by frontal deposition patterns and equatorial upwelling suggests a regional increase in the availability of silica in the eastern equatorial Pacific at this time. At Site 851, this increase in biogenic silica accumulation appears to have been enhanced by the advection of diatomaceous material from the frontal region. It is also interesting to note that a 6m thick section of LDM deposited at the same time as the '5.1-5-8Ma' depositional event has been located below the North Pacific polar front at ODP Sites 885/886 (Dickens and Barron, 1997). This provides evidence for massive increases in silica accumulation outside the equatorial region. The existence of a second region of elevated biogenic silica flux during this period of LDM accumulation ('5.5-5.8Ma') would result in much larger export of biogenic silica from the global ocean system than estimated above. The occurrence of this second area of elevated silica flux is consistent with the hypothesis of regional increases in silica availability during the deposition of the equatorial LDM deposits.

## 7.3 ESTIMATION OF ORGANIC CARBON FLUXES

The mass sinking diatoms from the surface to deep ocean also resulted in a massive organic carbon flux to the deep ocean. Remineralization of organic carbon occurs over geologically instantaneous timescales, so that deep sea sediments typically contain less than 0.5% organic carbon (Emerson and Hedges, 1988 and references therein). Since the residence time of the

deep ocean is in the order of 700-1000 years (Southam and Peterson, 1985), the $CO_2$ associated with the organic material is effectively removed from the atmosphere for that period.

### 7.3.1 Direct measurement of organic carbon in LDM deposits

The growth of moulds on core surfaces during storage makes accurate, high resolution measurement of relict organic carbon impossible for the LDM sediments. Mould colonies up to 6cm across were measured on the core surface, colonies near the edge of the core penetrated at least 2cm into the sediment (visible through the transparent core liner). While mould does not fix $CO_2$ from the air, it does redistribute organic carbon within the sediment, releasing a proportion of it during respiration. Consequently, the remaining organic carbon measured in these sediments may be regarded as a minimum value. Measurements of organic carbon in the lower 10cm of the '4.4Ma' LDM basal unit give a mean value of 0.86wt% (Appendix A10).

### 7.3.2 Methods of organic carbon flux estimation

Two methods are used to estimate the flux of organic carbon associated with diatom mats. The first method uses the Si/C ratio of diatoms combined with biogenic silica fluxes (calculated in Section 7.2). The second method uses the diatom rich Mediterranean sapropel (S-5) as an analogue for LDM deposition. Since this material accumulated in an anoxic environment where remineralization was either halted or much reduced, measured organic carbon contents should be closer to the original values of the freshly deposited material. These methods are examined in detail in the following sections.

### 7.3.3 Organic carbon flux estimation using diatom Silica/Carbon ratios

Diatom Si/C ratios have been used to estimate silica production in both global (Harriss, 1966; Lisitzin, 1972; Calvert, 1974; Wollast, 1974) and local silicon budgets (Nelson *et al.*, 1984). Given the volume of silica associated with LDM deposition it is possible to estimate the associated volume of organic carbon using the Si/C ratio of living diatoms in a similar way (Brzezinski, 1985). There are two major problems connected to this estimation method; a) the Si/C ratios measured for living diatoms are highly variable both between and within species. There are no published measurements for *Thalassiothrix* spp.; b) the Si/C of an individual diatom varies through it life-cycle and during sinking. These problems are examined in more detail in the following sections.

#### 7.3.3.1 Si/C - species variation

The variation of diatom Si/C within species is affected by environmental factors such as temperature (Durbin, 1977; Paasche, 1980), light intensity (Davis, 1976; Paasche, 1980), photoperiod (Eppley *et al.*, 1967) and nutrient limitation (Davis, 1976; Harrison *et al.*, 1976; Harrison *et al.*, 1977). The available data for Si/C ratios has been reviewed by Spencer (1983). An extensive study using cultures of 27 diatom species by Brzezinski (1985) showed

that despite the large differences in size and shape of the tested species, the majority of Si/C ratios fall within a factor of two of the mean in both continuous light and light-dark experiments (the results of the two light experiments not being statistically different). The relationship was further strengthened by dividing the tested species into two sets, greater and less then 20μm. The mean ratio for the 18 species greater than 20μm (the size range of *Thalassiothrix* was 0.15 ± 0.04 (mol/mol). Brzezinski (1985) suggests that the use of these ratios to convert field estimates of silicon to carbon units should yield results accurate to within a factor of three.

#### 7.3.3.2 Si/C - life-cycle variation

Silicon and carbon uptake in diatoms occur on similar timescales but are driven but different physiological mechanisms, and uptake of the two elements varies throughout the life-cycle. During early growth Si and C uptake occur at approximately constant rates and remineralization rates are very low. Consequently, the Si/C of the resulting biomass is very close to the initial Si/C production ratio. As the population ages, carbon degradation increases (through grazing and microbial activity) whereas Si dissolution stays low, resulting in an increasing Si/C biomass ratio. After death, carbon production ceases and silica dissolution increases slightly (due to the removal of the organic coating from frustules) but is still slower than carbon degradation. Thus, the Si/C of biogenic material sinking out of the euphotic zone is much higher (around an order of magnitude) than that of the original biogenic material.

SEM studies of laminated diatom oozes indicate that the diatoms were growing actively immediately prior to deposition (See Section 4.3.1), with no evidence for a decrease in silicification or gradually increasing nutrient stress. This suggests that prior to deposition the Si/C of the mats would have been similar to that during initial production. Rapid removal from the euphotic zone to the sea-floor (16-20 days, calculated using sinking rates from Alldredge and Gotschalk, 1989 and a water depth of 3330-3850m, see Section 2.5.2) would minimize changes to the Si/C ratio during sinking. This relationship supports the use of Si/C ratios measured for living diatoms in the estimation of carbon fluxes associated with the deposition of LDM sediments.

#### 7.3.3.3 Organic carbon flux of LDM deposits based on Si/C ratios

Given a biogenic silica flux of $8.1 \times 10^{-5}$ and $3.8 \times 10^{-4}$ molSi/cm$^2$/yr (which takes dissolution into account, Section 7.2.2) and using a Si/C (mol/mol) ratio of 0.15, the organic carbon flux associated with LDM accumulation is $5.4 \times 10^{-4}$ and $2.5 \times 10^{-3}$ molC/cm$^2$/yr. From the regional biogenic silica fluxes calculated in Section 7.2.5 (0.214-4.151TmolSi/yr), regional organic carbon flux can be estimated as 1.4-27.81TmolC/yr (Table 7.5). For comparison, modern

estimates of organic carbon primary production range from $3.7x10^3$ to $4.2x10^3$TmolC/yr (Longhurst *et al.*, 1995).

### 7.3.4 Comparison with organic carbon contents of Mediterranean sapropels

Sections of the Mediterranean sapropel S-5 are dominated by layers of the mat-forming diatom *Rhizosolenia.* and show strong similarities to the *T. longissima* dominated LDM sediments (e.g. dominance of giant diatoms, high levels of frustule preservation and lamina structure). Since the sapropels were deposited in an anoxic environment, organic carbon measurements should record the levels in material reaching the seafloor, following remineralization in the water column above the oxygen minimum zone. Eleven samples from diatom rich sections of the sapropel S-5 (ODP Hole 971C-2H-3, 128.29-121.9cm). The mean organic carbon content measured for these sediments is 4.35 wt%. Given a sedimentation rate of about 5.5cm/k.y. (estimated from lamina thickness, Kemp *et al.* in press) and DBD of $0.9g/cm^3$, this represents a flux to the deep ocean of $1.8x10^{-6}$molC/$cm^2$/yr (Table 7.6). Using this flux with the estimates of minimum (region with constant sedimentation rate only) and maximum areas of LDM deposition given in Section 7.2.3, suggests that LDM deposition results in a regional flux of 0.0063-0.025 TmolC/yr to the deep ocean.

Measurements of biogenic silica for these sapropel samples gives a mean content of 12.75wt%Si. Using the Si/C ratio published for *Rhizosolenia alata* (0.14, Brzezinski, 1985) suggests organic carbon export fluxes of $1.6x10^{-5}$molSi/$cm^2$/yr. This value is an order of magnitude greater than fluxes preserved in the sediment, suggesting ~90% of the initial organic carbon content was remineralized in the water column.

| | Flux per unit area | | Regional flux | |
|---|---|---|---|---|
| | molC/$cm^2$/yr | gC/$cm^2$/yr | TmolC/yr | gC/yr |
| Minimum organic carbon flux associated with LDM samples | 0.4-7.6x10-6 | 4.5-9.1x10-5 | 0.005-0.16 | 0.6-1.9x$10^{12}$ |
| Initial organic carbon flux (estimated using Si/C ratios) | 0.54-2.5x10-3 | 6.5-30.0x10-3 | 1.40-27.81 | 0.17-3.3x$10^{14}$ |
| Organic carbon flux at sediment surface (from comparison with Mediterranean sapropel S-5) | 3.8-7.7x10-5 | 4.6-9.2x10-4 | 0.48-1.60 | 5.7-19.2x$10^{12}$ |

Table 7.6. Minimum organic carbon flux associated with '4.4Ma' LDM deposits calculated from residual organic carbon compared with (1) initial estimates of initial organic carbon flux, calculated using the diatom Si/C ratio, and (2) estimates of organic carbon flux reaching the sea-floor calculated from measurements of organic carbon in the Mediterranean sapropel S-5.

### 7.3.5 Remineralization of organic carbon

To test the estimates of organic carbon flux calculated in Sections 7.3.3 and 7.3.4 remineralization rates need to be quantified. First-order degradation rates measured in laboratory and field experiments are highly variable (Emerson and Hedges, 1988 and references therein). The assumption that decomposing organic material has a constant

reactivity and thus decay rate is not consistent with field observations and laboratory studies. Microbial communities tend to sequentially utilize organic substrates in order of reactivity, most volatile first (e.g.Emerson *et al.*, 1985). As a result of this preferential uptake, the reactivity of the remaining organic carbon decreases over time (Berner *et al.*, 1980). On the basis of actual rate measurements Jørgensen (1979) divided organic matter into various groups of compounds of different reactivity, each undergoing first order first-order decomposition. This Multi-G model can be expressed as;

$$G_t = G_{01}\, e^{-k_1 t} + G_{02}\, e^{-k_2 t} + G_{NR} \qquad \text{Equation 7.1}$$

where $G_t$ is the concentration of organic carbon at time t (in years), $G_{01}$, $G_{02}$ and $G_{NR}$ are there initial concentrations of type 1, 2 and non-reactive compound groups respectively. $k_1$ is the first-order decay constant for the highly reactive type 1 compounds, and $k_2$ the first-order decay constant for the less reactive type 2 compounds (Westrich and Berner, 1984). The constants used in this study are given in Table 7.7.

| Constant | Definition of constant and rationale for choice of value | Value used in this study | Reference |
|---|---|---|---|
| $G_{01}$ | Concentration of type 1 (most reactive) compounds in initial organic carbon content, calculated from surface sediments from the eastern Equatorial Pacific | 80% | Hammond *et al.* (1996) |
| $G_{02}$ | Concentration of type 2 compounds in initial organic carbon content (reactive compounds not included in type 1), calculated from surface sediments from the eastern Equatorial Pacific | 19.8% | Hammond *et al.* (1996) |
| $G_{NR}$ | Concentration of non-reactive compounds in initial organic carbon content, calculated from surface sediments from the eastern Equatorial Pacific | 0.2% | Hammond *et al.* (1996) |
| $k_1$ | Decay constant of type 1 compounds, calculated using experimental decomposition of oxic plankton assemblages | $24yr^{-1}$ | Westrich and Berner (1984) |
| $k_2$ | Decay constant of type 2 compounds, calculated using experimental decomposition of oxic plankton assemblages | $3.2yr^{-1}$ | Westrich and Berner (1984) |

Table 7.7. Definitions and values of constants used in the multi-G model of organic carbon remineralization, with explanation of constant definitions and rationale for the choice of values used in this study.

#### 7.3.5.1 Estimating carbon flux to the deep ocean using diatom Si/C ratio

Given an average sediment composition for LDM material of 57.6wt% biogenic opal (24wt%BSi) and Si/C of 0.15 (Brzezinski, 1985) the organic carbon initially associated with

1g of sediment (dry weight) can be estimated as 0.68g. Since organic carbon typically accounts for around 50% of organic material (the remaining 50% being composed of nitrogen, oxygen etc. Parsons *et al.*, 1961), this translates to an initial organic carbon content for exported material of around 29%. Using the same method for sapropels containing 12.75%BSi with Si/C equal to 0.14 (value measured for*Rhizoslenia alata*, Brzezinski, 1985), the initial organic carbon content can be estimated as ~22wt%, see Appendix A10 for detailed working.

Both the sapropels and eastern Equatorial Pacific LDM deposits accumulated under around 3000m of water. Assuming a sinking rate of 150m/day for the diatom mats making up the LDM sediments (Section 2.5.2) gives a period of 20 days for remineralization in the water column. SEM examination of the diatomaceous layers in the S-5 sapropel shows that these layers consist of both intact and fragmented *Rhizosolenia* chains (Pearce *et al.*, in press). Laboratory studies have measured the sinking rates of dead *Rhizosolenia* chains as 69-84m/day (Villereal, 1988). Sinking at this rate through a water depth 3000m would take 35-44days. The proportion of initial organic carbon expected to reach the seafloor during both LDM and sapropel deposition is calculated using Equation 7.1 (Table 7.8).

| Remineral-ization period (days) | Initial organic carbon content (estimated using Si/C) | Organic carbon content of deposited material | Proportion of initial organic carbon remaining | Rationale for length of remineralization period |
|---|---|---|---|---|
| | | **'4.4Ma' LDM basal unit** | | |
| 0 | 29% | 29wt% | 100% | No remineralization |
| 20 | 29% | 12wt% | 41% | Estimated sinking period for LDM deposits at 147m/day (through 3000m) |
| 100 | 29% | 2.5wt% | 8.6% | Comparison to flux measured following JGOFS observations diatom concentration and sinking |
| | | **Mediterranean sapropel S-5** | | |
| 0 | 22% | 22wt% | 100% | No remineralization |
| 35 | 22% | 5.1wt% | 23% | Estimated sinking period for *Rhizosolenia* chains at 84m/day (through 3000m) |
| 44 | 22% | 3.0wt% | 14% | Estimated sinking period for *Rhizosolenia* chains at 69m/day (through 3000m) |

Table 7.8. Organic carbon remineralization over time for LDM and sapropel material estimated using the method given in Westrich and Berner (1984) showing proportion of initial organic carbon remaining after each remineralization period. Initial organic carbon content is estimated using the mean diatom Si/C ratio for LDM samples and the Si/C ratio published for *Rhizosolenia alata* for sapropel samples. The rationale for lengths of remineralization periods used in calculations is given in the last column. See Appendix A10 for detailed workings.

The mean of organic carbon measurements of sapropel samples (4.86wt%) falls between the organic carbon contents predicted by the Si/C initial organic carbon content and Multi-G remineralization model for the sinking rate range given above (3.0-5.1wt%). This supports

the use of these methods in the estimation of organic carbon fluxes associated with LDM deposition. The results of these models suggest that 41% the initial organic carbon reaches the deep ocean during LDM deposition.

#### 7.3.5.2 Testing the organic carbon remineralization calculations

Modern flux measurements can be used as a further constraint to verify both Si/C method of organic carbon estimation and the Multi-G model (and constants) given above. Measurements of organic carbon content are available for a modern diatom flux event in the Equatorial Pacific between 5° N and 5° S at 140° W (Smith *et al.*, 1996). This sedimentation event followed the observations of massive concentration of *Rhizosolenia* along the Equatorial front during the JGOFS Fall '92 survey. These deposits had organic carbon contents of between 1 and 2.84% and $^{324}$Th measurements indicate that the mats had been on the sea-floor for less than 100 days prior to sampling (Smith *et al.*, 1996). The organic carbon content expected in at the sediment surface 100days after the observed surface concentrations was estimated using the Si/C method of organic carbon estimation and the Multi-G model. Assuming an inital organic carbon content of 29% (estimated from comparision with LDM since no direct measurement are available), these models predict an organic carbon content of 2.5% (Table 7.5). This value is within the range of Smith *et al.*s' measurements, thus supporting the above use of Si/C ratios and modelled remineralization to estimate the organic carbon fluxes in LDM deposits.

### 7.3.6 Discussion of LDM organic carbon flux estimates

Estimates of organic carbon flux to the sea-floor associated with LDM deposition exceed modern flux measurements from sediment trap studies by at least two orders of magnitude (Table 7.9). Although organic carbon fluxes during normal deposition periods in the equatorial Pacific are generally higher than those measured in other regions, fluxes associated with LDM deposition are one to two orders of magnitude greater.

Assuming an annual biogenic silica flux rate of 0.76-2.78TmolSi/yr (Table 7.4) and Si/C of 0.15 suggests that annually LDM deposition in the eastern Equatorial Pacific was associated with the production of 5.1-18.5TmolC/yr of organic carbon. Modelled remineralization suggests that about 41% of this production (2.1-7.6TmolC/yr) reached the deep ocean. As a comparison, modern estimates of organic carbon primary production range from $3.7x10^3$ to $4.2x10^3$TmolC/yr (Longhurst *et al.*, 1995). If as much as 1% of this amount reaches the sea-floor (Lisitzin, 1972), the organic carbon flux associated with LDM deposition in the eastern Equatorial Pacific is equivalent to 5-21% of the modern annual organic carbon flux to the deep ocean.

| Location | Trap depth (m) | Depth above seafloor (m) | Organic carbon flux | | Reference |
|---|---|---|---|---|---|
| | | | (mol/cm$^2$/yr) | g/cm$^2$/yr | |
| **Eastern Equatorial Pacific, measured in LDM** | | | **0.4-7.6 x10$^{-6}$** | **4.5-9.1x10$^{-5}$** | **This study** |
| **Eastern Equatorial Pacific, initial flux estimated from LDM using Si/C** | | | **0.5-2.5 x10$^{-3}$** | **0.7-3.0x10$^{-2}$** | **This study** |
| **Eastern Equatorial Pacific, LDM deposits, flux reaching sea-floor** | | | **0.2-1.0 x10$^{-3}$** | **0.3-1.2x10$^{-2}$** | **This study** |
| **Mediterranean sapropel S-5** | | | **3.8-7.7x10$^{-5}$** | **4.6-9.2 x10$^{-4}$** | **This study** |
| South Pacific, Station P 50°N 145°W | 3800 | 520 | 1.1 x10-6 | 1.2 x10-4 | Honjo (1984) |
| Lofoten Basin, Arctic Ocean 69.5°N10°E | 2761 | 400 | 1.8 x10-6 | 1.1 x10-4 | Honjo et al, in Wefer (1989) |
| Bear Island, Arctic Ocean 75.9°N 11.5°E | 1700 | 418 | 2.4 x10-5 | 2.9 x10-4 | Honjo et al. (1987) |
| Norway Abyssal Plain 65.5°N 1°E | 2630 | 428 | 4.9 x10-6 | 5.9 x10-5 | Honjo et al. (1987) |
| W. Norwegian Sea 70°N 2.9°W | 2749 | 520 | 4.4 x10-6 | 5.3 x10-5 | Honjo et al. (1987) |
| Fram Strait 70.9°N 1.4°E | 2442 | 381 | 3.4x10-6 | 4.1x10-5 | Honjo et al. (1987) |
| Greenland Basin 74.6° 6.7°W | 2823 | 622 | 3.3 x10-6 | 4.0 x10-5 | Honjo et al. (1987) |
| Bransfield Strait, Antarctica 62.2°S 34.7°W | 1588 | 364 | 3.6 x10-5 | 4.3 x10-4 | Wefer et al. (1988) |
| Weddell Sea 62.5°S 34.7°W | 863 | 3017 | 2.1 x10-7 | 2.5 x10-6 | Fischer et al. (1988) |
| Tropical Pacific, Site C 1°N 139°W | 3495<br>1895<br>1095 | n.d.<br>n.d<br>n.d. | 1.3 x10-5<br>1.7 x10-5<br>1.3 x10-5 | 1.6 x10-4<br>2.1 x10-4<br>1.6 x10-4 | Dymond and Collier (1988) |
| Tropical Pacific, Site S 11°N 140°W | 3400 | n.d. | 5.0 x10-6 | 6.0 x10-5 | Dymond and Collier (1988) |
| Eastern Equatorial Pacific, 0° 140°W | 3618 | n.d. | 1.0 x10-5 | 1.2 x10-4 | Honjo et al. (1996) |
| California Current, 42°N 126°W | n.d. | n.d. | 1.9x10-5 | 2.3x-4 | Lyle et al. (1992) |
| California Current, 42°N 132°W | n.d. | n.d. | 9.0x10-6 | 1.1x-4 | Lyle et al. (1992) |
| Bering Sea, 58°N 179°E | 3137 | n.d. | 1.5x10-5 | 1.8x10-4 | Honjo et al. (in preparation) |
| Sea of Okhotsk, 53°N 149°E | 1061 | n.d. | 1.4x10-5 | 1.7x10-4 | Honjo et al. (in preparation) |
| North Atlantic, 34°N 21°W | 3700 | n.d. | 8.3 x10-6 | 1.0 x10-4 | Honjo and Manganini (1992) |
| North Atlantic, 48°N 21°W | 4500 | n.d. | 7.5x10-6 | 0.9 x10-4 | Honjo and Manganini (1992) |

Table 7.9 Organic carbon fluxes measured using sediment traps compared to estimated flux associated with LDM deposition in the eastern Equatorial Pacific and the Mediterranean sapropel S-5.

## 7.4 CARBONATE ACCUMULATION RATES DURING LDM DEPOSITION

Sedimentary carbonate contents can be estimated from measurements of wt% OPAL assuming negligible clay content using Equation 7.2;

wt% carbonate =100-wt%OPAL Equation 7.2Estimates

calculated using this equation agree closely with direct measurements of carbonate content made using the Carlo Erba method detailed in Section 3.6, see Figure 7.7. Carbonate accumulation rates of both laminated and non-laminated sediments (below and through the '4.4Ma' basal unit respectively) were calculated using mean carbonate contents and dry bulk densities for each sediment type and the sedimentation rates estimated in Chapter 5 (Table 7.10).

| Site | Estimated carbonate accumulation rate ($g/cm^2/yr$) | | | | |
|---|---|---|---|---|---|
| | Non-laminated sediments | | Laminated sediments | | |
| | Datum-based | GRAPE-based | GRAPE-based | Lamina-based | $^3$He-based |
| 847B | $5.3x10^{-3}$ | $12.2x10^{-3}$ | $6.4x10^{-3}$ | $5.8x10^{-3}$ | $7.2x10^{-3}$ |
| 850B | $2.1x10^{-3}$ | $10.9x10^{-3}$ | $2.6x10^{-3}$ | $4.9x10^{-3}$ | n.d. |

Table 7.10. Estimated carbonate accumulation rates for laminated and non-laminated sediments below and through the '4.4Ma' basal unit at Sites 847 and 850. Calculations assume a dry bulk density of 0.39 and $0.74g/cm^3$ for laminated and non-laminated sediments respectively (Mayer *et al.*, 199; CD ROM) and use sedimentation rate estimates given in Table 5.8.

Assuming that datum and GRAPE-based sedimentation rates represent lower and upper limiting for sedimentation of laminated and non-laminated sediments respectively (see Section 5.6), the carbonate accumulation rate for non-laminated sediments immediately below the '4.4Ma' LDM deposits is between $5.3x10^{-3}$ and $12.2x10^{-3}$ $g/cm^2/yr$ at Site 847 and $2.1x10^{-3}$ and $10.9x10^{-3}$ $g/cm^2/yr$ at Site 850. These rates are higher than carbonate accumulation rates calculated for these sites over other time periods (at Site 847 between 3Ma and 4Ma and from 5Ma to 6Ma carbonate accumulation rates were 1.15x10-3 and 1.71x10-3 g/cm2/yr, and at Site 850 over the same time periods carbonate accumulation rates were 1.11x10-3 and 3.79x10-3 g/cm2/yr respectively Farrell *et al.*, 1995).

Similarly, assuming the GRAPE and $He^3$-based sedimentation rates form the upper and lower limits respectively of sedimentation in laminated sections, carbonate accumulation rates for these sediments lie the ranges $6.4\text{-}7.2x10^{-3}$ $g/cm^2/yr$ at Site 847 and $2.6\text{-}4.9^{-3}$ $g/cm^2/yr$ at Site 850. The ranges of carbonate accumulation rate for laminated sediments are within the bands of error of those estimated for non-laminated sections with depositional event, but tend to be slightly lower. This suggests that carbonate accumulation rates did not alter significantly across the lower boundary of the '4.4Ma' LDM event but may have dropped slightly.

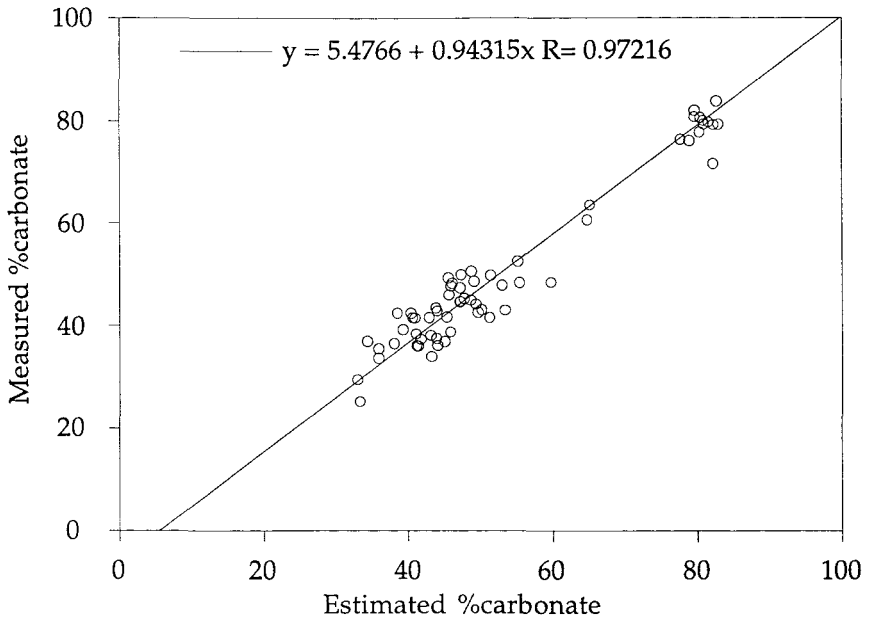


Figure 7.7. Comparision of measured carbonate values with those estimated for the same samples using the biogenic opal content. The relationship is closest to the accepted 1:1 correlation at higher carbonate contents (70-100% carbonate). At lower values this estimation method tends to overestimate the carbonate by up to 6% (at carbonate) suggesting either an increase in other sedimentary phases (e.g. organic carbon and clays) or a systematic under estimation of biogenic opal at higher concentrations

## 7.5 MODELLING CONTROLS ON SILICA FLUXES

The previous discussion suggests that LDM deposition in the eastern equatorial Pacific was due to a sudden increase in silica availability (Section 7.2.7). Carbonate production does not appear to change significantly during the deposition of LDM material (Section 7.4) suggestingthat the availability biolimiting nutrients (other than silica) did not change significantly during the deposition of LDM sediments. To investigate the influence of (1) upwelling rates and (2) the input dissolved silica on silica accumulation patterns, the global silica cycle was simplified in a two box model in which these two factors could be varied independently (Fig. 7.8a after Broecker, 1971; Broecker and Peng, 1987; Decker, 1991). When considering only the surface ocean, separated from the deep ocean by the thermocline, silica input from riverine and upwelling sources is balanced by the rain of opaline skeletons to the deep ocean plus a small amount lost through downwelling. The concentration of dissolved silica in the surface ocean is kept low by the extensive biological silica uptake. In contrast the deep ocean is relatively enriched by the dissolution of siliceous frustules in the water column. The silica balance of the surface ocean can be altered by changes in both the river input and upwelling rates. The model was used to investigate both the effect of stepwise changes in upwelling and river input (Experiment A) and changes in frustule dissolution on time taken for the model to return to a steady state (Experiment B). Full detail of the model calculations and assumptions are given in Appendix A11.

### 7.5.1 RESULTS OF THE TWO BOX MODEL

#### 7.5.1.1 Experiment A: Changing upwelling and riverine input

Increasing the modelled upwelling rate results in an immediate increase in silica availability at the surface. This increases surface productivity and biogenic silica flux to the deep ocean in proportion to the increase in silica availability. Assuming a constant rate of preservation in the frustules reaching the sea-floor, the total amount of silica reaching the sediment increases. If the silica input (i.e. riverine input) remains constant, as more silica is removed from the oceans into the sediment, silica levels in the deep ocean fall and thus the rate of silica input to the surface ocean through upwelling is reduced. In turn biological production and biogenic silica export is reduced and the cycle gradually returns to a new equilibrium with the silica sedimentation rate again equal to the riverine input rate (and the initial silica sedimentation rate), see Figure 7.8c. A similar feedback loop develops if upwelling is suddenly reduced. In this case less silica is supplied to the surface ocean resulting in decrease surface productivity and opal deposition. Productivity is now feed by the rivers and reduced upwelling. Since the transfer of dissolved silica from the deep to surface ocean through upwelling is reduced, the concentration of the deep ocean gradually increases. This results in an increase in silica concentrations of the upwelled waters until the initial rate of deposition is re-established. This return to initial conditions requires a time-span of $10^4$ years

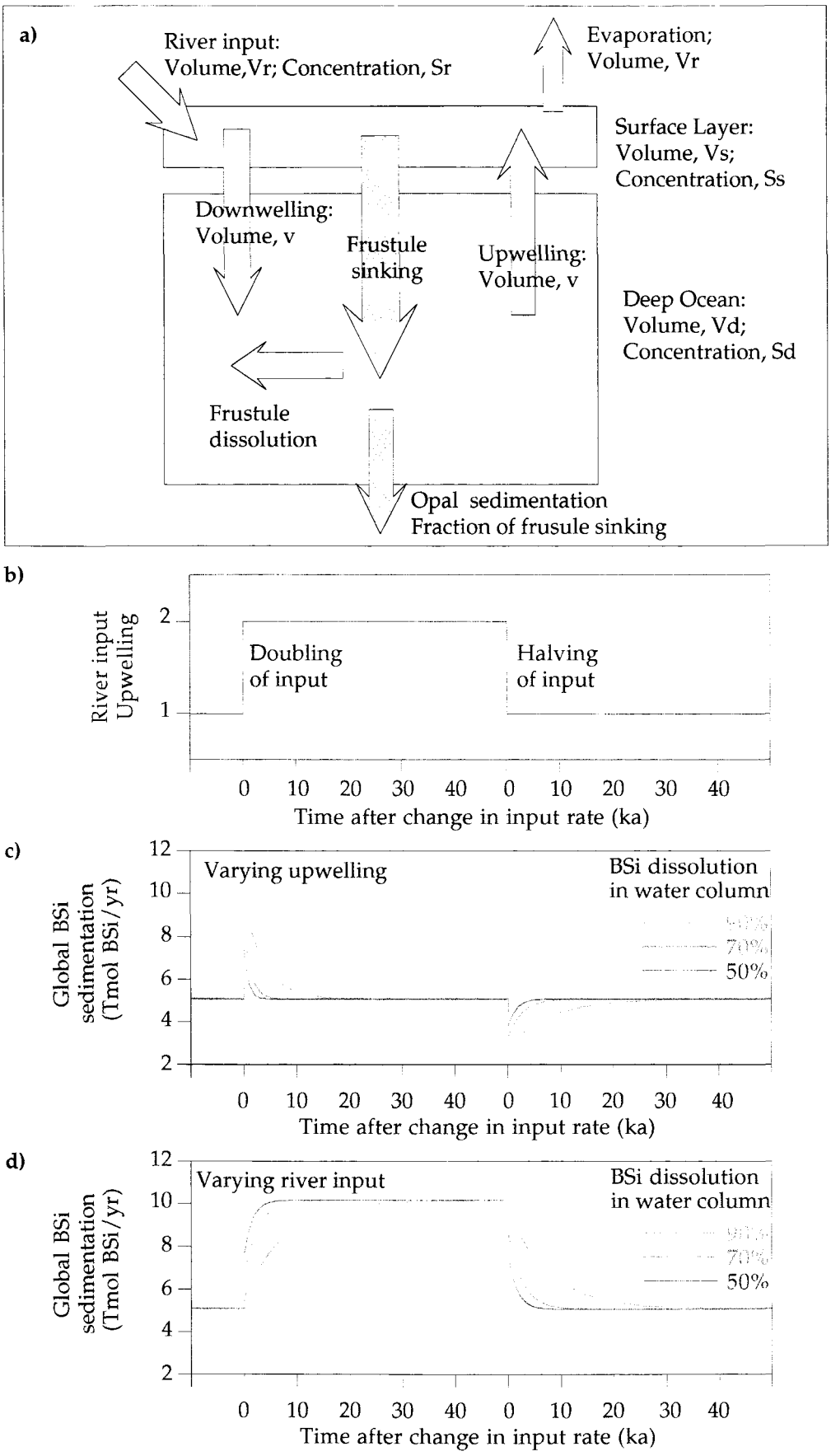


Figure 7.8. a) Simple box model used in estimation of timescales associated with variations in the global silica cycle (after Brocker and Peng, 1982 and Decker, 1991); b) assumed step-like changes in global upwelling/riverine input rates used to test the response of the model to changes in BSi inputs to the surface box; c) modelled effect of varying upwelling showing the influence of dissolution in the deep-ocean; and, d) the effect of varying river input again showing the influence of dissolution in the deep-ocean. These results demonstrate the importance of dissolution levels in the global silica cycle. The low levels of dissolution observed in the LDM deposits suggest a rapid return to stead state conditions.

(Decker, 1991). In contrast to changing upwelling rates, higher riverine silica input to the model results in a slow asymptotic increase in opal deposition with the gradual establishment of higher opal sedimentation rate balancing the elevated silica input (Fig. 7.8d). Modelling a decrease in riverine silica input results in the asymptotic decrease in opal sedimentation.

#### 7.5.1.2 Experiment B: varying frustule preservation levels

LDM deposits differ from other deep sea biosiliceous sediments in their level of frustule preservation (Section 4.4). The frustules making up these sediments are remarkably well preserved and represent around 60-80% of the surface silica uptake (see Section 4.4). In more typical sediments the opal fraction represents around 20% of surface silica production (Tréguer *et al.*, 1995 and references therein). Assuming that the LDM sediments represented about half of the annual global silica export (see Section 7.3), mean global preservation levels should be approximately 35-45%. The model was run with three different levels of frustule preservation (10%, 30% and 50%) while varying upwelling and riverine input as in Experiment A (Fig. 7.8c,d).

The principal effect of decreasing levels of dissolution in the deep box is to increase the response rate of the model to changes in input rates. Decreased dissolution rates result in a more rapid return to a steady state. Decreasing dissolution rates from 90% to 50% reduces the response time (time taken to return to a steady state) by 70-75%. In these cases the low levels of dissolution reduce the input of dissolved silica into the deep waters, resulting in a rapid reduction of silica concentration in the deep box. Interestingly, decreasing dissolution levels in model runs with varying upwelling rates, results in lower peak BSi sedimentation rates; peak silica sedimentation associated with 50% dissolution in the deep box represents around 79% of peak sedimentation associated with 90% dissolution.

### 7.5.3 Conclusions drawn from silica box model

The increases in silica sedimentation predicted by this model are proportional to the increase in input rates to the surface box. Doubling input rates via either upwelling or river input will approximately double the silica sedimentation rate. It is also important to remember that this type of silica spike only forms when upwelling rates change rapidly. In the case of slower changes (over several thousand years), feed-back mechanisms are able to keep the system in balance and the silica sedimentation rate stays approximately constant (Decker, 1991). Rapid changes in upwelling and riverine input of this order of magnitude are most commonly associated with the change from glacial to interglacial conditions. Sarnthein *et al.* (1987, 1988) concluded that strengthening of trade wind activity during glacial periods would increase upwelling rates significantly; riverine input of dissolved silica is estimated to approximately double during strong glaciations (Fröelich *et al.*, 1992). The silica

sedimentation rates associated with the '4.4Ma' LDM deposits (which account for 0.76-2.78TmolSi/yr) are consistent with the peak sedimentation rates estimated by doubling the input to the box model (increases of up to about 3-5 TmolBSi/yr depending on the level of dissolution assumed).

The box model results indicate that variations in upwelling are more effective in producing short-term ($10^4$ year) spikes (both positive and negative) in silica deposition than changes in riverine silica input. The duration of such elevated silica deposition periods is strongly dependant on the level of dissolution occurring in the deep ocean. The low levels of dissolution observed in the LDM sediments suggest silica deposition returned its original levels after around 7ka (decreasing to 50% of peak values after only 500 years). Sedimentation rates give a deposition period of around 1.4ka for the '4.4Ma' LDM event basal unit (see Section 5.6.2). This deposition period is comparable with the timescales associated with upwelling-induced peaks in silica sedimentation. However it is still unclear why the LDM deposits, like the observations of diatom accumulations along the equatorial front during the JGOFS Fall '92 survey (Barber, 1992), are dominated by a diatom that adapted to stratified conditions and not commonly found in the upwelling regions.

## 7.6 CHANGES ON OCEAN/ATMOSPHERE DYNAMICS COINCIDING WITH LDM DEPOSITION

LDM sediments located below the polar front in the North Pacific were deposited at the same time as the '5.1-5.8Ma' LDM at the EEP. This time coincident occurrence below two frontal regions suggests that the unusual surface water conditions which result in LDM deposition are causally linked to large-scale oceanographic change. The occurrence of massive biogenic silica and organic carbon fluxes to the deep ocean during LDM depositions suggests that these changes involved either (1) addition of nutrients to the ocean, or (2) the redistribution of nutrients within the ocean system. One mechanism capable of altering ocean/atmosphere dynamics in this way over the timescales of LDM deposition is the glacial/interglacial cycle.

Measurements of both $\delta^{18}O$ and $\delta^{13}C$ for benthic foraminifera from Hole 849B (0-5Ma) have been made by Mix (1995 and pers. comm.). Comparison of $\delta^{18}O$ measurements to the composite GRAPE record for Site 849 shows that the '4.4Ma' LDM depositional period was preceded by strong glacial/interglacial oscillations, with both glacial and interglacials becoming increasingly colder (Fig. 7.9). Similar oscillations have been observed in records for this interval at Site 846 (Shackelton *et al.*, 1995) and in the western equatorial Pacific (although in less detail Jansen *et al.*, 1993).

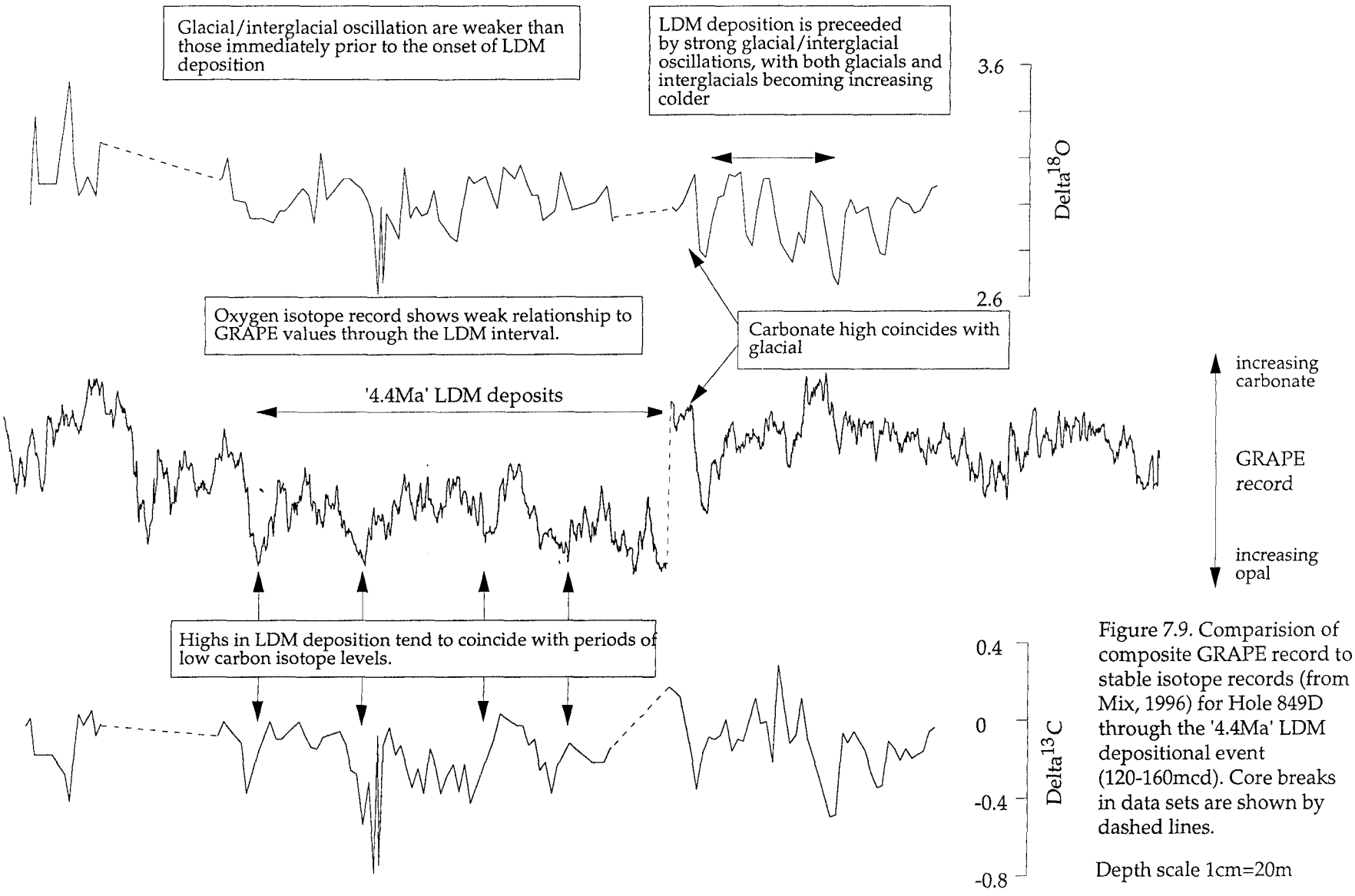


Figure 7.9. Comparision of composite GRAPE record to stable isotope records (from Mix, 1996) for Hole 849D through the '4.4Ma' LDM depositional event (120-160mcd). Core breaks in data sets are shown by dashed lines.

Depth scale 1cm=20m

The carbonate high identified immediately below the '4.4Ma' LDM correlates closely with the NS5 cold period (Fig. 7.9). The onset of LDM deposition appears to coincide with the transition from glacial to interglacial conditions (the NS5-NS4 transition using the labelling system of Shackleton *et al.* 1995). There are no $\delta^{18}O$ measurements over this interval, due to a core gap and low foram abundances in the LDM deposits. Additional sampling from Hole 849Bwould enable comparison above this gap. The relationship between $\delta^{18}O$ values and the GRAPE record within the '4.4Ma' LDM deposits is complex.

Within the '4.4Ma' LDM deposits, peaks in opal content tend to coincide with lows in the benthic foraminifera $\delta^{13}C$ record. It is also interesting to note that the deposition of the '6.1-6.1Ma' LDM (containing the datum B. *Amaurolithus amplificus* dated at 6.6Ma) coincides with the Miocene $\delta^{13}C$ shift dated at 6.57-6.69Ma (Haq *et al.*, 1980). This shift in $\delta^{13}C$ values (an decrease of around 0.8‰) is interpreted as reflecting a global change in ocean chemistry (Keigwin, 1987). The lack of $\delta^{13}C$ data from sites containing the '6.1-6.3Ma' LDM event makes the exact relationship between the LDM deposits and the carbon-isotopic shift indistinct.

The occurrence of LDM deposits and the use of a global increase in the availability of dissolved silica are consistent with the hypothesis proposed by Pollock (1997) to explain global cooling prior to the onset of Pliestocene glacial periods. In this model, silica enriched subglacial waters released by melting of the West Antartic Ice Sheet during interglacical periods are entrained in deep and intermendiate waters. Upwelling of these waters in both coastal and open-ocean regions then result in the proliferation of large diatom species with a high affinity for dissolved silica. These blooms enhance the rate of $CO_2$ drawdown and eventually result in global cooling. In the Neogene, the LDM deposits generally occur in the deglaciation following a strong glacial period. This suggets that, in constrast to the Pliestocene, the Neogene global climate system was less sensitive to oceanic $CO_2$ drawdown in triggering global cooling.

## 7.7 CHAPTER SUMMARY

The massive scale of biogenic silica flux associated with the '4.4Ma' LDM event is represented by (1) elevated flux per unit area, (2) the large area of LDM deposition and (3) the timescales of sustained LDM deposition. Regional export of biogenic silica associated with the '4.4Ma' LDM event falls in the range 0.76-2.78TmolSi/yr. This flux rate was sustained over about 1.46k.y. during the accumulation of the '4.4Ma' basal unit, and then occurred episodically (over 20-200year periods) for the next 57k.y. As a comparison, annual export of biogenic silica associated with LDM deposits represents 10-40% of modern annual

biogenic silica export. The lower limit of this regional flux range is comparable that of present day Antarctic shelf, the largest silica sink of the modern ocean system.

Measurements of biogenic opal at sites not containing the '4.4Ma' LDM deposits show a contemporaneous increase in biogenic silica sedimentation suggesting both (1) an increase in silica availability and (2) advection of diatom material from the frontal region. Simple box models of the global silica cycle and the sharp boundary at the base of the '4.4Ma' LDM unit suggest that this increase in silica availability is more likely be associated with an increase in upwelling than an increase in riverine input. However, the LDM deposits consist of up to 95% *Thalassiothrix*, a diatom typical of stratified regions and which is not thought to dominate in upwelling conditions. Although the diatom *Rhizosolenia*, observed in massive concentrations along the equatorial front during the JGOFS Fall '92 survey is also typical of stratified conditions. More detailed information on the life-styles of these two diatoms is needed to explain this apparent anachronism.

Organic carbon flux related to LDM deposition is estimated using (1) diatom Si/C ratios and modelled remineralization rates, and (2) comparison with the diatom rich layers of the Mediterranean sapropel S-5. The Si/C method is supported by comparison to modern measurements of modern flux events and the measurements of sapropel samples. These methods suggest that LDM deposition resulted in organic carbon fluxes of 5.1-18.5TmolC/yr, of which around 2.1-7.6TmolC/yr reached the deep ocean. This value represents 5-21% of modern organic carbon flux. Carbonate accumulation rates do not appear to alter significantly during the deposition of LDM material.

The co-occurrence of LDM deposits in the North Pacific during the '5.1-5.8Ma' LDM deposition event suggests LDM deposition is initiated by ocean-wide processes that result in either (1) addition of nutrients to the ocean, or (2) the redistribution of nutrients within the ocean system. Both the '4.4Ma' and '5.1-5.8Ma LDM deposits appear to coincide with major glaciations, but more detailed oxygen isotope stratigraphy is needed to determine the exact temporal relationship between LDM deposition and these glaciation events.

# CHAPTER 8: CONCLUSIONS

This chapter presents a summary of the results and conclusions of this high-resolution study of the '4.4Ma' LDM depositional event in the eastern equatorial Pacific Ocean and suggests a number of possible avenues for future research. The results and conclusions of this study can be divided into two sections; those relating to the factors influencing the deposition of LDM material, and; those related to the effects of LDM deposition on both local and global levels. These two sections will be discussed separately following a summary of the methods developed for use in this study.

This study developed three methods used in investigating the factors influencing the deposition of LDM material: (1) Modifications to the published methods of opal measurement allowed the use of millimetre scale sampling and the exploitation of the pure biogenic composition of siliceous material in LDM sediments. By using two stages of sediment dissolution, the relative content of diatom and radiolarian related opal of these sediments can be estimated using a simple linear relationship. (2) Development and testing of a new method for the quantification of diatom frustule dissolution in deep sea sediments using SEM observations. Although the method is currently limited to using *Thalassiothrix* spp., it would be possible to extend its to use other diatom species. Use of this method detected and quantified a the trend of increasing diatom frustule preservation levels with increasing sedimentary opal content. (3) Use of the Lomb method of spectral analysis instead of conventional Fourier methods to isolate periodicities within data-sets of both lamina couplet thickness and high resolution opal measurements. This method uses unevenly spaced data sets thus avoiding the use of intermediate interpolation stages. The use of unevenly spaced data also allows both the identification of significant frequencies below the mean sample frequency and the estimation of significance levels. Use of these three methods enabled this study of LDM material to be carried out at millimetre-scale resolution.

The millimetre-scale sampling possible through LDM intervals enables the construction of decadal (or shorter) scale records of silica fluxes to the deep ocean. Correlation of the records from the basal unit of the '4.4Ma' LDM depositional event at sites 847 and 850 show a remarkable similarity between the two sites. Closer examination of the sediments using BSEI techniques enabled detailed correlation of sedimentary features between these two sites. These sedimentary tie-points were used to map the opal records from site 850 onto the those of site 847 giving an increase of around 25% in the statistical correlation. This correlation

($r^2$=0.691) suggests the same depositional mechanism functioned along the Equatorial Front for lateral distances of over 2000km.

High resolution examination of LDM sediments using BSEI techniques identified the existence of lamina couplets within the '4.4Ma' basal unit at site 847 and 850. These couplets suggest a depositional regime of episodic depositional events (similar to that observed in the eastern equatorial Pacific by the JGOFS Fall '92 survey) separated by more normal deep sea sedimentation patterns. Measurement and subsequent spectral analysis lamina couplet thickness identified two significant frequencies within the lamina couplet record with periodicities of 6-7 and 21 couplets. Assuming the couplets represent annual events (consistent with sedimentation rate estimates), the 6-7 couplet periodicity is consistent with an El Niño-type regime. The 21 couplet periodicity could either be related to variation in the relative strength of these El Niño-type events, or other changes in the climate system over the North Pacific . Spectral analysis of the high-resolution biogenic opal records at sites 847 and 850 also demonstrated the existence of periodicities affecting this depositional mechanism with century-scale periods. Although no firm correlation with individual external forcing frequencies is possible (due to the uncertainties in sedimentation rates) the periodicities within the biogenic opal records have timescales that suggest the influence of extraterrestrial forcing mechanisms such as sun-spot variability.

Measurements of biogenic opal at sites not containing the '4.4Ma' LDM deposits show a contemporaneous increase in biogenic silica sedimentation indicating a global increase in silica availability. Simple box models of the global silica cycle and the sharp boundary at the base of the '4.4Ma' LDM unit suggest that this increase in silica availability is likely to be associated with an increase in upwelling rather than an increase in riverine input. However, the LDM deposits consist of up to 95% *Thalassiothrix*, a diatom typical of stratified regions and which is not thought to dominate in upwelling conditions. Moreover, the diatom *Rhizosolenia*, observed in massive concentrations along the equatorial front during the JGOFS Fall '92 survey is also typical of stratified conditions. More detailed information on the life-styles of these two diatoms is needed to explain this apparent contradiction.

On a local scale, LDM deposition resulted in a significant increase in sedimentation rates and a marked change in sediment composition and dissolution processes occurring within the sediment. In turn, this period of elevated local fluxes in the eastern equatorial Pacific appears to have affected global biogeochemical cycles.

This study uses four different methods to calculate sedimentation rates. The two methods based solely on material from laminated sections (annual lamina couplet-based and $^3$He-

based) give comparable rates (390m/Ma and 410m/Ma respectively) that are significantly greater than those obtained using the datum-based method and the GRAPE-based method (20-60m/Ma and 204m/Ma respectively). This demonstrates the magnitude of the difference between the sedimentation rates of the two sediment types, LDM and F-NO. The similarity between lamina couplet-based sedimentation rates calculated using annual depositional events and the $^{3}$He-based sedimentation rates, indicate the laminated intervals are related to annual or quasi-annual depositional events. Regardless of absolute rates, the $^{3}$He-based method indicates a 2.4 fold increase in sedimentation rate related to the onset of LDM deposition. Estimates of carbonate sedimentation rates for sediments below and through the '4.4Ma' basal unit indicate that there was very little change in carbonate accumulation patterns.

Quantification of diatom frustule dissolution showed a trend of increasing frustule preservation with increasing sedimentary opal content. This trend represents a positive feed-back mechanism enhancing the preservation of biogenic silica on the sea-floor. Increased flux of biogenic opal from the surface ocean results in increased frustule preservation on the sea-floor, resulting in enhanced levels of opal content and a net increase in sedimentation rates.

Regional export of biogenic silica associated with the '4.4Ma' LDM event falls in the range 0.38-2.78TmolSi/yr. The actual value is likely to fall in the upper end of this range since the depositional period used in the calculation of the lower sedimentation rate represents a significant under-estimate. The lower limit of this range is comparable to the annual export of biogenic silica over the modern Antarctic shelf. For comparison, estimated annual export of biogenic silica during LDM deposition represents 10-40% of modern annual biogenic silica export. Estimates of organic carbon fluxes associated with the '4.4Ma' LDM suggest an annual transport of 2.1-7.6Tmol organic carbon to the deep ocean. Compared to modern fluxes, this represents 5-21% of the estimated organic carbon transported to the sea-floor in the modern ocean, and is comparable with both; (1) measurements from sediment traps and on core-tops following the diatom mat concentration observed during the JGOFS Fall '92 survey; and (2) measurements of organic carbon in similar monospecific diatom-mat deposits in the Mediterranean sapropel S-5.

This study demonstrates the significance of frontal controlled LDM depositional events for both local and global biogeochemical cycles in the eastern equatorial Pacific. These results illustrate how restricted local events can have major implications for global biogeochemical processes. Similar LDM and mono-specific diatom concentrations located below other major ocean front systems (Gardener and Burkle, 1975; Jordan *et al.*, 1991; Bodén and Backman, 1995; Dickens and Barron, 1997; D.DeMaster pers.comm.) should be considered in the light of these findings.

## 8.1 DIRECTIONS FOR FUTURE RESEARCH

The controlling mechanisms of LDM deposition could be further investigated using the methods developed in this study to examine older LDM sections from both the eastern Equatorial and North Pacific. Comparision of lamina couplet thickness data from this study (Section 4.3) with similar data-sets from older LDM events could provide useful information on influence of the Panama Seaway on El Niño-like events.

Opal measurements made during this study (Section 6.4.3) indicate a strong difference in the radiolarian population between the Sites 847 and 850. This suggests a difference in growth conditions between these the sites which could be explored using species analysis of both radiolarian and diatom populations. Extending these studies over LDM events could also provide useful information on oceanographic changes associated with LDM deposition.

Stable isotope records across LDM deposits and correlation with such records at sites without LDM deposits suggest that the onset of deposition of the '4.4Ma' LDM coincided with a transition from glacial to interglacial conditions (Section 7.6). Detailed $\delta^{18}O$ measurements across this and other LDM deposits should clarify this suspected relationship between LDM deposition and the glacial-interglacial cycle. Correlation using biostratigraphic datums suggests that accumulation of the '6.1-6.3Ma' LDM deposits coincided with the global late Miocene carbon isotope shift (Section 7.6). LDM deposits associated with this event are found in both the eastern Equatorial Pacific and Equatorial Atlantic Oceans implying a massive export of both BSi and diatom related organic carbon. Measurement of $\delta^{13}C$ both across the '6.1-6.3Ma' LDM deposits and in other sediments accumulated across the time-interval could provide an interesting insight into the global influence of LDM accumulation on the global carbon cycle.

The box model used in Section 7.5 provided an insight into influence of upwelling and riverine input on silica availability in the world ocean. These results could be extended investigate the combined effect of varying upwelling and riverine input simultaneously. These modifications should allow the model to predict the opal sedimentation patterns associated with changes from glacial to interglacial more accurately.

# APPENDIX 1: OPAL ANALYSIS METHOD

This method is based on those of Mortlock and Frolich (1989), Strickland and Parsons (1972), DeMaster (1981) and Fanning and Pilson (1973). See Section 3.4.1 for the rationale and background to the choice of method.

## A.1.1 Overview of chemistry

This method is based on the dissolution of biogenic opal and subsequent measurement of dissolved silica in solution. The solubility of biogenic silica has been shown to increase significantly with increasing temperature and in alkaline solutions (Hurd, 1983 and references therein). This method uses a strong alkaline extraction solution (2M $Na_2CO_3$ or 2M NaOH) held at 85°C to dissolve the biogenic opal. Lithogenic clays are also attacked by alkaline solutions and can release silica into solution. The use of relatively strong alkaline extraction solutions, high temperatures and long dissolution periods compared to other laboratories (Conley, 1996) was possible during this study since there is neglible lithogenic material associated with the LDM sediments.

Once in solution, silica concentration is measured by reacting the sample solution with molybdate to form silicomolybdate. This yellow solution is then reduced using a metol and oxalic acid solution to give a more strongly colured blue compound. This reducing solution also decomposes phosphomolybdate or arsenomolybdate thus eliminating inference from any phosphate and aresenate content. Since only relatively short, straight-chain polymers of silicic acid react quickly with molybdate (less than three silicic acid units) this method only measures 'reactive' silicate.

## A1.2 Reagents

*Extraction Reagents*

1) *2M $Na_2CO_3$ solution.* Dissolve 2128g of anhydrous $Na_2CO_3$ in 1000ml of MilliQ. This produces a solution close to saturation. Full dissolution can be achieved by heating in a water bath at 50°C. Redissolve any crystals that may have formed immediately before use to by ultrasonification.

2) *2M NaOH solution.* Dissolve 80.00g of NaOH in 1000ml of MilliQ.

3) *1N HCl solution.* Add acid very slowly to MilliQ in large beaker and allow to cool.

4) *10% $H_2O_2$* . Dilute 30% $H_2O_2$ in the ratio 1 part $H_2O_2$ to 2 parts MilliQ, allow to cool.

*Stock reagents*

4) *Molybdate reagent.* Dissolve 16.0g of analytical reagent quality ammonium paramolybdate $(NH_4)_6Mo_7O_{24}.H_2O$ in a 1000ml of silica free MilliQ water. Store this solution in a tightly capped polyethylene bottle out of direct sunlight. The solution is stable indefinitely, but if a white precipitate forms or the solution turns faintly blue it should be discarded.

5) *Metol-sulphite reduction reagent.* Dissolve 12g (3g) of anhydrous sodium sulphite ($Na_2SO_3$) in 1000ml (250ml) of MilliQ, then add 20g (5g) of metol (paramethylaminophenol sulphate) and ultrasound until dissolved (usually 10minutes). Store in an amber ground glass stoppered bottle in a refrigerator. This solution is stable for 1-2 weeks provided the bottle is tightly capped. But should be made fresh for each analysis run if possible since crystals tend to form at the bottom of the bottle. Discard if the solution becomes a faint brown colour.

6) *Oxalic acid reagant.* Dissolve 60g of analytical quality oxalic acid dihydrate $(COOH)_2.2H_2O$ in 1000ml of MilliQ and store in polyethylene. Stable indefinitely.

7) *Sulphuric acid reagent.* Slowly add 300ml of concentrated (sp. gr. 1.82) analytical reagent quality sulphuric acid into 770ml of MilliQ. Cool to room temperature and store in polyethylene.

8) *Hydrochloric acid reagent.* Add 48ml of concentrated (12N) HCl to 925ml of MilliQ and store in polyethylene.

*Working Reagents*

9) *Molybdate working solution.* Mix molybdate stock reagent, HCl stock reagent and MilliQ in volume proportions of 1:1:5. Prepare this mixture for immediate use. It is stable for at least 6-12 hours. Store in polyethylene out of direct sunlight.

10) *Reducing working solution.* Mix equal volumes of metol-sulphite stock reagent, oxalic acid stock reagent and sulphuric acid stock reagent, adding the sulphuric acid last. It is stable for 4-6 hour, but should be prepared immediately before use.

*Standard Solutions*

11) *Working standards ($Na_2CO_3$ solutions)* Add primary standard (35.6mM; see Table A1.1 for volumes) to an acid cleaned 25ml polyethylene volumetric flask and fill to the line with MilliQ. Mix throughly and transfer to a wide necked polyethylene bottle. Add 5.3g $Na_2CO_3$ to each solution. This makes the solutions 2M in sodium carbonate so that they are matrix matched with the sample solutions. Before using, the solutions should be placed in an ultrasonic bath for 10 minutes to ensure all $Na_2CO_3$ is in solution. These standard solutions are stable for at least 3 months. Discard when the bottle is less than one-fourth of the initial volume to minimize evaporative concentration effects over time.

12) *Working standards ($Na_2CO_3$ solutions)* Make up as for $Na_2CO_3$ working standards, but addg 2g of NaOH to matrix match the solutions.

| Prepared standard concentration | Volume of 1000ppm silica standard | Volume of MilliQ water added |
|---|---|---|
| 1.43mM | 1 ml | 24 ml |
| 2.85mM | 2ml | 23 ml |
| 4.27mM | 3ml | 22 ml |
| 5.70mM | 4ml | 21 ml |
| 7.12mM | 5ml | 20 ml |

Table A1.1. Volumes of silica standard solution used in preparation of experimental standards

### A1.3 CLEANING

All equipment was cleaned by soaking overnight in a 10% Micro solution. Following this detergent residues were removed by rinsing in MilliQ and the equipment was air-dried overnight. To minimize risk of contamination equipment used in standard preparation and storage was also soaked in 10% HCl over night, rinsed in MilliQ and air-dried.

### A1.4 DOUBLE ALKALINE EXTRATION PROCEDURE

*Day 1.*

1) Freeze dry over night to remove excess water.

2) Samples were crushed in a plastic cup using a polypropelene test tube. Agate pestle and mortal traditionally used for sample crushing have high silica contents, and may contibute to the final Si concentration. Previously, forams have been crushed between two glass plates, but again there is the possibility of Si contamination.

3) Weigh out 5mg of the sample into 13ml polythene tubes. MF uses 25mg, in this study the high content of silica of LDM sediments allowed the scaling down of the whole procedure to use the more convient 13ml size tubes. Meaning that large batches came be processed in the centrifuge and water baths.

4) Add 1ml of 10% $H_2O_2$ solution, flick to mix. The samples were then placed in the ultrasounic bath (Decon FS100b) for 1 minute and allowed to stand for 30 minutes. This procedure removes organic matter.

5) Add 1ml of 1N HCl to remove the $CaCO_3$, flick to mix. The samples were then placed in the ultrasounic bath for 1 minute and allowed to stand for 30 minutes.

6) Add 8ml of MilliQ, flick to mix and then centrifuge at 3500 rpm for 15 minutes (MF uses a higher rpm for less time, but comparable results have been found using 3600rpm for 11 minutes at UEA).

7) The samples were placed in an oven (60°C) to dry overnight. The tubes should be uncapped to allow the moisture to escape but should be covered with foil to prevent material from the oven falling in. (n.b. samples containing a high proportion of clay should not be dried to hardness, but should remain moist to allow for dissaggregation during opal extration).

*Day 2.*

Samples are handed in sets of four to allow accurate timing of each step.

9) Add exactly 8ml of 2M $Na_2CO_3$ solution to the first four tubes. Cap and flick to mix.

11) Place in a heated ultrasonic bath for 1 minute

12) Transfer tubes to a constant temperature water bath at 85°C.

13) Repeat steps 9-12 for sets of four samples until all samples have been processed. Accurate timing of each step can be ensured by using set time intervals and recording actions in a chart of the form:

| Tube number | Time $Na_2CO_3$ added | 2hrs ultrasound | 4hrs ultrasound | 6hrs ultrasound | Time centrifuged | Comments |
|---|---|---|---|---|---|---|
| #1-4 | 8.05 | 10.10 | 12.10 | 14.10 | 15.10 | |
| #5-8 | 8.21 | 10.26 | 12.26 | 14.26 | 15.26 | *e.g. #5 - cap loose* |
| | | | | | | |

14) After 2 hours remove each sample set (of four tubes). Flick each tube to resupend the solids and place in a heated ultrasonic for 1 minute.

15) After 4 hours repeat stage 14.

16) After 6 hours repeat stage 14.

17) After 7 hours remove each sample set and immediately centrifuge at 3500rpm for 11 minutes. Pipette about 4ml of the clear supernatant into a polyethelene tube and store for subsequent analysis.

18) Decanted off the remaining supernant and dry the residue in an oven (at 60°C) over night. This residue is used in the second extraction stage.

*Day 3*

19) Using the dried residue samples from step 18, repeat steps 9-16 using 2M NaOH for alkaline dissolution (instead of 2M $Na_2CO_3$).

20) After 8 hours remove each sample set and immediately centrifuge at 3500rpm for 11 minutes. Pipette about 4ml of the clear supernatant into a polyethelene tube and store for subsequent analysis.

21) Decant and discard the remaining supernant

22) Slowly add 10%HCl solution until there is no further effervense (about 5ml), then top up tubes to 12ml using MilliQ

23) Centrifuge at 3500rpm for 11 minutes, decant and discard supernant.

24) Add 12ml MilliQ and flick to mix, then repeat step 22.

25) The rinsed residue can be checked using a smear slide to ensure complete dissolution of frustules

### A1.5 Analysis

SAFETY SPECTACLES AND GLOVES SHOULD BE WORN FOR THE WHOLE OF THIS PROCEDURE.

1) Place sample solutions in ultrasonic bath for 10 minutes to redissolve any precipitates.

2) Prepare tray of 15ml medicine cups. Allow three cups per sample or calibration standard. Calibrating each sets of analyses independently should minimize systematic errors associated with standard solutions and experimental conditions. Comparision of measurements from standard solutions from different analyses adds another test of long term statistical reproducibility

3) Add 7ml of molybdate solution each medicine cup.

4) Working at 30 second intervals, add 100µl of the sample or calibation standard solution to each cup, followed by two aliquots of 100µl of MilliQ to rinse the pipette tip, flick to mix.

5) Leave each cup for exactly 20 minutes to react. The time for formation of silicomolybdate is critical and must be the same (within 30s, Fanning and Pilson 1973) for each analysis carried out. By filling the tubes at 30s intervals these time can be accurately controlled.

6) Working at 30s intervals, pipette 3.0ml of the reducing working solution to each tube, flick to mix.

7) Leave the solutions to stand to complete the reaction of the silicomolybdate complex. The blue colour takes about three hours to develop. Solutions are stable for up to 12 hours.

8) Read the absorbances in using 5cm sipper cell against MilliQ in a spectrophotometer (Hitachi U-2000) set at 812nm. Measure the standard solutions first, using the spectrophotometer software to calculate the calibration curve, then measure the sample solutions.

### A1.6 Blanks and internal standards

*MilliQ blank.* The MilliQ blank is composed of MilliQ plus the colour forming reagents and is analysed with every batch of silica determinations to ensure there is no contamination. Provided high quality analytical grade chemicals are used, reagent blanks should have absorbances near zero (<0.001).

*Operational blank.* This is the alkaline extract that has been through the extraction and analytical processes without the added sediment sample. Two or three blanks are analysed together to provide replicate values. The absorbances should be less than 0.003 units higher than the zero standard calibration, and is used to correct the sample absorbances.

*Zero standard.* This acts as both a zero calibration and as a check on the operational blanks. It should display absorbances less than 0.002 higher than the reagent blank. This absorbance results from the silica in $Na_2CO_3$ and NaOH.

*Internal standards* With each extraction and analysis set two samples of each internal standard are run along side the actual samples. There are two internal standards a) a diatom rich mud from the Peruvian coast which contains 17.5±2%OPAL. The sample has been freeze-dried and thoughly homogenized and so should give consistent results. b) LDM remaining from the Hole 844B samples. Sediment left over after opal and other analysis processes were completed was collected and throughly homogenized to give a standard of 57.9±3%OPAL.

### A1.7 CALCULATIONS

$C_{STD}$ Silica concentration of the working standard (mM)

$C_S$ Silica concentration of the sample (mM)

$A_{STD}$ Absorbance of the standard (average of duplicates: absorbance units)

$A_s$ Absorbance of the sample (average of duplicates; absorbance units)

$A_O$ Absorbance of the operational blank (average of two pairs of duplicate; absorbance units)

$F$ F-factor (mM/Abs). F=1/S, where S is the slope of a linear regressio through the standard curve: a plot of $A_{STD}$ vs $C_{STD}$ for all the standards. The linear regression should yeild a correlation coefficient ($r^2$) greater than 0.99.

$M$ Sample mass (mg)

The concentration of dissolved silica in each sample is determined by the equation

$$C_S = F \times (A_S - A_O)$$

MF give typical values of $F$ as 9.20 ± 0.2 mM/Abs (thus an 8mM standard should give an aborbance of 0.87 Abs units) and values of S, expected from the standard curve, as 0.109 ± 0.002 Abs/mM. This calculation is carried out by the spectrophotometer software.

The weight percent of silicon is calculated as $\%Si_{OPAL} = 100 \times (C_S/M) \times (28.09 g\ mol^{-1}) \times (0.008\ l) \times (1000\ mg\ g^{-1}) \times (mol\ 1000\ mmol^{-1})$ i.e.

$$\%Si_{OPAL} = 22.472 \times (C_S/M)$$

For values expressed as weight percent of opal (under 30Ma old most diatomaceous sediments appear to display a relatively constant water content of about 10%), therefore;

$$\%OPAL = 2.4 \times \%Si_{OPAL}$$

### A1.8 STATISTICAL REPRODUCIBILITY

Long term statisitical reproducibility was determined using two internal standards measured with every sample set, see Section 3.4.2.3. Pooled precision for 35 duplicated samples of a range of opal contents (13-60% OPAL) gives a coefficient of variation of 1.45.

### A1.9 SOURCES OF ERROR

The main source of error is in the pipetting - from three sources;

1) Errors in pipette volumes were estimated using MilliQ at 20°C pipetted into a small glass jar with ground glass cap on balance. The pipettes were recalibrated as necessary and typically, measurements had accuracies of around ±0.1%. Errors associated with grease and dirt on the glass was minimized by using gloves.

2) Fluid clinging to the outside of the pipette tip can be transferred into test tubes during analysis, this effect being most marked when pipetting very small volumes (e.g. 25µl). To minimize this error, only the point of the pipette tip was allowed into the source liquid, it was not allowed to touch either the side of the liquid in the receiving test tube.

3) The 2M $Na_2CO_3$ solution is close to saturation and precipitates over any available surface, including the inside of the pippette tips. In order to reduce this problem the tips are rinsed with aliqouts of MilliQ (added to analysis solutions) immediately after each addition. This process was used for both samples and standards so the increased dilution by these aliquots does not need to be taken into consideration.

4) Spectrophotometer readings tend to drift, especially just after the machine is switched on. These errors were avoided by allowing the machine to warm up (about 15 minutes) before use.

5) Incomplete disolution of biogenic material reduces the $\%Si_{OPAL}$ measured. Smear slides of the centrifuge residue showed the level of dissolution reached. This error was minimized for LDM samples by using the double dissolution method (see Section 3.4.3).

6) Volume errors in working solutions are systematic through the experiment so long as the standards are calculated using the same set of solutions.

7) Balance errors were minimized by testing the balance regularly using a standard one gram weight and recalibrating as necessary (typically errors were less than 0.02mg).

## A1.10 VALIDATION OF DOUBLE DISSOLUTION ESTIMATES FOR T. LONGISSIMA GROUP DIATOM CONTENT

Point-counted samples giving species composition used to establish relationship between proportion of biogenic opal released in the second extraction stage and sample *Thalassiothrix* spp. content.

| SAMPLE ID | POINT COUNTS (% of species composition) | | | % SECOND EXTRACTION OPAL (as a proportion of total |
|---|---|---|---|---|
| | THALASSIOTHRIX | RADIOLARIANS | OTHER DIATOMS | |
| A1 | 59.0 | 10.3 | 30.8 | 16.89 |
| A2 | 68.2 | 13.2 | 18.6 | 14.14 |
| A3 | 70.2 | 7.5 | 22.4 | 14.40 |
| A4 | 55.0 | 15.7 | 29.3 | 20.06 |
| A5 | 65.9 | 17.0 | 17.0 | 18.58 |
| A6 | 63.1 | 14.5 | 21.2 | 17.87 |
| A7 | 65.9 | 14.3 | 19.8 | 18.94 |
| A8 | 61.5 | 22.9 | 20.8 | 20.04 |
| A9 | 68.5 | 5.6 | 25.8 | 21.89 |
| A10 | 60.2 | 7.9 | 32.0 | 31.88 |
| A11 | 56.3 | 10.7 | 23.3 | 28.27 |
| A12 | 62.4 | 11.8 | 25.8 | 31.91 |
| B1 | 67.9 | 15.0 | 17.1 | 8.87 |
| B2 | 78.9 | 7.0 | 14.0 | 7.96 |
| B3 | 75.3 | 5.9 | 18.9 | 6.07 |
| B4 | 74.0 | 8.3 | 17.8 | 11.7 |
| B5 | 70.3 | 12.2 | 17.5 | 8.31 |
| B6 | 75.0 | 10.7 | 14.9 | 9.61 |
| B7 | 70.5 | 9.8 | 19.7 | 4.75 |
| E1 | 51.3 | 17.6 | 31.1 | 22.41 |
| E2 | 62.8 | 11.7 | 25.5 | 16.21 |
| E3 | 56.8 | 10.8 | 34.6 | 31.97 |

# APPENDIX 2: ORGANIC AND INORGANIC CARBON DETERMINATION METHOD

## A2.1 INTRODUCTION

This method is based on that of Cutter and Radford-Knoery (1991). The rationale for this choice of this method is dicussed in Section 3.5.

## A2.2 PROCEDURES

1) Clean tin cups in furnace at 450-550°C overnight.

2) Freeze dry bulk samples over night, keep samples in dessicator after this to prevent re hydration and associated errors.

3) Powder and thoroughly homogenize samples using agate pestle and mortar, for small samples, crush between two plates of glass.

4) For each sample weigh approximately 5-10mg of the sample into each of two tin cups. Holding the rim of the cup with the curved forceps tap it on the glass plate to shake down the contents. Unconsolidated sediments can be pushed into the cup using the wrong end of the microspatula. Reserve one cup for organic carbon analysis and close the second for total carbon. Place the closed and open cups in corresponding hole in two microtest plates. To close the cup: a) holding the cup with the blunt forceps pinch the top shut using the curved forceps, b) fold the top over and pinch to seal, c) shape the cup into an approximate ball shape (this is to prevent the sample from catching on the sides of the auto-analyser or combustion column, or scratching the surfaces of the sample slide which could result in gas leaks). If any of the sample escapes onto the glass plate discard and replace the sample.

5) For the organic carbon samples, damp sediment with MilliQ, part fill each of the open cups with 10%HCl, to remove organic carbon. Evaporate off the acid on hot plate in a fume cupboard. Repeat this process until there is no effervesense to ensure complete removal of inorganic carbon. If any of the sample is lost due to explosive effervesense discard and replace.

6) Close these cups over the glass plate and form into balls as above, being careful to ensure that material is not lost. Material caught on the sides from scum floating on the surface of the acid, making material more likely to be lost at this stage. If any of the sample is lost discard and replace.

7) Place prepared samples in the autosampler of CN analyser and analysed.

## A2.3 CALIBRATION AND STANDARDS

1) Weight out at least three samples of Actinalide with a spread of masses (e.g. 4, 6 and 8mg), close cups and form into balls as above.

2) Run CN analyser for standards, entering weights of standard samples on to computer.

3) Recalculate standards as unknowns, they should scatter around calibration curve. If there is a cluster of higher points at one end of the curve and lower points at the other the standards could either be repeated or the curve could be tweeked. The values of blanks should be checked to evaluate carbon contamination from the cups or acid, which could result in this effect.

4) Try to balance the counts for standards and samples for carbon and nitrogen to within at least an order of magnitude.

5) Run internal standards with each run, preferably at both the begining and the end. This should be constant within and between runs.

### A2.4 BLANKS

With each run include;

1) Two-three empty cups moulded into balls, these should identify problems with carbon inclusions in the cups and insufficent cleaning.

2) Two-three acid blanks, cups which have been through the acid evaporation stage of the process without the sediment. These are to identify any carbon contained in the acids.

If the blanks show a carbon content the run should be repeated, if this is not possible the average blank values should be subtrated from the carbon values.

### A2.5 CALCULATIONS

Inorganic and total carbon values can be taken directly from the computer read-out provided by the software linked to the CN-analyser, giving $\%C_{org}$ and $\%C_{total}$. Values for inorganic (carbonate) carbon are calculated from the difference between $\%C_{total}$ and $\%C_{org}$.

$$\%CaCO_3 = 8.33 \times (C_{total} - C_{org})$$

# APPENDIX 3 : SPECTRAL ANALYSIS METHODS

## A3.1 INTRODUCTION

Conventional spectral analysis methods using fast fourier transforms (FFT) demand regular spaced data sets. The variable thickness of lamina couplets and colour bands within laminated sections (on which sampling was based) result in an uneven sample spacing. Interpolating the data sets on to an even spacing is one way of getting aroung this problem, but the interpolated data does not always give a convincing match with the original data, see Figure A3.1. When the interpolated data sets are analysed using FFT spectral analysis methods, large gaps between the original data points often result in a spurious bulge of power at low frequencies with wavelengths comparable to the data set gaps, see Figure A3.2. Linear interpolation produces better fits to the origonal data, but is prone to producing a low frequency power bulge. Cubic or higher order splines do not have as larger a tendency to produce the low frequency bulge, but may generate spurious peaks in the interpolated data set.

## A3.2 THE LOMB METHOD

A completely different method of spectral analysis was developed by Lomb (1976) and elaborated by Scargle (1982). The Lomb method uses unevely spaced data, calculating values only at the measured sample points. The method also weights the data on a 'per point' basis, rather than a 'per time interval' basis when interpolation could lead to serious errors. This method has the adavantage over FFT methods in that the use of unevenly spaced data allows the estimation of frequencies above the Nyquist frequency[1], although care must be taken. The uneven spacing results in some points having a much closer spacing, reducing the aliasing effect[1].

[1] The Nyquist frequency, $f_c$, is the inverse of twice the sample spacing $f_c=1/2\Delta$, where $\Delta$ is the sample spacing. Discrete sampling results in all of the spectral density ouside the range $-f_c<f<f_c$ being spuriously moved into this range, the aliasing effect.

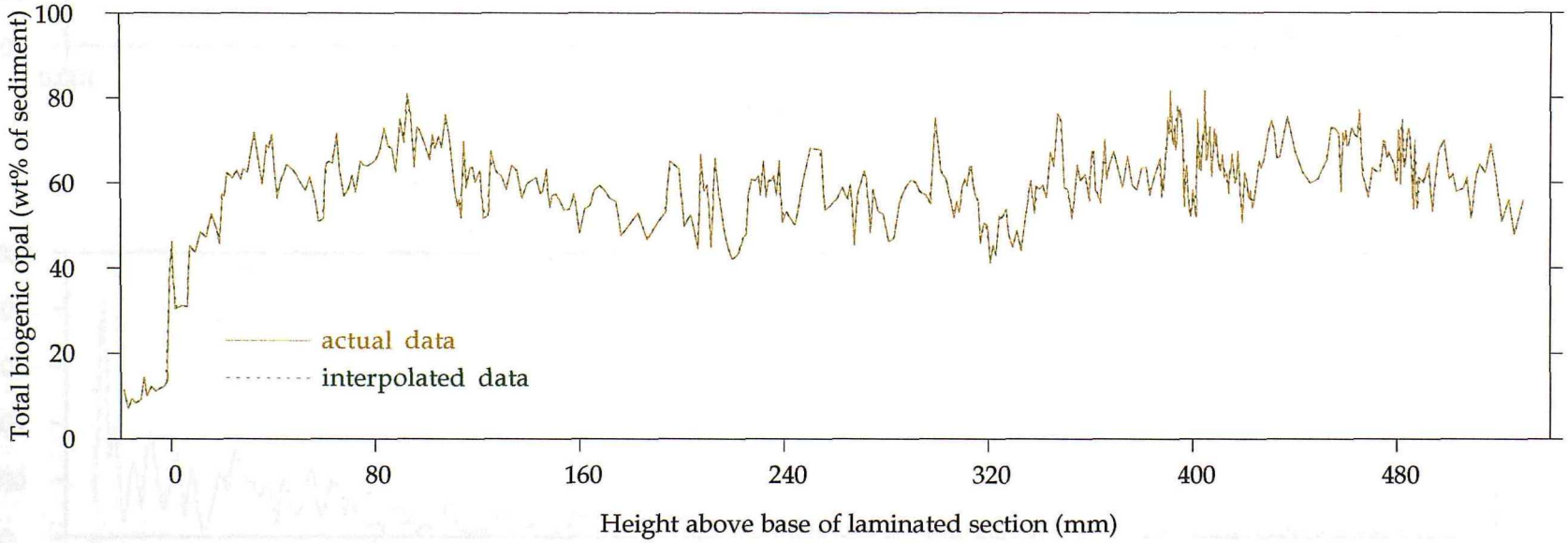


Figure A3.1. Comparision of actual and interpolated data-sets for the total opal content of the $OPAL850_{STRETCHED}$ record. Note the especially weak match between the two datasets in regions of closely spaced data points.

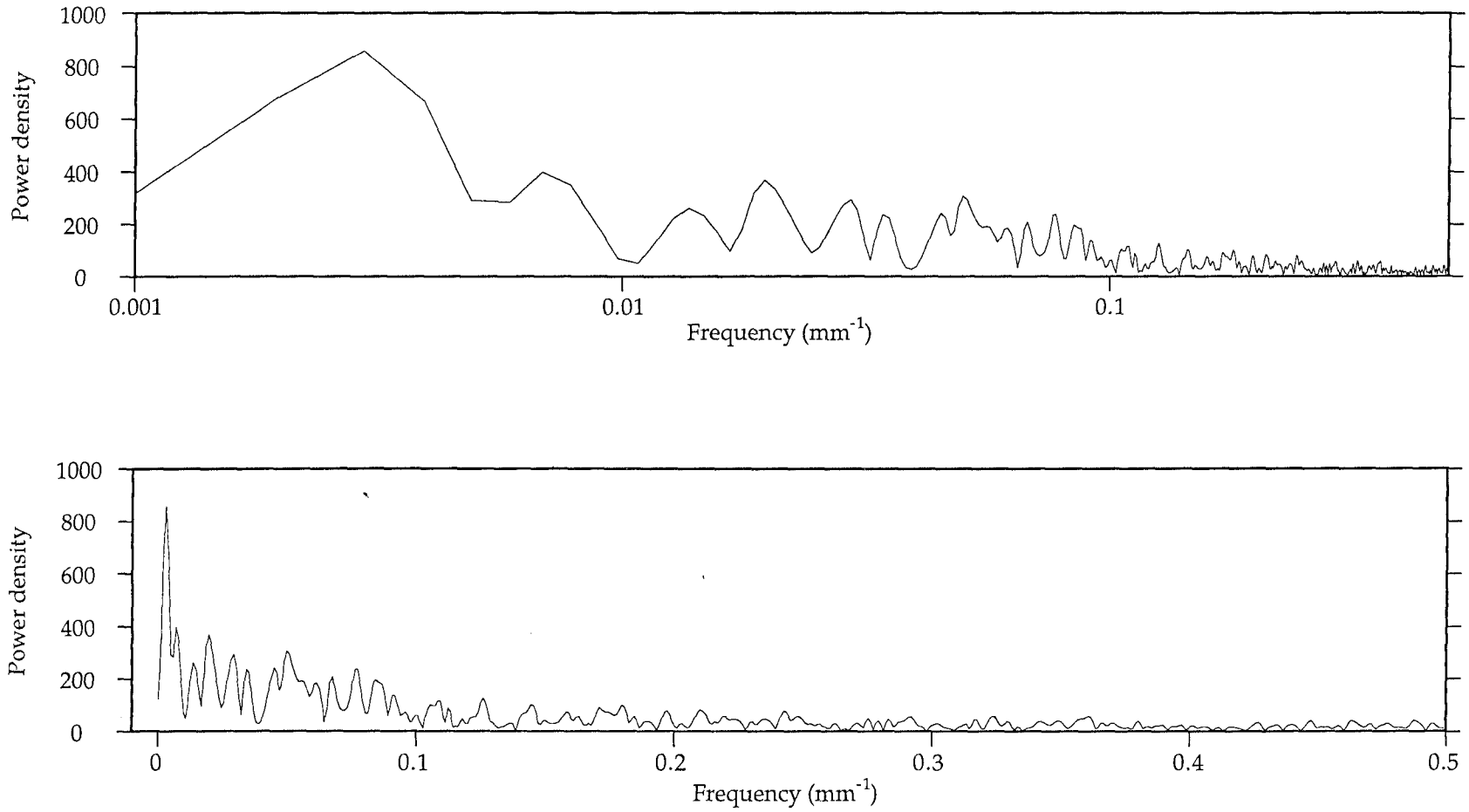


Figure A3.2. Power density spectrum for total opal record for interpolated $OPAL850_{STRETCHED}$ calculated using the standard fast fourier transform method (FFT). Plotted on both liner and log frequency axes for comparision.

For a data set $\{h_i\}$ sampled at times $\{t_i\}$, where i=1.....N, and given the definition of $\tau$ as;

$$\tan(2\omega\tau) = \frac{\Sigma_j \sin(\omega t_j)}{\Sigma_j \cos(\omega t_j)}$$ Equation A3.1

and the mean and population deviation respectively as;

$$\overline{h} = \frac{1}{N}\sum_1^N h_i \qquad \sigma^2 = \frac{1}{N-1}\sum_1^N (h_1 - \overline{h})^2$$ Equations A3.2 and A3.3

the normalized Lomb periodgram (with power density, P, as a function of angular frequency, $\omega$) is calculated as;

$$P_N(\omega) = \frac{1}{2\sigma^2}\left\{\frac{\Sigma_j\left[(h_j - \overline{h})\cos\omega(t_j - \tau)\right]^2}{\Sigma_j \cos^2\omega(t_j - \tau)} + \frac{\Sigma_j\left[(h_j - \overline{h})\sin\omega(t_j - \tau)\right]^2}{\Sigma_j \sin^2\omega(t_j - \tau)}\right\}$$

Equation A3.4

The power is calculated at a set of discrete frequencies $\{\omega_j\}$, this gives an approximation to the continous power spectrum, see Figure A3.3. The input frequency ranges from the inverse of the minimum spacing to the inverse [max($t_i$)-min($t_i$)] i.e. the frequency if the data set is one wavelength long.

### A3.3 Significance Levels

Assuming the measured data points are the sum of a periodic signal and independant (white) Gausian noise, the significance levels of peaks in power density need to be evaluated. White noise is noise which has equal power at all frequencies (Schwartz, 1970), i.e. the noise at any frequency is a) statistically independant of all other frequency components and, b) has the same probability density function as all the other components, meaning that the probability distribution of Gausian white noise has unit mean. Scargle (1982) showed that if the data points are independent Gausian variables (i.e. white noise), $P_N(\omega)$ has an exponential probablity distribution with unit mean (the Lomb periodogram is normalized by $\sigma^2$ in the denominator of Equation A3.4), i.e. the probablity that $P_N(\omega)$ is between some positive value $z$ and $dz$ is $\exp(-z)dz$. Scanning a given number of independant frequencies (M), the probablity that none of the given values are larger than $z$ is $(1-e^{-z})^M$,

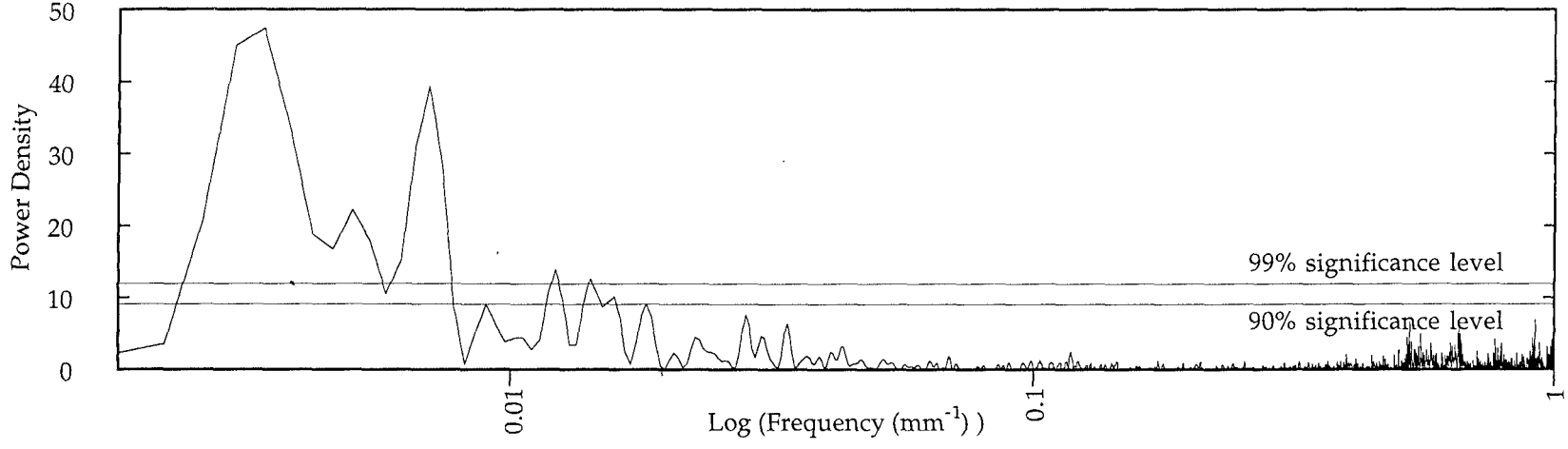


Figure A3.3. Power spectrum for total opal $OPAL850_{STRETCHED}$ record calculated using the Lomb method showing estimated significance levels. Note the absence of the low frequency bulge charateristic of interpolated data.

$$\text{Prob}(z > z_0) = 1 - (1 - e^{-z})^M \qquad \text{Equation A3.5}$$

Rearranging this equation in terms of $z_0$

$$z_0 = -\ln(1 - \sqrt[M]{1 - \text{Prob}(z > z_0)}) \qquad \text{Equation A3.6}$$

and taking Prob($z > z_0$) at standard significance levels (0.5, 0.1, 0.05 and 0.01) allows the calculation of the values of $z_0$ for each significance level, see Figure A3.3.

The number of independant frequencies, M, used is estimated from the power spectrum. In general M should be approximately equal to N (Press *et al.*, 1992) provided that 1) the frequency space of the poer spectra is oversampled by a factor of at least four (to make sure that as much information as possible is extracted) and, 2) the data is not clumped, for example, into groups of three data points.

## APPENDIX 4: STATISTICAL METHODS

The statistical methods used in this study are taken from Owen and Jones (1982). The two most commonly used methods, used for comparision of population means and testing the signifcane of correlation coefficient are summarized below. Long-term precision of chemical measurements was estimated using pooled standard deviation.

### A4.1 COMPARISION OF MEANS

This method is used to test whether two sample groups e.g. LDM and non-LDM samples are similar using sample population means and standard deviations (see p.318, Owen and Jones, 1982).

Assuming the samples are draw from the same overall population the means of the two group should be the same, i.e. the null hypothesis is;

$$H_0 : \mu_1 = \mu_2$$

Calculating the sample variance as;

$$s^2 = \frac{\Sigma x^2}{n} - \left(\frac{\Sigma x}{n}\right)^2 \qquad \text{Equation A4.1}$$

The standard deviation of the two sample populations can be calculated as;

$$\sigma^2 = \frac{ns^2}{n-1} \qquad \text{Equation A4.2}$$

If the null hypothesis holds the two sample sets were drawn from the same inital population which should have a variance of;

$$\sigma^2 = \frac{n_1 s_1 + n_2 s_2}{n_1 + n_2 - 2} \qquad \text{Equation A4.3}$$

The standard error of the two independent means is;

$$S_r = \sqrt{\frac{\sigma^2}{n_1} + \frac{\sigma^2}{n_2}} \qquad \text{Equation A4.4}$$

Using this value the test statistic, t can be calculated as;

$$t = \frac{|\overline{x}_1 - \overline{x}_2| - 0}{S_r} \qquad \text{Equation A4.5}$$

The sample groups are significantly different if the calculate value of t is greater than the

critical value of t for $(n_1+n_2-2)$ degrees of freedom found in standard statistical tables

### A4.2 SIGNIFICANCE OF CORRELATION COEFFICIENTS

This method is used to test the significance of correlation coefficents calculated for best-fit lines through scatter plots (for futher details refer to p363 of Owen and Jones, 1982). This method allows an estimation of the significance of a regression line, taking into account the number of data-points used in the calculations. Assuming the sample data set is drawn from a population with a zero correlation coefficient gives a null hypothesis of;

$$H_0 : r=0$$

If $H_0$ is true r should be distributed about zero with standard error and (n-2) degrees of freedom, i.e.;

$$S_r = \sqrt{\frac{1-r^2}{n-2}} \qquad \text{Equation A4.6}$$

The correlation is significant if the test statistic, t;

$$t = \frac{r-0}{S_r} \qquad \text{Equation A4.7}$$

is greater than the critical value for t with (n-2) degrees of freedom found in standard statisitical tables. All correlation coefficients given in this study are significant at the 95% level.

### A4.3 ESTIMATION OF PRECISION IN CHEMICAL EXPERIMENTS

Long-term precision of chemical methods is estimated using pooled standard deviations of internal standards calculated as;

$$s_{pooled} = \sqrt{\frac{\text{sample standard deviation}}{\text{no. measurements} - \text{no. samples}}} \qquad \text{Equation A4.8}$$

## APPENDIX 5: LAMINA COUPLET DATA

Measurements of lamina couplet thickness for lower 10.4cm of the '4.4Ma' LDM basal unit from Site 847B (ODP-138-847B-15H-7, 78-88cm). Measurements were made from x20 BSEI photomosiacs and scaled to account for sinkage during sample impregnation. Couplets are numbered upwards from lower boundary of basal unit.

| Couplet ID number | Cummulative thickness (mm, to centre of couplet) | Mat layer thickness (mm) | Mixed assemblage layer thickness (mm) | Total couplet thickness (mm) |
|---|---|---|---|---|
| 1 | 0.175 | 0.25 | 0.1 | 0.35 |
| 2 | 0.575 | 0.3 | 0.15 | 0.45 |
| 3 | 0.95 | 0.2 | 0.1 | 0.30 |
| 4 | 1.2 | 0.1 | 0.1 | 0.20 |
| 5 | 1.365 | 0.08 | 0.05 | 0.13 |
| 6 | 1.495 | 0.09 | 0.04 | 0.13 |
| 7 | 1.675 | 0.12 | 0.11 | 0.23 |
| 8 | 1.95 | 0.17 | 0.15 | 0.32 |
| 9 | 2.26 | 0.25 | 0.05 | 0.30 |
| 10 | 2.735 | 0.25 | 0.4 | 0.65 |
| 11 | 3.205 | 0.12 | 0.17 | 0.29 |
| 12 | 3.455 | 0.1 | 0.11 | 0.21 |
| 13 | 3.695 | 0.15 | 0.12 | 0.27 |
| 14 | 3.99 | 0.25 | 0.07 | 0.32 |
| 15 | 4.25 | 0.12 | 0.08 | 0.20 |
| 16 | 4.625 | 0.25 | 0.3 | 0.55 |
| 17 | 5.11 | 0.35 | 0.07 | 0.42 |
| 18 | 5.605 | 0.4 | 0.17 | 0.57 |
| 19 | 6.045 | 0.23 | 0.08 | 0.31 |
| 20 | 7.225 | 0 | 2.05 | 2.05 |
| 21 | 8.39 | 0.2 | 0.08 | 0.28 |
| 22 | 8.715 | 0.25 | 0.12 | 0.37 |
| 23 | 9.06 | 0.17 | 0.15 | 0.32 |
| 24 | 9.52 | 0.45 | 0.15 | 0.60 |
| 25 | 10.045 | 0.25 | 0.2 | 0.45 |
| 26 | 10.87 | 0 | 1.2 | 1.20 |

| Couplet ID number | Cummulative thickness (mm, to centre of couplet) | Mat layer thickness (mm) | Mixed assemblage layer thickness (mm) | Total couplet thickness (mm) |
|---|---|---|---|---|
| 27 | 11.83 | 0.37 | 0.35 | 0.72 |
| 28 | 12.325 | 0.17 | 0.1 | 0.27 |
| 29 | 12.58 | 0.17 | 0.07 | 0.24 |
| 30 | 12.955 | 0.26 | 0.25 | 0.51 |
| 31 | 13.39 | 0.22 | 0.14 | 0.36 |
| 32 | 13.76 | 0.27 | 0.11 | 0.38 |
| 33 | 14.2 | 0.45 | 0.05 | 0.50 |
| 34 | 14.575 | 0.2 | 0.05 | 0.25 |
| 35 | 14.95 | 0 | 0.5 | 0.50 |
| 36 | 15.425 | 0.25 | 0.2 | 0.45 |
| 37 | 15.825 | 0.15 | 0.2 | 0.35 |
| 38 | 16.12 | 0.12 | 0.12 | 0.24 |
| 39 | 16.35 | 0.1 | 0.12 | 0.22 |
| 40 | 16.59 | 0.12 | 0.14 | 0.26 |
| 41 | 16.95 | 0.32 | 0.14 | 0.46 |
| 42 | 17.5 | 0.54 | 0.1 | 0.64 |
| 43 | 17.93 | 0.07 | 0.15 | 0.22 |
| 44 | 18.32 | 0.4 | 0.16 | 0.56 |
| 45 | 18.775 | 0.17 | 0.18 | 0.35 |
| 46 | 19.15 | 0.25 | 0.15 | 0.40 |
| 47 | 19.545 | 0.31 | 0.08 | 0.39 |
| 48 | 19.975 | 0.3 | 0.17 | 0.47 |
| 49 | 20.37 | 0.22 | 0.1 | 0.32 |
| 50 | 20.705 | 0.25 | 0.1 | 0.35 |
| 51 | 21.13 | 0.2 | 0.3 | 0.50 |
| 52 | 21.55 | 0.24 | 0.1 | 0.34 |
| 53 | 21.905 | 0.28 | 0.09 | 0.37 |
| 54 | 22.34 | 0.35 | 0.15 | 0.50 |
| 55 | 22.775 | 0 | 0.37 | 0.37 |
| 56 | 23.16 | 0.15 | 0.25 | 0.40 |
| 57 | 23.595 | 0.35 | 0.12 | 0.47 |
| 58 | 23.955 | 0.05 | 0.2 | 0.25 |
| 59 | 24.21 | 0.1 | 0.16 | 0.26 |
| 60 | 24.465 | 0.15 | 0.1 | 0.25 |

| Couplet ID number | Cummulative thickness (mm, to centre of couplet) | Mat layer thickness (mm) | Mixed assemblage layer thickness (mm) | Total couplet thickness (mm) |
|---|---|---|---|---|
| 61 | 24.74 | 0.15 | 0.15 | 0.30 |
| 62 | 25.54 | 0 | 1.3 | 1.30 |
| 63 | 26.41 | 0.24 | 0.2 | 0.44 |
| 64 | 26.73 | 0.09 | 0.11 | 0.20 |
| 65 | 27.015 | 0.15 | 0.22 | 0.37 |
| 66 | 27.26 | 0.05 | 0.07 | 0.12 |
| 67 | 27.44 | 0.09 | 0.15 | 0.24 |
| 68 | 27.66 | 0.1 | 0.1 | 0.20 |
| 69 | 27.855 | 0.12 | 0.07 | 0.19 |
| 70 | 28.185 | 0.2 | 0.27 | 0.47 |
| 71 | 28.59 | 0.26 | 0.08 | 0.34 |
| 72 | 28.91 | 0.15 | 0.15 | 0.30 |
| 73 | 29.22 | 0.22 | 0.1 | 0.32 |
| 74 | 29.78 | 0.06 | 0.74 | 0.80 |
| 75 | 30.54 | 0.45 | 0.27 | 0.72 |
| 76 | 31.025 | 0.15 | 0.1 | 0.25 |
| 77 | 31.3 | 0.08 | 0.22 | 0.30 |
| 78 | 31.52 | 0.1 | 0.04 | 0.14 |
| 79 | 31.74 | 0.1 | 0.2 | 0.30 |
| 80 | 32.69 | 0 | 1.6 | 1.60 |
| 81 | 33.59 | 0.15 | 0.05 | 0.20 |
| 82 | 33.775 | 0.12 | 0.05 | 0.17 |
| 83 | 33.96 | 0.1 | 0.1 | 0.20 |
| 84 | 34.135 | 0.1 | 0.05 | 0.15 |
| 85 | 34.325 | 0.15 | 0.08 | 0.23 |
| 86 | 34.55 | 0.12 | 0.1 | 0.22 |
| 87 | 34.81 | 0.15 | 0.15 | 0.30 |
| 88 | 35.06 | 0.12 | 0.08 | 0.20 |
| 89 | 35.235 | 0.08 | 0.07 | 0.15 |
| 90 | 35.41 | 0.05 | 0.15 | 0.20 |
| 91 | 35.76 | 0.4 | 0.1 | 0.50 |
| 92 | 36.26 | 0.15 | 0.35 | 0.50 |
| 93 | 37.81 | 0 | 2.6 | 2.60 |
| 94 | 39.435 | 0.15 | 0.5 | 0.65 |

| Couplet ID number | Cummulative thickness (mm, to centre of couplet) | Mat layer thickness (mm) | Mixed assemblage layer thickness (mm) | Total couplet thickness (mm) |
|---|---|---|---|---|
| 95 | 39.845 | 0.1 | 0.07 | 0.17 |
| 96 | 40.115 | 0.2 | 0.17 | 0.37 |
| 97 | 40.65 | 0 | 0.7 | 0.70 |
| 98 | 41.11 | 0.1 | 0.12 | 0.22 |
| 99 | 41.455 | 0.35 | 0.12 | 0.47 |
| 100 | 41.915 | 0.25 | 0.2 | 0.45 |
| 101 | 42.265 | 0.1 | 0.15 | 0.25 |
| 102 | 42.725 | 0.5 | 0.17 | 0.67 |
| 103 | 43.385 | 0.35 | 0.3 | 0.65 |
| 104 | 43.86 | 0.25 | 0.05 | 0.30 |
| 105 | 44.22 | 0.25 | 0.17 | 0.42 |
| 106 | 44.715 | 0.45 | 0.12 | 0.57 |
| 107 | 45.725 | 0 | 1.45 | 1.45 |
| 108 | 46.65 | 0.15 | 0.25 | 0.40 |
| 109 | 46.955 | 0.17 | 0.04 | 0.21 |
| 110 | 47.145 | 0.1 | 0.07 | 0.17 |
| 111 | 47.34 | 0.15 | 0.07 | 0.22 |
| 112 | 47.72 | 0.3 | 0.24 | 0.54 |
| 113 | 48.16 | 0.27 | 0.07 | 0.34 |
| 114 | 48.43 | 0.18 | 0.02 | 0.20 |
| 115 | 48.73 | 0.13 | 0.27 | 0.40 |
| 116 | 49.205 | 0.45 | 0.1 | 0.55 |
| 117 | 49.53 | 0.05 | 0.05 | 0.10 |
| 118 | 49.755 | 0.1 | 0.25 | 0.35 |
| 119 | 50.045 | 0.08 | 0.15 | 0.23 |
| 120 | 50.27 | 0.12 | 0.1 | 0.22 |
| 121 | 50.53 | 0.25 | 0.05 | 0.30 |
| 122 | 50.815 | 0.15 | 0.12 | 0.27 |
| 123 | 51.15 | 0.3 | 0.1 | 0.40 |
| 124 | 51.51 | 0.2 | 0.12 | 0.32 |
| 125 | 51.895 | 0.25 | 0.2 | 0.45 |
| 126 | 52.77 | 0 | 1.3 | 1.30 |
| 127 | 53.595 | 0.15 | 0.2 | 0.35 |
| 128 | 53.895 | 0.12 | 0.13 | 0.25 |

| Couplet ID number | Cummulative thickness (mm, to centre of couplet) | Mat layer thickness (mm) | Mixed assemblage layer thickness (mm) | Total couplet thickness (mm) |
|---|---|---|---|---|
| 129 | 54.17 | 0.12 | 0.18 | 0.30 |
| 130 | 54.425 | 0.1 | 0.11 | 0.21 |
| 131 | 54.68 | 0.15 | 0.15 | 0.30 |
| 132 | 54.945 | 0.15 | 0.08 | 0.23 |
| 133 | 55.2 | 0.15 | 0.13 | 0.28 |
| 134 | 55.45 | 0.12 | 0.1 | 0.22 |
| 135 | 55.705 | 0.2 | 0.09 | 0.29 |
| 136 | 55.92 | 0.08 | 0.06 | 0.14 |
| 137 | 56.125 | 0.07 | 0.2 | 0.27 |
| 138 | 56.31 | 0.05 | 0.05 | 0.10 |
| 139 | 56.55 | 0.2 | 0.18 | 0.38 |
| 140 | 56.89 | 0.2 | 0.1 | 0.30 |
| 141 | 57.205 | 0.12 | 0.21 | 0.33 |
| 142 | 57.53 | 0.2 | 0.12 | 0.32 |
| 143 | 57.875 | 0.27 | 0.1 | 0.37 |
| 144 | 58.31 | 0.45 | 0.05 | 0.50 |
| 145 | 58.785 | 0.37 | 0.08 | 0.45 |
| 146 | 59.14 | 0.15 | 0.11 | 0.26 |
| 147 | 59.485 | 0.25 | 0.18 | 0.43 |
| 148 | 59.975 | 0 | 0.55 | 0.55 |
| 149 | 60.525 | 0.3 | 0.25 | 0.55 |
| 150 | 60.875 | 0.05 | 0.1 | 0.15 |
| 151 | 61.075 | 0.1 | 0.15 | 0.25 |
| 152 | 61.375 | 0.27 | 0.08 | 0.35 |
| 153 | 62.025 | 0 | 0.95 | 0.95 |
| 154 | 63.025 | 0 | 1.05 | 1.05 |
| 155 | 63.67 | 0.1 | 0.14 | 0.24 |
| 156 | 63.9 | 0.13 | 0.09 | 0.22 |
| 157 | 64.16 | 0.22 | 0.08 | 0.30 |
| 158 | 64.41 | 0.1 | 0.1 | 0.20 |
| 159 | 64.735 | 0.25 | 0.2 | 0.45 |
| 160 | 65.16 | 0.26 | 0.14 | 0.40 |
| 161 | 65.61 | 0 | 0.5 | 0.50 |
| 162 | 66.115 | 0.25 | 0.26 | 0.51 |

| Couplet ID number | Cummulative thickness (mm, to centre of couplet) | Mat layer thickness (mm) | Mixed assemblage layer thickness (mm) | Total couplet thickness (mm) |
|---|---|---|---|---|
| 163 | 66.57 | 0.31 | 0.09 | 0.40 |
| 164 | 66.92 | 0.25 | 0.05 | 0.30 |
| 165 | 67.145 | 0.06 | 0.09 | 0.15 |
| 166 | 67.4 | 0.29 | 0.07 | 0.36 |
| 167 | 67.955 | 0 | 0.75 | 0.75 |
| 168 | 68.46 | 0.22 | 0.04 | 0.26 |
| 169 | 68.655 | 0.07 | 0.06 | 0.13 |
| 170 | 68.855 | 0 | 0.27 | 0.27 |
| 171 | 69.13 | 0.08 | 0.2 | 0.28 |
| 172 | 69.5 | 0.24 | 0.22 | 0.46 |
| 173 | 69.855 | 0.15 | 0.1 | 0.25 |
| 174 | 70.08 | 0.07 | 0.13 | 0.20 |
| 175 | 70.33 | 0.09 | 0.21 | 0.30 |
| 176 | 70.495 | 0.01 | 0.02 | 0.03 |
| 177 | 70.525 | 0.01 | 0.02 | 0.03 |
| 178 | 70.555 | 0.01 | 0.02 | 0.03 |
| 179 | 70.67 | 0.01 | 0.19 | 0.20 |
| 180 | 70.9 | 0.06 | 0.2 | 0.26 |
| 181 | 71.505 | 0 | 0.95 | 0.95 |
| 182 | 72.095 | 0.15 | 0.08 | 0.23 |
| 183 | 72.295 | 0.12 | 0.05 | 0.17 |
| 184 | 72.505 | 0.12 | 0.13 | 0.25 |
| 185 | 72.795 | 0.18 | 0.15 | 0.33 |
| 186 | 73.12 | 0.2 | 0.12 | 0.32 |
| 187 | 73.505 | 0 | 0.45 | 0.45 |
| 188 | 73.855 | 0 | 0.25 | 0.25 |
| 189 | 74.175 | 0.25 | 0.14 | 0.39 |
| 190 | 74.495 | 0.15 | 0.1 | 0.25 |
| 191 | 74.83 | 0.22 | 0.2 | 0.42 |
| 192 | 75.34 | 0.45 | 0.15 | 0.60 |
| 193 | 75.865 | 0.2 | 0.25 | 0.45 |
| 194 | 76.34 | 0.42 | 0.08 | 0.50 |
| 195 | 76.795 | 0.26 | 0.15 | 0.41 |
| 196 | 77.15 | 0.15 | 0.15 | 0.30 |

| Couplet ID number | Cummulative thickness (mm, to centre of couplet) | Mat layer thickness (mm) | Mixed assemblage layer thickness (mm) | Total couplet thickness (mm) |
|---|---|---|---|---|
| 197 | 77.515 | 0.25 | 0.18 | 0.43 |
| 198 | 77.855 | 0.2 | 0.05 | 0.25 |
| 199 | 78.205 | 0.35 | 0.1 | 0.45 |
| 200 | 78.805 | 0 | 0.75 | 0.75 |
| 201 | 79.305 | 0.18 | 0.07 | 0.25 |
| 202 | 79.53 | 0 | 0.2 | 0.20 |
| 203 | 79.83 | 0.15 | 0.25 | 0.40 |
| 204 | 80.255 | 0.2 | 0.25 | 0.45 |
| 205 | 80.59 | 0 | 0.22 | 0.22 |
| 206 | 80.85 | 0 | 0.3 | 0.30 |
| 207 | 81.11 | 0.13 | 0.09 | 0.22 |
| 208 | 81.355 | 0.16 | 0.11 | 0.27 |
| 209 | 81.65 | 0 | 0.32 | 0.32 |
| 210 | 82.01 | 0 | 0.4 | 0.40 |
| 211 | 82.345 | 0 | 0.27 | 0.27 |
| 212 | 82.58 | 0.15 | 0.05 | 0.20 |
| 213 | 82.755 | 0.05 | 0.1 | 0.15 |
| 214 | 83.03 | 0 | 0.4 | 0.40 |
| 215 | 83.36 | 0.16 | 0.1 | 0.26 |
| 216 | 83.615 | 0.12 | 0.13 | 0.25 |
| 217 | 83.96 | 0.22 | 0.22 | 0.44 |
| 218 | 84.305 | 0.16 | 0.09 | 0.25 |
| 219 | 84.56 | 0.15 | 0.11 | 0.26 |
| 220 | 84.845 | 0.17 | 0.14 | 0.31 |
| 221 | 85.1 | 0.1 | 0.1 | 0.20 |
| 222 | 85.355 | 0.25 | 0.06 | 0.31 |
| 223 | 85.66 | 0.2 | 0.1 | 0.30 |
| 224 | 85.885 | 0.1 | 0.05 | 0.15 |
| 225 | 86.07 | 0.14 | 0.08 | 0.22 |
| 226 | 86.515 | 0.3 | 0.37 | 0.67 |
| 227 | 87.05 | 0.18 | 0.22 | 0.40 |
| 228 | 87.4 | 0.1 | 0.2 | 0.30 |
| 229 | 87.68 | 0.16 | 0.1 | 0.26 |
| 230 | 87.91 | 0.15 | 0.05 | 0.20 |

| Couplet ID number | Cummulative thickness (mm, to centre of couplet) | Mat layer thickness (mm) | Mixed assemblage layer thickness (mm) | Total couplet thickness (mm) |
|---|---|---|---|---|
| 231 | 88.16 | 0.15 | 0.15 | 0.30 |
| 232 | 89.26 | 0 | 1.9 | 1.90 |
| 233 | 90.585 | 0 | 0.75 | 0.75 |
| 234 | 91.035 | 0.05 | 0.1 | 0.15 |
| 235 | 91.19 | 0.1 | 0.06 | 0.16 |
| 236 | 91.57 | 0.25 | 0.35 | 0.60 |
| 237 | 92.105 | 0.2 | 0.27 | 0.47 |
| 238 | 92.425 | 0.12 | 0.05 | 0.17 |
| 239 | 92.76 | 0.07 | 0.43 | 0.50 |
| 240 | 93.135 | 0.12 | 0.13 | 0.25 |
| 241 | 93.42 | 0.25 | 0.07 | 0.32 |
| 242 | 93.68 | 0.09 | 0.11 | 0.20 |
| 243 | 93.855 | 0.09 | 0.06 | 0.15 |
| 244 | 94.04 | 0.07 | 0.15 | 0.22 |
| 245 | 94.375 | 0.35 | 0.1 | 0.45 |
| 246 | 94.75 | 0.2 | 0.1 | 0.30 |
| 247 | 95.4 | 0 | 1 | 1.00 |
| 248 | 96.075 | 0.2 | 0.15 | 0.35 |
| 249 | 96.615 | 0 | 0.73 | 0.73 |
| 250 | 97.205 | 0.25 | 0.2 | 0.45 |
| 251 | 97.605 | 0.25 | 0.1 | 0.35 |
| 252 | 97.89 | 0.14 | 0.08 | 0.22 |
| 253 | 98.14 | 0.18 | 0.1 | 0.28 |
| 254 | 98.69 | 0 | 0.82 | 0.82 |
| 255 | 99.17 | 0.06 | 0.08 | 0.14 |
| 256 | 99.325 | 0.1 | 0.07 | 0.17 |
| 257 | 99.635 | 0.11 | 0.34 | 0.45 |
| 258 | 99.985 | 0.15 | 0.1 | 0.25 |
| 259 | 100.235 | 0.1 | 0.15 | 0.25 |
| 260 | 100.575 | 0.18 | 0.25 | 0.43 |
| 261 | 100.96 | 0.16 | 0.18 | 0.34 |
| 262 | 101.33 | 0.25 | 0.15 | 0.40 |
| 263 | 101.59 | 0.07 | 0.05 | 0.12 |
| 264 | 101.825 | 0.25 | 0.1 | 0.35 |

| Couplet ID number | Cummulative thickness (mm, to centre of couplet) | Mat layer thickness (mm) | Mixed assemblage layer thickness (mm) | Total couplet thickness (mm) |
|---|---|---|---|---|
| 265 | 102.215 | 0.15 | 0.28 | 0.43 |
| 266 | 102.52 | 0.1 | 0.08 | 0.18 |
| 267 | 102.75 | 0.17 | 0.11 | 0.28 |
| 268 | 102.965 | 0.08 | 0.07 | 0.15 |
| 269 | 103.24 | 0.15 | 0.25 | 0.40 |
| 270 | 103.59 | 0.24 | 0.06 | 0.30 |
| 271 | 103.875 | 0.1 | 0.17 | 0.27 |
| 272 | 104.18 | 0 | 0.34 | 0.34 |
| 273 | 104.415 | 0.07 | 0.06 | 0.13 |
| 274 | 104.535 | 0.06 | 0.05 | 0.11 |
| 275 | 104.66 | 0.05 | 0.09 | 0.14 |

# APPENDIX 6: DISSOLUTION INDEX CALCULATION AND RESULTS

The dissolution index was used to quantify the level of frustule dissolution observed in *T. longissima* Group diatoms. The index is calculated using SEM observations of morphological changes in the frustules, such as the loss of the delicate porate cribrum and the progessive enlargement of the aerolae. Biogenic silica loss was related to these morphological changes through dissolution experiments (see Section 4.4.2 in main text).

## A6.1 SAMPLE PREPARATION

Changes in dissolution were quantified using the mean dissolution index assigned to 500 frustules along a line across an SEM strew mount. Sediment used in the strew mounts was cleaned to remove carbonate and organic carbon prior to inspection. A 5-10mg subsample was taken from samples spaced at approximately 10cm intervals through the basal units of the '4.4Ma' LDM event for Sites 847 and 850. Each sample was cleaned using 2ml of 10%$H_2O_2$ and 2ml 10% HCl to remove organic material and carbonate respectively. The samples were placed in an ultra-sonic bath for 1 minute and left for an hour after each addition to ensure effective cleaning. Microscope examination before and after sonication indicated that this process did not damage the frustules. Then 8ml of MilliQ water was added to each sample and the samples were centrifuged at 3600rpm for 12 minutes, the supernatant was removed and the water addition-centrifugation-decantation step was repeated to removed any residual salts. The samples were then oven-dried at 40°C overnight. If any salts were visible in the dried samples the water addition-centrifugation-decantation step was repeated. The sample were then resuspended in 1ml of MilliQ, shaken vigorously and placed in an ultrasonic bath for 2 minutes to ensure complete disaggregation of the sediment. Using a Finnpipette, 50µL of each suspension was transfered to an SEM stub (with carbon disk), the stubs were dried and gold-coated. The sample was taken from the middle of the suspension to minimize inclusion of any aggregated sediment and to ensure inclusion of smaller particles.

## A6.2 INDEX CALCULATION AND COUNTING CRITERIA

Sample dissolution index was calculated as the mean of dissolution indicies assigned to 500 individual frustules from a transect across the sample strew mount. Individual frustules were assigned an index (between 1 and 5) referring to the degree of dissolution observed, the highest index representing the greatest level of dissolution. Index values were assigned on the

following basis:

**Index 5** - No sides bars; edges of frustule smooth with the stumps of bars originally separating areolae rounded; ridges associated with these bars still present but with a smoothed profile; frustule surface pitted.

**Index 4** - Side bars coming away or recently lost; stumps of areolae bars jagged; ridges associated with these bars well defined with a sharp profile; some spine bases still present but no evidence of the porate cribrum.

**Index 3** - Areolae holes enlarged - as a rule of thumb, hole diameter>bar width; bars narrow in both horizonal and vertical directions creating a dip in the frustule profile; commonly evidence for initial fracture across narrowest section; ridges associated with the bars are well defined with the scallop pattern on the inner section visible; spine basses are present with relict spines - possible to determine spine orientation in about 50% of cases.

**Index 2** - Little or no areolae hole enlargement - as a rule of thumb, hole diameter < bar width; relict cribrum - centre cross bar continous with relict cross bars to either side; direction of spines clearly discernable; little or no surface etching.

**Index 1** - Pristine frustules; complete porate cribrum (compared to SEM images in Round *et al.* 1990, p426-427)

The following criteria were used to minimize the chance of counting fragments of the same frustule as individuals:

a) No side sections counted

b) Only sections >10μm long included

### A6.3 Relating sample dissolution index to amount of BSi lost

Sample dissolution indicies were related to the amount of biogenic silica lost by dissolving replicates of a single sample in 2M $Na_2CO_3$. These sample replicates were prepared and placed in a constant temperature water bath as detailed in Appendix A1 (Section A1.4, steps 1-13). Two of the replicates removed from the heated water bath at 1 hour intervals. These samples were immediately centrifuged at 3500rpm for 11 minutes, and about 4ml of the clear supernatant into a polyethelene tube and store for subsequent silica analysis. The remaining supernant was discrded and the sample residues were acidified using gradual addition of 10%HCl until there was no visible effervesense. Another 0.5Ml of 10% HCl was added and the solution was left to stand for an hour. MilliQ was then added to a volume of 12ml. The samples were centrifuged at 3500rpm for 11 minutes and the supernant was discarded, 12ml of MilliQ was added and mixed thoroughly. The samples were then centrifuged again at 3500rpm for 11 minutes and the supernant dicarded. This rinsing step was repeated twice to ensure complete removal of salts. The residues were resuspended and used to prepare strew mounts for dissolution index measurement as detailed above.

**A6.4 RESULTS**

| SAMPLE ID | SAMPLE TYPE | DISSOLUTION INDEX | Wt% FIRST EXTACTION OPAL | Wt% SECOND EXTACTION OPAL | Wt% TOTAL OPAL |
|---|---|---|---|---|---|
| A1 | laminated | 3.97 | 28.90 | 5.89 | 34.87 |
| A2 | laminated | 3.27 | 67.70 | 11.15 | 78.88 |
| A3 | laminated | 3.54 | 66.70 | 11.24 | 77.89 |
| A4 | laminated | 3.84 | 59.24 | 14.87 | 74.11 |
| A5 | laminated | 3.46 | 62.47 | 14.26 | 76.73 |
| A6 | laminated | 4.01 | 26.82 | 5.67 | 32.61 |
| A7 | laminated | 4.10 | 26.80 | 6.26 | 33.06 |
| A8 | laminated | 4.04 | 28.10 | 7,04 | 35.14 |
| A9 | laminated | 4.08 | 28.80 | 8.07 | 36.87 |
| A10 | laminated | 4.28 | 19.27 | 9.02 | 28.29 |
| A11 | laminated | 4.45 | 21.60 | 8.51 | 30.10 |
| A12 | laminated | 4.34 | 24.47 | 11.47 | 35.94 |
| A13 | laminated | 3.57 | 54.52 | 9.61 | 64.13 |
| A14 | laminated | 3.58 | 48.96 | 14.49 | 63.45 |
| A15 | laminated | 3.77 | 45.04 | 12.83 | 57.87 |
| A16 | laminated | 3.26 | 51.87 | 11.06 | 62.93 |
| A17 | laminated | 3.56 | 52.79 | 10.58 | 63.37 |
| A18 | laminated | 3.54 | 36.94 | 10.08 | 47.02 |
| A19 | laminated | 3.69 | 46.64 | 11.25 | 57.89 |
| A20 | laminated | 3.32 | 46.15 | 9.79 | 55.94 |
| A21 | laminated | 3.38 | 51.66 | 14.70 | 66.36 |
| A22 | laminated | 3.54 | 32.67 | 13.51 | 46.18 |
| A23 | laminated | 3.60 | 43.10 | 13.87 | 56.97 |
| A26 | laminated | 3.39 | 34.96 | 12.24 | 47.20 |
| B1 | laminated | 3.21 | 75.27 | 7.18 | 80.99 |
| B2 | laminated | 3.86 | 72.61 | 6.15 | 77.3 |
| B3 | laminated | 3.66 | 72.91 | 4.62 | 76.07 |
| B4 | laminated | 3.63 | 72.00 | 9.59 | 81.59 |
| B5 | laminated | 3.45 | 71.25 | 6.46 | 77.71 |
| B6 | laminated | 3.19 | 71.09 | 7.23 | 75.22 |
| B7 | laminated | 3.71 | 70.64 | 3.66 | 77.10 |

| SAMPLE ID | SAMPLE TYPE | DISSOLUTION INDEX | Wt% FIRST EXTACTION OPAL | Wt% SECOND EXTACTION OPAL | Wt% TOTAL OPAL |
|---|---|---|---|---|---|
| B8 | laminated | 3.49 | 44.71 | 3.79 | 48.50 |
| B9 | laminated | 3.47 | 62.17 | 9.79 | 71.96 |
| B10 | laminated | 3.45 | 46.28 | 4.58 | 50.86 |
| B11 | laminated | 3.32 | 69.95 | 5.17 | 75.12 |
| B12 | laminated | 3.50 | 50.03 | 3.65 | 53.68 |
| B13 | laminated | 3.68 | 34.72 | 7.38 | 42.10 |
| B14 | laminated | 3.54 | 44.82 | 6.94 | 51.76 |
| B15 | laminated | 3.36 | 65.18 | 5.77 | 77.76 |
| B16 | laminated | 3.45 | 57.49 | 6.63 | 64.12 |
| B17 | laminated | 3.79 | 39.19 | 6.45 | 45.64 |
| C1 | laminated | 3.98 | 25.70 | 6.76 | 32.73 |
| D1 | normal marine | 3.57 | 7.31 | 3.17 | 10.52 |
| D2 | normal marine | 3.82 | 7.47 | 3.04 | 10.49 |
| D3 | normal marine | 3.91 | 6.47 | 3.02 | 9.10 |
| D4 | normal marine | 3.70 | 7.07 | 2.62 | 9.46 |
| D5 | normal marine | 3.77 | 4.86 | 2.39 | 7.59 |
| D6 | normal marine | 3.68 | 5.30 | 2.54 | 7.85 |
| D7 | normal marine | 3.91 | n.d. | n.d. | 11.14 |
| D8 | normal marine | 3.84 | n.d. | n.d. | 18.66 |
| D9 | normal marine | 3.97 | n.d. | n.d. | 17.27 |
| D10 | normal marine | 4.02 | n.d. | n.d. | 12.11 |
| D11 | normal marine | 3.84 | n.d. | n.d. | 8.55 |
| D12 | normal marine | 3.90 | n.d. | n.d. | 15.33 |
| D13 | normal marine | 3.86 | n.d. | n.d. | 12.67 |
| D14 | normal marine | 3.70 | 10.09 | 3.23 | 13.32 |
| D15 | normal marine | 3.77 | 8.22 | 2.71 | 10.93 |
| D16 | normal marine | 3.89 | 9.33 | 3.15 | 12.48 |
| E1 | non-laminated | 3.80 | 7.37 | 0.75 | 8.12 |
| E2 | non-laminated | 3.87 | 17.53 | 5.05 | 22.58 |
| E3 | non-laminated | 3.86 | 16.63 | 6.59 | 23.22 |
| E4 | non-laminated | 3.79 | 20.85 | 4.19 | 25.04 |
| E5 | non-laminated | 3.92 | 30.18 | 7.21 | 37.39 |
| E6 | non-laminated | 3.70 | 29.93 | 7.75 | 36.68 |

| SAMPLE ID | SAMPLE TYPE | DISSOLUTION INDEX | Wt% FIRST EXTACTION OPAL | Wt% SECOND EXTACTION OPAL | Wt% TOTAL OPAL |
|---|---|---|---|---|---|
| E7 | non-laminated | 3.71 | 11.40 | 0.2 | 11.59 |
| E8 | non-laminated | 3.62 | 11.04 | 0.10 | 11.15 |
| E9 | non-laminated | 3.90 | 17.48 | 3.23 | 20.71 |
| E10 | non-laminated | 4.02 | 14.86 | 3.19 | 17.75 |
| E11 | non-laminated | 3.81 | 5.03 | 0.83 | 5.86 |

Sample ID prefix codes

A - samples from Site 847 '4.4'Ma LDM basal unit

B - samples from Site 850 '4.4'Ma LDM basal unit

C- samples from Site 849 '4.4'Ma LDM basal unit

D - samples from normal marine foram-nannofossil ooze above and below LDM units and from sites with not LDM deposits

E- samples from non-laminated sections within the '4.4'Ma LDM deposits

Samples from Site 848 were not analysed using the double dissolution method as the levels of silica and silica preservation are too low for significant levels to be detected in the second extraction stage.

## APPENDIX 7: TRACE ELEMENT ANALYSES

ICP measurement were carried out by John Thompson at Southampton Oceanography Centre for four samples below, through and above the '4.4Ma' LDM deposits from ODP Site 850.

| | Above basal unit (72cm above lower boundary) | Within basal unit (immediately above lower boundary ) | Below basal unit (immediately below lower boundary) | Below basal unit (85cm below lower boundary) |
|---|---|---|---|---|
| | 850B-10H-7, 1-3cm | 850B-10H-7, 75cm | 850B-10H-7, 76cm | 850B-11X-1, 74-76cm |
| Al% | 0.2074 | 0.2153 | 0.1621 | 0.1814 |
| Fe% | 0.1883 | 0.4193 | 0.5721 | 0.2140 |
| Ca% | 19.4881 | 15.4228 | 30.6972 | 31.3194 |
| Mg% | 0.2305 | 0.2320 | 0.1681 | 0.2212 |
| Mn% | 0.0543 | 0.0318 | 0.0820 | 0.0756 |
| Na% | 1.3430 | 1.5832 | 0.9704 | 1.1277 |
| Si% | 17.1662 | 23.4590 | 5.3011 | 4.2691 |
| Ti% | 0.0080 | 0.0076 | 0.0063 | 0.0066 |
| Ba ppm | 1074.2 | 840.7 | 1242.3 | 1370.9 |
| Cr ppm | 3.606 | 0.961 | 1.923 | 0.829 |
| Sr ppm | 1016.1 | 857.0 | 1552.8 | 1561.9 |
| V ppm | 20.35 | 27.42 | 17.26 | 21.36 |
| Zr ppm | 9.563 | 8.04 | 8.04 | 7.654 |

# APPENDIX 8: HIGH RESOLUTION MEASUREMENTS OF BIOGENIC OPAL

## A8.1 HOLE 847B-15H-7, 49CM TO 15H-6, 130CM ('4.4MA' LDM BASAL UNIT)

Cummulative thickness is measured upward from ODP-138-847B-15H-7, 49cm

| Cummulative thickness (mm) | %1st extraction opal | %2nd extraction opal | %opal (total) |
|---|---|---|---|
| 2.12 | 17.84 | 3.23 | 21.07 |
| 4.24s | 14.68 | 3.79 | 18.47 |
| 6.36 | 14.45 | 3.38 | 17.83 |
| 8.48 | 13.39 | 3.69 | 17.08 |
| 10.6 | 15.16 | 3.95 | 19.11 |
| 12.72 | 15.26 | 4.3 | 19.56 |
| 15.37 | 15.85 | 3.8 | 19.65 |
| 16.96 | 15.8 | 3.39 | 19.19 |
| 18.02 | 15.31 | 5.04 | 20.35 |
| 19.61 | 14.56 | 3.19 | 17.75 |
| 21.2 | 14.13 | 3.2 | 17.33 |
| 22.26 | 15.82 | 4.57 | 20.39 |
| 23.32 | 18.24 | 4.08 | 22.32 |
| 24.38 | 28.97 | 6.31 | 35.28 |
| 24.91 | 28.98 | 5.89 | 34.87 |
| 25.44 | 46.52 | 9.5 | 56.02 |
| 25.97 | 48.3 | 10.62 | 58.92 |
| 26.5 | 52.41 | 9.56 | 61.97 |
| 27.56 | 44.42 | 8.41 | 52.83 |
| 28.62 | 54.52 | 9.61 | 64.13 |
| 29.68 | 50 | 10.75 | 60.75 |
| 30.74 | 42.58 | 10.2 | 52.78 |
| 31.8 | 49.95 | 9.65 | 59.6 |
| 33.39 | 41.27 | 9.67 | 50.94 |
| 34.24 | 41.89 | 9.42 | 51.31 |
| 34.98 | 35.57 | 9.31 | 44.88 |
| 35.78 | 34.19 | 8.81 | 43 |
| 36.57 | 39.96 | 8.66 | 48.62 |
| 37.63 | 48.16 | 10.95 | 59.11 |
| 38.43 | 46.4 | 9.78 | 56.18 |
| 39.22 | 51.54 | 9.97 | 61.51 |
| 42.4 | 48.95 | 10.43 | 59.38 |
| 43.46 | 49.1 | 15.02 | 64.12 |
| 45.16 | 44.7 | 21.01 | 65.71 |

| Cummulative thickness (mm) | %1st extraction opal | %2nd extraction opal | %opal (total) |
|---|---|---|---|
| 46.22 | 45.99 | 12.29 | 58.28 |
| 47.59 | 47.04 | 9.85 | 56.89 |
| 48.39 | 50.14 | 8.71 | 58.85 |
| 48.97 | 48.16 | 10.47 | 58.63 |
| 49.5 | 48.35 | 10.59 | 58.94 |
| 51.09 | 44.14 | 8.71 | 52.85 |
| 51.62 | 43.1 | 11.03 | 54.13 |
| 52.47 | 34.84 | 6.77 | 41.61 |
| 53 | 37.95 | 6.66 | 44.61 |
| 53.74 | 41.54 | 8.32 | 49.86 |
| 54.48 | 46.9 | 7.51 | 54.41 |
| 57.24 | 34.99 | 7.93 | 42.92 |
| 58.83 | 46.19 | 7.76 | 53.95 |
| 59.36 | 50.18 | 6.95 | 57.13 |
| 60.1 | 49.36 | 6.73 | 56.09 |
| 61.69 | 46.15 | 9.79 | 55.94 |
| 63.28 | 46.97 | 7.99 | 54.96 |
| 65.72 | 42.99 | 8.36 | 51.35 |
| 67.31 | 46.67 | 8.25 | 54.92 |
| 68.9 | 33.66 | 6.67 | 40.33 |
| 71.02 | 39.69 | 9.05 | 48.74 |
| 73.14 | 44.32 | 9.84 | 54.16 |
| 75.26 | 38.63 | 8.55 | 47.18 |
| 77.91 | 47.5 | 9.13 | 56.63 |
| 80.03 | 59.32 | 7.44 | 66.76 |
| 82.15 | 57.5 | 9.58 | 67.08 |
| 84.27 | | 10.6 | |
| 85.86 | 47.48 | 9.32 | 56.8 |
| 87.45 | 45.87 | 8.79 | 54.66 |
| 89.04 | 43.99 | 8.28 | 52.27 |
| 90.63 | 37.48 | 9.09 | 46.57 |
| 91.69 | 42.83 | 9.86 | 52.69 |
| 93.28 | 36.54 | 10.44 | 46.98 |
| 94.34 | 43.3 | 11.19 | 54.49 |
| 95.4 | 43.43 | 7.19 | 50.62 |
| 97.52 | 41.9 | 8.45 | 50.35 |
| 99.64 | 48.78 | 8.78 | 57.56 |
| 100.5 | 43.41 | 11.57 | 54.98 |
| 101.3 | 40.4 | 12.15 | 52.55 |
| 103 | 46.96 | 8.46 | 55.42 |
| 104.2 | 44.23 | 12.31 | 56.54 |
| 105.9 | 52.37 | 9.59 | 61.96 |

| Cummulative thickness (mm) | %1st extraction opal | %2nd extraction opal | %opal (total) |
|---|---|---|---|
| 106.7 | 45.91 | 12.49 | 58.4 |
| 108.4 | 46.82 | 12.39 | 59.21 |
| 110 | 50.31 | 12.81 | 63.12 |
| 110.4 | 51.96 | 9.28 | 61.24 |
| 112.1 | 48.69 | 14.49 | 63.18 |
| 113.7 | 47.3 | 12.25 | 59.55 |
| 115.8 | 45.84 | 10.75 | 56.59 |
| 116.7 | 58.83 | 8.88 | 67.71 |
| 118.7 | 56.3 | 8.99 | 65.29 |
| 120.8 | 54.92 | 11.49 | 66.41 |
| 121.2 | 41.45 | 9.8 | 51.25 |
| 122.9 | 45.28 | 9.2 | 54.48 |
| 124.1 | 47.19 | 7.27 | 54.46 |
| 125.8 | 50.96 | 9.3 | 60.26 |
| 127.4 | 47.11 | 9.22 | 56.33 |
| 129.1 | 62.18 | 9.59 | 71.77 |
| 130.8 | 49.69 | 9.14 | 58.83 |
| 132 | 57.56 | 10.28 | 67.84 |
| 133.7 | 58.09 | 10.57 | 68.66 |
| 134.5 | 59.69 | 10.57 | 70.26 |
| 135.3 | 65.82 | 10.23 | 76.05 |
| 137 | 60.95 | 9.33 | 70.28 |
| 138.2 | 59.07 | 11.07 | 70.14 |
| 139.5 | 63.02 | 11.86 | 74.88 |
| 141.1 | 67.32 | 11.67 | 78.99 |
| 142.8 | 50.61 | 11.73 | 62.34 |
| 145.3 | 47.59 | 10.92 | 58.51 |
| 146.1 | 46.72 | 7.39 | 54.11 |
| 146.9 | 50.51 | 8.37 | 58.88 |
| 147.8 | 45.76 | 10.32 | 56.08 |
| 148.6 | 48.58 | 10.83 | 59.41 |
| 149 | 57.52 | 11.46 | 68.98 |
| 149.4 | 52.77 | 14.32 | 67.09 |
| 151.1 | 50.57 | 12.21 | 62.78 |
| 152.4 | 51.66 | 14.7 | 66.36 |
| 153.2 | 53.71 | 6.79 | 60.5 |
| 154.4 | 48.8 | 5.54 | 54.34 |
| 156.5 | 45.46 | 9.36 | 54.82 |
| 157.7 | 51.22 | 4.69 | 55.91 |
| 159 | 47.65 | 7.53 | 55.18 |
| 159.8 | 59.42 | 6.86 | 66.28 |
| 161.5 | 62.74 | 5.9 | 68.64 |

| Cummulative thickness (mm) | %1st extraction opal | %2nd extraction opal | %opal (total) |
|---|---|---|---|
| 162.7 | 62.52 | 6.91 | 69.43 |
| 164.4 | 56.33 | 9.95 | 66.28 |
| 165.2 | 62.1 | 7.57 | 69.67 |
| 166 | 50.72 | 7.52 | 58.24 |
| 167.7 | 35.98 | 11 | 46.98 |
| 169.4 | 32.63 | 10.02 | 42.65 |
| 170.6 | 41.09 | 6.89 | 47.98 |
| 171.9 | 37.04 | 6.1 | 43.14 |
| 173.1 | 35.06 | 5.24 | 40.3 |
| 174.3 | 41.65 | 7.44 | 49.09 |
| 175.2 | 45.17 | 4.25 | 49.42 |
| 176.8 | 36.86 | 6.34 | 43.2 |
| 178.5 | 46.14 | 4.36 | 50.5 |
| 180.1 | 45.06 | 9.6 | 54.66 |
| 181.8 | 49.18 | 11.78 | 60.96 |
| 183.5 | 47.35 | 9.69 | 57.04 |
| 184.7 | 40.56 | 11.29 | 51.85 |
| 186.4 | 40.91 | 8.94 | 49.85 |
| 188.9 | 39.6 | 9.06 | 48.66 |
| 190.1 | 40.37 | 7.19 | 47.56 |
| 190.5 | 47.65 | 7.78 | 55.43 |
| 191.4 | 45.8 | 7.23 | 53.03 |
| 191.8 | 45.7 | 8.7 | 54.4 |
| 192.6 | 39.59 | 7.54 | 47.13 |
| 194.3 | 41.66 | 9.19 | 50.85 |
| 195.9 | 44.14 | 7.81 | 51.95 |
| 196.7 | 43.74 | 8.52 | 52.26 |
| 198 | 36.1 | 8.7 | 44.8 |
| 199.7 | 45.11 | 8.08 | 53.19 |
| 200.9 | 34.38 | 14.32 | 48.7 |
| 202.7 | 41.95 | 6.73 | 48.68 |
| 204.7 | 49.9 | 6.81 | 56.71 |
| 206.5 | 45.77 | 13 | 58.77 |
| 208.9 | 43.28 | 14.1 | 57.38 |
| 211.3 | 51.71 | 12.71 | 64.42 |
| 212.4 | 49.79 | 13.93 | 63.72 |
| 213.6 | 46.88 | 12.47 | 59.35 |
| 215.4 | 48.4 | 7.64 | 56.04 |
| 217.8 | 43.04 | 12.83 | 55.87 |
| 219.5 | 40.86 | 10.26 | 51.12 |
| 220.7 | 42.91 | 6.69 | 49.6 |
| 222.5 | 38.5 | 18.97 | 57.47 |

| Cummulative thickness (mm) | %1st extraction opal | %2nd extraction opal | %opal (total) |
|---|---|---|---|
| 223.7 | 44.51 | 14.82 | 59.33 |
| 224.3 | 50.91 | 8.12 | 59.03 |
| 225.5 | 40.38 | 11.56 | 51.94 |
| 226 | 41.67 | 8.99 | 50.66 |
| 227.2 | 35.76 | 13.14 | 48.9 |
| 228.4 | 38.41 | 12.04 | 50.45 |
| 229 | 51.61 | 9.92 | 61.53 |
| 231.4 | 43.15 | 11.63 | 54.78 |
| 233.7 | 45.01 | 12.59 | 57.6 |
| 236.7 | 55.82 | 10.52 | 66.34 |
| 238.5 | 51.19 | 12.62 | 63.81 |
| 239.8 | 44.57 | 9.63 | 54.2 |
| 240.8 | 46.56 | 6.35 | 52.91 |
| 241.9 | 48.57 | 7.14 | 55.71 |
| 242.8 | 55.34 | 8.1 | 63.44 |
| 243.8 | 52.92 | 8.36 | 61.28 |
| 245.3 | 51.48 | 6.37 | 57.85 |
| 246.3 | 50.15 | 14.82 | 64.97 |
| 247.6 | 50.19 | 7.21 | 57.4 |
| 248.4 | 53.68 | 9.97 | 63.65 |
| 249.5 | 48.14 | 9.77 | 57.91 |
| 250.5 | 56.77 | 8.41 | 65.18 |
| 251.4 | 56.71 | 6.93 | 63.64 |
| 252.4 | 57.75 | 9.74 | 67.49 |
| 253.1 | 43.91 | 11.56 | 55.47 |
| 254.7 | 46.87 | 10.4 | 57.27 |
| 256.2 | 47.24 | 11.22 | 58.46 |
| 258 | 32.63 | 11.25 | 43.88 |
| 260 | 36.81 | 15.36 | 52.17 |
| 261.8 | 41.59 | 12.87 | 54.46 |
| 261.8 | 40.15 | 9.29 | 49.44 |
| 262.4 | 41.28 | 13.89 | 55.17 |
| 263.4 | 36.9 | 12.74 | 49.64 |
| 264.3 | 40.26 | 13.28 | 53.54 |
| 265.1 | 39.08 | 15.39 | 54.47 |
| 266 | 38 | 13.95 | 51.95 |
| 267 | 52.67 | 13.51 | 66.18 |
| 268 | 39.68 | 13.13 | 52.81 |
| 268.5 | 38.74 | 12.66 | 51.4 |
| 269.5 | 43.64 | 16.18 | 59.82 |
| 270.5 | 47.31 | 11.48 | 58.79 |
| 271.3 | 35.52 | 14.88 | 50.4 |

| Cummulative thickness (mm) | %1st extraction opal | %2nd extraction opal | %opal (total) |
|---|---|---|---|
| 272.1 | 52.85 | 14.4 | 67.25 |
| 273 | 54.85 | 11.28 | 66.13 |
| 273.6 | 49.07 | 11.77 | 60.84 |
| 274 | 37.51 | 11.26 | 48.77 |
| 275 | 55.77 | 11.07 | 66.84 |
| 276 | 37.34 | 11.35 | 48.69 |
| 277 | 35.75 | 13.16 | 48.91 |
| 278 | 43.08 | 11.14 | 54.22 |
| 279 | 59.72 | 11.89 | 71.61 |
| 279.6 | 53.48 | 12.57 | 66.05 |
| 280.4 | 59.96 | 12.54 | 72.5 |
| 281.1 | 51.3 | 11.75 | 63.05 |
| 281.6 | 60.71 | 13 | 73.71 |
| 282.1 | 40.45 | 13.01 | 53.46 |
| 282.6 | 67.73 | 11.15 | 78.88 |
| 283.5 | 50.08 | 9.8 | 59.88 |
| 284.3 | 60.81 | 10.45 | 71.26 |
| 285.1 | 50.93 | 12.85 | 63.78 |
| 285.9 | 58 | 13.02 | 71.02 |
| 286.8 | 41.37 | 11.6 | 52.97 |
| 287.5 | 52.14 | 16.52 | 68.66 |
| 288.4 | 47.77 | 17.12 | 64.89 |
| 289.1 | 51.73 | 14.01 | 65.74 |
| 290.5 | 50.81 | 13.21 | 64.02 |
| 291.1 | 49.12 | 13.68 | 62.8 |
| 292.3 | 44.52 | 13.74 | 58.26 |
| 293 | 48.5 | 15.98 | 64.48 |
| 293.8 | 45.74 | 12.83 | 58.57 |
| 294.5 | 42.36 | 16.79 | 59.15 |
| 295.2 | 54.96 | 12.04 | 67 |
| 296 | 36.04 | 8.87 | 44.91 |
| 297 | 39.26 | 12.91 | 52.17 |
| 298.5 | 47.72 | 12.91 | 60.63 |
| 300.7 | 57.68 | 10.46 | 68.14 |
| 302 | 45.77 | 12.08 | 57.85 |
| 302.9 | 45.61 | 9.53 | 55.14 |
| 303.8 | 49.95 | 7.33 | 57.28 |
| 305.1 | 46.21 | 9.7 | 55.91 |
| 306.2 | 55.29 | 11.3 | 66.59 |
| 307.1 | 57.77 | 12.03 | 69.8 |
| 308.6 | 54.14 | 9.55 | 63.69 |
| 309.5 | 54.51 | 9.79 | 64.3 |

| Cummulative thickness (mm) | %1st extraction opal | %2nd extraction opal | %opal (total) |
|---|---|---|---|
| 310.1 | 51.87 | 11.06 | 62.93 |
| 310.7 | 55.23 | 12.93 | 68.16 |
| 312.4 | 47.88 | 13.38 | 61.26 |
| 313.7 | 49.65 | 8.48 | 58.13 |
| 314.6 | 60.16 | 13.49 | 73.65 |
| 315.5 | 56.68 | 12.07 | 68.75 |
| 316.4 | 55.72 | 10.88 | 66.6 |
| 317.9 | 51.38 | 8.47 | 59.85 |
| 319.2 | 56.97 | 12.71 | 69.68 |
| 320.9 | 66.74 | 11.24 | 77.98 |
| 322.6 | 55.65 | 8.07 | 63.72 |
| 324.3 | 55.17 | 10.23 | 65.4 |
| 324.3 | 53.4 | 8.22 | 61.62 |
| 325.1 | 40.84 | 11.56 | 52.4 |
| 326.9 | 43.92 | 12.44 | 56.36 |
| 327.8 | 49.26 | 8.18 | 57.44 |
| 329.1 | 35.57 | 10.32 | 45.89 |
| 330.4 | 38.92 | 7.36 | 46.28 |
| 332.2 | 39.43 | 8.34 | 47.77 |
| 334 | 37.1 | 9.45 | 46.55 |
| 335.7 | 36.38 | 11.38 | 47.76 |
| 337 | 45.65 | 12.5 | 58.15 |
| 337.9 | 42.2 | 12.37 | 54.57 |
| 338.8 | 40.29 | 11.17 | 51.46 |
| 340.1 | 43.66 | 10.1 | 53.76 |
| 341.5 | 46.72 | 10.65 | 57.37 |
| 342.3 | 42.77 | 11.62 | 54.39 |
| 343.7 | 43.82 | 11.36 | 55.18 |
| 344.8 | 42.21 | 12.04 | 54.25 |
| 346.1 | 41.81 | 9.47 | 51.28 |
| 347.2 | 40.41 | 16.24 | 56.65 |
| 349 | 52.26 | 9.41 | 61.67 |
| 349.9 | 56.9 | 11.21 | 68.11 |
| 351.4 | 35.96 | 11.93 | 47.89 |
| 353.1 | 56.31 | 13.73 | 70.04 |
| 355.8 | 45.03 | 10.37 | 55.4 |
| 356.6 | 46.28 | 8.18 | 54.46 |
| 358.9 | 60.48 | 9.41 | 69.89 |
| 359.7 | 58.77 | 11.37 | 70.14 |
| 360.6 | 59.24 | 14.87 | 74.11 |
| 361.5 | 48.88 | 10.55 | 59.43 |
| 362.2 | 43.41 | 13.87 | 57.28 |

| Cummulative thickness (mm) | %1st extraction opal | %2nd extraction opal | %opal (total) |
|---|---|---|---|
| 363.1 | 63.72 | 10.78 | 74.5 |
| 363.9 | 51.14 | 10.8 | 61.94 |
| 365.2 | 62.47 | 14.26 | 76.73 |
| 367 | 59.24 | 8.45 | 67.69 |
| 369.6 | 50.84 | 12.76 | 63.6 |
| 372.3 | 52.83 | 11.48 | 64.31 |
| 375.8 | 49.98 | 13.06 | 63.04 |
| 377.7 | 54.1 | 10.76 | 64.86 |
| 378.5 | 68.67 | 8.18 | 76.85 |
| 379.4 | 60.91 | 10.52 | 71.43 |
| 380.2 | 49.86 | 12.51 | 62.37 |
| 381.6 | 61.3 | 12.81 | 74.11 |
| 383.3 | 44.03 | 13.36 | 57.39 |
| 384.2 | 49.67 | 14.38 | 64.05 |
| 386.9 | 45.4 | 11.89 | 57.29 |
| 388.6 | 49.23 | 10.59 | 59.82 |
| 390.2 | 55.35 | 13.8 | 69.15 |
| 391.1 | 43.21 | 14.39 | 57.6 |
| 393.3 | 49.54 | 15.65 | 65.19 |
| 396 | 47.77 | 10.61 | 58.38 |
| 398.5 | 47.76 | 7.6 | 55.36 |
| 400.1 | 50.45 | 15.2 | 65.65 |
| 401.7 | 36.79 | 14.88 | 51.67 |
| 402.8 | 45.9 | 11.35 | 57.25 |
| 405.5 | 45.47 | 13.49 | 58.96 |
| 407.7 | 40.16 | 15.82 | 55.98 |
| 409.3 | 33.75 | 11.34 | 45.09 |
| 412 | 33.83 | 14.76 | 48.59 |
| 413.6 | 48.69 | 11.04 | 59.73 |
| 415.2 | 52.79 | 10.58 | 63.37 |
| 416.8 | 44.75 | 13.12 | 57.87 |
| 418.4 | 43.93 | 12.24 | 56.17 |
| 420 | 48.66 | 10.87 | 59.53 |
| 421.6 | 52.08 | 10.69 | 62.77 |
| 423.2 | 52.87 | 11.46 | 64.33 |
| 425.3 | 50.32 | 10.48 | 60.8 |
| 427.4 | 54.03 | 8.47 | 62.5 |
| 429.4 | 48.34 | 10.96 | 59.3 |
| 431.4 | 50.3 | 8.37 | 58.67 |
| 433.4 | 53.85 | 11.52 | 65.37 |
| 435.9 | 51.04 | 11.48 | 62.52 |
| 436.4 | 56.35 | 7.98 | 64.33 |

| Cummulative thickness (mm) | %1st extraction opal | %2nd extraction opal | %opal (total) |
|---|---|---|---|
| 437.9 | 44.81 | 8.18 | 52.99 |
| 439.4 | 48.49 | 11.24 | 59.73 |
| 440.9 | 49.39 | 8.85 | 58.24 |
| 442.9 | 44.07 | 7.88 | 51.95 |
| 444.4 | 38.02 | 11.79 | 49.81 |
| 446.4 | 41.16 | 9.02 | 50.18 |
| 448.4 | 38.41 | 12.64 | 51.05 |
| 450.4 | 36.62 | 10.28 | 46.9 |
| 451.4 | 44.1 | 14.4 | 58.5 |
| 452.6 | 39.67 | 14.27 | 53.94 |
| 455 | 42.5 | 12 | 54.5 |
| 456.8 | 45.64 | 8.53 | 54.17 |
| 458.6 | 38.73 | 8.63 | 47.36 |
| 459.8 | 45.35 | 10.43 | 55.78 |
| 462.6 | 44.09 | 9.99 | 54.08 |
| 464 | 42.93 | 10.76 | 53.69 |
| 466.3 | 35.67 | 12.31 | 47.98 |
| 468 | 34.96 | 12.24 | 47.2 |
| 469.7 | 30.81 | 8.7 | 39.51 |
| 471.4 | 35.33 | 10.44 | 45.77 |
| 472.2 | 36.86 | 10.34 | 47.2 |
| 473 | 34.7 | 12.04 | 46.74 |
| 475 | 32.16 | 13.02 | 45.18 |
| 477.2 | 32.21 | 11.01 | 43.22 |
| 479.4 | 37.91 | 9.84 | 47.75 |
| 483 | | | |
| 485.2 | 26.72 | 10.79 | 37.51 |
| 486.9 | 28.85 | 12.02 | 40.87 |
| 488.6 | 32.47 | 11.67 | 44.14 |
| 490.8 | 30.14 | 10.8 | 40.94 |
| 493.6 | 29.22 | 11.43 | 40.65 |
| 495.8 | 31.19 | 11.42 | 42.61 |
| 498 | 32.68 | 8.6 | 41.28 |
| 499.4 | 36.94 | 10.08 | 47.02 |
| 500.3 | 32.41 | 12.98 | 45.39 |
| 501.2 | 50.63 | 8.2 | 58.83 |
| 503.1 | 46.15 | 6.42 | 52.57 |
| 505.2 | 43.46 | 9.06 | 52.52 |
| 507.3 | 51.61 | 7.62 | 59.23 |
| 508.9 | 39.48 | 5.31 | 44.79 |
| 510.4 | 30.41 | 8.72 | 39.13 |
| 512 | 38.22 | 7.37 | 45.59 |

| Cummulative thickness (mm) | %1st extraction opal | %2nd extraction opal | %opal (total) |
|---|---|---|---|
| 513 | 41.3 | 6.06 | 47.36 |
| 514 | 36.88 | 9.28 | 46.16 |
| 516 | 35.78 | 9.92 | 45.7 |
| 519 | 46.58 | 5.93 | 52.51 |
| 521 | 39.95 | 9.89 | 49.84 |
| 523 | 46.61 | 7.4 | 54.01 |
| 525 | 53.44 | 5.55 | 58.99 |
| 527 | 55.45 | 6.77 | 62.22 |
| 528.5 | 61.6 | 5.78 | 67.38 |
| 530 | 63.34 | 5.39 | 68.73 |
| 532 | 52.47 | 10.24 | 62.71 |
| 533 | 31.61 | 8.86 | 40.47 |
| 536.3 | 47.8 | 10.03 | 57.83 |
| 539.1 | 38.7 | 14.77 | 53.47 |
| 541.3 | 30.05 | 14.16 | 44.21 |
| 543 | 32.37 | 10.8 | 43.17 |
| 544.5 | 40.23 | 12.72 | 52.95 |
| 546.5 | 33.37 | 10.71 | 44.08 |
| 548.5 | 37.41 | 11.45 | 48.86 |
| 550.5 | 38.58 | 11.8 | 50.38 |
| 552.5 | 39.95 | 11.78 | 51.73 |
| 554.5 | 46.62 | 11.25 | 57.87 |
| 556.5 | 41.91 | 11.37 | 53.28 |
| 559 | 38.65 | 10.08 | 48.73 |
| 561 | 39.66 | 12.83 | 52.49 |
| 562.5 | 39.06 | 11.86 | 50.92 |
| 564 | 37.06 | 12.63 | 49.69 |
| 565.1 | 38.19 | 13.29 | 51.48 |
| 566.2 | 41.04 | 11.34 | 52.38 |
| 567.7 | 34.83 | 11.01 | 45.84 |
| 569.2 | 37.76 | 10.25 | 48.01 |
| 572.2 | 30.39 | 8.15 | 38.54 |
| 574.7 | 31.25 | 7.69 | 38.94 |
| 576.2 | 38.18 | 5.48 | 43.66 |
| 578.2 | 26.82 | 5.79 | 32.61 |
| 580.3 | 28.1 | 7.04 | 35.14 |
| 582.4 | 26.8 | 6.26 | 33.06 |
| 585.6 | 31.3 | 7.81 | 39.11 |
| 588.8 | 35.35 | 9.24 | 44.59 |
| 590.9 | 28.8 | 8.07 | 36.87 |
| 593 | 33.83 | 6.8 | 40.63 |
| 595 | 35.83 | 6.21 | 42.04 |

| Cummulative thickness (mm) | %1st extraction opal | %2nd extraction opal | %opal (total) |
|---|---|---|---|
| 598 | 38.02 | 10.68 | 48.7 |
| 601 | 45.4 | 12.47 | 57.87 |
| 604 | 40.42 | 7.9 | 48.32 |
| 606 | 36.45 | 12.39 | 48.84 |
| 608.6 | 33.89 | 10.94 | 44.83 |
| 611.2 | 26.02 | 10.37 | 36.39 |
| 613.4 | 19.27 | 9.02 | 28.29 |
| 615.3 | 21.6 | 8.51 | 30.11 |
| 616.6 | 24.47 | 11.47 | 35.94 |

### A8.1 HOLE 850B-10H-7, 82-21 CM ('4.4MA' LDM BASAL UNIT)

Cummulative thickness is measured upward from ODP-138-850B-10H-7, 81cm

| Cummulative thickness (mm) | %1st extraction opal | %2nd extraction opal | Total %opal |
|---|---|---|---|
| 1.8 | 11.38 | 5.71 | 11.59 |
| 3.6 | 7.17 | 2.51 | 7.18 |
| 4.95 | 8.33 | 2.85 | 9.43 |
| 6.75 | 8.24 | 2.57 | 8.35 |
| 8.55 | 8.97 | 2.58 | 9.09 |
| 9.9 | 14.18 | 2.65 | 14.39 |
| 10.8 | 9.97 | 2.51 | 9.99 |
| 12.6 | 11.13 | 3.25 | 12.23 |
| 14.4 | 11.04 | 2.57 | 11.15 |
| 16.2 | 11.77 | 2.58 | 11.89 |
| 17.55 | 12.09 | 2.56 | 12.17 |
| 18.9 | 13.23 | 2.65 | 13.45 |
| 20.7 | 32.24 | 4.85 | 35.67 |
| 20.7 | 42.51 | 5.08 | 46.27 |
| 21.6 | 29.26 | 3.25 | 30.36 |
| 23.85 | 30.09 | 3.27 | 31.21 |
| 25.65 | 30.03 | 3.15 | 30.98 |
| 26.55 | 42.24 | 4.57 | 45.26 |
| 28.35 | 40.46 | 4.73 | 43.71 |
| 30.15 | 44.71 | 5.1 | 48.5 |
| 31.95 | 43.9 | 4.84 | 47.31 |
| 33.75 | 48.64 | 5.35 | 52.79 |
| 35.55 | 44.88 | 5.48 | 49.22 |
| 36.45 | 41.36 | 5.5 | 45.74 |
| 37.35 | 54.4 | 4.54 | 57.37 |
| 38.25 | 52.97 | 5.11 | 56.78 |
| 39.15 | 58.38 | 4.04 | 62.42 |
| 40.95 | 55.92 | 5.18 | 61.1 |
| 42.3 | 58.9 | 4.08 | 62.98 |
| 43.65 | 56.35 | 4.42 | 60.77 |
| 44.55 | 58.83 | 4.44 | 63.27 |
| 45.9 | 55.78 | 6.67 | 62.45 |
| 48.15 | 62.17 | 9.79 | 71.96 |
| 50.85 | 53.6 | 5.87 | 59.47 |
| 52.2 | 60.95 | 7.95 | 68.9 |
| 53.1 | 62.65 | 5.53 | 68.19 |
| 54 | 65.92 | 5.53 | 71.45 |

| Cummulative thickness (mm) | %1st extraction opal | %2nd extraction opal | Total %opal |
|---|---|---|---|
| 54.9 | 56.91 | 6.81 | 63.72 |
| 55.8 | 51.23 | 5.05 | 56.28 |
| 57.15 | 54.56 | 6.59 | 61.15 |
| 58.05 | 57.02 | 5.06 | 62.08 |
| 58.95 | 60.04 | 4.34 | 64.38 |
| 61.65 | 55.38 | 7.34 | 62.73 |
| 63.45 | 54.93 | 5.34 | 60.27 |
| 65.25 | 51.85 | 6.35 | 58.19 |
| 66.6 | 56.83 | 4.58 | 61.41 |
| 67.95 | 53.74 | 4.13 | 57.87 |
| 69.51 | 46.28 | 4.58 | 50.86 |
| 71.07 | 47.27 | 4.26 | 51.53 |
| 71.85 | 59.96 | 4.92 | 63.43 |
| 72.24 | 60.96 | 5.09 | 64.58 |
| 73.02 | 61.67 | 4.89 | 65.09 |
| 74.19 | 60.33 | 5.73 | 64.6 |
| 75.75 | 66.52 | 6.57 | 71.63 |
| 76.53 | 59.77 | 4.83 | 63.14 |
| 78.09 | 53.54 | 4.71 | 56.8 |
| 79.65 | 55.93 | 4.15 | 58.62 |
| 80.82 | 59.55 | 3.72 | 61.8 |
| 81.99 | 55.04 | 4.21 | 57.79 |
| 83.55 | 61.7 | 4.87 | 65.1 |
| 84.33 | 61.15 | 4.6 | 64.29 |
| 85.89 | 60.78 | 4.68 | 64.01 |
| 87.45 | 61.65 | 4.45 | 64.65 |
| 89.01 | 62.66 | 4.58 | 65.78 |
| 90.18 | 65.2 | 4.53 | 68.27 |
| 91.35 | 68.55 | 5.89 | 72.99 |
| 92.52 | 64.48 | 5.64 | 68.66 |
| 93.69 | 63.94 | 5.56 | 68.04 |
| 94.86 | 58.58 | 5.38 | 62.5 |
| 96.03 | 69.95 | 6.63 | 75.12 |
| 97.2 | 65.62 | 5.29 | 69.45 |
| 98.37 | 75.27 | 7.18 | 80.99 |
| 99.15 | 72.61 | 6.15 | 77.3 |
| 100.32 | 58.98 | 6.15 | 63.67 |
| 101.1 | 69.03 | 5.64 | 73.21 |
| 101.88 | 67.38 | 6.51 | 72.43 |
| 103.44 | 63.5 | 7.22 | 69.26 |
| 105 | 60.19 | 6.63 | 65.37 |
| 105.78 | 65.49 | 7.29 | 71.31 |

| Cummulative thickness (mm) | %1st extraction opal | %2nd extraction opal | Total %opal |
|---|---|---|---|
| 106.56 | 63.39 | 6.14 | 68.07 |
| 107.73 | 66.85 | 5.68 | 71.08 |
| 108.51 | 63.65 | 5.98 | 68.17 |
| 109.68 | 72.91 | 4.62 | 76.07 |
| 110.85 | 66.81 | 5.29 | 70.64 |
| 112.41 | 55.43 | 5.33 | 59.3 |
| 113.19 | 51.85 | 4 | 54.4 |
| 113.58 | 52.76 | 4.72 | 56.02 |
| 114.36 | 48.32 | 4.73 | 51.59 |
| 115.14 | 64.59 | 6.7 | 69.83 |
| 115.92 | 54.72 | 6.08 | 58.82 |
| 117.09 | 58.37 | 7.08 | 63.55 |
| 117.87 | 59.51 | 6.23 | 63.77 |
| 118.65 | 54.74 | 7.3 | 60.15 |
| 120.21 | 58.65 | 6.36 | 63.05 |
| 120.99 | 47.16 | 6.36 | 51.57 |
| 122.55 | 48.03 | 6.32 | 52.39 |
| 123.33 | 63.44 | 6.11 | 67.58 |
| 124.89 | 58.22 | 6.22 | 62.48 |
| 126.45 | 57.25 | 6.49 | 61.79 |
| 128.01 | 54.47 | 5.94 | 58.41 |
| 129.57 | 59.17 | 6.92 | 64.18 |
| 131.13 | 58.1 | 6.84 | 63.01 |
| 132.69 | 51.29 | 7 | 56.39 |
| 134.25 | 55.48 | 6.31 | 59.83 |
| 135.81 | 55.74 | 6.88 | 60.7 |
| 136.98 | 57.5 | 5.81 | 61.3 |
| 138.15 | 52.5 | 6.84 | 57.42 |
| 138.93 | 54.49 | 5.57 | 58.03 |
| 140.1 | 59.8 | 5.64 | 63.41 |
| 140.49 | 54.29 | 5.54 | 57.8 |
| 140.88 | 51.74 | 4.55 | 54.16 |
| 141.66 | 53.62 | 5.35 | 56.92 |
| 142.83 | 53.72 | 5.86 | 57.58 |
| 145.17 | 50.03 | 5.67 | 53.68 |
| 146.73 | 50.18 | 5.57 | 53.72 |
| 148.29 | 53.96 | 5.43 | 57.36 |
| 149.85 | 44.85 | 5.34 | 48.14 |
| 151.41 | 50.13 | 5.79 | 53.91 |
| 152.97 | 49.66 | 6.93 | 54.68 |
| 154.53 | 55.4 | 5.09 | 58.42 |
| 156.09 | 55.65 | 5.74 | 59.38 |

| Cummulative thickness (mm) | %1st extraction opal | %2nd extraction opal | Total %opal |
|---|---|---|---|
| 157.65 | 52.92 | 7.12 | 58.14 |
| 159.21 | 52.61 | 5.63 | 56.21 |
| 160.8 | 45.29 | 5.73 | 55.62 |
| 162.4 | 38.3 | 5.22 | 47.7 |
| 164 | 39.24 | 5.96 | 49.98 |
| 166 | 42.72 | 5.65 | 52.9 |
| 168 | 38.02 | 4.82 | 46.7 |
| 170 | 39.13 | 6.15 | 50.24 |
| 172 | 42.94 | 5.69 | 53.19 |
| 173 | 57.51 | 4.25 | 65.14 |
| 175 | 53.54 | 5.38 | 63.24 |
| 176 | 42.13 | 4.18 | 49.63 |
| 177.5 | 42.24 | 4.92 | 51.1 |
| 179.5 | 41.55 | 6.04 | 52.45 |
| 181 | 40.94 | 4.96 | 49.86 |
| 183.5 | 35.82 | 4.76 | 44.39 |
| 185 | 53.32 | 7.39 | 66.68 |
| 186.8 | 48.49 | 7.86 | 58 |
| 188.6 | 50.67 | 7.34 | 59.54 |
| 190.4 | 37.11 | 6.47 | 44.92 |
| 192.7 | 56.04 | 8.18 | 65.93 |
| 195 | 48.01 | 6.54 | 55.91 |
| 197.6 | 40.05 | 6.82 | 48.29 |
| 199.7 | 35.97 | 7.18 | 44.64 |
| 201.8 | 34.72 | 6.12 | 42.1 |
| 203.9 | 36.93 | 4.8 | 42.7 |
| 205 | 35.8 | 6.32 | 43.43 |
| 207.4 | 39.8 | 5.69 | 46.66 |
| 207.3 | 40.27 | 5.68 | 47.12 |
| 209.3 | 40.76 | 5.77 | 47.73 |
| 210.3 | | | |
| 212.2 | 50.89 | 4.7 | 56.54 |
| 214.1 | 53.62 | 5.95 | 60.79 |
| 216 | 52.9 | 6.3 | 60.5 |
| 217 | 55.29 | 5.27 | 61.64 |
| 218.5 | 51.59 | 4.53 | 57.03 |
| 220 | 59.08 | 5.09 | 65.21 |
| 221.4 | 50.89 | 2.78 | 56.54 |
| 222.8 | 53.62 | 3.47 | 60.79 |
| 224.2 | 52.9 | 3.67 | 60.5 |
| 225.6 | 55.29 | 3.1 | 61.64 |
| 226.5 | 51.59 | 2.69 | 57.03 |

| Cummulative thickness (mm) | %1st extraction opal | %2nd extraction opal | Total %opal |
|---|---|---|---|
| 227.4 | 59.08 | 3 | 65.21 |
| 228.8 | 40.82 | 4.69 | 50.67 |
| 231.8 | 44.29 | 4.28 | 53.25 |
| 234.8 | 41.53 | 4.07 | 50.03 |
| 237.1 | 51.72 | 4.32 | 60.76 |
| 240.9 | 57.13 | 5.22 | 68.18 |
| 242 | 59.74 | 3.87 | 67.8 |
| 243.7 | 42.03 | 5.45 | 53.57 |
| 246.5 | 42.95 | 5.46 | 54.51 |
| 248.2 | 45.64 | 5.12 | 56.44 |
| 249.9 | 47.14 | 5.57 | 58.94 |
| 251 | 45.32 | 5.14 | 56.17 |
| 252.2 | 50.65 | 4.33 | 59.72 |
| 253 | 40.56 | 4.84 | 45.41 |
| 253.8 | 44.61 | 5.17 | 55.53 |
| 254 | 46.72 | 5.64 | 58.67 |
| 255.6 | 48.14 | 4.96 | 58.59 |
| 256.8 | 51.77 | 5.27 | 62.92 |
| 258.4 | 51.04 | 4.66 | 60.84 |
| 259.8 | 36.61 | 5.48 | 48.22 |
| 261.6 | 47.68 | 5.17 | 58.6 |
| 263 | 44.59 | 4.32 | 53.63 |
| 264.4 | 43.59 | 4.5 | 53.04 |
| 266.3 | 44.29 | 3.98 | 52.58 |
| 268.2 | 37.92 | 3.96 | 46.19 |
| 270.1 | 41.66 | 5.34 | 47.06 |
| 272.5 | 45.38 | 4.8 | 55.49 |
| 274.1 | 47.07 | 5.7 | 59.15 |
| 275.7 | 50.2 | 4.93 | 60.58 |
| 277.3 | 49.02 | 10.81 | 60.43 |
| 279.4 | 48.35 | 9.03 | 57.81 |
| 281 | 46.47 | 10.13 | 57.13 |
| 282.6 | 45.32 | 9.18 | 54.94 |
| 284.1 | 64.93 | 9.97 | 75.42 |
| 284.6 | 55.6 | 9.76 | 65.85 |
| 286.6 | 55.31 | 7.06 | 62.61 |
| 289.1 | 57.29 | 3.58 | 60.76 |
| 290 | 44.82 | 6.74 | 51.76 |
| 290.5 | 52.31 | 3.48 | 55.67 |
| 290.93 | 47.81 | 5.26 | 53.068 |
| 292.31 | 53.84 | 5.24 | 59.088 |
| 293.24 | 55.57 | 5.4 | 60.974 |

| Cummulative thickness (mm) | %1st extraction opal | %2nd extraction opal | Total %opal |
|---|---|---|---|
| 294.16 | 53.73 | 5.57 | 59.298 |
| 295.09 | 58.69 | 4.99 | 63.678 |
| 295.78 | 58.78 | 5.12 | 63.904 |
| 296.71 | 53.17 | 5.54 | 58.716 |
| 297.4 | 51.67 | 5.35 | 57.02 |
| 298.33 | 51.15 | 4.9 | 56.048 |
| 299.25 | 40.98 | 4.82 | 45.796 |
| 299.95 | 42.79 | 6.15 | 48.936 |
| 300.87 | 46.05 | 4.48 | 50.534 |
| 301.8 | 45.05 | 4.7 | 49.751 |
| 302.73 | 36.58 | 4.62 | 41.201 |
| 303.65 | 40.99 | 4.4 | 45.39 |
| 304.58 | 39.02 | 3.96 | 42.977 |
| 305.5 | 46.38 | 5.8 | 52.174 |
| 306.43 | 45.84 | 5.83 | 51.678 |
| 307.82 | 49.93 | 3.76 | 53.69 |
| 308.56 | 42.69 | 5.48 | 48.174 |
| 309.94 | 39.01 | 5.79 | 44.803 |
| 311.33 | 44.53 | 4.24 | 48.773 |
| 312.72 | 39.22 | 4.79 | 44.006 |
| 314.11 | 44.59 | 7.61 | 52.198 |
| 315.5 | 51.64 | 8.98 | 60.623 |
| 316.42 | 47.13 | 5.72 | 52.853 |
| 316.89 | 53.87 | 5.35 | 59.222 |
| 317.81 | 52.12 | 6.42 | 58.541 |
| 318.74 | 52.7 | 6.84 | 59.54 |
| 319.66 | 49.85 | 6.43 | 56.275 |
| 320.59 | 60.88 | 6.26 | 67.138 |
| 321.51 | 58.17 | 5.59 | 63.761 |
| 322.44 | 70.91 | 5.33 | 76.236 |
| 323.36 | 68.13 | 6.43 | 74.563 |
| 324.29 | 50.25 | 8.62 | 58.871 |
| 325.22 | 48.69 | 9.8 | 58.481 |
| 326.14 | 41.67 | 9.79 | 51.456 |
| 327.07 | 48.74 | 9.46 | 58.203 |
| 327.99 | 53.24 | 10.96 | 64.198 |
| 329.38 | 51.85 | 8.52 | 60.366 |
| 331.23 | 51.44 | 10.52 | 61.954 |
| 332.16 | 51.82 | 7.91 | 59.73 |
| 333.08 | 45.27 | 10.53 | 55.797 |
| 334.01 | 58.72 | 8.74 | 67.463 |
| 334.93 | 57.01 | 10.47 | 67.486 |

| Cummulative thickness (mm) | %1st extraction opal | %2nd extraction opal | Total %opal |
|---|---|---|---|
| 335.86 | 50.68 | 7.42 | 58.102 |
| 336.78 | 48.05 | 9.26 | 57.309 |
| 337.71 | 47.18 | 8.02 | 55.197 |
| 338.63 | 53.01 | 8 | 61.003 |
| 339.56 | 62.15 | 8.07 | 70.216 |
| 340.49 | 51.83 | 8.81 | 60.634 |
| 341.41 | 57.01 | 6.62 | 63.628 |
| 342.34 | 60.68 | 6.58 | 67.263 |
| 343.26 | | | |
| 344.19 | 53.34 | 5.55 | 58.886 |
| 345.11 | 59.93 | 6.26 | 66.189 |
| 346.04 | 53.28 | 6.13 | 59.406 |
| 346.96 | 51.99 | 6.31 | 58.301 |
| 347.89 | 55.43 | 8.03 | 63.459 |
| 348.82 | 55.44 | 8.12 | 63.563 |
| 349.51 | 51.06 | 5.89 | 56.945 |
| 350.2 | 52.76 | 7.86 | 60.624 |
| 351.59 | 58.11 | 7.66 | 65.777 |
| 352.98 | 50.3 | 6.25 | 56.55 |
| 353.67 | 54.8 | 6.19 | 60.991 |
| 354.6 | 53.92 | 4.22 | 58.142 |
| 356.45 | 62.12 | 4.99 | 67.115 |
| 357.38 | 58.89 | 8.58 | 67.471 |
| 358.3 | 70.03 | 5.44 | 75.477 |
| 359.23 | 66.42 | 5.58 | 72.001 |
| 359.92 | 65.53 | 6.03 | 71.562 |
| 360.85 | 72 | 9.59 | 81.594 |
| 361.77 | 71.25 | 6.46 | 77.71 |
| 362.7 | 62.81 | 6.93 | 69.743 |
| 364.09 | 63.75 | 5.24 | 68.997 |
| 365.01 | 67.47 | 6.22 | 73.69 |
| 365.71 | 60.97 | 6.8 | 67.767 |
| 366.63 | 63.81 | 5.6 | 69.408 |
| 367.56 | 71 | 7.23 | 78.222 |
| 369.41 | 68.45 | 6.89 | 75.343 |
| 370.1 | 68.25 | 8.96 | 77.215 |
| 371.03 | 67.3 | 7.72 | 75.017 |
| 372.42 | 63.97 | 6.56 | 70.522 |
| 373.8 | 47.49 | 6.77 | 54.256 |
| 375.19 | 56.22 | 5.8 | 62.015 |
| 376.58 | 58.43 | 5.63 | 64.055 |
| 378.43 | 46.41 | 7.17 | 53.583 |

| Cummulative thickness (mm) | %1st extraction opal | %2nd extraction opal | Total %opal |
|---|---|---|---|
| 379.82 | 45.55 | 6.43 | 51.974 |
| 381.21 | 48.25 | 6.19 | 54.441 |
| 382.13 | 51.5 | 6.8 | 58.293 |
| 383.52 | 46.68 | 7.78 | 54.463 |
| 384.45 | 46.44 | 5.91 | 52.348 |
| 385.37 | 45.42 | 6.53 | 51.946 |
| 386.3 | 67.64 | 7.37 | 75.012 |
| 387.22 | 62.58 | 6.16 | 68.738 |
| 388.15 | 56.73 | 6.35 | 63.08 |
| 389.07 | 58.16 | 7.36 | 65.52 |
| 390 | 56.33 | 6.52 | 62.849 |
| 390.9 | 65.18 | 5.67 | 71.76 |
| 391.8 | 64.23 | 5.66 | 69.99 |
| 392.7 | 75.04 | 6.43 | 81.63 |
| 393.6 | 57.25 | 7.66 | 65.21 |
| 394.5 | 56.1 | 8.88 | 65.39 |
| 396.3 | 64.32 | 8.43 | 73.11 |
| 398.1 | 53.85 | 7.31 | 61.42 |
| 399.9 | 64.27 | 7.95 | 72.55 |
| 400.9 | 62.02 | 6.37 | 68.55 |
| 401.4 | 65.52 | 5.87 | 71.51 |
| 403.2 | 56.81 | 6.96 | 63.99 |
| 404.7 | 55.9 | 6.73 | 62.83 |
| 406.2 | 59.92 | 6.54 | 66.64 |
| 407.7 | 55.12 | 5.94 | 61.18 |
| 409.8 | 55.5 | 6.52 | 62.2 |
| 411.4 | 51.74 | 5.61 | 57.45 |
| 411.9 | 57 | 5.82 | 62.93 |
| 412.4 | 54.96 | 6.91 | 62.1 |
| 413.5 | 56.82 | 9.47 | 66.76 |
| 415.6 | 50.2 | 9.29 | 59.95 |
| 416.6 | 52.4 | 8.22 | 60.97 |
| 417.6 | 62.56 | 4.76 | 67.33 |
| 418.6 | 55.23 | 7.37 | 62.86 |
| 420.6 | 43.18 | 7.07 | 50.48 |
| 422.6 | 55.35 | 6.89 | 62.46 |
| 424.1 | 51.85 | 4.7 | 60.14 |
| 425.6 | 45.12 | 6.21 | 56.1 |
| 426.6 | 47.86 | 5.82 | 58.13 |
| 427.6 | 43.53 | 5.92 | 54 |
| 429.9 | 47.45 | 5.78 | 57.65 |
| 432.6 | 54.83 | 5.83 | 65.12 |

| Cummulative thickness (mm) | %1st extraction opal | %2nd extraction opal | Total %opal |
|---|---|---|---|
| 433.9 | 55.04 | 4.8 | 63.5 |
| 436.1 | 57.36 | 4.68 | 65.61 |
| 437.1 | 62.62 | 5.2 | 71.78 |
| 437.9 | 62.5 | 6.83 | 74.58 |
| 438.7 | 60.39 | 6.83 | 72.45 |
| 439.3 | 52.16 | 7.68 | 65.74 |
| 440.1 | 54.64 | 6.41 | 65.97 |
| 442.1 | 60.77 | 7.71 | 75.6 |
| 444.2 | 56.49 | 6.16 | 67.37 |
| 446.2 | 48.61 | 7.82 | 62.44 |
| 448.24 | 47.75 | 6.86 | 59.87 |
| 450.2 | 49.55 | 6.41 | 60.89 |
| 452.6 | 54.17 | 6.45 | 65.57 |
| 455 | 62.39 | 6.06 | 73.09 |
| 457.4 | 63.07 | 5.52 | 72.82 |
| 459.8 | 61.69 | 5.5 | 71.39 |
| 461.6 | 49.55 | 4.67 | 57.78 |
| 462.2 | 63.73 | 4.57 | 71.78 |
| 463.4 | 59.03 | 6.03 | 69.68 |
| 464.2 | 61 | 6.41 | 72.33 |
| 465 | 60.67 | 4.54 | 68.68 |
| 465.8 | 57.19 | 6.48 | 68.64 |
| 467.7 | 61.39 | 6.44 | 72.77 |
| 470.2 | 65.14 | 3.33 | 70.99 |
| 471.5 | 59.65 | 6.24 | 70.67 |
| 472.8 | 70.64 | 3.66 | 77.1 |
| 474.7 | 56.74 | 3.03 | 62.06 |
| 476.6 | 53.92 | 3.25 | 59.63 |
| 478.5 | 48.93 | 5.27 | 56.57 |
| 481 | 53.58 | 6.9 | 63.58 |
| 483.3 | 54.85 | 5.31 | 62.55 |
| 485.8 | 54.93 | 5.4 | 62.75 |
| 488.1 | 60.25 | 4.89 | 67.33 |
| 489.3 | 61.82 | 5.58 | 69.9 |
| 491.5 | 58.63 | 7.45 | 69.42 |
| 493.3 | 56.77 | 6.32 | 65.93 |
| 495.1 | 57.36 | 6.85 | 67.29 |
| 503.3 | 57.49 | 6.63 | 64.12 |
| 504.9 | 54.56 | 5.99 | 60.55 |
| 506.5 | 53.76 | 6.65 | 60.41 |
| 508.1 | 67.28 | 5.17 | 72.46 |
| 509.7 | 63.38 | 6.91 | 70.29 |

| Cummulative thickness (mm) | %1st extraction opal | %2nd extraction opal | Total %opal |
|---|---|---|---|
| 511.3 | 54.03 | 5.64 | 59.67 |
| 512.9 | 68.54 | 6.48 | 75.02 |
| 514 | 61.23 | 5.34 | 66.57 |
| 515.6 | 58.44 | 5.28 | 63.72 |
| 517.2 | 58.52 | 6.09 | 64.61 |
| 518.3 | 59.07 | 7.9 | 66.97 |
| 519.3 | 63.23 | 8.28 | 71.51 |
| 520.8 | 66.2 | 6.5 | 72.7 |
| 521.8 | 63.71 | 8.09 | 71.81 |
| 522.8 | 62.45 | 7.96 | 70.41 |
| 523.8 | 59.73 | 6.99 | 66.72 |
| 525.3 | 53.69 | 8.56 | 62.25 |
| 526.8 | 44.18 | 9.66 | 53.85 |
| 527.8 | 49.84 | 9.78 | 59.61 |
| 528.8 | 60.14 | 10.01 | 70.15 |
| 529.8 | 47.21 | 10.51 | 57.73 |
| 531.6 | 45.34 | 8.74 | 54.08 |
| 532.5 | 48.57 | 7.34 | 55.91 |
| 533.4 | 52.2 | 9.29 | 61.48 |
| 534.9 | 51.78 | 8.25 | 60.03 |
| 536.3 | 54.88 | 9.82 | 64.7 |
| 537.2 | 46.55 | 6.75 | 53.29 |
| 539 | 59.35 | 8.23 | 67.58 |
| 540.5 | 61.57 | 8.39 | 69.95 |
| 542 | 53.37 | 7.39 | 60.76 |
| 543 | 55.55 | 6.57 | 62.12 |
| 544 | 49.91 | 7.97 | 57.88 |
| 546 | 50.47 | 8.33 | 58.8 |
| 547 | 53.52 | 7.8 | 61.32 |
| 548 | 47.95 | 3.66 | 51.61 |
| 549.5 | 58.37 | 3.63 | 62 |
| 550.5 | 60.95 | 3.49 | 64.44 |
| 552 | 58.51 | 3.78 | 62.29 |
| 553.5 | 57.35 | 11.79 | 69.14 |
| 555 | 56.15 | 5.57 | 61.71 |
| 556.5 | 42.99 | 7.88 | 50.88 |
| 558.5 | 46.27 | 9.79 | 56.06 |
| 560 | 39.98 | 7.85 | 47.83 |
| 562.5 | 44.31 | 11.71 | 56.02 |
| 564.5 | 44.11 | 8.52 | 52.63 |
| 566 | 38.2 | 7.89 | 46.09 |
| 568 | 42.26 | 8.33 | 50.59 |

| Cummulative thickness (mm) | %1st extraction opal | %2nd extraction opal | Total %opal |
|---|---|---|---|
| 570 | 42.34 | 8.86 | 51.21 |
| 571.5 | 42.75 | 7.07 | 49.82 |
| 573.5 | 42.56 | 6.34 | 48.9 |
| 575.5 | 45.83 | 7.27 | 53.11 |
| 577.5 | 41.47 | 7.39 | 48.86 |
| 580 | 40.11 | 8.11 | 48.23 |
| 581.5 | 38 | 7.73 | 45.73 |
| 583.2 | 38.94 | 7.26 | 46.2 |
| 584.9 | 52.83 | 6.85 | 59.68 |
| 586.6 | 48.03 | 7.98 | 56.01 |
| 589.5 | 42.61 | 6.52 | 49.13 |
| 591.5 | 46.11 | 7.46 | 53.56 |
| 593.5 | 46.13 | 7.94 | 54.07 |
| 595.5 | 40.77 | 7.21 | 47.98 |
| 597.5 | 48.48 | 7.31 | 55.79 |
| 599.5 | 39.19 | 6.45 | 45.64 |
| 601 | 48.76 | 5.11 | 53.86 |

# APPENDIX 9: LOW RESOLUTION OPAL MEASUREMENTS AND POINT COUNTS

## A9.1 SITE 848: OPAL RESULTS

Low levels of biogenic opal and high levels of frustule dissolution in these sediments resulted in insignificant levels of second extraction opal. OPAL measurements for samples from this site were made using a single 7 hour extraction period.

| Sample | %OPAL |
|---|---|
| 4H-5, 25-27 | 11.14 |
| 4H-6, 74-76 | 18.66 |
| 5H-1, 77-79 | 17.28 |
| 5H-2, 125-127 | 12.11 |
| 5H-4, 25-27 | 8.55 |
| 5H-5, 76-78 | 15.33 |
| 5H-6, 125-127 | 12.67 |
| 6H-1, 125-127 | 19.03 |
| 6H-3, 25-27 | 12.21 |
| 6H-4, 75-77 | 13.09 |

## A9.2 SITE 849: OPAL RESULTS

| Sample | %1st extraction OPAL | %2nd extraction OPAL |
|---|---|---|
| 12H-5, 27-29 | 7.37 | 0.75 |
| 12H-5, 76-78 | 5.03 | 0.83 |
| 12H-5, 98-100 | 4.64 | 0.47 |
| 12H-5, 125-127 | 4.80 | 0.27 |
| 12H-6,5-7 | 6.47 | 1.22 |
| 12H-6, 25-27 | 6.55 | 1.78 |
| 12H-6, 50-52 | 4.72 | 0.48 |
| 12H-6, 98-100 | 15.42 | 5.07 |
| 12H-6, 122-124 | 17.53 | 5.05 |
| 12H-6, 145-147 | 18.28 | 5.42 |
| 12H-7, 41-43 | 12.17 | 4.93 |
| 12H-7, 71-75 | 16.63 | 6.59 |
| 13H-1, 25-27 | 10.49 | 2.85 |
| 13H-1, 84-86 | 28.48 | 5.82 |
| 13H-2, 10-12 | 36.02 | 6.94 |
| 13H-2, 71-73 | 36.72 | 4.50 |
| 13H-2, 100-102 | 24.03 | 4.95 |
| 13H-2, 145-147 | 20.85 | 4.19 |
| 13H-3, 25-27 | 29.66 | 6.21 |

| Sample | %1st extraction OPAL | %2nd extraction OPAL |
|---|---|---|
| 13H-3, 50-52 | 22.56 | 6.12 |
| 13H-3, 70-72 | 22.09 | 6.87 |
| 13H-3, 100-102 | 31.21 | 7.36 |
| 13H-3, 125-127 | 30.18 | 7.21 |
| 13H-4, 73-75 | 25.03 | 8.00 |
| 13H-4, 125-127 | 29.93 | 7.75 |
| 13H-5, 25-27 | 23.01 | 4.90 |
| 13H-5, 50-52 | 24.81 | 6.76 |
| 13H-5, 76-78 | 24.97 | 5.97 |
| 13H-5, 125-127 | 25.70 | 6.76 |
| 13H-5, 144-146 | 25.95 | 5.97 |
| 13H-6, 25-27 | 18.36 | 4.43 |
| 13H-6, 72-74 | 20.12 | 5.65 |
| 13H-6, 100-102 | 23.36 | 7.94 |
| 13H-6, 125-127 | 21.78 | 7.00 |
| 14X-2, 27-29 | 29.28 | 9.75 |
| 14X-2, 75-77 | 31.82 | 14.23 |
| 14X-2, 96-98 | 25.00 | 10.50 |
| 14X-2, 144-146 | 27.23 | 11.39 |
| 14X-3, 7-9 | 35.77 | 13.69 |
| 14X-3, 71-73 | 29.71 | 15.61 |
| 15X-2, 144-146 | 9.33 | 3.15 |
| 15X-3, 98-100 | 12.18 | 8.19 |
| 15X-4, 145-147 | 8.22 | 2.71 |
| 15X-5, 144-146 | 10.09 | 3.23 |
| 15X-6, 50-52 | 12.95 | 4.85 |

### A9.3 SITE 850: OPAL RESULTS

| Sample | %1st extraction OPAL | %2nd extraction OPAL |
|---|---|---|
| 10H-7,1-3 | 27.15 | 12.14 |
| 10H-7,17-19 | 33.51 | 16.70 |
| 10H-7,36-38 | 44.93 | 12.82 |
| 10H-7,56-58 | 37.58 | 15.86 |
| 10H-7,70-72 | 44.10 | 16.32 |
| 11X-1,6-8 | 7.31 | 3.17 |
| 11X-1,25-27 | 7.48 | 3.04 |
| 11X-1,50-52 | 7.47 | 3.02 |
| 11X-1,74-76 | 6.47 | 2.62 |
| 11X-1,99-101 | 7.07 | 2.39 |
| 11X-1,123-125 | 4.86 | 2.54 |
| 11X1,143-145 | 5.30 | 2.56 |

### A9.4 SITE 851: OPAL RESULTS

| Sample | %1st extraction OPAL | %2nd extraction OPAL |
|---|---|---|
| 7H-4, 99-101 | 12.38 | 3.43 |
| 7H-5, 50-52 | 5.82 | 1.22 |
| 7H-5, 145-147 | 9.44 | 2.59 |
| 7H-6, 100-102 | 13.12 | 3.87 |
| 7H-7, 47-49 | 8.34 | 2.58 |
| 7H-7, 7-9 | 8.82 | 2.67 |
| 8H-1, 50-52 | 10.01 | 3.20 |
| 8H-1, 125-127 | 6.26 | 1.56 |
| 8H-2, 146-148 | 5.41 | 1.67 |
| 8H-2, 50-52 | 5.08 | 1.54 |
| 8H-3, 100-102 | 5.63 | 1.57 |
| 8H-4, 50-52 | 5.11 | 0.98 |
| 8H-4, 100-102 | 4.52 | 0.79 |
| 8H-5,73-75 | 5.87 | 1.67 |
| 8H-5,125-127 | 4.94 | 1.46 |
| 8H-6,52,54 | 3.79 | 1.06 |
| 8H-7,2-4 | 7.39 | 2.50 |
| 9H-1,50-52 | 7.63 | 3.06 |
| 9H-1,100-102 | 13.09 | 3.08 |
| 9H-2,49-51 | 18.50 | 5.35 |
| 9H-2,100-102 | 22.53 | 6.93 |
| 9H-3,50-52 | 11.43 | 4.80 |
| 9H-3,100-103 | 14.92 | 5.73 |
| 9H-4,50-52 | 11.29 | 5.04 |
| 9H-4,100-102 | 8.39 | 3.14 |
| 9H-5,50-52 | 6.21 | 1.86 |
| 9H-5,100-102 | 11.37 | 3.74 |
| 9H-6,50-52 | 6.52 | 2.39 |
| 9H-6,99-101 | 10.00 | 2.43 |

### A9.5 SITE 847: POINT-COUNT RESULTS (%)

For dissolution index and opal measurement data for these samples see Appendix A6.

| Sample ID | %second extraction opal (of total opal) | Composition of biosiliceous assemblage (as % of total biosiliceous frustules) | | | |
|---|---|---|---|---|---|
| | | %T. longissima Group | % radiolarian and silicoflagellates | %other diatoms | % non-T. longissima Group biosiliceous frustules |
| a1 | 16.89 | 59 | 10.3 | 30.8 | 41 |
| a2 | 14.14 | 68.2 | 13.2 | 18.6 | 31.8 |
| a3 | 14.4 | 70.2 | 7.5 | 22.4 | 29.9 |
| a4 | 20.06 | 55 | 15.7 | 29.3 | 45 |
| a5 | 18.58 | 65.9 | 17 | 17 | 34.1 |
| a6 | 17.87 | 63.1 | 14.5 | 21.2 | 36.9 |
| a7 | 18.94 | 65.9 | 14.3 | 19.8 | 34.1 |
| a8 | 20.04 | 61.5 | 22.9 | 20.8 | 38.5 |
| a9 | 21.89 | 68.5 | 5.6 | 25.8 | 31.5 |
| a10 | 31.88 | 60.2 | 7.9 | 32 | 39.8 |
| a11 | 28.27 | 56.3 | 10.7 | 23.3 | 43.4 |
| a12 | 31.91 | 62.4 | 11.8 | 25.8 | 37.6 |

### A9.6 SITE 850: POINT-COUNT RESULTS (%)

For dissolution index and opal measurement data for these samples see Appendix A6.

| Sample ID | %second extraction opal (of total opal) | Composition of biosiliceous assemblage (as % of total biosiliceous frustules) | | | |
|---|---|---|---|---|---|
| | | %T. longissima Group | % radiolarian and silicoflagellates | %other diatoms | % non-T. longissima Group biosiliceous frustules |
| b1 | 8.87 | 67.9 | 15 | 17.1 | 32.1 |
| b2 | 7.96 | 78.9 | 7 | 14 | 21.1 |
| b3 | 6.07 | 75.3 | 5.9 | 18.9 | 24.7 |
| b4 | 11.75 | 74 | 8.3 | 17.8 | 26 |
| b5 | 8.31 | 70.3 | 12.2 | 17.5 | 29.7 |
| b6 | 9.61 | 75 | 10.7 | 14.9 | 25 |
| b7 | 4.75 | 70.5 | 9.8 | 19.7 | 29.5 |

## A9.6 SITE 851: POINT-COUNT RESULTS (PER MG)

| Sample | mbsf | Radiolarian frustules per mg | Centric diatom frustules per mg | Thalassiothrix frustule per mg |
|---|---|---|---|---|
| 8H-3,100-102 | 68.5 | 463.04 | 268.35 | 635.91 |
| 8H-6, 50-52 | 72.5 | 443 | 342 | 390.9 |
| 9H-1,100-102 | 75 | 801.67 | 577.59 | 797.39 |
| 9H-2,49-51 | 75.99 | 529.04 | 435.35 | 3169 |
| 9H-2,100-102 | 76.5 | 706.35 | 1236.6 | 7894.9 |
| 9H-3,50-52 | 77.5 | 529.55 | 430.41 | 2830.1 |
| 9H-5,50-52 | 80.5 | 586.17 | 342.14 | 1291.5 |
| 9H-6,99-101 | 82.49 | 1010.3 | 517.71 | 1484.1 |

## APPENDIX 10: CARBON ANALYSIS RESULTS

Sample section ODP-138-847B-15H-7, 74-81cm. Mean sample layer thickness is 1.1mm, sample layers numbered upwards from base (15H-7, 81cm).

The growth of mould on these core sections (see Section 3.5) means that carbon has been redistributed over distance of 1-5cm. Hence, these measurements should only be used as a guide to bulk sediment organic carbon contents. Mean organic carbon content is 0.85% (SD=0.48).

| Sample layer ID number | % Organic carbon | % Carbonate |
|---|---|---|
| 1 | 0.91 | 76.24 |
| 2 | 1.02 | 79.87 |
| 3 | 0.68 | 71.72 |
| 4 | 0.84 | 79.44 |
| 5 | 0.76 | 79.43 |
| 6 | 0.85 | 80.69 |
| 7 | 0.79 | 77.87 |
| 8 | 1.34 | 80.13 |
| 9 | 1.01 | 82.16 |
| 10 | 1.63 | 79.33 |
| 11 | n.d. | n.d. |
| 12 | 1.56 | 80.95 |
| 13 | 0.89 | 76.46 |
| 14 | 0.65 | 60.71 |
| 15 | 0.74 | 63.62 |
| 16 | 0.68 | 42.99 |
| 17 | 0.55 | 33.67 |
| 18 | 1.18 | 44.71 |
| 19 | 0.67 | 33.82 |
| 20 | 0.67 | 33.82 |
| 21 | 0.68 | 39.29 |
| 22 | 0.52 | 42.53 |
| 23 | 0.53 | 48.74 |
| 24 | 0.62 | 50.68 |
| 25 | 0.53 | 52.62 |
| 26 | 0.56 | 53.06 |
| 27 | 0.58 | 49.89 |
| 28 | n.d. | n.d. |
| 29 | n.d. | n.d. |
| 30 | n.d. | n.d. |
| 31 | 1.76 | 41.66 |

| Sample layer ID number | % Organic carbon | % Carbonate |
|---|---|---|
| 32 | 0.82 | 35.57 |
| 33 | 0.64 | 36.96 |
| 34 | 0.56 | 37.43 |
| 35 | 0.63 | 38.26 |
| 36 | 0.67 | 41.64 |
| 37 | 0.68 | 36.25 |
| 38 | 0.74 | 36.13 |
| 39 | 0.94 | 38.5 |
| 40 | 0.79 | 47.44 |
| 41 | 0.80 | 47.85 |
| 42 | 1.32 | 50.22 |
| 43 | 1.19 | 48.41 |
| 44 | 1.39 | 43.18 |
| 45 | 1.30 | 46.07 |
| 46 | 1.34 | 44.69 |
| 47 | 3.79 | 48.4 |
| 48 | 1.27 | 41.64 |
| 49 | 0.79 | 37.61 |
| 50 | 0.70 | 36.29 |
| 51 | 0.63 | 37.00 |
| 52 | 0.70 | 45.03 |
| 53 | 0.74 | 55.04 |
| 54 | 0.77 | 48.54 |
| 55 | 0.82 | 41.6 |
| 56 | 0.69 | 38.84 |
| 57 | 0.85 | 34.95 |
| 58 | 0.75 | 27.49 |
| 59 | 0.61 | 25.33 |
| 60 | 0.61 | 29.56 |
| 61 | 0.68 | 34.4 |
| 62 | 0.51 | 34.09 |
| 63 | 0.64 | 41.77 |
| 64 | 0.53 | 45.41 |
| 65 | 0.39 | 43.09 |
| 66 | 0.36 | 49.99 |
| 67 | 0.57 | 47.91 |
| 68 | 0.37 | 44.26 |
| 69 | 0.49 | 42.00 |

## APPENDIX 11: SILICA FLUX BOX-MODEL

This model is based on that of Broecker (1971) and Broecker and Peng (1987) and used in Decker (1991). See Figure 7.8a for schematic diagram of the model and definition of notation.

### A11.1 PARAMETERS AND VARIABLES

| Symbol | Parameter/variable | Magnitude (if variable, at t=0) | Reference |
|---|---|---|---|
| $V_S$ | volume of surface box, constant | 3.6 x $10^{16}$ $m^3$ | Libes, 1992; Broecker and Peng, 1985 |
| $[S_S]$ | concentration, constant | 1.8 x$10^{-3}$ gSi/$m^3$ | Tréguer *et al*, 1995 |
| $V_D$ | volume of deep box, constant | 1.1 x $10^{18}$ $m^3$ | Libes, 1992; Broecker and Peng, 1985 |
| $[S_D]$ | concentration of deep box, function of time | 3.6 x$10^{-3}$ gSi/$m^3$ | Tréguer et al, 1995 |
| v(t) | volume flux between boxes (+ve downwards), function of time | 1.1 x $10^{15}$ $m^3$/yr | Broecker and Peng, 1985 |
| E(t) | export of solid silica from surface box to deep box, function of time | gSi/yr | this study |
| alpha | proportion of solid silica dissolved in water column, constant | 0.9-0.5 | Heath, 1974; this study |
| I(t) | input of silica via rivers | 2.0 x $10^{11}$gSi/yr | calculated from Tréguer *et al*, 1995 and Libes, 1992 |

Table A14.1. Parameters and variables used in box model of Si flux. Where the value of a parameter was changed between model runs the range of values used is given.

### A11.2 ASSUMPTIONS

a) the silica concentration of the surface box is held low and constant to biogenic uptake of silica

b) a constant proportion of exported solid silica (alpha) is dissolved in the water column and surface sediment

### A11.3 EQUATIONS

Using the relationship of silica concentration in the deep box to water exchange through up- and downwelling and export and dissolution of solid silica

$$\frac{d[S_D]}{dt} = \frac{v(t)}{V_D}\left([S_S]-[S_D]\right) + \frac{\alpha E(t)}{V_D} \qquad \text{Equation A11.1}$$

where;

$$E(t) = I(t) + v(t)\left([S_D]-[S_S]\right) \qquad \text{Equation A11.2}$$

Subsistuting; $A=\left(\frac{1-\alpha}{V_D}\right)$ and $f(t) = \frac{\alpha}{V_D}.I(t)+v(t).A.[S_S]$, into Equations A11.1 and A11.2 gives;

$$\frac{d[S_D]}{dt} = -v(t).A.[S_D] + f(t) \qquad \text{Equation A11.3}$$

**A11.4 SOLUTION**

Following the model of Decker (1991) step-like changes in the global upwelling/riverine input rate are assumed, see Figure 7.8b. Hence, each stage of the input function both inputs can be considered as constants. Integrating (3) assuming v(t) and f(t) are constant gives the solution;

$$S_D = \frac{f_0}{A.v_0} + K.e^{-v_0.A.t} \qquad \text{Equation A11.4}$$

where $f_0$ and $v_0$ are the values of v(t) and f(t) at the begining of each input stage. K is the intergration constant and is also unique to each input stage. K is calculated by setting t equal to zero and $S_D$ to the value of $S_D$ at the end of the previous input stage.

## REFERENCES

Agterberg, F. P. and I. Banerjee (1969). "Stochastic model for the deposition of varves in glacial Lake Barlow-Ojibway, Ontario, Canada." Canadian Journal of Earth Sciences **6**: 625-652.

Alldredge and Gotschalk (1989). "Direct observations of mass flocculation of diatom blooms, characteristic, settling velocities and formation of diatom aggregates." Deep-Sea Research **36**: 159-171.

Alldredge, A. L. and M. W. Silver (1982). "Abundance and production rates of floating diatom mats (*Rhizosolenia castracanei* and *R. imbricata*) of the eastern Pacific Ocean." Marine Biology **66**: 83-88.

Aller, R. C. (1978). The effect of animal-sediment interations on geochemical processes near the sediment water interface. Estuarine Interactions. M. L. Wiley, Academic Press: 157-172.

Aller, R. C. (1980). "Quantifying solute distributions in the bioturbated zone of marine sediments by defining and avergae microenvironment." Geochimica et Cosmochimica Acta **44**: 1955-1965.

Altabet, M. A. (1988). "Variations in nitrogen isotopic composition between sinking and suspended particles: implications for nitrogen cycling and particle transformation in the open ocean." Deep-Sea Research **35A**(4): 535-554.

Altabet, M. A. (1989). "A time-series study of the vertical structure of nitrogen and particle dynamics in the Sargasso Sea." Limnology and Oceanography **34**(7): 1185-1201.

Anderson, R. Y. (1986). "The varve micocosm: propagator of cyclic bedding." Paleoceanography **1**: 373-382.

Anderson, R. Y. and D. W. Kirkland (1960). "Origin, varves and cycles of Jurassic Toldilto Formation, New Mexico." American Assoication of Petroleum Geology Bulletin **44**: 37-52.

Anderson, R. Y. and D. W. Kirkland (1969). Paleoecology of and early Pleistocene lake on the High Plains of Texas.

Anderson, R. Y. and L. H. Koopmans (1969). "Statistical analysis of Rita Blanca varve time-series." Memiors of Geological Society of America Bulletin **113**: 59-75.

Anderson, R. Y., B. K. Linsley and J. V. Gardner (1990). "Expression of seasonal and ENSO forcing in climatic variability at lower that ENSO frequencies: evidence from Pleistocene marine varves off California." Palaeogeography, Palaeoclimatology, Palaeoecology. **78**: 287-300.

Andreae, M. O. and P. N. Fröelich (1981). "Determination of germanium in natural waters by graphite furnace atomic absorption spectrometry with hydride generation." Analytical Chemistry **53**: 287-291.

Archer, D., M. Lyle, M. Rodgers and P. Froelich (1993). "What controls opal preservation in tropical deep-sea sediments?" Paleoceanography **8**(1): 7-21.

Arrhenius, G. (1952). "Sediment cores from the East Pacific." Reports of the Swedish Deep Sea Expendition **5**: 1-228.

Attolini, M. R., M. Galli and T. Nanni (1988). Long and short cycle in solar activity during the last milennia. Secular solar and geomagnetic varations in the last 10,000 years. F. R. Stephenson and A. W. Wolfendale. Dordrecht, Kluwer Academic: 49-68.

Backman, J. and I. Raffi (in press). .

Baksi, A. K., V. Hsu, M. O. McWilliams and E. Farrar (1992). "$^{40}Ar/^{39}Ar$ dating of the Brunhes-Matuyama geomagnetic field reversal." Science **256**: 356-357.

Bandy, O. L. (1970). "Upper Cretaceous-Cenozoic paleobathymetric cycle eastern Panama and nothern Columbia." Transactions of the Gulf Coast Association Geology Society **20**: 181-193.

Bandy, O. L. and R. E. Casey (1973). "Reflector horizons and paleobathymetric history, eastern Panama." Geological Society of America Bulletin **84**: 3081-3086.

Barber, R. T. (1992). "Fall survey cruise finds cooling conditions in equatorial Pacific." US JGOFS News 4(1): 1-6.

Barron, J. A. and G. Keller (1983). "Paleotemperature oscillations in the Middle and Late Miocene of the northeastern Pacific." Micropaleotology **29**: 150-181.

Battarbee, R. W. (1973). "A new method for the estimation of absolute microfossil numbers, with reference especially to diatoms." Limnology and Oceanography **18**: 647-653.

Becking, L. G. M. and D. Moore (1959). "Density distribution in sediments." Journal of Sedimentary Petrology **29**: 47-55.

Beer, J., U. Siegenthaler and A. Blinov (1988). Temporial $^{10}Be$ variations in ice: information on solar activity and geomagnetic field intensity. Secular solar and geomagnetic varations in the last 10,000 years. F. R. Stephenson and A. W. Wolfendale. Dordrecht, Kluwer Academic: 297-313.

Beers, J. R., F. M. H. Reid and G. L. Stewart (1975). "Microplankton of the North Pacific Central Gyre population structure and Abundance, June 1973." Internationale Revue ges. Hydrobiol. **60**(5): 607-638.

Bender, M. L. and M. J. McPhaden (1990). "Anomalus nutrient distribution in the equatorial Pacific April 1988: evidence for rapid biological uptake." Deep Sea Research **37**: 1075-1084.

Berger, W. H. (1976). Biogenous deep sea sediments. Chemical Oceanography. J. P. Riley and R. Chester. **Vol. 5**: 305-388.

Berger, W. H. (1992). Pacific carbonate cycles revisited: arguments for and against productivity control. Centenary of Japanese Micropaleóntolgy. K. Ishizaki and T. Saito. Tokyo, Terra Scientific Publishing Company: 15-25.

Berggren, W. A., D. V. Kent and J. J. Flynn (1985). Jurassic to Paleogene: Part 2. Paleogene and chronostratigraphy. The Chronology of the Geological Record. N. J. Snelling. **10:** 141-195.

Berggren, W. A., D. V. Kent and J. J. Flynn (1985). The Neogene: Part 2. Neogene geochronology and chronostratigraphy. The Chronology of the Geological Record. N. J. Snelling: 221-260.

Berggren, W. A., D. V. Kent, C. C. Swisher and M.-P. Aubry (1995). A revised Cenozoic geochronology and chronostratigraphy. Geochronology, timescales and global stratigraphic correlation. W. A. Berggren, D. V. Kent, M.-P. Aubry and J. Hardenbol. Tulsa, Society of Sedimentary Geology, Special Publication. **54:** 129-212.

Berner, W., H. Oeschger and B. Stauffer (1980). "Information on the $CO_2$ cycle from ice core studies." Radiocarbon **22**: 227-235.

Blakely, R. J. (1974). "Geomagnetic reversals and crustal spreading rates during the Miocene." Journal of Geophysical Research **79**: 2979-2985.

Bodén, P. and J. Backman (1996). "A laminated sediment sequence from the North Atlantic Ocean and its climatic record." Geology **24**(6): 507-510.

Booth, B. C. and P. J. Harrison (1979). "Effect of silicate limiation on vlave morphology in *Thalassiosira* and *Coscinodiscus* (Bacillariophyceace)." Journal of Phycology **15**: 326-329.

Boudreau, B. P. (1990). "Asymptotic forms and solutions of the model for silica-opal diagenesis in bioturbated sediments." Journal of Geophysical Research **95**(C5): 7367-7379.

Broecker and Peng (1987). Tracers in the Sea.

Broecker, W. S. (1971). "A kinematic model for the chemical composition of the sea water." Quaternary Research **1**: 188-207.

Brzezinski, M. A. (1985). "The Si:C:N ratio of marine diatoms: Interspecific variability and the effect of some environmental variables." Journal of Phycology **21**: 347-357.

Burton, J. D., T. M. Leatherhaed and P. S. Liss (1970). "The reactivity of dissolved silica in some natural waters." Limnology and Oceanography **15**: 473-476.

Calvert, S. E. (1974). "Deposition and diagenesis of silica in marine sediments." Special Publication of International Association of Sedimentology **1**: 273-299.

Cande, S. C. and D. V. Kent (1992). "A new geomagnetic polarity time scale for the Late Cretaceous and Cenozoic." Journal of Geophysical Research **97**: 13917-13951.

Cande, S. C. and Y. Kristofferson (1977). "Late Cretaceous magnetic anomalies in the North Atlantic." Earth and Planetary Science Letters **35**: 25-224.

Cane, M. A. (1983). "Oceanographic events during El Niño." Science **222**: 1189-1195.

Carpenter, E. J., G. R. Harbison, L. P. Madin, N. R. Swanberg, D. C. Biggs, E. M. Hulburt, V. L. McAlister and M. J.J. (1977). "*Rhizosolenia* mats." Limnology and Oceanography **22**(4): 739-741.

Casey, R. E., A. L. Weinheimer and C. O. Nelson (1989). California El Niño and related changes of the California Current system from recent and fossil radiolarian records. Aspects of Climatic Variability in the Pacific and Western Americas, American Geophysical Union. **55:** 85-92.

Chave, K. E. (1965). "Calcium carbonate: association with organic matter in surface water." Science **148**: 1723-1724.

Chavez, F. P. and R. T. Barber (1987). "An estimate for the new production in the central and eastern tropical Pacific." Deep Sea Research **34**: 1229-1243.

Chavez, F. P., K. R. Buck and R. T. Barber (1990). "Phytoplankton taxa in relation to primary production in the equatorial Pacific." Deep-Sea Research **37**(11): 1733-1752.

Collins, L. S., A. G. Coates, W. A. Berggren, M.-P. Aubry and J. Zhang (1996). "The late Miocene Panama isthmian strait." Geology **24**(8): 687-690.

Conley, D. (1996). Comparative analyses of the measurement of biogenic silica in sediments. OPALEO: On the use of opal as a paleo-productivity proxy, Brest, Institut Universitaire Européen de la Mar, Université de Bretagne Occidentale.

Conley, D. J. (in press). "Comparative analyses of the measurement of biogenic silica in sediments." Marine Chemistry.

Cox, A., R. R. Doell and G. B. Dalrymple (1964). "Geomagnetic polarity epochs." Science **143**: 351-352.

Cullen, J. J. (1991). "Hypotheses to explain high-nutrient conditions in the open sea." Limnology and Oceanography **36**(8): 1578-1599.

Cutter, G. A. and J. Radford-Knoery (1991). Determination of carbon, nitrogen, sulfur, and inorganic sulfur species in marine particles. Marine Particles: Analysis and Charcterisation. Geophysical Monograph 63., Ameriacn Geophysical Union.

Davis, C. O. (1976). "Continous culture of marine diatoms under silica limitation. II. Effect of light intensity on growth and nutrient uptake of *Skeletonema costatum*." Journal of Phycology **12**: 291-300.

Dean, W. E. J. (1974). "Determination of carbonate and organic matter in calcareous sediments and sedimentary rock by loss on ignition: comparision with other methods." Journal of Sedimentary Petrology **44**(1): 242-248.

Decker, K. (1991). Rhythmic bedding of siliceous sediments - an overview. Cycles and events in stratigraphy. G. Einsele, W. Ricken and A. Seilacher. Berlin, Springer-Verlag: 464-479.

DeMaster, D. J. (1981). "The supply and accumulation of silica in the marine environment." Geochimica et Cosmochimica Acta. **45**: 1715--1732.

DeMaster, D. J., O. Ragueneau and C. A. Nittrouer (1996). "Preservation efficiencies and accumulation rates for biogenic silica and organic C, N, and P in high-latitude sediments: The Ross Sea." Journal of Geophysical Research **101**(C8): 18,501-18,518.

DeVries, T. J. (1987). "A review of geological evidence for ancient El Niño activity in Peru." Journal of Geophysical Research **92**(C13): 14,1471-14,479.

Dickens, G. R. and J. A. Barron (1997). "A rapidly deposited pennate diatom ooze in Upper Miocene-Lower Pliocene sediment beneath the North Pacific polar front." Marine Micropalaeotology **31**: 177-182.

Dugdale, R. C., F. P. Wilkerson, R. T. Barber and F. R. Chavez (1992). "Estimating new production in the equatorial Pacific Ocean at 150W." Journal of Geophysical Research **97**(C1): 681-686.

Dugdale, R. C., F. P. Wlikerson and H. J. Minas (1995). "The role of a silicate pump in driving new production." Deep-Sea Research **42**(5): 697-720.

Düing, W., P. Hisard, E. Katz, J. Meincke, L. Miller, K. V. Moroshkin, G. Philander, A. A. Ribnikov, K. Voigt and R. Weisberg (1975). "Meanders and long waves in the equatorial Atlantic." Nature **257**: 280-284.

Dunbar, R. B., G. M. Wellington, M. W. Colgan and P. W. Glynn (1994). "Eastern Pacific sea surface temperatures since 1600A.D.: The $\delta^{18}O$ record of climate variability in Galápagos corals." Paleoceanography **9**: 291-315.

Duque-Caro, H. (1972). "Relaciones en la bioestratigrafia y la cronoestratigrafia en la llamado geosiclinal de Bolivar." Ingeominas Bol. Geol. **19**(3): 25-68.

Duque-Caro, H. (1975). "Los foraminiferos plactionicos y el Terciario de Columbia." Rev. Esp. Micropaleontol. 7(3): 403-427.

Duque-Caro, H. (1990). "Neogene stratigraphy, paleoceanography and paleobiology in northwest South America and the evolution of the Panama Seaway." Palaeogeography, Palaeclimatology, Palaeoecology **77**(3/4): 203-234.

Durbin, E. G. (1977). "Studies of the autecology of the marine diatom *Thalassiosira nordenskioeldii*. II. The influence of cell size on growth rate, and carbon, nitrogen, chlorophyll *a* and silica content." Journal of Phycology **13**: 150-155.

Duursma, E. K. (1961). "Dissolved organic carbon, nitrogen and phosphorus in the sea." Netherlands Journal of Sea Research **1**: 1-148.

Dymond, J. and R. Collier (1988). "Biogenic particle fluxes in the Equatorial Pacific: evidence for both high and low productivity during the 1982-1983 El Niño." Global Biogeochemical Cycles **2**(2): 129-137.

Eddy, J. A. (1988). Variability of the present and ancient Sun: a test of solar uniformitarianism. Secular solar and geomagnetic varations in the last 10,000 years. F. R. Stephenson and A. W. Wolfendale. Dordrecht, Kluwer Academic: 1-24.

Eggimann, D. W., F. T. Manheim and P. R. Betzer (1980). "Dissolution and analysis of amorphous silica in marine sediments." Journal of Sedimentary Petrology **50**: 215-225.

Eisma, D. and S. J. Van Der Gaast (1971). "Determination of opal in marine sediments by X-ray diffraction." Netherlands Journal of Sea Research **5**: 382-389.

Eldin, G., A. Moliere and G. Reverdin (1992). "Acoustic doppler current profiling along the Pacific equator from 95°W to165°W." Geophysical Research Letters **19**: 913-916.

Emerson, S. R., K. Fischer, C. Reimers and D. Heggie (1985). "Organic carbon dynamics and preservation in deep-sea sediments." Deep Sea Research **32**(1): 1-22.

Emerson, S. R. and J. I. Hedges (1988). "Processes controlling the organic carbon content of open ocean sediments." Paleoceanography 3(5): 621-634.

Emiliani, C., S. Gartner and B. Lidz (1972). "Neogene sedimentation on the Blake Plateau and the emergence of the central American isthmus." Palaeogeography, Palaeclimatology, Palaeoecology **11**(1): 1-10.

Enfield, D. B. and S. L. Cid (1991). "Low-frequency changes in El Niño-Southern Oscillation." Journal of Climate **4**: 1137-1146.

Eppley, R. W., R. W. Holmes and E. Paasche (1967). "Periodicity in cell division and physiological behavior of *Ditylum brightwellii*, a marine planktonic diatom during growth in light-dark cycles." Arch. Microbiology **56**: 305-323.

Erez, J., K. Takahashi and S. Honjo (1982). "In-situ dissolution experiment of radiolaria in the central North Pacific Ocean." Earth and Planetary Scientific Letters **59**: 245-254.

Fairbridge, R. W. (1984). Plametary periodicities and terrestrial climate stress. Climate change on yearly to millenial basis. N. A. Mürner and W. Karlen. Boston, Reidel: 509-520.

Fairbridge, R. W. and J. E. Saunders (1987). The Sun's orbit, AD 750-2050: Basis for new perspectives on planetary dynamics and the Earth-Moon linkage. Climate - history, periodicity, predictability. M. S. Rampino, J. E. Saunders, W. S. Newman and L. K. Künigsson. New York, Van Nostrand Reinhold: 446-471.

Farley, K. A. (1995). "Cenozoic variations in the flux of interplanetary dust recorded by 3He in a deep-sea sediment." Nature **376**(6536): 153-156.

Farrell, J. W., I. Raffi, T. R. Janecek, D. W. Murray, M. Levietan, K. A. Dadey, K.-C. Emeis, M. Lyle, J.-A. Flores and S. Hovan (1995). Late Neogene sedimentation patterns in the eastern Equaotorial Pacific Ocean. Proceedings of the Ocean Drilling Program, Scientific Results. N. G. Piasis, L. A. Mayer, T. R. Janecek, A. Palmer-Julson and T. H. van Andel. **138:** 717-767.

Feistner, K. W. A. (1992). Geochemistry and carbonate diagenesis of the Kimmeridge Clay, Dorest coast, U.K., Cambridge.

Feynman, J. (1982). "Geomagnetic and solar wind cycles." Journal of Geophysical Research **87**(A8): 6163-6162.

Fielder, P. C., F. P. Chavez, D. W. Behringer and S. B. Reilly (1992). "Physical and biological effects of Los Niños in the eastern tropical Pacific, 1986-1989." Deep-Sea Research **39**(2): 199-219.

Fröelich, P. N. (1980). "Analysis of organic carbon in marine sediment." Limonology and Oceanography **25**: 564-572.

Fröelich, P. N., V. Blanc, R. A. Mortlock, S. N. Chillrud, W. Dunstan, A. Udomkit and T.-H. Peng (1992). "River fluxes of dissolved silica to the ocean were higher during glacials: Ge/Si in diatoms, rivers and oceans." Paleoceanography **7**(6): 739-767.

Gage, J. D. and P. A. Tyler (1991). Deep-Sea Biology. Cambridge, Cambridge University Press.

Gardener, J. V. and L. H. Burkle (1975). "Upper Pleistoncene Ethmodiscus rex ooze from the eastern Equatorial Atlantic." Micropalaeontology **21**(2): 236-242.

Gehlen, M. and W. van Raaphorst (1993). "Early diagenesis of silica in sandy North Sea sediments: quantification of the solid phase." Marine Chemistry **42**: 71-83.

Gibbs, R. J. (1977). "Effects of combustion temperature andtime, and of the oxidation agent used in organic and nitrogen analysis of sediments and dissolved organic material." Journal of Sedimentary Petrology **47**: 547-550.

Gleissberg (1958). "The 80-year sunspot cycle." British Astronomical Association Journal **68**(150).

Glenn, C. R. and K. Kelts (1991). Sedimentary rhythms in lake deposits. Cycels and Events in Stratigraphy. G. Einsele, W. Ricken and A. Seilacher. Berlin, Springer-Verlag: 188-221.

Goldstein, J. I., D. E. Newbury, P. Echlin, D. C. Joy, C. Fiori and E. Lifshin (1981). Scanning Electron Microscopy and X-ray Microanalysis. New York, Plenum Press.

Goulterman, H. E. E. (1969). Methods for Chemical Analysis of Fresh Water. Oxford, Blackwells.

Graham, N. E. (1994). "Decadal-scale variability in the tropical and North Pacific during the 1970s and 1980s: observations and model results." Climate Dynamics **10**: 135-162.

Hallegraeff, G. M. (1986). "Taxonomy and morphology of the marine planktonic diatoms *Thalassionema* and *Thalassiothrix*." Diatom Research **1**(1): 57-80.

Halpern, D. and P. Freitag (1987). "Vertical motion in the upper ocean of the equatorial eastern Pacific." Oceanologica Acta **Vol. Spec. 6**: 19-26.

Halpern, D., R. Knox and D. Luther (1988). "Observations of 20-day period merdional current oscillations in the upper ocean along the Pacific Equator." Journal of Physical Oceanography **18**: 1514-1534.

Hamilton, E. L. (1976). "Variations of density and porosity with depth in deep-sea sediments." Journal of Sedimentary Petrology **46**: 280-300.

Hansen, D. V., C. A. Paul and R. Legeckis (1980). "Comparision of satellite and direct current observations of long waves in the eastern tropical Pacific during FGGE." Transactions American Geophysical Union **61**.

Haq, B. U., J. Hardenbol and P. R. Vail (1987). "The chronology of fluctuating sea level since the Triassic." Science **235**: 1156-1167.

Haq, B. U., J. Hardenbol and P. R. Vail (1988). Mesozoic and Cenozoic chronostratigraphy and cycles of sea level change. Sea Level Changes - An Intergrated Approach. C. K. S. C. Wilgus, H. W. Posamentier, C. A. Ross and J. C. Van Wagoner. Tusla, Society of Economic Paleontologists and Mineralogists. **42:** 71-108.

Haq, B. U. and I. Takayama (1984). Neogene calcareous nannoplankton datum planes and their calibration to magnetostratigraphic. Pacific Neogene datum planes. N. Ikebe and R. Tschui. Tokyo: 27-32.

Haq, B. U., T. R. Worsley, L. H. Burckle, R. G. Douglas, L. D. Keigwin, N. D. Opdyke, S. M. Savin, M. A. Sommer, E. Vincent and F. Woodruff (1980). "Late Miocene marine carbon isotopic shift and synchroneity of some phytoplankton biostratigraphic events." Geology 8: 427-431.

Harrison, P. J., H. L. Conway and C. O. Davis (1977). "Marine diatoms grown in chemostats under silicate or ammonium limitation. III. Cellular chemical compositions and morphology of *Chaetoceros*
*deblis, Skeletonema costatum* and *Thalassiosira gravida*." Marine Biology **35**: 177-186.

Harrison, P. J., H. L. Conway and R. C. Dugdale (1976). "Marine diatoms grown in chemostats under silicate or ammonium limitation. I. Cellular chemical composition and steady state growth kinetics of *Skeletonema costatum*." Marine Biology **35**: 177-186.

Harriss, R. C. (1966). "Biological buffering of oceanic silica." Nature **308**: 51-54.

Hasle, G. R. and H. J. Semina (1987). "The marine planktonic diatoms *Thalassiothrix longissima* and *Thalassiothrix anarctica* with comments on *Thalassionema* spp and *Synedra reinboldii*." Diatom Research **2**(2): 175-192.

Haslett, S. K. and B. M. Funnell (1996). Sea-surface temperature variation and palaeo-upwelling throughout the Plio-Pleistocene Olduvai subshron of the eastern equatorial Pacific: an analysis oof radiolarian data from ODP Sites 677, 847, 850 and 851. Microfossil and Oceanic Environments. A. Moguilevvsky and R. Whatley. Aberystwyth, University of Wales, Aberystwyth-Press.

Hedges, R. T. and J. H. Stern (1984). "Carbon and nitrogen determination of carbonate containing soils." Limonolgy and Oceanography **29**: 756-763.

Heirtzler, J. R., G. O. Dickson, E. Herron, M., W. C. Pitman and X. Le Pichon (1968). "Marine magnetic anomalies, geomagnetic field reversals, and motion of the oean floor and continents." Journal of Geophysical Research **73**: 2119-2136.

Hilgen, F. J. (1991). "Extension of the astronically calibrated (polarity) time scale to the Miocene-Pliocene boundary." Earth and Planetary Science Letters **107**: 349-368.

Hirota, J. and J. P. Spyzer (1975). "Carbon and nitrogen determinations of carbonate-containing solids." Limonolgy and Oceanography **20**: 896-900.

Honjo, S., J. Dymond, R. Collier and S. J. Mamganini (1995). "Export production of particles to the interior of the equatorial Pacific Ocean during the 1992 EqPac experiment." Deep-Sea Research II **42**: 831-870.

Hurd, D. C. (1972). "Factors affecting solution rate of biogenic opal in silica." Earth and Planetary Scientific Letters **15**: 411-417.

Hurd, D. C. (1983). Physical and chemical properties of siliceous skeletons. Silicon Geochemistry and Biogeochemistry. S. R. Aston. London, Academic Press: 187-244.

Jansen, E., L. A. Mayer, J. Backman, R. M. Leckie and T. Takayama (1993). Evolution of Pliocene climate cyclicity at Hole 806B (5-2Ma): Oxygen isotope record. Proceedings of the Ocean Drilling Program, Scientific Results, Leg 130. W. H. Berger, L. W. Kroenke, L. A. Mayer and e. al.

Jordan, R. W., J. Priddle, C. J. Pudsey, P. F. Barker and M. J. Whitehouse (1991). "Unusual diatom layers in Upper Pleistocene sediments from the northern Weddell Sea." Deep-Sea Research **38**(7): 829-843.

Jørgensen, B. B. (1979). "A comparision of methods for the quantification of bacterial sulphate reduction in coastal marine sediments II. Calculation from mathematical models." Journal of Geomicrobiology **1**(1): 29-47.

Kamatani, A., N. Ejiri and P. Treguer (1988). "The dissolution kinetics of diatom ooze from the Antarctic area." Deep-Sea Research **35**(7): 1195-1203.

Karl, D. M. and M. o. t. w. group (1991). Major Bioelements. Marine Particles: Analysis and Charaterisation. D. C. Hurd and D. W. Spencer, American Geophysical Union. **Geophysical Monograph 63**.

Keigwin, L. (1982). "Isotopic paleoceanography of the Caribbean and East Pacific: Role of Panama uplift in late Neogene time." Science **217**: 350-353.

Keigwin, L. D. (1978). "Pliocene closure of the Isthmus of Panama based on biostratigraphic evidence from nearby Pacific Ocean and Caribbean Sea cores." Geology **6**(10): 630-634.

Keigwin, L. D. (1987). "Toward a high-resolution chronology for latest Miocen paleoceanographic events." Paleoceanography **2**(6): 639-660.

Keir, R. S. and W. H. Berger (1985). Late Holocene carbonate dissolution in the equatorial Pacific: reef growth or neoglaciation? The Carbon Cycle and Atmospheric $CO_2$: Natural Variations Archean to Present. E. T. Sundquist and W. S. Broecker, American Geophysical Union. **32**: 208-219.

Keller, G. (1985). Depth stratification of planktonic foraminifera. The Miocene Ocean: Paleoceanography and biogeography. J. P. Kennet, Geological Society of America. **Memoir 163**: 177-193.

Kemp, A. E. S. (1995). Neogene and Quaternary pelagic sediments and depositional history of the eastern Equatorial Pcific Ocean (Leg 138). Proceedings of the Ocean Drilling Program, Scientific Results, Vol 138. N. G. Pisias, L. A. Mayer, A. Palmer-Julson and T. H. van Andel. College Station, TX., Ocean Drilling Program.

Kemp, A. E. S. and J. G. Baldauf (1993). "Vast Neogene laminated diatom mat deposits from the eastern equatorial Pacific Ocean." Nature **362**: 141-143.

Kemp, A. E. S., J. G. Baldauf and R. B. Pearce (1995). Origins and paleoceanographic significance of laminated diatom ooze from the eastern Equatorial Pacific Ocean. Proceedings of the Ocean Drilling Program, Scientific Results, Vol 138. N. G. Pisias, L. A. Mayer, A. Palmer-Julson and T. H. van Andel. College Station, TX., Ocean Drilling Program.

Kerr, R. A. (1990). "Sunspot-weather link is down but not out." Science **248**: 684-685.

King, P., H. Kennedy, P. P. Newton, T. D. Jickells, T. Brand, S. Calvert, H. Etchber, R. Head, A. Khripounoff, B. Manighetti and J. C. Miquel (in press). "Analysis of total organic carbon and total nitrogen in sediment trap material and marine sediment: and interlaboratry calibration." in press.

King, S. C., A. E. S. Kemp and J. W. Murray (1995). Benthic foraminifer assemblages in Neogene laminated diatom ooze deposits in the eastern Equatorial Pacific Ocean (Site 844). Proceedings of the Ocean Drilling Program, Scientific Results, Vol 138. N. G. Pisias, L. A. Mayer, A. Palmer-Julson and T. H. van Andel. College Station, TX., Ocean Drilling Program.

Klitgord, K. D., S. P. Heustis, J. D. Mudie and R. L. Parker (1975). "An analysis of near-bottom magnetic anomalies: sea-floor spreading and the magnetized layer." Geophysical Journal of the Royal Astronomical Society **43**: 387-424.

Krom, M. D. and R. A. Berner (1983). "A rapid method for determination of organic and carbonate carbon in geochemical samples." Journal of Sedimentary Petrology **53**(660-663).

Labeyrie, L. D. and A. Juillet (1982). "Oxygen isotope exchangeablity of diatom value silica; interpretation and consequences for paleoclimatic studies." Geochimica et Cosmochimica Acta **46**: 967-975.

Landén, A., O. Holby and P. J. Hall (1996). "Determination of biognic opal in marine sediments - selection of pretreatment method and sample size." Vatten **52**: 85-92.

Le, J. and N. J. Shackleton (1992). "Carbonate dissolution fluctuations in the western equatorial Pacific during the late Quaternary." Paleoceanography **7**: 21-42.

Ledford-Hoffman, P. A., D. J. DeMaster and C. A. Nittrouer (1986). "Biogenic-silica accumulation in the Ross Sea and the importance of Anártic continental-shelf deposists in the marine silca budget." Geochimica et Cosmochimica Acta **50**: 2099-2110.

Legeckis, R. (1979). "Long waves in the Eastern Equatorial Pacific Ocean: A view from a geostationary satellite." Science **197**: 1179-1181.

Legeckis, R., W. Pichel and G. Nesterczuk (1983). "Equatorial long waves in geostationary satellelite observations and in multichannel sea surface temperature analysis." Bulletin American Meteorological Society **64**(2): 133-139.

Lewin, J. C. (1957). " Silicon metabolism in diatoms. IV - Growth and frustule fromation in *Navicula pelliculosa.*" Canadian Journal of Microbiology **3**: 427.

Libes, S. M. (1992). An Introduction to Marine Biochemistry. New York, John Wiley and Sons, Inc.

Lisitzin, A. P. (1972). Sedimentation in the World Ocean., Society of Economic Paleontology and Mineralogy.

Lomb, N. R. (1976). "Least squares frequency analysis of of unevenly spaced data." Astrophysics and Space Science **39**: 447-462.

Longhurst, A., S. Sathyendranath, T. Platt and C. Caverhill (1995). "An estimate of global primary production in the ocean from sallelite radiometer data." Journal of Plankton Research **17**: 1245-1271.

Lowrie, W. and W. Alvarez (1981). "One hundred million years of geomagnetic polarity history." Geology **9**: 392-397.

Luther, D. and E. S. Johnson (1990). "Eddy energetics in the upper equatorial Pacific during the Hawaii to Tahiti Shuttle Experiment." Journal of Physical Oceanography **20**: 913-944.

Manighetti, B. (1993). The Glacial to Holocene sedimentary regime in the NE Atlantic Ocean., Cambridge.

Mayer, L., N. Pisias, T. Janecek and e. al (1992). Proceedings of the Ocean Drilling Program, Intitial Reports.

Mayer, L. A. (1979). "Deep sea carbonates: acoustic, physical and stratigraphic properties." Journal of Sedimentary Petrology **49**: 819-836.

Mayer, L. A. (1991). "Extraction of high-resolution carbonate data for palaeoclimate reconstruction." Nature **352**: 148-150.

Mayer, L. A., F. Theyer, E. Thomas and e. al. (1985). Inital Reports of the Deep Sea Drilling Project: Leg 85. Washington, D.C., US Government Printing Office.

Mazzei, R., I. Raffi, D. Rio, N. Hamilton and M. B. Cita (1979). Calibration of the late Neogene calcareous plankton datum planes with the paleomagnetic record of Site 397 and correlation with Moroccan and Mediterranean sections. Initial Reports of the Deep Sea Drilling Program. U. von Rad, W. B. F. Ryan and e. al. College Station. **47:** 375-389.

McCave, I. N. and S. B. S. Party (1994). Cruise Report, RRS Charles Darwin 88., University of Cambridge, Earth Sciences Department.

McDougall, K. (1985). Miocene to Pleistocene benthic foraminifers and paleoceanography of the Middle America slope. DSDP Leg 84, Initial Reports**:** 363-418.

McDougall, K. (1996). "Benthic foraminiferal response to the emergence of the Isthmus of Panama and coincident paleoceanographic changes." Marine Micropaleontology **28**: 133-169.

McGlone, M. S. and A. P. Kershaw (1992). El Niño/Southern Oscillation climatic variability in Australasian and South American paleoenvironmental records. El Niño. Historical and Paleoclimatic Aspects of the Southern Oscillation. H. F. Diaz and V. Karkgraf. Cambridge, Cambridge University Press.

Meko, D. M. (1992). Spectral properties of tree-ring data in the United States Southwest as related to El Niño/Southern Oscillation. El Niño. Historial and Paleoclimatic Aspects of the Southern Oscillation. H. F. Diaz and V. Markgraf. Cambridge, Cambridge University Press.

Mikkelsen, N. (1977). "On the origin of *Ethmodiscus* ooze." Marine Micropaleontology **2**: 35-46.

Mikolajewicz, U., E. Maier-Reimer, T. Crowley and K.-Y. Kim (1993). "Effect of Drake and Panamanian gateways on circulation of an ocean model." Paleoceanography **8**(4): 409-426.

Moore, T. C., N. J. Shackleton and N. G. Pisias (1993). "Paleoceanography and the diachrony of radiolarian events in the Eastern Equatorial Pacific." Paleoceanography **8**(5): 567-586.

Mortlock, R. A. and P. N. Froelich (1989). "A simple method for the rapid determination of biogenic opal in pelagic marine sediments." Deep-Sea Research **36**(9): 1415-1426.

Muller, P. J. and R. Schneider (1993). "An automated leaching method for the determination of opal in sediments and particulate matter." Deep-Sea Research **40**(425-444).

Murnane, R. J. and R. F. Stallard (1990). "Germanium and silicon in rivers of the Orinoco drainage basin." Nature **344**: 749-752.

Murray, J. W., J. Downs, S. S., C. L. Wei and H. Jannasch (1989). "Nutrient assimilation, export production and 234Th scavenging in the eastern equatorial Pacific." Deep-Sea Research **36A**(10): 1471-1489.

Nelson, D. M., G. F. Riedel, R. Millan-Nunez and J. R. Lara-Lara (1984). "Silicon uptake in algae with no known Si requirement. I. True cellular uptake and pH-induced precipitation by *Phaeodacty;um tricornutum* (Bacillariophyceae) and *Platymonas* sp. (Prasinophyceae)." Journal of Phycology **20**: 141-147.

Ness, G., S. Levi and R. Couch (1980). "Marine magnetic anomaly timescales for the Cenozoic and Late Cretaceous: A Precis, critique, and synthesis." Reviews of Geophysis and Space Physics **18**: 753-770.

Nieuenhuize, J., Y. E. M. Maas and J. J. Middelburg (1994). "Rapid analysis of organic carbon and nitrogen in particulate materials." Marine Chemistry **45**: 217-224.

Nigrini, C. and J.-P. Caulet (1992). "Late Neogene radiolarian assemblages characteristic of Indo-Pacific areas of upwelling." Micropaleontology **38**: 139-164.

Ninkovitch, D. and N. J. Shackleton (1975). "Distribution, stratigraphic position and age of age layer 'L' in Panama Basin region." Earth and Planetary Scientific Letters **27**: 20-34.

Norton, J. G. and D. R. McLain (1994). "Diagnostic patterns of seasonal and interannual temperature variation off the west coast of the United States: Local and remote large-scale atmospheric forcing." Journal of Geophysical Research **99**(C8): 16,019-16,030.

Owen, F. and R. Jones (1982). Statistics. London, Pitman Publishing.

Paasche, E. (1973). "Silicon and the ecology of marine plankton diatoms. I. *Thalassiosira pusedonana (Cyclotella nana)* grown in a chemostat with silicon as limiting nutrient." Marine Biology **19**: 117-126.

Paasche, E. (1980). "Silicon content of five marine plankton diatom species measured with a rapid filter method." Limnology and Oceanography **25**: 474-480.

Parsons, T. R., K. Stephens and J. D. H. Strickland (1961). "On the chemical composition of eleven species of marine phytoplankers." Journal of the Fisheries Research Board of Canada **18**: 1001-1016.

Pearce, R. B., A. E. S. Kemp, J. G. Baldauf and S. C. King (1995). High resolution sedimentology and micropaleontology of laminated diatomaceous sediments from the easteen Equatorial Pacific Ocean. Proceedings of the Ocean Drilling Program, Scientific Results, Vol

138. N. G. Pisias, L. A. Mayer, A. Palmer-Julson and T. H. van Andel. College Station, TX., Ocean Drilling Program.

Pella, E. and B. Columbo (1973). "Study of carbon, hydrogen and nitrogen determined by combustion-gas chromatography." Mikrochimica Acta **3**: 697-719.

Perigaud, C. (1990). "Sea level oscillations observed with Geosat along the two shear fronts of
the Pacific north equatorial countercurrent." Journal of Geophysical Research **95**((C5)): 7239-7248.

Philander, S. G. (1990). El Niño, La Niña, and the Southern Oscillation. London, Academic Press Limited.

Philander, S. G. H. (1978). "Instabilites of zonal equatorial currents: II." Journal of Geophysical Research. **83**: 3679-3682.

Philander, S. G. H., D. Halpern, D. Hansen, R. Legeckis, L. Miller, C. Paul, R. Watts, R. Weisburg and M. Wimbush (1985). "Long waves in the equatorial Pacific Ocean." Eos, Transactions American Geophysical Union. **66**: 154.

Pichon, J.-J., G. Bareille, M. Labracherie, L. D. Labeyrie, A. Baudrimont and J.-T. Turon (1992). "Quantification of the biogenic silica dissolution in the Southern Ocean sediments." Quaternary Research **37**: 361-378.

Pike, J. (1996). High Resolution Palaeoceanography and Palaeoclimatology from Late Pleistocene and Holocene Laminated Sediments, Gulf of California. Department of Oceanography, University of Southampton: 285.

Pisias, N. G. and T. C. J. Moore (1981). "The evolution of Pleistocene climate: a time series approach." Earth and Planetary Science Letters **52**: 450-458.

Pisias, N. G. and W. L. Prell (1985). Changes in calcium carbonate accumulation in the equatorial Pacific during the
Late Cenozoic: evidence from HPC Site 572. The carbon cycle and atmospheric CO2: natural variations
Archean to Present. E. T. Sundquist and W. S. Broecker. Washington D.C., American Geophysical Union: 443-454.

Pollock, D. E. (1997). "The role of diatoms, dissolved silica and Antartic glaciation in glacial/interglacial climate change: a hypothesis." Global and Planetary Change **14**(3/4): 113-125.

Pollock, E. N. and S. J. West (1973). Atomic Absorption Newsletter **12**(1): 6-12.

Press, W. H., S. A. Teukolsky, W. T. Vetterling and B. P. Flannery (1992). Numerical recipes in C: The art of scientific computing. Cambridge, Cambridge University Press.

Pullen, P. E., R. Bern stein and D. Halpern (1987). "Equatorial long-wave characteristics determined from satellite sea surface temperature and in situ data." Journal of Geophysical Research **92 (C1)**: 742-748.

Quilty, P. G., K. R. Kerry and H. J. Marchant (1984). "A seasonally recurrent patch of Anarctic planktonic diatoms." Search **16**(1-2): 48.

Rabouille, C., J.-F. Gaillard, P. Tréguer and M.-A. Vincendeau (1997). "Biogenic silica cycling in surfical sediments across the Polar Front of the Southern Ocean (Indian Sector)." Deep-Sea Research II **44**(5): 1151-1176.

Raffi, I. and J.-A. Flores (1995). Pleistocene through Miocene calcarceous nannofossils from eastern equatorial Pacific Ocean (ODP Leg 138). Proceedings of the Ocean Drilling Program, Scientific Results. N. G. Pisias, L. A. Mayer, T. R. Janacek, A. Palmer-Julson and T. H. van Andel. College Station. **138**.

Raffi, I., D. Rio, A. d'Afri, E. Fornaciari and S. Rochetti (1995). Quantitative distribution paaterns and biomagnetostratigraphy of middle and late Miocene calcareous nannofossils from equatorial Indian and Pacific Oceans (Legs 115, 130 and 138). Proceedings of the Ocean Drilling Program, Scientific Results. N. G. Pisias, L. A. Mayer, A. Palmer-Julson and T. H. van Andel. College Station. **138**.

Renne, P. R., R. Walter, K. Verosub, M. Sweitzer and J. Aronson (1993). "New data from Hadar (Ethopia) support orbitally tuned timescale to 3.3Ma." Geophysical Research Letters **20**: 1067-1070.

Rio, D., I. Raffi and G. Villa (1990). Pliocene-Pleistocene calcareous nannofossil distribution patterns in western Mediterranean. Proceedings of Ocean Drilling Program, Scientific Results. K. A. Kastens, J. Mascle and e. al. College Station. **107:** 513-533.

Roberts, A. A., J. G. Palacas and I. C. Frost (1973). "Determination of organic carbon in modern carbonate sediments." Journal of Sedimentary Petrology **43**(4): 1157-1159.

Round, F. E., R. M. Crawford and D. G. Mann (1990). The Diatoms: biology and morphology of the genera. Cambridge, C.U.P.

Ruddiman, W. F., M. E. Raymo and A. McIntyre (1986). "Matuyama 41,000 year cycles: North Atlantic and Northern hemisphere ice sheets." Earth and Planetary Science Letters **80**: 251-261.

Rugers van der Loeff, M. M. and G. W. Berger (1993). "Scavenging of $^{230}$Th and $^{231}$Pa near the Antarctic Polar Front in the South Atlantic." Deep-Sea Research **40**: 339-357.

Saito, K. and M. Ozima (1976). $^{40}$Ar-$^{39}$Ar ages of submarine rock from the Line Islands: implications on the origin of the Line Islands. The geophysics of the Pacific Ocean and its origin. Washington D.C., American Geophysical Union. **Monograph 19.**

Sarnthein, M. and J. Fenner (1988). "Global wind-induced change of deep-sediment budgets, new ocean production and $CO_2$ reserviors Ca. 3.3-3.25Ma BP." Philosophical Transactions of the Royal Society of London B **318**: 487-504.

Sarnthein, M., K. Winn, J. C. Duplessey and M. R. Fontugne (1987). Palaeoproductivity of oceanic upwelling and the effect on atmospheric $CO_2$ and climate change during deglaciation times. Abrupt Climate Change. W. H. Berger and L. D. Labeyrie. Dordrecht, Reidel: 311-337.

Scargle, J. D. (1982). "Studies of astronomical time-series analysis II. Statistical aspects of spectral analysis." Astrophysical Journal **263**: 835-853.

Schink, D. R., K. A. Fanning and M. E. Q. Pilson (1974). "Dissolved silica in the upper pore waters of the Atlantic Ocean floor." Journal of Geophysical Research **79**: 2243-2250.

Schink, D. R., N. L. Guinasso Jr and K. A. Fanning (1975). "Processes affecting the concentration of silica at the sediment-water interface of the Atlantic Ocean." Journal of Geophysical Research **80**(21): 3013-3031.

Schneider, D. (1995). Paleomagnetism of some ODP Leg 138 sediments: Miocene magnetostratigraphic miscellany. Proceedings of the Ocean Drilling Program, Scientific Results. N. G. Pisias, L. A. Mayer, T. R. Janacek, A. Palmer-Julson and T. H. van Andel. College Station. **138**.

Schove, D. J., Ed. (1983). Sunspot Cycles. Benchmark Papers in Geology 68. Stroudsburg, Hutchinson Ross.

Schrader, H.-J. (1971). "Fecal pellets: Role in sedimentation of pelagic diatoms." Science **174**: 55-57.

Schwartz, M. (1970). Information Transmission, Modulation, and Noise. New York, McGraw-Hill.

Shackelton, N. J., M. A. Hall and D. Pate (1995). Pliocene Stagle isotope stratigraphy of Site 846. Proceedings of the Ocean Drilling Program, Scientific Results, Vol 138. N. G. Piasis, L. A. Mayer, A. Palmer-Julson and T.-H. van Andel. College Station, Texas: 337-355.

Shackleton, N. J., A. Berger and W. R. Peltier (1990). "An alturnative astronomical calibration of the lower Pleistocene timescale based on ODP Site 677." Transactions of Royal Society of Edinburgh, Earth Science. **81**: 251-261.

Shackleton, N. J., S. Crowhurst, T. Halgelberg, N. G. Pisias and D. A. Schneider (1995). A new late Neogene timescale: Application to Leg 138 Sites. Proceedings of Ocean Drilling Program, Scientific Results, Vol 138. N. G. Pisias, L. A. Mayer, T. R. Janecek, A. Palmer-Julson and T. H. van Andel: 73-101.

Shemesh, A., L. H. Burkle and P. N. Froelich (1989). "Dissolution and preservation of Antartic diatoms and the effect on sediment thanatocoenoses." Quaternary Science **31**: 288-308.

Sims, J. R. and V. A. Haby (1971). "Simplified colorimeteric determination of soil organic matter." Soil Science **112**: 1387-141.

Smayda, T. J. (1970). "The suspension and sinking of phytoplankton in the sea." Oceanogr. mar. Biol. A. Rev. **8**: 353-414.

Smith, C. R., D. J. Hoover, S. E. Doan, R. H. Pope, D. J. DeMaster, F. C. Dobbs and M. A. Altabet (1996). "Phytodetritus at the abyssal seafloor across 10° of latitude in the central equatorial Pacific." Deep-Sea Research II **43**: 1309-1338.

Smith, R. L. (1982). Circulation patterns in upwelling regimes. Coastal Upwelling: Its record. E. Suess and J. Thiede. New York, Pleumn: 13-37.

Sonett, C. P. (1984). "Very long solar periods and the radiocarbon record." Reviews of Geophysics and Space Physics **22**: 239-254.

Southam, J. R. and W. H. Peterson (1985). Transient response of the marine carbon cycle. The carbon cycle and atmospheric CO2: natural variations Archean to Present. E. T. Sundquist and W. S. Broecker. Washington D.C, American Geophysical Union: 89-98.

Stabell, B. (1986). "Variations of diatom flux in the eastern equatorial Atlantic during the last 400,000 years ('Meteor' cores 13519 and 13521)." Marine Chemistry **72**(3/4): 305-322.

Strickland, J. D. H. and T. R. Parsons (1972). A Practical Handbook of Seawater Analysis., Fisheries Research Board of Canada.

Stuvier, M. and T. F. Braziunas (1988). The solar companant of the atmospheric $^{14}C$ record. Secular solar and geomagnetic varations in the last 10,000 years. F. R. Stephenson and A. W. Wolfendale. Dordrecht, Kluwer Academic: 245-266.

Stuvier, M. and T. F. Braziunas (1989). "Atmospheric $^{14}C$ and century scale oscillations." Nature **338**: 405-408.

Stuvier, M. and P. M. Grootes (1980). Trees and the ancient record of heliomagnetic cosmic ray flux modulation. The ancient Sun. J. A. Eddy and R. B. Merrill. New York, Pergamon: 165-173.

Stuvier, M. and P. D. Quay (1980). "Changes in atmospheric carbon-14 attributed to a variable sun." Science **207**: 11-19.

Talwani, M., C. C. Windisch and M. G. Langesth (1971). "Rekjanes Ridge crest: A detailed geophysical study." Journal of Geophysical Research **76**: 473-517.

Tauxe, L., A. Deino, A. Behrensmeyer and R. Potts (1992). "Pinning down the Brunhes/Matayama and upper Jaramillo boundaries: a reconciliation of orbital and isotopic time scales." Earth and Planetary Science Letters **109**: 561-572.

Thomas, W. H. (1979). "Anomalous nutrient chlorophyll inter-relationa in the offshore eastern tropical Pacific Ocean." Journal of Marine Research **37**(2): 327-335.

Thunell, R. C., C. J. Pride, E. Tappa and F. E. Muller-Karger (1994). "Biogenic silica fluxes and accumulation rates in the Gulf of California." Geology **22**: 303-306.

Tréguer, P., D. M. Nelson, A. J. van Bennekon, D. J. DeMaster, A. Leynart and B. Quéguiner (1995). "The silica balance in the world ocean: a reestimate." Science **268**: 375-379.

Trenberth, K. E. and J. H. Hurrell (1994). "Decadal atmosphere-ocean variations in the Pacific." Climate Dynamics **9**: 303-319.

Tsunogai, S. and S. Noriki (1991). "Particulate fluxes of carbonate and organic carbon in the ocean. Is the marine biological activity working as a sink of anthropogenic carbon?" Tellus **43B**: 256-266.

van Andel, T. H., G. R. Heath, B. T. Malfal, D. E. Heinrichs and J. I. Ewing (1971). "Tectonics of the Panama Basin, eastern equatorial Pacific." Geological Society of America Bulletin **83**(6): 1482-1508.

van Andel, T. H., G. R. Heath and T. C. J. Moore (1975). "Cenozoic history and palaeoceanography of the central equatorial Pacific Region." Memoir of Geological Society of America **143**.

Verado, D. J., P. N. Froelich and A. McIntyre (1990). "Determinations of organic carbon and nitrogen in marine sediments using the Carlo Erba NA-1500 analyzer." Deep-Sea Research **37**: 157-165.

Villareal, T. A. (1988). "Positive buoyancy in the oceanic diatom *Rhizosolenia debyana* H. Peragallo." Deep-Sea Research **35**(6): 1037-1045.

Villareal, T. A. (1992). "Buoyancy properties of the giant diatom *Ethmodiscus*." Journal of Plankton Research **14**: 459-463.

Villareal, T. A., M. A. Altabet and K. Culver-Rymsza (1993). "Nitrogen transport by vertically migrating diatom mats in the North Pacific Ocean." Nature **363**: 709-712.

Villareal, T. A. and E. J. Carpenter (1989). "Nitrogen fixation, suspension characteristics and chemical composition of *Rhizosolenia* mats in the Central North Pacific Gyre." Biological Oceanography 6: 327-345.

Villareal, T. A. and E. J. Carpenter (1994). "Chemical composition and photosynthetic charateristics of *Ethmodiscus rex* (Bacillariophyceae): evidence for vertical migration." Journal of Phycology 30(1): 1-8.

Walanus, A. (1989). "Periodicities in sequence of laminae thickness in laminated sediments from the Gosciaz Lake." Geochronomet 5(989): 53-62.

Walsh, J. (1976). "Herbivory as a factor in nutirent distribution in the sea." Limonology and Oceanography 21: 1-13.

Walsh, T. W., S. V. Smith and S. Vink (1991). Review of particulate C:N:P methods used by UH/HIMB analytical services. Marine particles: Analysis and Characterisation. Geophysical Monograph 63. D. C. Hurd and D. W. Spencer, American Geophysical Union: 91-99.

Walter, R. C., A. Deino, P. Renne and L. Tauxe (1992). "Refining the Plio-Pleistocene GPTS using laser fusion $^{40}Ar/^{39}Ar$ tephrochronology: Case studies from the East African Ridge." Eos (Supplement) 73: 629.

Wefer, G. (1989). Particle flux in the Ocean: Effects of episodic production. Productivity of the Ocean: Present and Pat. W. H. Berger, V. S. Smetacek and G. Wefer. Chichester, John Wiley and Sons: 139-153.

Weinheimer, A. L., T. L. Carson, C. R. Wigley and R. E. Casey (1986). "Radiolarian responses to Recent and Neogene California El Niño and anti-El Niño events." Palaeography, Palaeoclimatology, Palaeoecology. 53: 3-25.

Weinreich, N. and F. Theyer (1985). "Paleomagnetisum of Deep Sea Drilling Project Leg 85 sediments: Neogene magnetostratigraphy and tectonic history of central Equatorial Pacific." Proceedings of the Ocean Drilling Project 85: 849-904.

Weliky, K., P. J. Müller, K. Fischer and E. Suess (1983). "Problems with accurate carbon measurements in marine sediments and particulate matter in seawater. A new approach." Limonolgy and Oceanography 28: 1252-1259.

Westrich, J. T. and R. A. Berner (1984). "The role of sedimentary organic matter in bacterial sulfate reduction: The G model tested." Limnology and Oceanography 29(2): 236-249.

Willet, H. C. (1987). Climatic responses to variable solar activity - past, present and predicted. Climate-history, periocity, and predictability. M. S. Rampino, J. E. Sanders, W. S. Newman and L. K. Künigsson. New York, Van Nostrand Reinhold: 404-414.

Willey, J. D. and A. J. Spivack (1997). "Dissolved silica concentrations and reactions in pore water from continental slope sediments off shore from Capre Hatteras, North Carolina, USA." Marine Chemistry 56: 227-238.

Wilson, D. and A. Leetmaa (1988). "Acoustic doppler current profiling in the equatorial Pacific in 1984." Journal of Geophysical Research 93: 13,947-13,966.

Wollast, R. (1974). The silica problem. Marine Chemistry. E. D. Goldberg. New York, London, Sydney, Toronto, Wiley-Interscience. 5: 359-392.

Wollast, R. and F. DeBroeu (1971). "Study of behaviour of dissolved silica in the estuary of the Schedlt." Geochimica et Cosmochimica Acta 35: 613-620.

Wyrtki, K. (1966). "Oceanography of the eastern Equatorial Pacific Ocean." Oceangraphic Marine Biology Annual Review 4: 33-68.

Yoder, J. A., S. Ackelson, R. Barber and P. Flament (1994). "A line in the sea." Nature 371: 689-692.